

## RF Pulsed Heating\*

David P. Pritzkau  
Stanford Linear Accelerator Center  
Stanford, CA 94309

SLAC-Report-577  
December 2001

Prepared for the Department of Energy  
under contract number DE-AC03-76SF00515

Printed in the United States of America. Available from the National Technical Information Service, U.S. Department of Commerce, 5285 Port Royal Road, Springfield, VA 22161.

---

\*Ph.D. thesis, Stanford Linear Accelerator Center, Stanford, CA 94309.

# RF PULSED HEATING

A DISSERTATION  
SUBMITTED TO THE DEPARTMENT OF APPLIED PHYSICS  
AND THE COMMITTEE ON GRADUATE STUDIES  
OF STANFORD UNIVERSITY  
IN PARTIAL FULFILLMENT OF THE REQUIREMENTS  
FOR THE DEGREE OF  
DOCTOR OF PHILOSOPHY

David Peace Pritzkau

August 2001

I certify that I have read this dissertation and that in my opinion it is fully adequate, in scope and quality, as a dissertation for the degree of Doctor of Philosophy.

---

Professor Robert H. Siemann  
(Principal Adviser)

I certify that I have read this dissertation and that in my opinion it is fully adequate, in scope and quality, as a dissertation for the degree of Doctor of Philosophy.

---

Professor Roger H. Miller

I certify that I have read this dissertation and that in my opinion it is fully adequate, in scope and quality, as a dissertation for the degree of Doctor of Philosophy.

---

Professor Helmut Wiedemann

Approved for the University Committee on Graduate Studies:

# Abstract

RF pulsed heating is a process by which a metal is heated from magnetic fields on its surface due to high-power pulsed RF. When the thermal stresses induced are larger than the elastic limit, microcracks and surface roughening will occur due to cyclic fatigue. Pulsed heating limits the maximum magnetic field on the surface and through it the maximum achievable accelerating gradient in a normal conducting accelerator structure. An experiment using circularly cylindrical cavities operating in the  $TE_{011}$  mode at a resonant frequency of 11.424 GHz is designed to study pulsed heating on OFE copper, a material commonly used in normal conducting accelerator structures. The high-power pulsed RF is supplied by an X-band klystron capable of outputting 50 MW, 1.5  $\mu$ s pulses. The test pieces of the cavity are designed to be removable to allow testing of different materials with different surface preparations. A diagnostic tool is developed to measure the temperature rise in the cavity utilizing the dynamic Q change of the resonant mode due to heating. The diagnostic consists of simultaneously exciting a  $TE_{012}$  mode to steady-state in the cavity at 18 GHz and measuring the change in reflected power as the cavity is heated from high-power pulsed RF. Two experimental runs were completed. One run was executed at a calculated temperature rise of 120 K for  $56 \times 10^6$  pulses. The second run was executed at a calculated temperature rise of 82 K for  $86 \times 10^6$  pulses. Scanning electron microscope pictures show extensive damage occurring in the region of maximum temperature rise on the surface of the test pieces.

# Acknowledgements

By far one of the most difficult parts of writing this dissertation is acknowledging all of the people who have helped or influenced me during my graduate years. There are simply too many to list.

I would first like to thank my research adviser and mentor Professor Robert Siemann. His guidance and assurance in my abilities have contributed enormously to my professional growth as a scientist. Even with a busy schedule, he has always found the time to offer his insights and advice. He has truly made my experience at SLAC a rich and rewarding one.

I would also like to thank the many members of the Accelerator Research Departments A and B and the Klystron department at SLAC. I am particularly grateful to Dr. David Whittum for his help in many aspects of microwave engineering and also to Professor Roger Miller for his valuable insights. I am equally grateful to Dr. Dennis Palmer and Dr. Eric Colby who were always willing to offer their advice and encouragement every step of the way. I am also grateful to Scott Beebe, Chris Pearson, Rich Talley, Bob Vanderzyl, Dr. Arnold Vlieks, and Chuck Yoneda for their help and support of my experiment. I am especially grateful to Al Menegat for his assistance throughout the experiment. His stories have also helped to keep me amused during the rough times. I would also like to thank Professor Helmut Wiedemann for his valuable comments on this manuscript.

I must also thank my fellow graduate students who have helped to make life interesting and rewarding at SLAC. I would especially like to thank my officemate Boris Podobedov for many interesting discussions that have helped me to grow as a scientist.

I would like to thank my parents who have gently guided and supported me throughout my life. It is with their love and encouragement that I have achieved my highest of aspirations. Were it not for the many sacrifices that my mother made for me, I would not be in this position today. Thus, I dedicate this dissertation to her.

Last I would like to thank my future wife Sharlene. Her everlasting love and support for me during the stressful times over the past year were instrumental to the completion of my thesis. She has been and will remain my guiding light in life.

# Contents

<b>Abstract</b>	<b>iv</b>
<b>Acknowledgements</b>	<b>v</b>
<b>1 Introduction</b>	<b>1</b>
1.1 Description of RF Pulsed Heating . . . . .	1
1.2 Relevance of RF Pulsed Heating to Accelerator Physics . . . . .	2
1.3 Thermal Fatigue of Metals . . . . .	5
1.3.1 Linear Elasticity and Thermal Stress . . . . .	6
1.3.2 Strength of Materials . . . . .	13
1.3.3 Cyclic Fatigue . . . . .	18
1.3.4 Thermal Fatigue Due to Pulsed Heating . . . . .	25
<b>2 Experimental Setup</b>	<b>29</b>
2.1 Cavity Design . . . . .	29
2.1.1 Choice Of Cavity Mode . . . . .	30
2.1.2 Choice Of Cavity Dimensions . . . . .	32
2.1.3 Choice Of Temperature Diagnostic . . . . .	36
2.1.4 Input Couplers . . . . .	38
2.1.5 Endcaps . . . . .	47
2.1.6 Water-Cooling . . . . .	55
2.1.7 Cold-Test Results . . . . .	65
2.2 Klystron setup . . . . .	78
2.2.1 Two-cavity setup . . . . .	79

2.2.2	One-cavity setup . . . . .	82
2.3	Diagnostic setup . . . . .	83
2.3.1	Measurement of Pulsed Temperature Rise and Cavity Q . . . . .	84
2.3.2	Measurement of Pulse Count . . . . .	87
<b>3</b>	<b>Theory</b>	<b>88</b>
3.1	Thermoelasticity . . . . .	88
3.2	Heat Conduction . . . . .	91
3.2.1	Green's Function Solutions . . . . .	92
3.2.2	1D Solution For Semi-Infinite Body . . . . .	94
3.2.3	Heat Conduction in Two Dimensions . . . . .	101
3.3	Pulsed Heating of Test Cavity . . . . .	109
3.3.1	Constant Cavity Parameters . . . . .	111
3.3.2	Temperature-Dependent Parameters . . . . .	112
3.3.3	Measurement of Pulsed Temperature Rise . . . . .	120
<b>4</b>	<b>Results</b>	<b>133</b>
4.1	First Test . . . . .	133
4.1.1	Run-Up Procedure . . . . .	135
4.1.2	Measurement of RF Power . . . . .	135
4.1.3	High-Power Results . . . . .	139
4.1.4	Endcap Removal . . . . .	150
4.1.5	Visual Inspection of Copper Endcap Surface . . . . .	150
4.1.6	Damage to High-Power Coupling Aperture . . . . .	153
4.1.7	Internal Cross-Section . . . . .	155
4.1.8	Scanning Electron Microscope Inspection of Copper Endcap Surface . . . . .	157
4.2	Second Test . . . . .	167
4.2.1	Run-Up Procedure . . . . .	167
4.2.2	Measurement of RF Power . . . . .	168
4.2.3	High-Power Results . . . . .	169
4.2.4	Visual Inspection of Copper Endcap Surface . . . . .	189

4.2.5	Scanning Electron Microscope Inspection of Copper Endcap Surface . . . . .	191
<b>5</b>	<b>Conclusion</b>	<b>196</b>
<b>A</b>	<b>Resonant Cavities</b>	<b>199</b>
A.1	Maxwell's Equations . . . . .	199
A.2	Expansion of Electromagnetic Fields in Cavities . . . . .	201
A.2.1	Basis Functions . . . . .	202
A.2.2	Cavity Modes . . . . .	203
A.3	Time-domain . . . . .	212
A.3.1	Perturbation From Lossy Walls . . . . .	215
A.3.2	Perturbation From Connecting Waveguide . . . . .	218
A.3.3	Mode Amplitudes . . . . .	221
A.3.4	Constant Cavity Parameters . . . . .	226
A.4	Cavity Circuit Parameters . . . . .	228
A.4.1	Cavity Response . . . . .	228
A.4.2	Reflection Coefficient For One-Port Cavity . . . . .	231
A.4.3	S-parameters For Two-Port Cavity . . . . .	240
A.4.4	Q Measurement With Lossy Coupling . . . . .	246
<b>B</b>	<b>SEM Pictures of Endcaps</b>	<b>251</b>
B.1	Endcap 1L1 . . . . .	251
B.2	Endcap 1R1 . . . . .	251
B.3	Endcap 2L1 . . . . .	251
B.4	Endcap 2R1 . . . . .	252
B.5	Endcap 1L2 . . . . .	252
B.6	Endcap 1R2 . . . . .	252
	<b>Bibliography</b>	<b>267</b>

# List of Tables

1.1	Parameters of fully annealed OFE copper at room temperature. . . .	4
2.1	Cavity design parameters for TE <sub>011</sub> mode. . . . .	36
2.2	Cavity design parameters for TE <sub>012</sub> mode. . . . .	38
2.3	Piston assembly and copper endcap surface preparation. . . . .	50
2.4	2D MAFIA simulation for endcaos with groove legnth of 0.99 mm. .	53
2.5	2D MAFIA simulation for endcaps with groove lengths of 2.49 mm. .	54
2.6	Parameters for water at room temperature. . . . .	57
2.7	Flow parameters for water-cooling of endcaps. . . . .	59
2.8	Flow parameters for water-cooling of the cavity body. . . . .	59
2.9	Measured parameters for the TE <sub>011</sub> mode of cavities 1 and 2. . . . .	67
2.10	Measured parameters for TE <sub>011</sub> mode of modified cavity. . . . .	71
2.11	Measured parameters for the TE <sub>012</sub> mode of modified cavity with high- power coupling aperture taped. . . . .	73
2.12	Two-port measurement of TE <sub>012</sub> mode with 2.49 mm axial grooves on endcaps. . . . .	75
2.13	Cold-test results of TE <sub>011</sub> mode for cavity 1 with 2.49 mm axial grooves on the endcaps. . . . .	76
2.14	Cold-test results of TE <sub>012</sub> mode for cavity 1 with 2.49 mm axial grooves on the endcaps. . . . .	78
3.1	Normalized temperature rise at surface for various skin-depths. . . .	99
3.2	Thermal data of pure copeer. . . . .	100
3.3	First 10 values of $\beta_m$ and $K_m$ . . . . .	105

3.4	Temperature rise for 1-D and 2-D equations at position $r = 1.0607$ cm for time $t = 1.0$ $\mu$ s. . . . .	105
3.5	Cavity design parameters from Chapter 2. . . . .	110
3.6	Data for temperature dependence of electrical resistivity for pure copper. . . . .	114
3.7	Cavity design parameters for the TE <sub>012</sub> mode from Chapter 2. . . . .	123
4.1	Cavity Q measurements of cavity 1 and 2 using HP8510C network analyzer before and after first high-power test. . . . .	139
4.2	Measurement of coupling coefficients for cavities 1 and 2 at end of high-power test. . . . .	142
4.3	Comparison of measurement of $Q_L$ for cavities 1 and 2 in the time and frequency-domain at the end of the first high-power test. . . . .	147
4.4	Widths of regions of surface roughening and cracks for each endcap from first high-power test. . . . .	164
4.5	Average radius and standard deviation of the distribution of crack positions shown in Figure 4.24 for each endcap. . . . .	165
4.6	Cavity Q measurements of TE <sub>011</sub> mode of cavity 1 using a network analyzer before and after second high-power test. . . . .	169
4.7	Cavity Q measurements of TE <sub>012</sub> mode of cavity 1 using a network analyzer before and after second high-power test. . . . .	170
4.8	Cavity Q measurements of TE <sub>012</sub> mode of cavity 1 using a network analyzer at resonant frequency 17.856 GHz. . . . .	171
4.9	Electrical resistivities of cavity endcaps and sidewall. . . . .	172
4.10	Electrical resistivities of endcaps in band of damage after second high- power test. . . . .	173
4.11	Measurement of $\beta$ at end of second high-power test. . . . .	174
4.12	Measurement of $Q_L$ at end of second high-power test. . . . .	176
4.13	Measurement of $\beta_1$ of TE <sub>012</sub> mode. . . . .	179
4.14	Measurement of $Q_L$ for TE <sub>012</sub> mode after second high-power test. . . . .	181
4.15	Widths of regions of surface roughening and cracks for endcaps 1L2 and 1R2. . . . .	195

# List of Figures

1.1	Gradient limits . . . . .	3
1.2	Stress components on an infinitesimal cube inside a body . . . . .	8
1.3	Block of material . . . . .	11
1.4	Static and cyclic stress-strain curves for fictitious material. . . . .	14
1.5	Detailed stress-strain curve for fictitious material. . . . .	14
1.6	Loading and unloading stress-strain curve for fictitious material. . . . .	15
1.7	Stress-strain curve showing offset yield stress. . . . .	16
1.8	Monotonic stress-strain curve showing elastic and plastic strain . . . . .	17
1.9	Cyclic stress-strain curve created by connecting tips of hysteresis loops. . . . .	19
1.10	Hysteresis loop . . . . .	19
1.11	Stabilized hysteresis curve from cyclic stress-strain curve. . . . .	21
1.12	Bauschinger effect . . . . .	22
1.13	Strain-life curve . . . . .	24
1.14	Metal surface being heated with a fast high-power source [41]. . . . .	26
1.15	Linear-elastic/perfectly-plastic stress-strain diagram for pulsed heating of metal surface [41]. . . . .	27
2.1	Circularly cylindrical cavity of radius $R$ and length $d$ . . . . .	30
2.2	Field pattern of $TE_{011}$ mode . . . . .	31
2.3	Temperature rise on cavity endcaps as function of $d$ and $Q_{ext}$ . . . . .	34
2.4	Temperature rise on cavity endcaps and sidewall. . . . .	34
2.5	Temperature rise on cavity endcaps as function of $\beta$ . . . . .	35
2.6	Field pattern of the $TE_{012}$ mode in a circularly cylindrical cavity of radius $R$ and length $d$ . . . . .	37

2.7	WR-90 waveguide with the dominant $TE_{10}$ mode shown. . . . .	39
2.8	Cavity-waveguide coupling configuration for $TE_{011}$ mode. . . . .	40
2.9	Coupling aperture at end of waveguide. . . . .	41
2.10	Geometry of high-power coupler modeled in GdfidL. . . . .	43
2.11	Field pattern of $TE_{011}$ mode modeled in GdfidL. . . . .	44
2.12	Determination of resonant frequency and $Q_{ext}$ for $TE_{011}$ mode. . . . .	45
2.13	Cavity-waveguide coupling configuration to excite $TE_{012}$ mode. . . . .	46
2.14	Geometry of diagnostic coupler modeled in GdfidL. . . . .	48
2.15	Field pattern of $TE_{012}$ mode modeled in GdfidL. . . . .	49
2.16	Determination of resonant frequency and $Q_{ext}$ for $TE_{012}$ mode. . . . .	50
2.17	Assembly schematic of endcap and piston. . . . .	51
2.18	Picture of RF breakdown along endcap piston due to $TE_{31}$ coaxial mode. . . . .	52
2.19	Close-up of endcap with grooves. . . . .	52
2.20	Spring gasket from BalSeal. . . . .	52
2.21	Assembly schematic of cavity with endcaps. . . . .	56
2.22	Schematic of spiral cut into back of endcaps. . . . .	58
2.23	Schematic of cooling tubes around circumference of cavity body. . . . .	60
2.24	Average temperature rise on cavity endcaps. . . . .	63
2.25	Average temperature rise on cavity sidewall. . . . .	64
2.26	Cavity body with endcap shown outside. . . . .	66
2.27	Magnitude and phase of the reflection coefficient for the $TE_{011}$ mode of cavity 1. . . . .	67
2.28	Magnitude and phase of the reflection coefficient for the $TE_{011}$ mode of cavity 2. . . . .	68
2.29	S-parameters for $TE_{012}$ mode of cavity 1. . . . .	69
2.30	S-parameters for $TE_{012}$ mode of cavity 2. . . . .	70
2.31	Picture of modified cavity used to test endcaps with different groove lengths. . . . .	71
2.32	$TE_{012}$ and $TE_{611}$ modes with high-power coupling aperture taped. . . . .	72
2.33	Reflection from diagnostic port of $TE_{012}$ mode with no grooves and copper tape removed. . . . .	73

2.34	Reflection from diagnostic port of TE <sub>012</sub> mode with 0.99 mm axial grooves on the endcaps. . . . .	74
2.35	Reflection from diagnostic port of TE <sub>012</sub> mode with 2.49 mm axial grooves on the endcaps. . . . .	75
2.36	Magnitude and phase of the reflection coefficient for the TE <sub>011</sub> mode of cavity 1 with 2.49 mm axial grooves on the endcaps. . . . .	76
2.37	S-parameters for TE <sub>012</sub> mode of cavity 1 with 2.49 mm axial grooves on endcaps. . . . .	77
2.38	Schematic of the two-cavity setup for high power tests. . . . .	79
2.39	Picture of two-cavity setup. . . . .	80
2.40	Close-up of one cavity of the two-cavity setup. . . . .	81
2.41	Schematic of the one-cavity setup for high-power tests. . . . .	83
2.42	Schematic of the diagnostic setup to measure pulsed temperature rise and cavity Q. . . . .	85
2.43	Example of reflected waveform from cavity when RF switch is opened. . . . .	87
3.1	One-dimensional semi-infinite slab. . . . .	95
3.2	Temperature rise at various times in conductor. . . . .	98
3.3	1-D and 2-D temperature rises for various times. . . . .	106
3.4	Relative error between 1-D and 2-D temperature rises for various times. . . . .	107
3.5	Point of maximum temperature rise for endcaps and cavity sidewall. . . . .	113
3.6	Surface temperature rise of endcaps and cavity sidewall as function of position during time of maximum temperature rise. . . . .	113
3.7	A plot of the linear fit of the electrical resistivity to temperature. . . . .	115
3.8	Comparison of expansion coefficient of magnetic field. . . . .	119
3.9	Comparison of temperature rise for cavity endcaps and sidewall. . . . .	119
3.10	Absolute error in temperature rise of cavity endcaps. . . . .	120
3.11	Comparison of variable $\rho_{res}$ with constant $\rho_{res}$ on the temperature rise of the cavity endcaps. . . . .	121
3.12	Comparison of variable $\rho_{res}$ with constant $\rho_{res}$ . on the temperature rise of the cavity sidewall. . . . .	121

3.13	Change in $Q_{011}$ and $Q_{012}$ due to heating of cavity. . . . .	122
3.14	Magnitude and phase of reflected signal from diagnostic port due to the change in $Q_{012}$ from pulsed heating. . . . .	125
3.15	Magnitude and phase of reflected signal from diagnostic port due to the change in $Q_{012}$ from pulsed heating and the fictitious change in $\omega_{012}$ . . . . .	128
3.16	Extracted $Q_{012}$ and $\omega_{012}$ from reflected signal data in Figure 3.15. . . . .	129
3.17	The extracted temperature rise of the cavity endcaps from $Q_{012}$ simulated data and the relative error. . . . .	131
4.1	A picture of the two-cavity setup attached to the klystron. The XL-3 klystron is seen in the background. The cavities are on the left and right of the setup in the lower part of the picture. . . . .	134
4.2	Schematic of 55-dB directional coupler. . . . .	136
4.3	Crystal calibrations for forward and reflected power. . . . .	137
4.4	Forward and reflected high-power waveforms for cavity 1 from first high-power test. . . . .	138
4.5	Variation of nominal value of $\beta$ for cavities 1 and 2 versus pulse count. . . . .	143
4.6	Forward waveforms for cavity 2 at 32 and 56 million pulses. . . . .	144
4.7	Reflected waveform from cavity 1 at end of first high-power test. . . . .	146
4.8	$Q_L$ for cavities 1 and 2 versus pulse count. . . . .	148
4.9	$Q_0$ for cavities 1 and 2 versus pulse count. . . . .	149
4.10	Picture of endcap 2L1. . . . .	151
4.11	Picture of high-power coupling aperture of cavity 1 after first high-power test. . . . .	154
4.12	Internal cross-section of endcap 2L1. . . . .	156
4.13	Schematic of creation of intrusions and extrusions on surface. . . . .	157
4.14	Comparison snapshot of region of maximum temperature rise to region of zero temperature rise. . . . .	158
4.15	Two close-ups of cracks. . . . .	159
4.16	Fatigue slip bands in area of maximum temperature rise on endcap 2R1. . . . .	159

4.17	Fatigue slip bands in area of maximum temperature rise on endcap 2R1. . . . .	160
4.18	Instance of cracks occurring along grain boundaries on endcap 1L1. . .	161
4.19	Two close-ups of cracks appearing in Figure 4.18. . . . .	161
4.20	Grain-boundary cracks in area of maximum temperature rise on endcap 2R1. . . . .	162
4.21	Cracks occurring in area of maximum temperature rise on endcap 1L1.	163
4.22	Close-ups of two cracks from Figure 4.21. . . . .	163
4.23	Random scans along diameters of each endcap from first high-power test. . . . .	164
4.24	Positions of cracks in densest areas on copper endcaps from first high-power test. . . . .	166
4.25	Forward power waveform for TE <sub>011</sub> mode during second high-power test.	168
4.26	Reflected waveform for TE <sub>011</sub> mode during second high-power test. .	169
4.27	Reflected waveform from TE <sub>011</sub> mode at end of second high-power test.	175
4.28	Measurement of $\beta$ and loaded Q of the TE <sub>011</sub> mode during the second high-power test. . . . .	176
4.29	Measurement of $Q_0$ during the second high-power test. . . . .	177
4.30	Forward and reflected waveforms from TE <sub>012</sub> mode using crystal detectors. . . . .	178
4.31	Measurement of $\beta_1$ versus pulse count for second high-power test. . .	180
4.32	Measurement of $Q_L$ versus pulse count for second high-power test. . .	181
4.33	Measurement of $Q_0$ versus pulse count for second high-power test. . .	182
4.34	Quadrature outputs from quadrature mixer during a typical measurement of reflected power from TE <sub>012</sub> mode. . . . .	183
4.35	Measured and theoretical reflection coefficients from TE <sub>012</sub> mode. . .	184
4.36	Measured and theoretical prediction in change of phase of reflected power from TE <sub>012</sub> mode. . . . .	185
4.37	Measured and theoretical prediction of change in $Q_{012}$ during a high-power pulse. . . . .	185

4.38	Measured and theoretical prediction of maximum temperature rise on endcaps. . . . .	186
4.39	Measurement of maximum pulsed temperature rise on the endcaps for the first 20 million pulses of the second high-power test. . . . .	187
4.40	Evolution of long-time effect on measurement of pulsed temperature rise on wider time scales. . . . .	188
4.41	Disappearance of stress-wave response in $TE_{012}$ mode. . . . .	189
4.42	Picture of endcaps 1L2 and 1R2 after second high-power test. . . . .	190
4.43	Grain-boundary cracks on endcap 1R2 in area of maximum temperature rise. . . . .	192
4.44	Grain-boundary crack on endcap 1R2 in area of maximum temperature rise. . . . .	192
4.45	Comparison between regions of maximum temperature rise and zero temperature rise on endcap 1R2. . . . .	193
4.46	Grain-boundary crack on endcap 1L2 in area of maximum temperature rise. . . . .	194
4.47	Random scans along diameters of endcaps 1L2 and 1R2. . . . .	195
A.1	Cylindrical waveguide of arbitrary cross-section with axis along $\hat{z}$ . . .	204
A.2	Closed cavity of length $d$ with arbitrary cross-section. . . . .	206
A.3	Circularly cylindrical cavity of radius $R$ and length $d$ . . . . .	208
A.4	Cavity with connecting waveguide. . . . .	214
A.5	Conductor with coordinate $\xi$ normal to the surface and pointing into the conductor. . . . .	216
A.6	$V_1^-(t)/V_1^+$ for various $\beta$ . . . . .	234
A.7	$ V_1^-(t)/V_1^+ ^2$ for various $\beta$ . . . . .	236
A.8	$S_{11}(\omega)$ . . . . .	238
A.9	S-parameters of two-port cavity for $\beta_1 = 0.75$ and $\beta_2 = 0.15$ . . . . .	243
A.10	Output from QZERO program. . . . .	247
B.1	Pictures of cracks on endcap 1L1. . . . .	253
B.2	Pictures of cracks on endcap 1L1 at high magnification. . . . .	254

B.3	Pictures of cracks on endcap 1R1. . . . .	255
B.4	Pictures of cracks on endcap 1R1 at high magnification. . . . .	256
B.5	Pictures of cracks on endcap 2L1. . . . .	257
B.6	Pictures of cracks on endcap 2L1 at high magnification. . . . .	258
B.7	Pictures of cracks on endcap 2R1. . . . .	259
B.8	Pictures of cracks on endcap 2R1 at high magnification. . . . .	260
B.9	Pictures of damage on endcap 1L2. . . . .	261
B.10	Additional pictures of damage on endcap 1L2. . . . .	262
B.11	Pictures of cracks on endcap 1L2 at high magnification. . . . .	263
B.12	Pictures of damage on endcap 1R2. . . . .	264
B.13	Additional pictures of damage on endcap 1R2. . . . .	265
B.14	Pictures of cracks on endcap 1R2 at high magnification. . . . .	266

# Chapter 1

## Introduction

### 1.1 Description of RF Pulsed Heating

Pulsed heating is a transient process by which materials (usually metals) are heated by a pulsing source. This type of heating is in contrast to steady-state heating in which the source is always active. Hence, pulsed heating causes the temperature in the material or on its surface to cycle with the same repetition rate as the source. After the source is switched off, the temperature inside the material usually decays close to its ambient value by the time the source is active again.

*RF (Radio Frequency)* is a term used to denote time-varying electromagnetic fields. Essentially, *RF pulsed heating* is a process in which a metal is heated with a pulsed RF source of power. The basic mechanism of this process is the local Joule heating that occurs on the metal surface due to eddy currents created from pulsed RF. Intuitively, if we ignore radiation effects, the heat deposited on the surface of the metal must flow into the material. The heat flow is governed by the well-known heat diffusion equation

$$\nabla^2 T(\vec{r}, t) + \frac{1}{k} g(\vec{r}, t) = \frac{1}{\alpha_d} \frac{\partial T}{\partial t}, \quad (1.1)$$

where  $T(\vec{r}, t)$  is temperature (K),  $\vec{r}$  is position (m),  $t$  is time (s),  $g(\vec{r}, t)$  is power per unit volume ( $\text{W}/\text{m}^3$ ),  $k$  is thermal conductivity ( $\text{W}/\text{m}\cdot\text{K}$ ),  $\alpha_d = k/\rho c_\varepsilon$  is thermal diffusivity ( $\text{m}^2/\text{s}$ ) where  $\rho$  is density in ( $\text{kg}/\text{m}^3$ ) and  $c_\varepsilon$  is specific heat at constant

strain in (J/kg·K). It will be shown later that the temperature rise on the surface of the metal is maximum for heat deposited on the surface.

Stress is induced on the metal surface when the heating occurs faster than the metal has time to expand. The thermal expansion of metal is limited in time by the velocity of sound in the material. If the induced stress from each RF pulse is above a certain threshold, known as the yield strength, then damage in the form of microcracks will eventually occur. The damage may not manifest until after many RF pulses are applied to the material. This damage process is known as *thermal fatigue* which is described in more detail in section 1.3. Thermal fatigue from pulsed heating may eventually cause the material to be unusable.

## 1.2 Relevance of RF Pulsed Heating to Accelerator Physics

The frontier of accelerator physics aims to achieve higher center-of-mass energies for particle collisions. Under present technology, the cost and length of conventional RF accelerators become prohibitive at center-of-mass energies starting at 1 TeV. Current research is ongoing in advanced accelerator concepts to achieve such energies with reasonable cost. One such focus of this research is to attain higher gradients in RF linear accelerators. In order to obtain reasonable accelerator lengths and AC power requirements it is necessary to operate at shorter wavelengths as compared to the linear accelerator at SLAC (currently operating at  $\lambda = 10.5$  cm) [58]. Such research involves studying the limits of high gradients due to phenomena such as RF breakdown, dark current trapping and, of course, pulsed heating. It is interesting to consider these limitations as a function of RF wavelength.

Dark current trapping occurs when field emitted electrons are accelerated to relativistic energies in an RF cycle and trapped by a travelling RF wave in the accelerator [50]. This phenomenon can cause beam loading and random deflecting wakefields

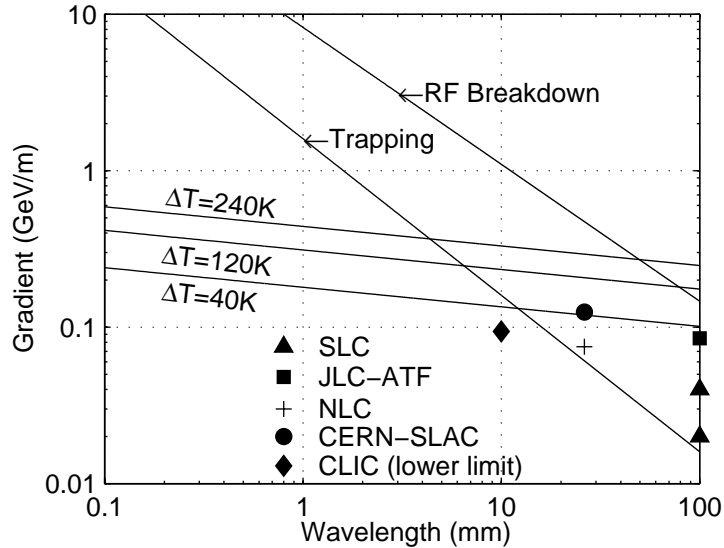


Figure 1.1: Gradient limits due to dark current trapping, RF breakdown, and pulsed heating. The data points represent gradient achieved with reasonable dark current [50].

and occurs when the gradient exceeds [58]

$$G_{trap} = \frac{1.6 \text{ MeV}}{\lambda}. \quad (1.2)$$

RF breakdown is characterized by pulse shortening and high-power spikes caused by the emission of absorbed gas from the surface of the metal into the high-power vacuum device. There is little understanding of the underlying causes of RF breakdown, but with the guidance of some experiments [35, 56] a convenient scaling is obtained [58]

$$G_{break} = \frac{1.1 \text{ GeV/m}}{[\lambda(\text{cm})]^{7/8}}. \quad (1.3)$$

These two scalings are shown in Figure 1.1 along with gradients measured at different wavelengths [50].

Pulsed heating can cause another limit to high gradients which arises when the metal surface yields due to pulsed temperature rises. This limitation is considered in more detail in the sections that follow, but the criterion is related to the induced stress

$\rho$	$8.95 \times 10^3 \text{ kg/m}^3$
$c_\varepsilon$	$385 \text{ J/kg} \cdot \text{K}$
$k$	$391 \text{ W/m} \cdot \text{K}$
$\alpha$	$1.67 \times 10^{-5} \text{ K}^{-1}$
$E$	$1.23 \text{ GPa}$
$\nu$	$0.345$
$\sigma_y$	$34 \text{ MPa}$
$\sigma'_f$	$426 \text{ MPa}$ [7, p. 88]
$\varepsilon'_f$	$0.29$ [7, p. 88]
$b$	$-0.11$ [7, p. 88]
$c$	$-0.51$ [7, p. 88]
$\sigma_c$	$5.8 \times 10^7 \text{ S}$

Table 1.1: Parameters of fully annealed OFE copper at room temperature.

exceeding the yield strength of the material. Equation (1.29) gives the temperature rise at which the induced stress from pulsed heating of a metal surface will exceed its yield strength. Noting that damage will accumulate when the temperature rise is twice this value (see section 1.3.4) and using the values given in Table 1.1 for fully annealed OFE copper, we expect the damage threshold to be  $\Delta T = 40 \text{ K}$ . Other sources have quoted a threshold value for damage to be  $\Delta T = 110 \text{ K}$  for OFE copper due to heating from pulsed electron flux [23, 42]. The calculation of the  $\Delta T = 110 \text{ K}$  threshold assumed that the dynamic yield strength is about three times higher than the static one quoted in Table 1.1. The value of the yield strength of copper in the regime of RF pulsed heating is not known. It is also not known if damage due to pulsed heating from RF is different from pulsed electron flux since electrons have a higher penetration depth than electromagnetic fields in metal.

A convenient scaling for pulsed temperature rise is [58]

$$\Delta T = \frac{G^2 \sqrt{T_p}}{Z_H^2} \frac{R_s}{\sqrt{\pi \rho c_\varepsilon k}}, \quad (1.4)$$

where  $G$  is unloaded gradient,  $T_p$  is the RF pulse length,  $R_s$  is the surface resistance,  $\rho$  is the density,  $c_\varepsilon$  is the specific heat at constant strain, and  $k$  is the thermal

conductivity. The impedance  $Z_H$  is the ratio

$$Z_H = \frac{G}{H_{max}}, \quad (1.5)$$

where  $H_{max}$  is the maximum surface magnetic field. The surface resistance is given by

$$R_s = \sqrt{\frac{\pi \mu C_{light}}{\lambda \sigma_c}}, \quad (1.6)$$

where  $\lambda$  is the RF wavelength and  $\sigma_c$  is the metal conductivity. Equation (1.4) will be derived in Chapter 3. If we use the values for NLC (Next Linear Collider,  $\lambda = 2.6\text{cm}$ ),  $Z_H = 300\Omega$  and  $T_p = 360\text{ns}$ , scale RF pulse length with filling time,  $T_p \sim \lambda^{3/2}$  [34, 50] and use the values in Table 1.1 we get

$$G_{pulse} = (28 \text{ MeV/m}) \frac{\Delta T^{1/2}}{[\lambda(\text{mm})]^{1/8}}. \quad (1.7)$$

Various temperature rises have been plotted in Figure 1.1. As Figure 1.1 shows, pulsed heating becomes an important impediment to higher gradients at shorter wavelengths as compared to RF breakdown and dark current trapping. Based on the above results, an experiment, which is described in Chapter 2, has been created to test OFE copper at various temperature rises. The goal is to experimentally demonstrate the dangers of pulsed heating to future accelerator designs.

### 1.3 Thermal Fatigue of Metals

Analysis of heating is important for determining the behavior of the material in various applications. Specifically, one worries about damage induced in the material by thermal loads that render the material unusable. Usually the first criterion that is met is that the temperature rise due to pulsed heating must be less than the melting point of the material. In high-power RF applications, which due to electric breakdown in air must be performed under high vacuum, this criterion limits the energy that may be applied in a single pulse. There are, of course, other limits to high-power RF, such as RF breakdown, that do not directly depend on Joule heating. Such limitations

will not be discussed here.

The melting of metal is an important, and perhaps obvious, limitation of high power. However, damage to metals may occur from thermally-induced stress due to temperature changes much lower than necessary to melt the surface. “Damage” is used loosely to describe an unwanted permanent change in the material. For some applications damage could simply mean cracks of a certain length on the surface (*fracture*). For other applications, damage could be nothing more than *surface roughening* in which the surface finish of a metal is no longer as good as it was initially.

Obviously the amount of stress necessary to cause damage depends on the properties of the material. However, damage may not occur in metals until stress has been repeatedly applied many times. This type of damage mechanism is known as *fatigue* or *cyclic fatigue*. When the stress is thermally-induced this mechanism is known as *thermal fatigue*. The level of stress necessary to cause fatigue is much lower than that which is necessary to cause damage in one pulse or cycle. Before we discuss thermal fatigue in more detail, it would be worthwhile to review some elasticity theory.

### 1.3.1 Linear Elasticity and Thermal Stress

Forces distributed over the surface of a body are called *surface forces*. The surface force per unit area is known as *stress*. Internal stresses in a body are surface forces that result from physical contact between two imaginary surfaces in the body. The deformation of a body is found by considering the *displacements* of particles in the body. Only displacements that result in deformation of the body and not rigid-body movement are considered. *Strains* are the relative elongations or distortion of angles between these sets of particles.

In general, materials will deform under applied loads or stresses. The *theory of elasticity* [8, 12, 29, 52, 55] describes such deformations as long as the deformations are “small” in the sense that when the loads disappear so do the deformations. A material is said to be elastic in this range of stresses. When the applied stress is larger than this *elastic limit* then permanent deformation will occur. Basically, when these stresses are removed the material will not revert back to its original size or shape

depending on the nature of the applied stress. The material is said to be *plastic* in this region, and the *theory of plasticity* [8] will be needed to describe the deformation of the material.

In this section we will only discuss *linear elasticity* in order to place more emphasis on the basic physics involved in the study of pulsed heating. Linear elasticity describes the situation in which the stress is proportional to the strain. This property depends on the material, but it is usually a good assumption in practice. Also, we will assume that the material is isotropic, meaning that the properties of the material do not depend on the coordinate direction. We will limit our discussion to cartesian coordinates for purposes of illustration.

Based on the assumptions given above, there are a total of 15 components needed to describe the material under applied loads. In cartesian coordinates these components are the 6 stress components  $\sigma_{xx}, \sigma_{yy}, \sigma_{zz}, \sigma_{xy}, \sigma_{yz}, \sigma_{xz}$ , the 6 strain components  $\varepsilon_{xx}, \varepsilon_{yy}, \varepsilon_{zz}, \varepsilon_{xy}, \varepsilon_{yz}, \varepsilon_{xz}$ , and the 3 displacement components  $u_x, u_y, u_z$ . We only need six stress components and six strain components instead of nine, because we assumed the material is isotropic which gives  $\sigma_{ij} = \sigma_{ji}$  and  $\varepsilon_{ij} = \varepsilon_{ji}$ . Figure 1.2 shows the positive orientation of the stress components on an infinitesimal cube inside a body.

It must be remembered that stress and strain are second-order tensors. One cannot think of these components as vector components unless you define a reference plane. Hence the shear stress components  $\sigma_{xy}, \sigma_{yz}, \sigma_{xz}$  may be zero with respect to one plane and nonzero with respect to another. This fact will be important when considering metals with grain boundaries.

There are 15 equations necessary to uniquely solve for the stress, strain, and displacement in a body. The first three equations involve the stress components and are known as the *equilibrium equations*. These equations are independent of the material properties and are derived solely from the consideration of equilibrium of the body:

$$\left. \begin{aligned} \frac{\partial \sigma_{xx}}{\partial x} + \frac{\partial \sigma_{xy}}{\partial y} + \frac{\partial \sigma_{xz}}{\partial z} + F_x &= 0 \\ \frac{\partial \sigma_{xy}}{\partial x} + \frac{\partial \sigma_{yy}}{\partial y} + \frac{\partial \sigma_{yz}}{\partial z} + F_y &= 0 \\ \frac{\partial \sigma_{xz}}{\partial x} + \frac{\partial \sigma_{yz}}{\partial y} + \frac{\partial \sigma_{zz}}{\partial z} + F_z &= 0 \end{aligned} \right\}, \quad (1.8)$$

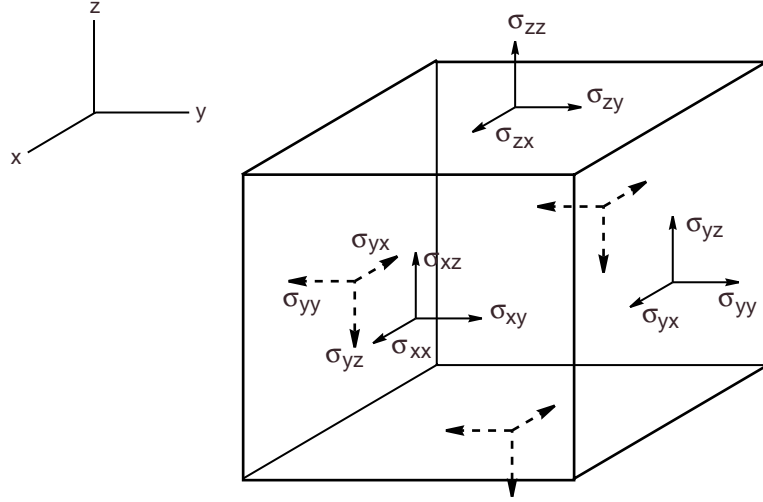


Figure 1.2: Stress components on an infinitesimal cube inside a body. Arrows show direction of positive stress.

where  $F_x$ ,  $F_y$ , and  $F_z$  are *body force intensities* or body forces per unit volume. Body forces are forces associated with the mass of the body and are distributed throughout its volume. Body forces also include the effect of inertia forces which are important in the study of pulsed heating. The inertia forces are given below

$$F_x = -\rho \frac{\partial^2 u_x}{\partial t^2}, \quad F_y = -\rho \frac{\partial^2 u_y}{\partial t^2}, \quad F_z = -\rho \frac{\partial^2 u_z}{\partial t^2}, \quad (1.9)$$

where  $\rho$  is the mass density of the material ( $\text{kg/m}^3$ ).

The next set of equations are known as the *strain-displacement relations*. They are derived from purely geometrical considerations and are also independent of material properties.

$$\left. \begin{aligned} \varepsilon_{xx} &= \frac{\partial u_x}{\partial x} \\ \varepsilon_{yy} &= \frac{\partial u_y}{\partial y} \\ \varepsilon_{zz} &= \frac{\partial u_z}{\partial z} \\ \varepsilon_{xy} &= \frac{1}{2} \left( \frac{\partial u_x}{\partial y} + \frac{\partial u_y}{\partial x} \right) \\ \varepsilon_{yz} &= \frac{1}{2} \left( \frac{\partial u_y}{\partial z} + \frac{\partial u_z}{\partial y} \right) \\ \varepsilon_{xz} &= \frac{1}{2} \left( \frac{\partial u_x}{\partial z} + \frac{\partial u_z}{\partial x} \right) \end{aligned} \right\} \quad (1.10)$$

The last six equations are known as the *stress-strain relations* or *generalized Hooke's law*. They are constitutive relations that depend directly on the properties of the material. As mentioned before, these relations embody the assumptions of linear elasticity:

$$\left. \begin{aligned} \varepsilon_{xx} &= \frac{1}{E}[\sigma_{xx} - \nu(\sigma_{yy} + \sigma_{zz})] + \alpha T \\ \varepsilon_{yy} &= \frac{1}{E}[\sigma_{yy} - \nu(\sigma_{zz} + \sigma_{xx})] + \alpha T \\ \varepsilon_{zz} &= \frac{1}{E}[\sigma_{zz} - \nu(\sigma_{xx} + \sigma_{yy})] + \alpha T \\ \varepsilon_{xy} &= \frac{1}{2G}\sigma_{xy} \\ \varepsilon_{yz} &= \frac{1}{2G}\sigma_{yz} \\ \varepsilon_{xz} &= \frac{1}{2G}\sigma_{xz} \end{aligned} \right\}, \quad (1.11)$$

where  $E$  is Young's modulus (Pa),  $\alpha$  is the coefficient of linear thermal expansion ( $\text{K}^{-1}$ ),  $T$  is temperature (K),  $\nu$  is Poisson's ratio, and  $G = E/2(1 + \nu)$  is the shear modulus (Pa). Hooke's law may also be written in terms of stresses:

$$\left. \begin{aligned} \sigma_{xx} &= \lambda e + 2\mu\varepsilon_{xx} - (3\lambda + 2\mu)\alpha T \\ \sigma_{yy} &= \lambda e + 2\mu\varepsilon_{yy} - (3\lambda + 2\mu)\alpha T \\ \sigma_{zz} &= \lambda e + 2\mu\varepsilon_{zz} - (3\lambda + 2\mu)\alpha T \\ \sigma_{xy} &= 2\mu\varepsilon_{xy} \\ \sigma_{yz} &= 2\mu\varepsilon_{yz} \\ \sigma_{xz} &= 2\mu\varepsilon_{xz} \end{aligned} \right\}, \quad (1.12)$$

where  $e = \varepsilon_{xx} + \varepsilon_{yy} + \varepsilon_{zz}$  is known as the *dilatation*, and  $\lambda$  and  $\mu$  are known as the Lamé elastic constants and are related to  $E$  and  $\nu$  as follows:

$$\lambda = \frac{\nu E}{(1 + \nu)(1 - 2\nu)}, \quad (1.13a)$$

$$\mu = \frac{E}{2(1 + \nu)} = G. \quad (1.13b)$$

The following relations also hold:

$$E = \frac{(3\lambda + 2\mu)\mu}{\lambda + \mu}, \quad (1.14a)$$

$$\nu = \frac{\lambda}{2(\lambda + \mu)}. \quad (1.14b)$$

Notice that thermal strain is also included in equations (1.11) with the  $\alpha T$  term. Since thermal expansion is isotropic (it can only change the size of a body and not its shape), the shear strains  $\varepsilon_{xy}$ ,  $\varepsilon_{yz}$ , and  $\varepsilon_{xz}$  are not affected by temperature. Also note that these equations assume that the reference temperature is 0 K. We will keep this assumption for convenience.

According to Hooke's law, once the stress and temperature distributions in a body are known, the strain distribution is easily found. If the body is simply heated with no applied surface forces then equations (1.11) reduce to the common thermal-expansion equation  $\Delta L = \alpha L \Delta T$  where  $L$  is the length of the body in a particular coordinate direction. Using this fact as a guide, we can separate the normal strains  $\varepsilon_{xx}$ ,  $\varepsilon_{yy}$ , and  $\varepsilon_{zz}$  in equations (1.11) into mechanical and thermal strains  $\varepsilon_{total} = \varepsilon_{mech} + \varepsilon_{therm}$ . This distinction will help us understand the physical mechanism behind thermal stresses.

*Thermal stresses* arise when a body is heated but is constrained from expanding. We can imagine heating a long, thin bar that is clamped at its ends. Because the bar is constrained, the total strain is zero since the bar cannot physically expand. A mechanical strain is set up from the constraint to oppose the thermal expansion. This constraint causes stress to build up in the bar.

Since the 15 equations of elasticity are linear, it is perhaps more intuitive to think of this example in terms of superposition. First, we heat up the bar without any constraints and allow it to expand longitudinally. Next, we physically compress the bar back to its original length. The stress necessary to create this mechanical strain is the same as the thermal stress that would arise if we prevented the bar from expanding originally. Thus thermal stresses are the same as physical stresses.

It will be interesting to further explore these ideas with some calculations. Let us

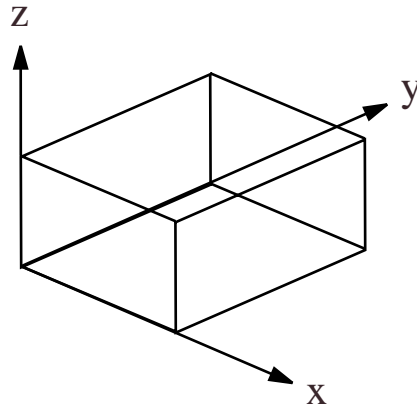


Figure 1.3: Block of material

examine a block of material as shown in Figure 1.3 that is initially at a temperature of 0 K. We will heat the material to a temperature  $T$  under various mechanical constraints. All results are derived using Hooke's law (1.11) or (1.12):

Case 1: No constraints in all directions ( $\sigma_{xx} = \sigma_{yy} = \sigma_{zz} = 0$ )

$$\varepsilon_{xx} = \varepsilon_{yy} = \varepsilon_{zz} = \alpha T.$$

Case 2: Constrained in x-direction, but free to expand in y and z-directions

$$(\sigma_{yy} = \sigma_{zz} = 0, \varepsilon_{xx} = 0)$$

$$\sigma_{xx} = -E\alpha T$$

$$\varepsilon_{yy} = \varepsilon_{zz} = \alpha T(1 + \nu).$$

Case 3: Constrained in x and y-directions, but free to expand in z-direction

$$(\sigma_{zz} = 0, \varepsilon_{xx} = \varepsilon_{yy} = 0)$$

$$\sigma_{xx} = \sigma_{yy} = -\frac{E\alpha T}{1-\nu}$$

$$\varepsilon_{zz} = \frac{1+\nu}{1-\nu}\alpha T.$$

Case 4: Constrained in all directions ( $\sigma_{xx} = \sigma_{yy} = \sigma_{zz} = -\frac{E\alpha T}{1-2\nu}$ )

$$\varepsilon_{xx} = \varepsilon_{yy} = \varepsilon_{zz} = 0.$$

For most metals,  $\nu \simeq 1/3$ . Therefore, one can see that the more mechanical constraints placed on a body, the higher the thermal stress will be when the body is heated. Also note that the stresses derived above are compressive. If we had started with the material stress-free at a temperature  $T$  and then let it cool down to 0 K, the stresses would be tensile but with the same magnitude as given earlier.

A material subjected to pulsed heating would behave similarly to the example considered above. The major difference is that the mechanical constraint is due to the inertia of the material itself, because the body or the surface of the material is heated and cooled on a small time scale. Therefore one must take into account the propagation of sound waves in the material which will cause the stress in the material to relax over time as the body is allowed to expand. The physics of this situation is contained in the equations (1.8), (1.9), (1.10), and (1.11). Therefore, a full dynamic calculation must be done before the stress can be determined. However, as a first approximation, if the body is large enough in a certain dimension we may assume that the total strain in that dimension is zero during the heating of the material. The results derived in the example above then directly apply. This simplification will serve as a guide to understanding the dynamic stresses that exist due to pulsed heating.

### 1.3.2 Strength of Materials

The knowledge of the stress and strain in a body are important for the study of fatigue of materials. There are some empirical relationships that relate the lifetime of a given material to the stress or strain state that exists in the body. These relations are obviously important for engineering designs of mechanical components. We will attempt to extend these ideas to the study of pulsed heating, but first we must review some details about the strength of materials [3, 49].

Many studies on the fatigue of materials focus on uniaxial fatigue where the applied stress or strain on a body occurs in only one direction. Studies of multiaxial fatigue are harder to interpret and there is much more data available for materials experiencing uniaxial loads. So in this section, stress and strain are to mean stress and strain in the direction of the uniaxial load.

All metals follow a characteristic curve known as the *stress-strain curve*. These curves basically describe the behavior of a material under applied stresses or strains and are divided into two classes, the *static or monotonic stress-strain curve* and the *cyclic stress-strain curve*. The static stress-strain curve describes the behavior of a material under a static or non-varying load while the cyclic stress-strain curve describes the behavior of a material under a cyclic load. Metals in general behave differently under these two conditions. An example is shown in Figure 1.4. Although these curves will vary from material to material, they all have some general characteristics that most metals share.

Figure 1.5 shows a particular stress-strain curve in detail. For low values of stress or strain the curve is linear with the proportionality constant being Young's modulus  $E$ . This region of the curve describes linear elastic deformation in which the deformation disappears when the load is removed. Some materials deviate from linearity when the stress is above the *proportional limit*. This region of the curve describes nonlinear elastic deformation. Although the strain varies nonlinearly with respect to the applied stress, the deformation still disappears when the load is removed. The curve is basically retraced back to the origin as the material is unloaded. When the applied stress is above the *elastic limit*, the material will experience a permanent deformation that remains after the load is removed. For some materials it is hard

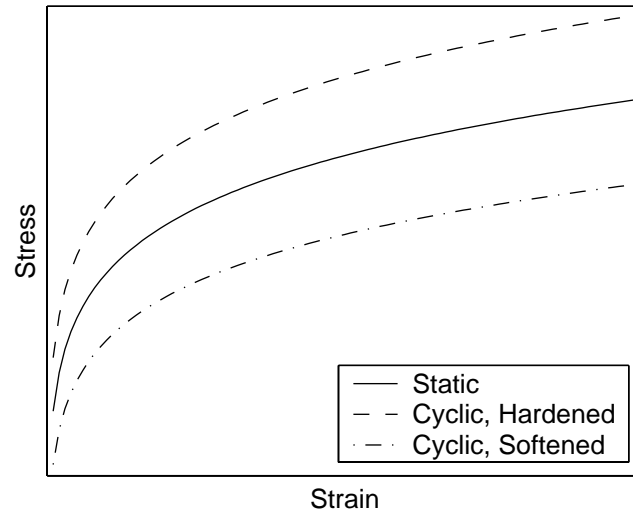


Figure 1.4: Static and cyclic stress-strain curves for fictitious material.

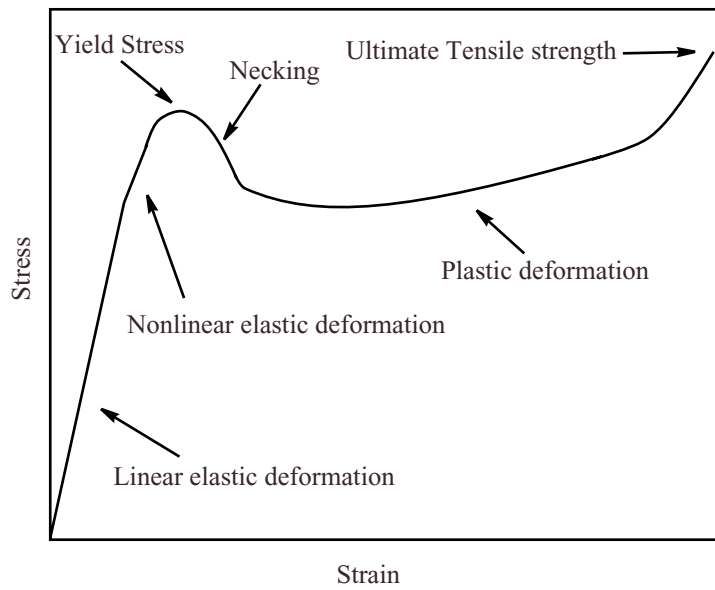


Figure 1.5: Detailed stress-strain curve for fictitious material.

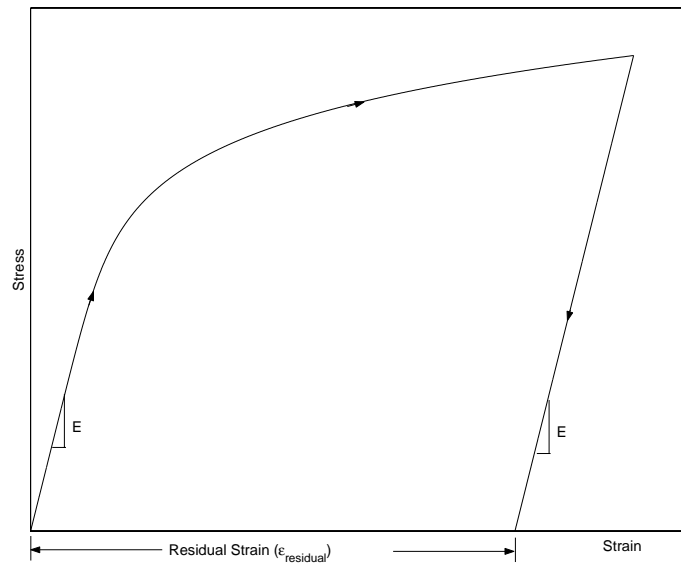


Figure 1.6: Loading and unloading stress-strain curve for fictitious material.

to distinguish between the proportional limit and the elastic limit since their values are close to each other. Above the elastic limit the material will unload along a path parallel to the elastic region offset from the origin as shown in Figure 1.6.

The elastic limit signifies the beginning of the yielding process. Microscopically, the planes of atoms in the material begin to *slip* to new equilibrium positions which results in permanent deformation. For some metals like iron, there is a point where the stress-strain curve has zero slope. This point is called the *yield stress* after which *plastic deformation* will occur. These metals also exhibit dips in their stress-strain curves known as *necking*. Other metals like copper, which begin to show slip but do not have zero slopes in their stress-strain curves or necking, have their yield stress determined by drawing a line parallel to the elastic deformation region but offset by an amount of 0.2 percent on the strain axis as shown in Figure 1.7. This point is called the *offset yield stress*.

Most materials can be classified into two different groups depending on how they behave in the plastic deformation regime. Most metals are termed *ductile* because they show significant yielding evident in the amount of slip in the material under test. Materials that are highly resistant to slip are termed *brittle*. The stress required

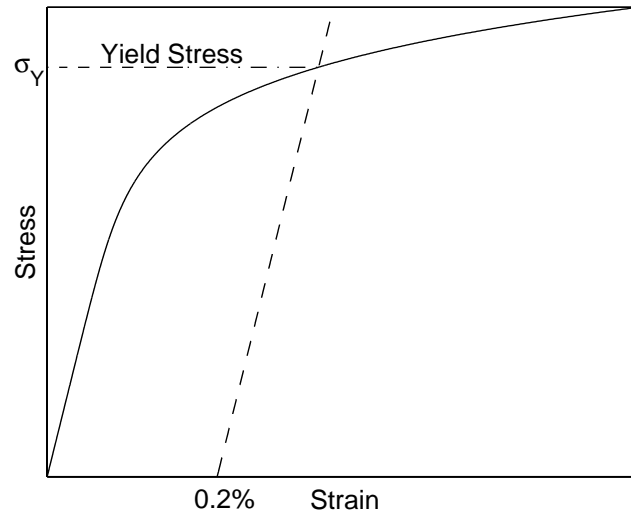


Figure 1.7: Stress-strain curve showing offset yield stress.

to cause slip in brittle materials is so high that the material simply fractures first. The tensile stress required to cause *fracture* in either ductile or brittle materials, defined by the separation of a block of material into two or more pieces, is denoted the *ultimate tensile strength* or *UTS* or  $\sigma_{UTS}$ .

As mentioned before, plastic deformation will occur when the applied stress exceeds the yield strength of the material. The material will no longer unload along the original path in the stress-strain curve. The material will unload along a path that is parallel to the elastic deformation region and is known as the *unloading curve*. As shown in Figure 1.6, *residual strain* will be left in the material when the applied stress is zero.

So far the discussion of the stress-strain curve only involved the use of tensile stresses. Most of the points made above also apply to compression. However, there is no general fracture point for compression. The material is more likely to *buckle* before it fractures. By convention compressive stresses and strains are negative.

For most metals the monotonic stress-strain curve can be modeled using a power function for stress as a function of plastic strain

$$\sigma = K(\varepsilon_p)^n, \quad (1.15)$$

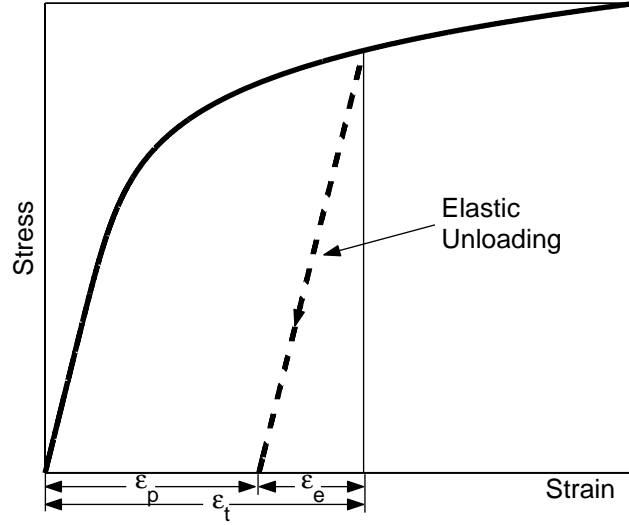


Figure 1.8: Monotonic stress-strain curve showing elastic and plastic strain

where  $K$  is the *strength coefficient* and  $n$  is the *strain hardening exponent*. By knowing the stress at final fracture called the *fracture strength*,  $\sigma_f$ , and the strain at final fracture called the *fracture ductility*,  $\epsilon_f$ , one can determine  $K$  using equation (1.15)

$$K = \frac{\sigma_f}{\epsilon_f^n}. \quad (1.16)$$

The total strain can be expressed as (see Figure 1.8)

$$\epsilon_t = \epsilon_e + \epsilon_p. \quad (1.17)$$

If we define the elastic strain as

$$\epsilon_e = \frac{\sigma}{E}, \quad (1.18)$$

then equation (1.17) can be expressed as

$$\epsilon_t = \frac{\sigma}{E} + \left(\frac{\sigma}{K}\right)^{1/n}. \quad (1.19)$$

We stated previously that the static and cyclic stress-strain curves are usually different (see Figure 1.4). This difference is due to the phenomenon known as *strain*

*hardening* and *strain softening*. Some metals like copper experience strain hardening where the metal gets stronger after a certain amount of cycles. The static stress-strain curve will gradually change towards the cyclic stress-strain curve and eventually stabilize there. For metals that strain-harden like fully-annealed OFE copper this means that the stress necessary to induce a certain strain will be higher than a previously unloaded sample. The opposite condition occurs for materials that strain-soften. This phenomenon is important in the consideration of cyclic fatigue.

### 1.3.3 Cyclic Fatigue

A large amount of information has been gathered on the area of cyclic fatigue of metals. Only some of the relevant basics will be introduced here and can be found in many references [3, 7, 22, 44, 53].

It is known that damage due to fatigue does not occur until the material undergoes plastic deformation in which the applied stress exceeds the yield strength of the material. When this condition occurs failure of metals due to cyclic fatigue is characterized by three stages: cyclic hardening/softening, crack nucleation, and crack propagation.

#### Cyclic Hardening/Softening

*Cyclic hardening/softening* or strain hardening/softening is the process by which the static stress-strain curve of a material transforms and stabilizes to the cyclic stress-strain curve. Usually cyclic hardening/softening only occurs during the first few percent of the cycles to failure. For stress amplitudes larger than the yield strength, the stress-strain history of the material follows a hysteresis loop in which a material unloads along a different path from the static stress-strain curve (see Figure 1.6). To establish the cyclic stress-strain curve, materials are tested at several different stress amplitudes above the yield strength until a stable hysteresis loop is found for each stress amplitude. The cyclic stress-strain curve is created by connecting the tips of these hysteresis loops (see Figure 1.9).

Figure 1.10 shows one particular hysteresis loop in detail in which a material is

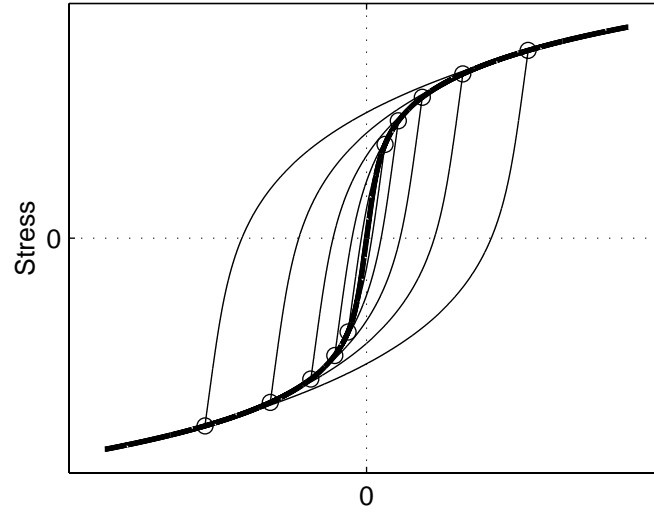


Figure 1.9: Cyclic stress-strain curve created by connecting tips of hysteresis loops.

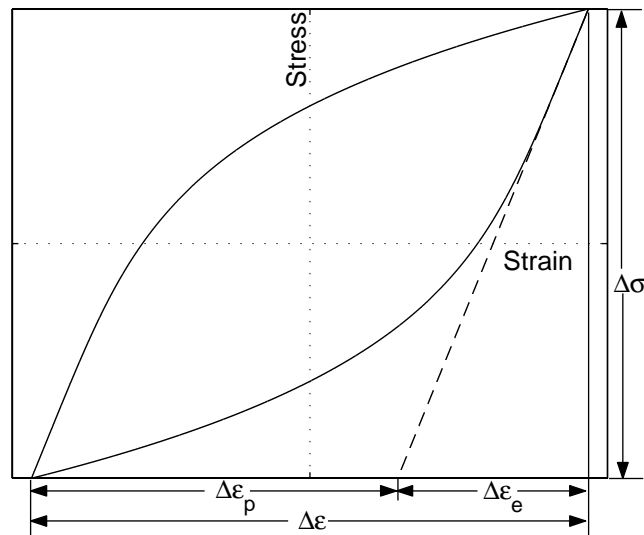


Figure 1.10: Hysteresis loop

cyclically loaded in tension and compression. The total stress range,  $\Delta\sigma$ , is the total height of the loop and the total strain range,  $\Delta\varepsilon$ , is the total width of the loop. The total strain is the sum of the elastic and plastic strain ranges as shown in Figure 1.10

$$\Delta\varepsilon = \Delta\varepsilon_e + \Delta\varepsilon_p. \quad (1.20)$$

Using Hooke's law, the elastic term can be replaced with  $\Delta\sigma/E$ . If we define the stress amplitude as  $\sigma = \Delta\sigma/2$  and the strain amplitude as  $\varepsilon = \Delta\varepsilon/2$  then the cyclic stress-strain curve may also be represented by a power law function similar to the static stress-strain curve (see equation (1.19))

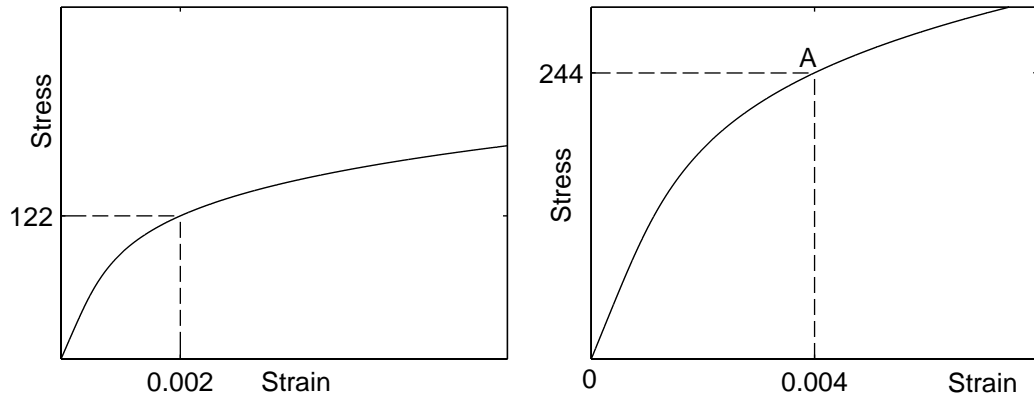
$$\varepsilon = \frac{\sigma}{E} + \left(\frac{\sigma}{K'}\right)^{1/n'}, \quad (1.21)$$

where  $K'$  is the cyclic strength coefficient and  $n'$  is the cyclic strain hardening exponent.  $\sigma$  and  $\varepsilon$  are understood to be the cyclically stable stress and strain amplitudes respectively.

The hysteresis loops may be found by doubling the cyclic stress-strain curve in Figure 1.11(a) to get the curve in Figure 1.11(b) and finally shifting the origin of the coordinates as in Figure 1.11(c). Multiplying equation (1.21) by 2 we get the general hysteresis curve equation

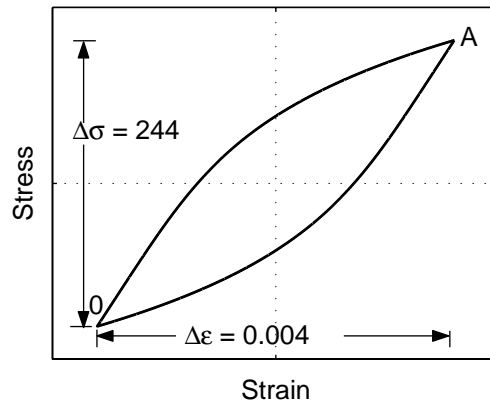
$$\Delta\varepsilon = \frac{\Delta\sigma}{E} + 2 \left(\frac{\Delta\sigma}{2K'}\right)^{1/n'}. \quad (1.22)$$

Another important behavior of metals is known as the Bauschinger effect [5] shown in Figure 1.12. If a material is loaded in tension beyond its yield strength for example, then the material will undergo plastic strains in compression before the original yield point in compression is reached. This behavior is common in metals that are cyclically loaded in the plastic region.



(a) Stabilized cyclic stress-strain curve

(b) Stabilized hysteresis curve



(c) Stabilized hysteresis loop

Figure 1.11: Stabilized hysteresis curve from cyclic stress-strain curve.

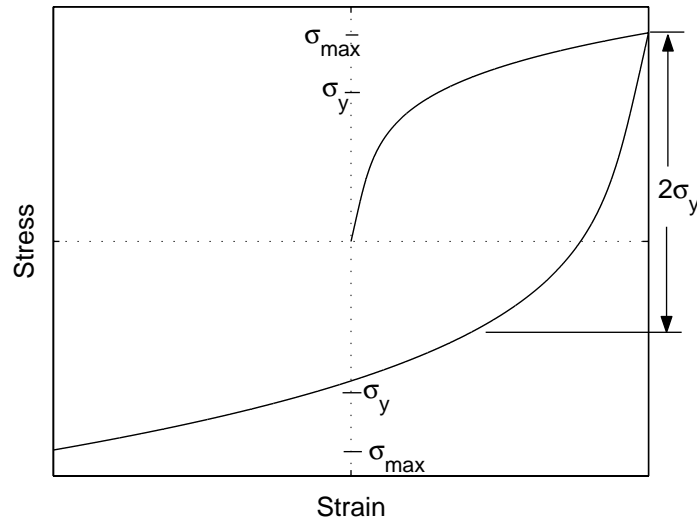


Figure 1.12: Bauschinger effect

### Crack Nucleation

This stage of the fatigue process is governed by the nucleation or initiation of cracks in the metal. These cracks usually develop on the free surface of the material and are most likely due to localized concentration of plastic strain or imperfections in the lattice.

The *lifetime* of a material, defined as the number of cycles to failure, depends largely upon the definition of failure. Some definitions of failure require cracks to reach certain lengths. This failure occurs during the crack propagation stage. Other definitions simply require a density of cracks to develop; this failure is largely governed by the crack nucleation stage. Lifetime curves have been developed for many metals under uniaxial loads for this type of failure.

Two common methods have been developed to characterize metal fatigue. One method developed decades ago is known as the stress-life method. The stress-life method is conducted by cyclically loading the material at a constant stress amplitude and is useful when the plastic strains are small. Basically, the number of cycles to failure is recorded for various stress amplitudes. Some metals, such as various types of steels, also have *endurance limits*, stress levels below which materials can be

loaded indefinitely without failure. Other metals like copper do not have an obvious endurance limit. In this case endurance limits are defined at the stress amplitude that will cause failure at  $10^7$  or  $10^8$  cycles.

Since it is known that plastic strains are responsible for the accumulation of damage in a material, the strain-life method is usually used to characterize metal fatigue. This method is performed by cyclically loading a material under constant total strain or plastic strain amplitudes and recording the number of cycles to failure. Fatigue due to pulsed heating is best described using the strain-life approach, since total strain is proportional to temperature rise (see equations (1.11)).

*High-cycle fatigue* is the region of the strain-life curve where the plastic strains are small and the number of cycles to failure is large. The results from the stress-life method are usually in good agreement with the strain-life method in this region. However, the strain-life method is better at characterizing materials in the region of *low-cycle fatigue* where the plastic strains are large and the number of cycles to failure are low.

In 1910, Basquin [4] observed that stress-life data could be parametrically modeled as

$$\sigma = \sigma'_f (2N_f)^b, \quad (1.23)$$

where  $\sigma$  is stress amplitude,  $N_f$  is number of cycles to failure ( $2N_f$  is number of reversals to failure),  $\sigma'_f$  is the *fatigue strength coefficient* and  $b$  is the *fatigue strength exponent*. In the 1950s, Coffin [13] and Manson [36] independently observed that plastic strain-life data could be parametrically modeled as

$$\varepsilon_p = \varepsilon'_f (2N_f)^c, \quad (1.24)$$

where  $\varepsilon_p$  is plastic strain amplitude,  $\varepsilon'_f$  is the *fatigue ductility coefficient* and  $c$  is the *fatigue ductility exponent*. Because of their work, the strain-life curve is also known as the Manson-Coffin curve. Since the total strain is the sum of the elastic and plastic strains (equation (1.17)), the strain-life method can be modeled using the *strain-life relation*

$$\varepsilon = \frac{\sigma'_f}{E} (2N_f)^b + \varepsilon'_f (2N_f)^c. \quad (1.25)$$

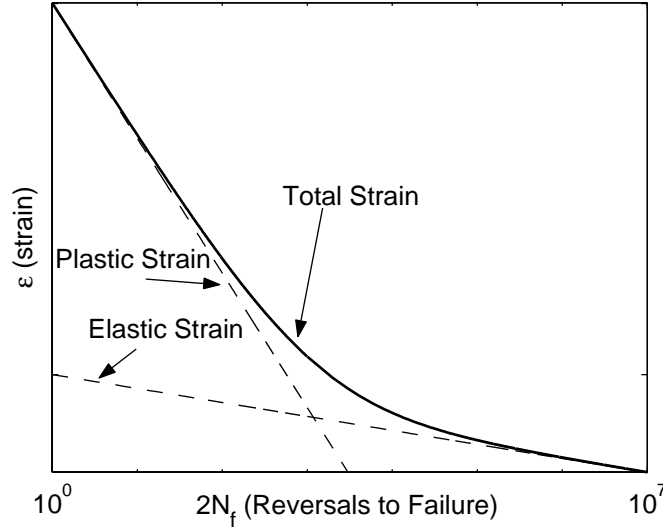


Figure 1.13: Strain-life curve

A log-log plot of this relation along with the elastic and plastic components is shown in Figure 1.13. From equations (1.21) and (1.25) we also get the following useful relations

$$K' = \frac{\sigma_f'}{(\varepsilon_f')^{n'}}, \quad (1.26a)$$

$$n' = \frac{b}{c}. \quad (1.26b)$$

For constant strain-amplitude loading, the fatigue of most ductile metals are characterized well with power-law parameterizations given by equation (1.25). The parameters  $\sigma_f'$ ,  $\varepsilon_f'$ ,  $b$  and  $c$  have been experimentally determined for fully-annealed copper (see Table 1.1). It is believed that fatigue of copper from pulsed heating can also be parametrically modeled with equation (1.25), since a material is loaded under constant total strain from constant temperature rises. However, the values of the parameters may be different.

There are other effects such as surface finish, environment, mean stress, mean

strain, variable amplitude loading, multiaxial fatigue and strain rate that may affect the lifetime of the material.

### Crack Propagation

Once cracks have nucleated, *fracture mechanics* must be used to describe their propagation. Fracture mechanics is ultimately used to predict the number of cycles for cracks to lengthen from an initial critical length to some arbitrary length defined as failure for the specimen. This stage of the fatigue process needs to be studied if one wants to predict the finite life of a component. The total lifetime of a specimen is the number of cycles it takes for cracks to nucleate (found from the strain-life curve) plus the number of cycles it takes for the cracks to reach a particular length. However, since there is limited knowledge when the cracks will initiate and then propagate due to pulsed heating, we will only consider the crack nucleation stage as defined by the strain-life curve.

#### 1.3.4 Thermal Fatigue Due to Pulsed Heating

Thermal fatigue is basically cyclic fatigue induced from cyclic thermal loads. This type of fatigue, however, is usually complicated by effects such as *creep* where the strain increases when a high temperature is held at a steady value for some period of time. Fortunately, these effects do not occur from pulsed heating since the temperature rises and falls on a fast time scale. Since the stress from pulsed heating is induced by the mechanical constraint imposed by the inertia of the material, results from Section 1.3.3 directly apply. However, the analysis becomes more complicated when the temperature dependence of the thermal and mechanical properties of the material is considered. It will be instructive to consider a simple step-by-step example of the stress-strain response of a metal under pulsed heating [41].

We will use a block of material initially at a temperature of 0 K (see Figure 1.14). The free surface of the metal will be heated with a fast high-power source. Since the surface is free to expand into the vacuum, the normal stress at the surface can be approximated as zero. We will assume that the transverse dimensions of the material

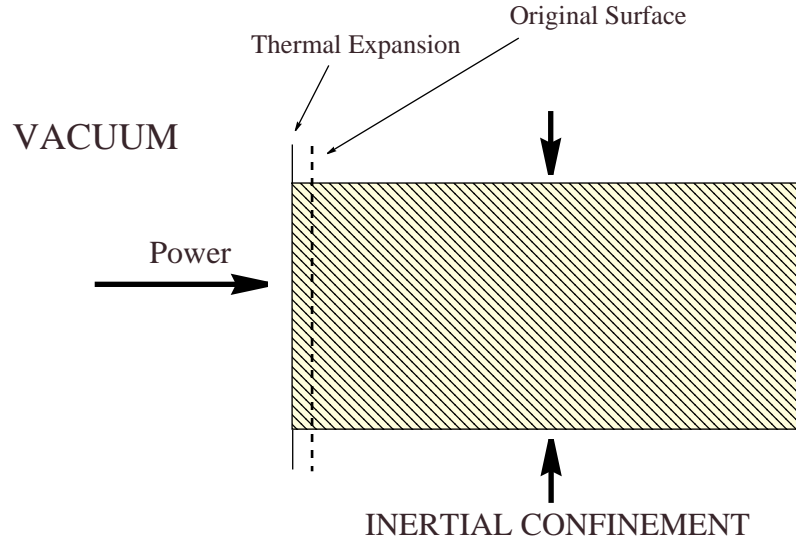


Figure 1.14: Metal surface being heated with a fast high-power source [41].

are large enough such that the metal remains inertially confined during the heating and cooling of the surface. This assumption implies that the total transverse strain is zero. Using these assumptions and equations (1.11) and (1.12) we have

$$\left. \begin{aligned} \sigma_N = \varepsilon_{TT} = 0 \\ \sigma_T = -\frac{E\alpha T}{1-\nu} \\ \varepsilon_N = \frac{1+\nu}{1-\nu}\alpha T \end{aligned} \right\}, \quad (1.27)$$

where  $\sigma_N$  is normal stress,  $\sigma_T$  is transverse stress,  $\varepsilon_N$  is normal strain and  $\varepsilon_{TT}$  is total transverse strain. Since the total transverse strain is zero, the transverse mechanical strain  $\varepsilon_{TM}$  must be the opposite of the transverse thermal strain or

$$\varepsilon_{TM} = -\alpha T. \quad (1.28)$$

It is the mechanical strain that must be considered in the stress-strain response of the metal. Equations (1.27) and (1.28) show that a positive temperature rise will result in compressive stresses and mechanical strains.

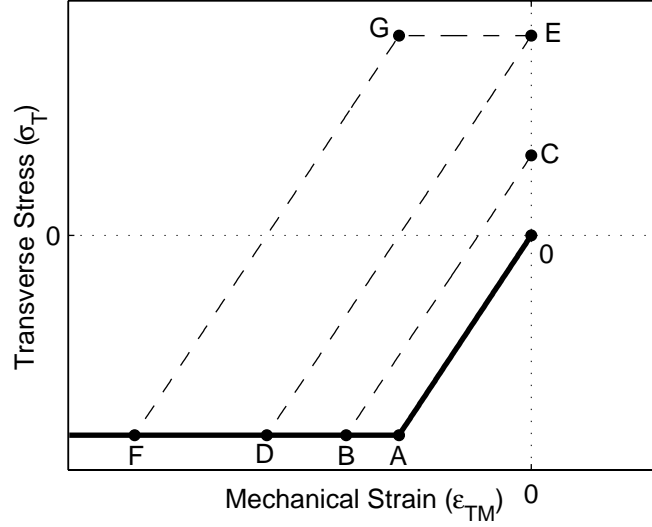


Figure 1.15: Linear-elastic/perfectly-plastic stress-strain diagram for pulsed heating of metal surface [41].

For simplicity we will also use a linear-elastic/perfectly-plastic model for the stress-strain response of the material. In this model the stress is constant at the yield stress when the mechanical strain is above the yield strain (shown as point A in Figure 1.15). Using equations (1.27) the temperature at which the yield stress,  $\sigma_y$  occurs is

$$T_y = \frac{(1 - \nu)\sigma_y}{E\alpha}. \quad (1.29)$$

From equation (1.28) the yield strain is

$$\varepsilon_y = \frac{(1 - \nu)\sigma_y}{E}. \quad (1.30)$$

Now we will consider the response of the material due to pulsed heating. Because of our simplified model, we are ignoring cyclic-hardening and the Bauschinger effect. The surface of the metal will be heated to a temperature rise of  $T_{max}$  and then cooled back down to zero. Refer to Figure 1.15 for the following discussion. If  $T_{max} < T_y$  the material will cycle along the line OA where point A represents the yield strain.

No plastic strain will occur and hence no damage will occur. If  $T_y < T_{max} < 2T_y$  the material will compress along line OA and plastic strain will accumulate along the path AB during the heating of the surface. The surface will then cool down along the path BC until the temperature rise and hence the mechanical strain is zero. Notice residual stress is now left on the surface. At this temperature rise, subsequent pulses will cycle along the line BC and no more plastic strain or damage will occur. When  $T_{max} > 2T_y$  the material will follow the path OABDF during the heating of the surface. When the surface cools down to 0 K, the material will follow the path FGE where point G is also the yield stress. Since the temperature rise is not zero when the material reaches point G, plastic deformation will occur along the path GE until the mechanical strain is reduced to zero. Subsequent pulses will cause the material to follow the path EDFGE since the yield strain is exceeded in both compression and tension. Plastic strain and hence damage will be accumulated in every pulse until failure occurs.

Comparing Figure 1.15 to Figure 1.10, one should notice that the hysteresis loop from pulsed heating cycles about a mean compressive strain. Also, we assumed that the material is still inertially confined when the temperature rise reduces to zero. Due to heat diffusion, the metal surface will take much longer to cool down than to heat up. The material may be able to expand and relieve the stress in that time. Ultimately, this condition means the hysteresis loop will cycle about a mean compressive stress. These factors may have an important effect on the lifetime of the material. More detailed calculations of the thermal response of copper to pulsed heating is presented in Chapter 3.

# Chapter 2

## Experimental Setup

As mentioned in the previous chapter, we must design an experiment to test the surface of OFE copper for damage from thermal fatigue due to RF pulsed heating. This chapter will describe the design of the experiment and the test structure. We will discuss cold-test results of the test structure and the modifications used. Chapter 4 will describe the results of the high-power tests.

### 2.1 Cavity Design

Since we are interested in the RF performance of future accelerators, we chose to use a simple resonant cavity constructed from OFE copper. It might be helpful to refer to Appendix A for a review of resonant cavities.

There are a few requirements a test structure should have. The first requirement is removable test pieces so future tests may be conducted at different temperature rises as well as with different materials and surface preparations. Second, there should be no perpendicular electric fields on the cavity surface in order to avoid RF breakdown. Hence, we may isolate the effects of pulsed heating. Third, the cavity should be designed to minimize the heating on the parts that cannot be simply replaced. This allows several tests to be performed before the need to replace the entire cavity.

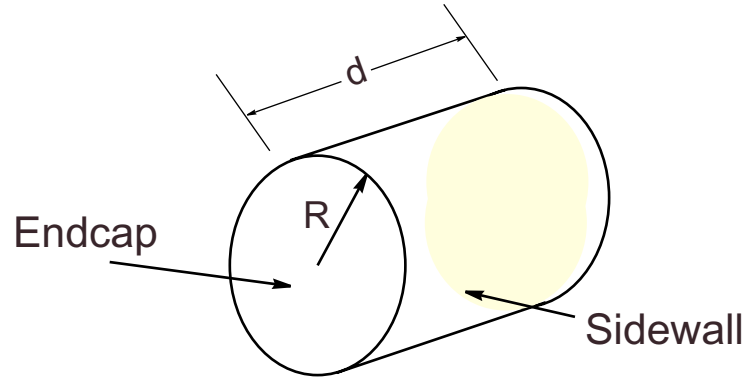


Figure 2.1: Circularly cylindrical cavity of radius  $R$  and length  $d$ . The endcaps are the test pieces and the sidewall is to be re-used in future tests.

### 2.1.1 Choice Of Cavity Mode

Noting the above design philosophy, we must choose an operating frequency and mode for the cavity. In order to have removable test pieces, the surface currents in the cavity must not require contact between the test piece and the rest of the cavity. Also, there must be no perpendicular electric fields on the cavity surface. The only geometry that allows this is a circular cylindrical geometry. One such cavity is shown in Figure 2.1. The endcaps will be the test pieces of the experiment. The sidewall of the cavity will be re-used in future tests.

Looking at equations (A.44), no TM modes can be used because of the nonzero  $E_z$  fields where  $\hat{z}$  is the axial direction of the cavity. In order for the endcaps to be easily removable, we do not want the requirement of physical contact between the endcaps and the sidewall. A good mode to accomplish this is the  $TE_{011}$  mode (see Figure 2.2 for the mode pattern). From equations (A.34) the cavity fields for the  $TE_{011}$  mode

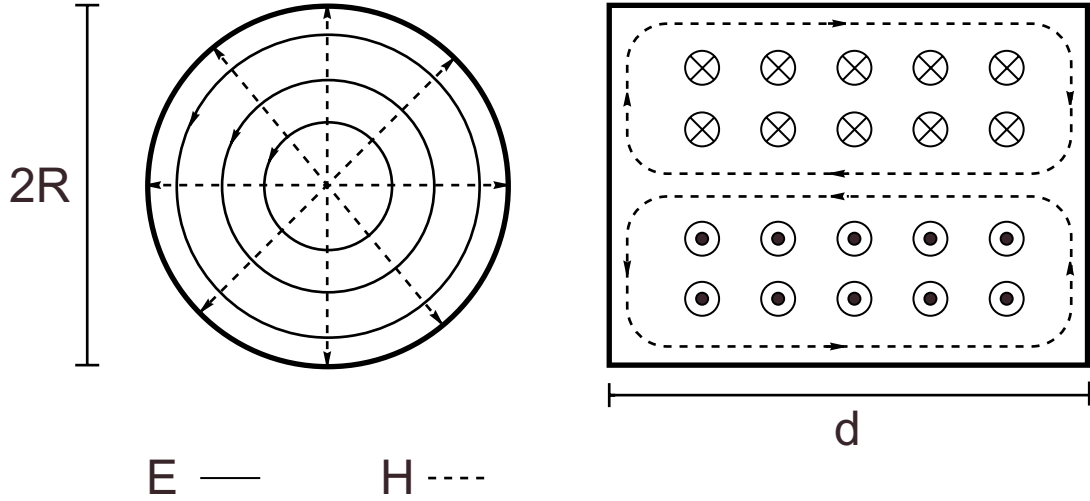


Figure 2.2: Field pattern of the  $TE_{011}$  mode in a circularly cylindrical cavity of radius  $R$  and length  $d$ .

for a cavity of radius  $R$  and length  $d$  are

$$H_z = A_{TE}^{011} \sin\left(\frac{\pi z}{d}\right) J_0\left(\frac{x'_{01} r}{R}\right), \quad (2.1a)$$

$$H_r = A_{TE}^{011} \frac{\pi R}{d x'_{01}} \cos\left(\frac{\pi z}{d}\right) J'_0\left(\frac{x'_{01} r}{R}\right), \quad (2.1b)$$

$$E_\phi = -A_{TE}^{011} \frac{\omega_{011} R}{c x'_{01}} \sin\left(\frac{\pi z}{d}\right) J'_0\left(\frac{x'_{01} r}{d}\right), \quad (2.1c)$$

$$A_{TE}^{011} = \sqrt{\frac{2}{\pi d \omega_{011} R^2}} \frac{c x'_{01}}{|J_0(x'_{01})|}, \quad (2.1d)$$

where the angular resonant frequency is

$$\omega_{011} = c \sqrt{\left(\frac{x'_{01}}{R}\right)^2 + \left(\frac{\pi}{d}\right)^2}. \quad (2.2)$$

The magnetic field at the endcaps is purely radial. Therefore the surface current  $\vec{J}_s = \hat{n} \times \vec{H}$  is purely azimuthal, so no current flows between the endcaps and the

sidewall.

The electric field in the cavity is also azimuthal, so there is no perpendicular electric field on any surface in the cavity. This helps avoid electric field breakdown. However, the use of a coupling aperture will change this fact as it modifies the fields near that region.

We need to choose a frequency where a high-power klystron is available for use. At SLAC, there are 50 MW X-band klystrons available that operate at 11.424 GHz and 60 MW S-band klystrons that operate at 2.856 GHz. Looking ahead to Section 3.3.1, we will derive the temperature rises of the endcaps and the sidewall knowing the input power and unloaded and external Q's of the cavity. These temperature rises are given by equations (3.72–3.73). Assuming constant coupling ( $\beta$  is constant), constant power and constant pulse length, the frequency scaling for temperature rise according to equations (3.72–3.73) is

$$\Delta T \propto \frac{R_s Q_L^2}{\omega^3 L^5} \propto \frac{R_s Q_{011}^2}{\omega^3 L^5} \propto \frac{\omega^{1/2} \omega^{-1}}{\omega^3 \omega^{-5}} \propto \omega^{3/2}. \quad (2.3)$$

where L is a characteristic length. Hence, for a given power input and pulse length, it is best to use the highest frequency possible. So we will choose 11.424 GHz as the cavity's resonant frequency.

### 2.1.2 Choice Of Cavity Dimensions

Since we want to use the endcaps as the test surface and we want to re-use the cavity sidewall, we need to choose the cavity dimensions such that the temperature rise on the endcaps is maximum while being low on the sidewall. The strain in the copper is proportional to temperature (see section 1.3.1). According to the strain-life relation, equation (1.25), the number of cycles to failure follows a power law with strain. Therefore, several high-power tests may be conducted with different endcaps before the cavity sidewall becomes significantly damaged from pulsed heating.

Since we will optimize the dimensions of the cavity at the fixed frequency of

11.424 GHz, the radius  $R$  of the cavity is a function of the cavity length  $d$

$$R = \frac{x'_{01}}{\sqrt{\left(\frac{\omega_{011}}{c}\right)^2 - \left(\frac{\pi}{d}\right)^2}}. \quad (2.4)$$

The unloaded  $Q$  of the cavity depends on its dimensions. Using equations (A.73) and (A.34) the unloaded  $Q$  for mode  $\text{TE}_{nmp}$  is

$$Q_{nmp} = \frac{dR^4 \omega_{nmp}^{5/2} \sqrt{2\mu_c \sigma}}{4c^2 x_{nm}'^2} \frac{1 - \frac{n^2}{x_{nm}'^2}}{\frac{1}{2}dR \left[ 1 + \left(\frac{np\pi R}{dx_{nm}'^2}\right)^2 \right] + \left(\frac{p\pi R^2}{dx_{nm}'}\right)^2 \left(1 - \frac{n^2}{x_{nm}'^2}\right)}. \quad (2.5)$$

Hence the unloaded  $Q$  for the  $\text{TE}_{011}$  mode is

$$Q_{011} = \frac{dR^4 \omega_{011}^{5/2} \sqrt{2\mu_c \sigma}}{4c^2 x_{01}'^2} \frac{1}{\frac{1}{2}dR + \left(\frac{\pi R^2}{dx_{01}'}\right)^2}. \quad (2.6)$$

We may use equation (3.72) to find the maximum temperature rise on the endcap normalized to the input power by varying the cavity length  $d$  and the cavity's external quality factor,  $Q_{ext}$ . The location of the maximum temperature rise on the endcap occurs at  $r = (x'_{11}/x'_{01})R = 0.4805R$ . The location of the maximum temperature rise on the sidewall occurs at  $z = d/2$ . The results are shown in Figure 2.3. This plot indicates that the optimum cavity length is  $d = 1.85$  cm and the optimum external  $Q$  is  $Q_{ext} = 16770$ . This corresponds to a cavity radius  $R = 2.27$  cm.

Using the optimum value for external  $Q$ , Figure 2.4 shows the normalized heating on the endcaps and the sidewall as a function of cavity length. At the optimum cavity length, the ratio between the maximum temperature rise on the endcaps to the maximum temperature rise on the sidewall is 2.11. At this length, the unloaded  $Q$  of the cavity is  $Q_{011} = 21280$ . Using this value of the unloaded  $Q$ , Figure 2.5 shows the variation of the normalized temperature rise on the endcaps as a function of the coupling,  $\beta = Q_{011}/Q_{ext}$ . The optimum cavity coupling is  $\beta = 1.28$ .

During the initial design, the cavity dimensions were optimized without taking the fill-time of the cavity into account (the bracket term in equation (3.72)). When leaving

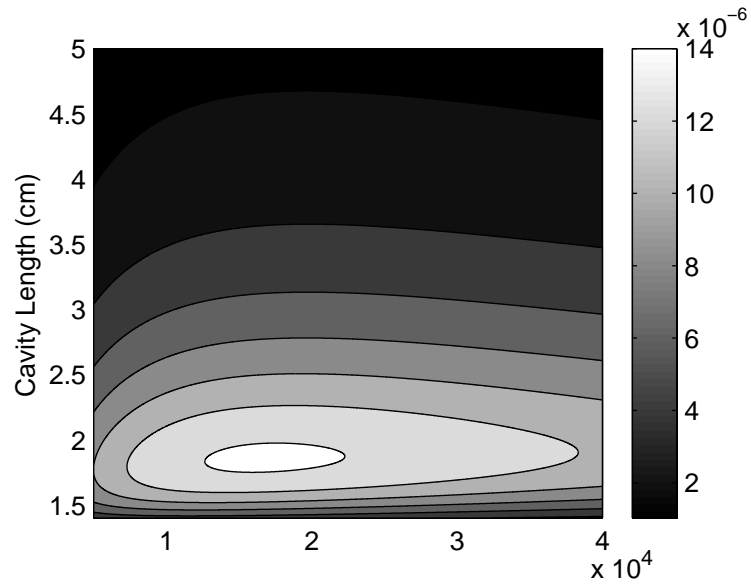


Figure 2.3: Temperature rise on cavity endcaps normalized to input power as a function of the cavity length  $d$  and the external quality factor,  $Q_{ext}$ .

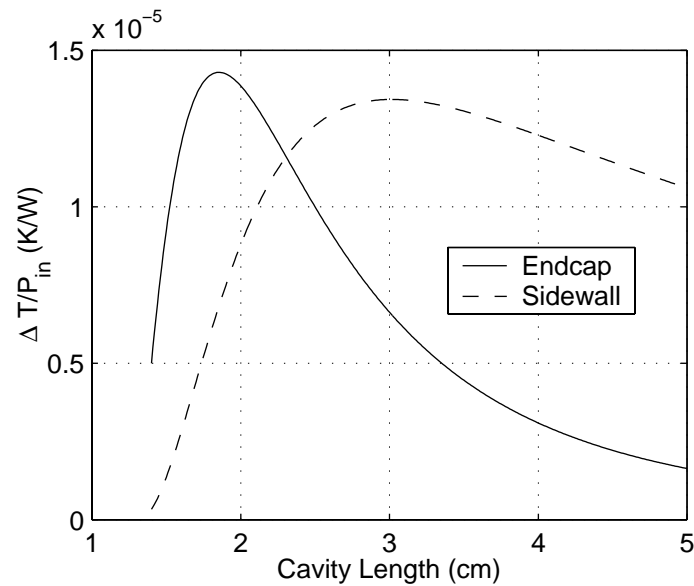


Figure 2.4: Temperature rise on cavity endcaps and sidewall normalized to input power as a function of cavity length  $d$  using  $Q_{ext} = 16770$ .

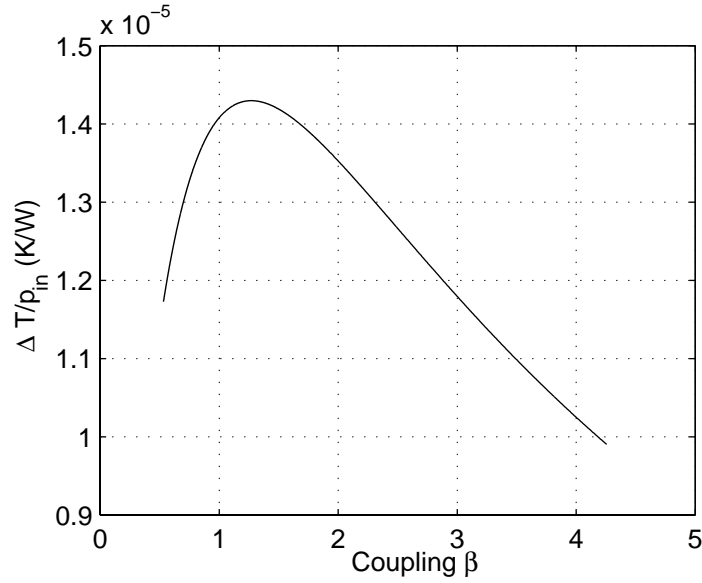


Figure 2.5: Temperature rise on cavity endcaps normalized to input power as a function of the coupling  $\beta = Q_{011}/Q_{ext}$  calculated at cavity length 1.85 cm.

this term out, the optimum cavity length becomes  $d = 1.90$  cm corresponding to a cavity radius  $R = 2.21$  cm. The cavity coupling was correctly optimized as a function of  $\beta$  but with  $Q_{ext} = 17110$  to account for the change in  $Q_{011}$ . At this cavity length the temperature rise on the endcaps is reduced by only 0.4%. The ratio between the maximum temperature rise on the endcaps to the maximum temperature rise on the sidewall is reduced to 1.90. In a later section, we will show that the coupling aperture reduces the resonant frequency, hence the cavity radius was reduced to compensate.

The theoretical values for  $Q_{011}$  and  $Q_{ext}$  given earlier assume a perfect cavity. In reality, the surface finish of the cavity is not perfect and will cause more power loss in the surface than previously estimated. Since the temperature rise in the cavity varies slowly with small changes of  $\beta$  from the optimum value, it would be safe to assume an approximate 10% degradation in  $Q$  of the constructed cavity. Table 2.1 shows the final design parameters for the cavity.

$f_{\text{res}}$	11.424 GHz
$d$	1.90 cm
$R$	2.2075 cm
$Q_0$	21900
Estimated $Q_0$	19710
$Q_{\text{ext}}$	15400
$Q_L$	8650
$\beta$	1.28
$R_a$	3.75 mm
$d_a$	1.88 mm

Table 2.1: Cavity design parameters for  $\text{TE}_{011}$  mode.

### 2.1.3 Choice Of Temperature Diagnostic

We are mainly interested in the damage on the copper surface that will occur due to RF pulsed heating and its effects on the RF properties of the cavity. We believe a method that will allow us to measure  $Q$  degradation as well as monitor the dynamic RF changes in the cavity would best suit our needs. We also believe such a method would be easier to implement than to measure the surface temperature directly (i.e. infrared radiation). This can be done by exciting the cavity with another mode at steady-state under low power.

In steady-state, the reflected power measured from the cavity in this mode would be constant if no changes occurred to the RF properties of the cavity. However, when the temperature of the cavity surface rises from pulsed heating from the high-power mode, the unloaded  $Q$  of both modes will change. This change is due to the temperature dependence of the electrical conductivity of copper. Consequently, the coupling to the low-power mode will change which can be measured from its reflected power. With knowledge of the field pattern of this mode, the maximum temperature rise on the endcaps may be extracted from the dynamic  $Q$  change. The details of how the temperature is extracted is given in Section 3.3.3. Between high-power RF pulses, the temperature rise of the surface of the copper will reduce to zero. By measuring the  $Q$  of the low-power mode during this time, we may also measure long-term  $Q$  degradation of the cavity to determine permanent damage to the cavity surface.

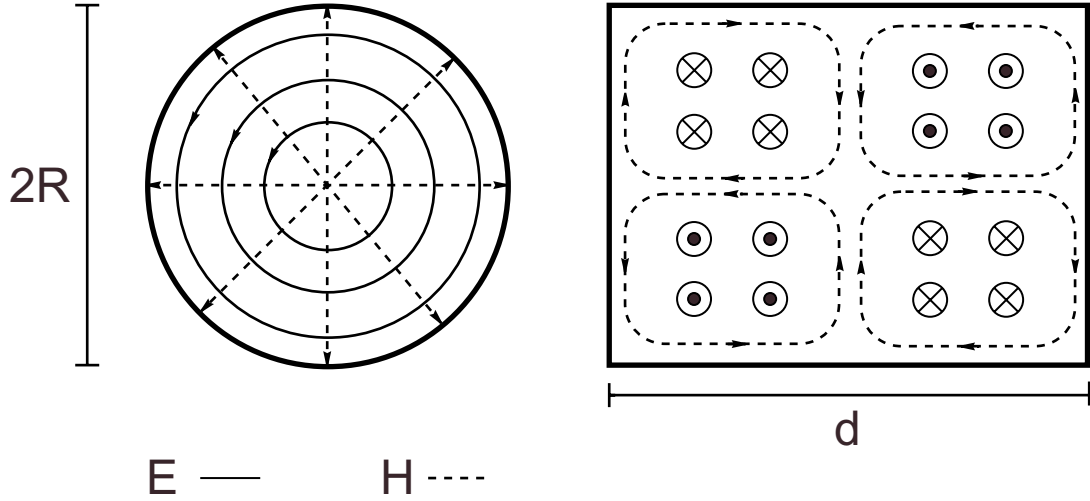


Figure 2.6: Field pattern of the  $TE_{012}$  mode in a circularly cylindrical cavity of radius  $R$  and length  $d$ .

A natural choice for the low-power mode is the  $TE_{012}$  mode (see Figure 2.6 for the mode pattern). This mode has the same field pattern on the endcaps as the  $TE_{011}$  mode, which is the surface we are interested in. Also, this mode does not require physical contact between the endcaps and the sidewall. This is necessary in order to accommodate the high-power  $TE_{011}$  mode. The fields are

$$H_z = A_{TE}^{012} \sin\left(\frac{2\pi z}{d}\right) J_0\left(\frac{x'_{01} r}{R}\right), \quad (2.7a)$$

$$H_r = A_{TE}^{012} \frac{2\pi R}{dx'_{01}} \cos\left(\frac{2\pi z}{d}\right) J'_0\left(\frac{x'_{01} r}{R}\right), \quad (2.7b)$$

$$E_\phi = -A_{TE}^{012} \frac{\omega_{012} R}{cx'_{01}} \sin\left(\frac{2\pi z}{d}\right) J'_0\left(\frac{x'_{01} r}{d}\right), \quad (2.7c)$$

$$A_{TE}^{012} = \sqrt{\frac{2}{\pi d} \frac{c}{\omega_{011} R^2} \frac{x'_{01}}{|J_0(x'_{01})|}}, \quad (2.7d)$$

$f_{\text{res}}$	17.820 GHz
$Q_0$	21960
Estimated $Q_0$	19760
$Q_{\text{ext}}$	19760
$Q_L$	9880
$\beta$	1.0
$R_a$	2.85 mm
$d_a$	1.034 mm

Table 2.2: Cavity design parameters for  $\text{TE}_{012}$  mode.

where the angular resonant frequency is

$$\omega_{012} = c \sqrt{\left(\frac{x'_{01}}{R}\right)^2 + \left(\frac{2\pi}{d}\right)^2}. \quad (2.8)$$

From equation (2.5) the unloaded  $Q$  of this mode is

$$Q_{012} = \frac{dR^4 \omega_{012}^{5/2} \sqrt{2\mu_c \sigma}}{4c^2 x_{01}'^2} \frac{1}{\frac{1}{2}dR + \left(\frac{2\pi R^2}{dx_{01}'}\right)^2}. \quad (2.9)$$

Using the cavity dimensions given in Table 2.1,  $Q_{012} = 21960$  and the resonant frequency is 17.820 GHz. With no high-power in the cavity, we would like the reflected power from the  $\text{TE}_{012}$  mode to be zero for easy measurement. Thus we would like the coupling to be  $\beta = 1$  or  $Q_{\text{ext}} = Q_{012} = 19760$  where we have assumed an approximate 10% degradation in  $Q$  due to surface finish. Table 2.2 contains the design parameters for the  $\text{TE}_{012}$  mode.

### 2.1.4 Input Couplers

The cavity will require input couplers to establish the two resonant modes. The use of water-cooling will make coupling through the endcaps difficult. It is simpler to cut circular apertures into the sidewall of the cavity and couple the power to the cavity with waveguides.

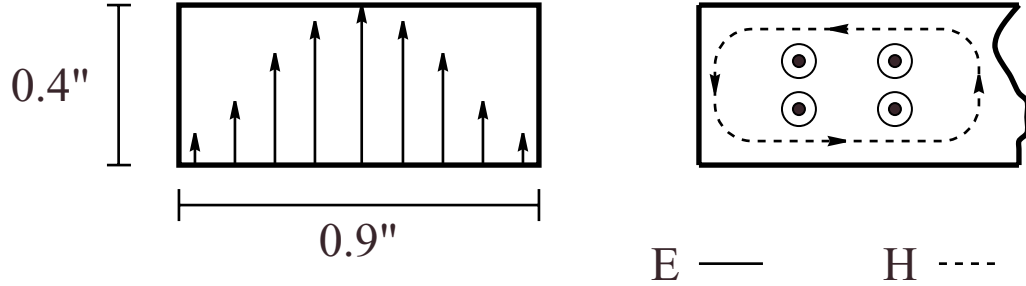


Figure 2.7: WR-90 waveguide with the dominant  $TE_{10}$  mode shown.

We will use the Kroll-Yu(KY)/Kroll-Lin(KL) methods [25, 26] to determine the proper dimensions of the coupling apertures with computer simulation. The simulation is performed in the frequency domain in which the cavity and the waveguide coupler is modeled. The waveguide is shorted at a length  $D$  from the coupling aperture. The length of the waveguide will modify the eigenfrequencies of the waveguide-loaded cavity. The equation used to model a waveguide-loaded cavity is

$$\tan [k(\omega)D + \chi(u) + \chi'(u)(\omega - u)] = \frac{v}{\omega - u}, \quad (2.10)$$

where  $k$  is the guided wavenumber,  $\omega$  is the angular frequency of the waveguide-cavity system,  $D$  is the distance from the shorting-plane of the waveguide to the coupling aperture and  $\chi$  and  $\chi'$  parameterize the effect of distant cavity resonances. The resonant frequency of the cavity is given by  $u$  and the external Q is  $Q_{ext} = u/(2v)$ . By varying the waveguide length  $D$  and computing the eigenfrequency  $\omega$ , the parameters  $u$ ,  $v$ ,  $\chi$  and  $\chi'$  can be determined with a nonlinear least-squares fit to equation (2.10). Normally, only two to four separate simulations are needed to find  $Q_{ext}$  using the KL/KY methods; however, it is more accurate to fit equation (2.10) with several data points because  $Q_{ext}$  is high.

### High-Power Coupler

At X-band frequencies, the standard rectangular waveguide to use is WR-90 whose dimensions are shown in Figure 2.7. At these frequencies only the dominant  $TE_{10}$

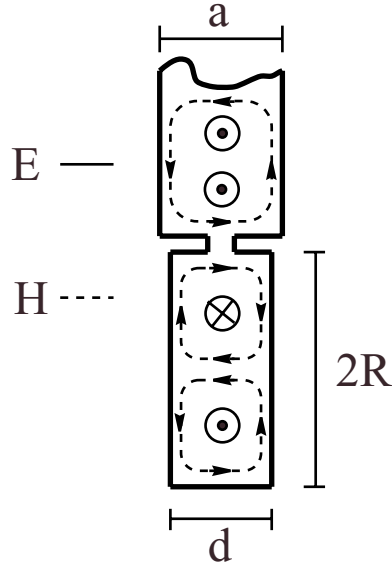


Figure 2.8: Cavity-waveguide coupling configuration to excite the  $TE_{011}$  mode for a circularly cylindrical cavity of radius  $R$  and length  $d$  and waveguide width  $a$ .

mode propagates. We will couple to the  $TE_{011}$  mode of the cavity using the magnetic field. The maximum magnetic field along the cavity sidewall occurs in the middle at  $z = d/2$ , so we will mount the waveguide there. Thus, the waveguide-cavity configuration will be as shown in Figure 2.8. Notice that the width of the waveguide is longer than the cavity length. Hence the cavity sidewall will be made longer than necessary in order to mount the waveguide. The endcaps will be mounted on pistons that will be inserted into the cavity to the correct length. The design of the endcaps is discussed in Section 2.1.5.

For ease of machining we decided to use a circular aperture to couple the waveguide to the cavity. The aperture is in the center of the waveguide cross-section as shown in Figure 2.9. From Table 2.1, we need to determine the dimensions of the circular aperture to give  $Q_{ext} = 15400$  or  $\beta = 1.28$ . A good starting point is to use the estimate given in [15] for  $\beta$  for a waveguide-cavity system. The importance of Gao's

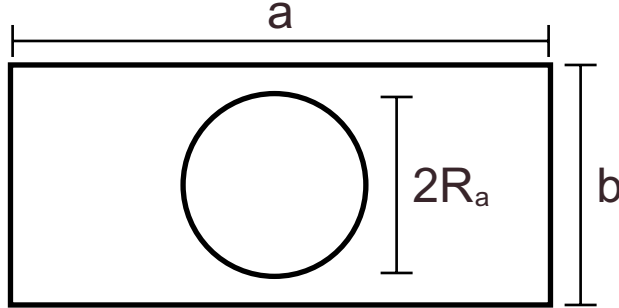


Figure 2.9: Coupling aperture at the end of the waveguide.  $R_a$  is the aperture radius,  $a$  and  $b$  is the width and height of the waveguide respectively.

finding is that the coupling scales as

$$\beta \propto R_a^6 e^{-(4\pi/\lambda)d_a} \sqrt{(\lambda/(3.41R_a))^2 - 1}, \quad (2.11)$$

where  $\lambda$  is the RF wavelength,  $R_a$  is the aperture radius and  $d_a$  is the aperture thickness. After using the initial estimate, we can use this scaling to change the aperture dimensions to arrive at the desired coupling.

The cavity-waveguide structures were simulated with finite-difference time-domain codes using rectangular coordinates. Hence, curved boundaries are difficult to simulate accurately. Initially MAFIA [16] was used to find the aperture dimensions for the coupling. It was necessary to use manual control over the placement of the mesh lines. In our attempts to accurately model the aperture geometry, not enough mesh lines were used in the waveguide. Therefore, the scattering of the fields near the aperture were not accurately computed. This resulted in errors for the coupling values when the cavities were cold-tested. This will be described further in Section 2.1.7. After the construction of the cavities, an improved meshing routine in GdfidL [10] allowed us to more accurately compute the coupling between the waveguide and cavity. The results from GdfidL compare favorably with the cold-test results. The aperture dimensions for the high-power coupler are given in Table 2.1.

Due to the placement of the high-power coupler and the symmetry of the electric and magnetic fields, it was only necessary to model 1/4 of the waveguide-loaded cavity

as shown at the top of Figure 2.10. Notice that there is a groove at the outer radius of the endcap. This groove is used to eliminate the degeneracy between the  $TE_{011}$  mode and the  $TM_{111}$  mode. It will be discussed further in Section 2.1.5. A close-up of the modelling of the coupling aperture is shown at the bottom of Figure 2.10. Figure 2.11 shows pictures of the electric and magnetic fields from a typical simulation run.

Many simulation runs were used at different waveguide lengths  $D$  to determine the resonant frequency and the external  $Q$ . We used a mesh spacing of 0.3 mm. The data were fit to equation (2.10). The result is shown in Figure 2.12. Although the simulated resonant frequency is 11.430 GHz, the cavity is easily tunable by moving the endcaps.

### Diagnostic Coupler

We will excite the  $TE_{012}$  mode in a way similar to that of the high-power coupler. However, we must pick a waveguide dimension such that 11.424 GHz does not propagate along the waveguide. This is necessary in order to protect the diagnostic electronics from damage due to high power.

WR-42 has a width of 0.42 inches corresponding to a cutoff frequency of 14.051 GHz for the dominant  $TE_{10}$  mode. This waveguide will suit our needs. However, we will also need a vacuum window for the diagnostic port. Vacuum windows for WR-62 that operate around 18 GHz were made available to us. The cutoff frequency for WR-62 is 9.518 GHz, so WR-42 must be used. Since the height of the waveguide does not affect the cutoff frequency, we used a waveguide with the width of a WR-42 (0.42 inches) and the height of a WR-62 (0.311 inches). This allows us to taper the width of the waveguide to WR-62 to allow the use of available vacuum windows.

The waveguide must be sufficiently long to attenuate the high power that will leak into it from the  $TE_{011}$  mode. We would like the maximum output power to be approximately -50 dBm to put it about 20 dB below the minimum power level measurable at the diagnostic frequency. Assuming that the maximum input power to the cavity is 25 MW=104 dBm, we need an attenuation of 154 dB. Power in a cutoff waveguide dissipates as

$$P = P_0 e^{-2k_{loss}d}, \quad (2.12)$$

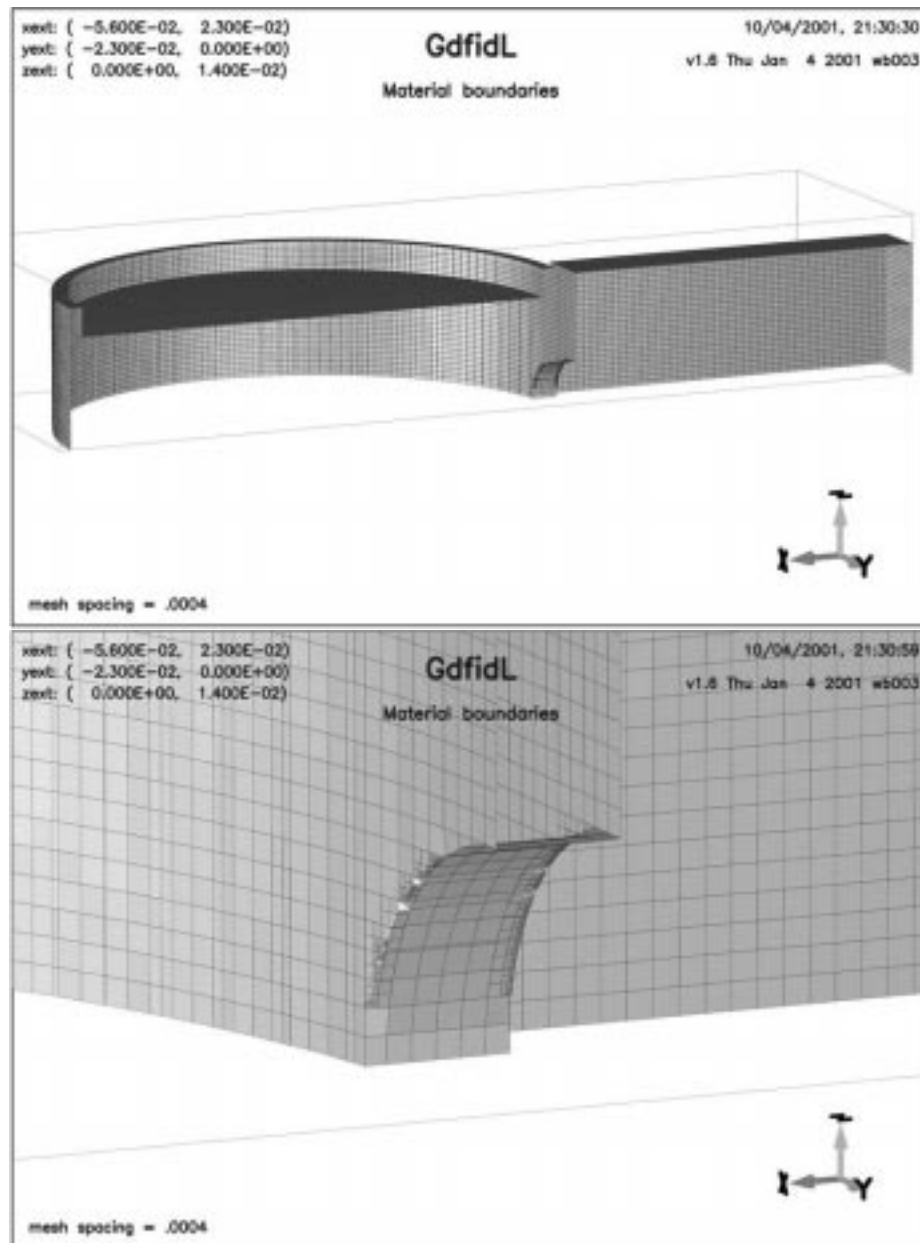


Figure 2.10: Geometry of high-power coupler modeled in GdfidL. Only 1/4 of the waveguide-loaded cavity structure is needed because of symmetry. A close-up of the high-power coupling aperture is on the bottom.

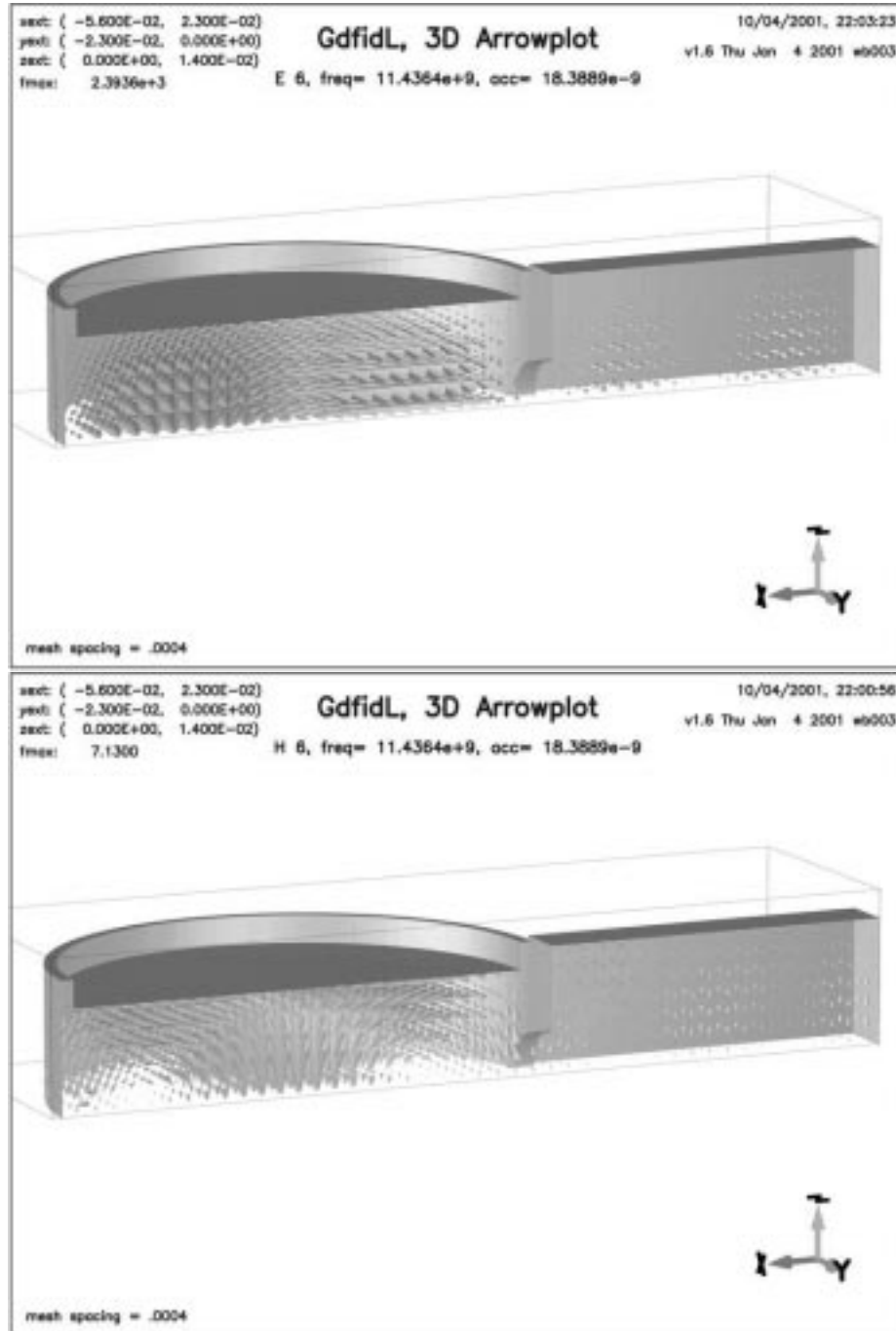


Figure 2.11: The field pattern of the  $TE_{011}$  mode modeled in GdfidL. The electric field is on the top and the magnetic field is on the bottom.

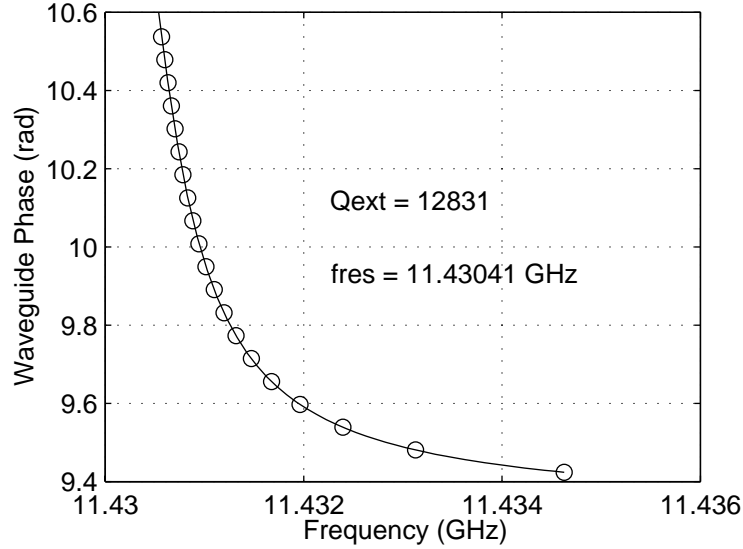


Figure 2.12: Determination of resonant frequency and  $Q_{ext}$  for the  $TE_{011}$  mode from equation (2.10) with a mesh spacing of 0.3 mm. Waveguide phase is  $k(\omega)D$ . The aperture has a radius  $R_a = 3.75$  mm and thickness  $d_a = 1.88$  mm.

where  $P_0$  is the input power.  $k_{loss}$  is given by

$$k_{loss} = \sqrt{\left(\frac{\pi}{a}\right)^2 - \left(\frac{2\pi f}{c}\right)^2}, \quad (2.13)$$

where  $a$  is the width of the cutoff waveguide. In this case,  $k_{loss} = 171.45$  Np/m = 1489.2 dB/m. Thus we need a waveguide length of approximately 10.4 cm.

In order to couple to the  $TE_{012}$  mode, we need to place the waveguide center at the maximum of the magnetic field along the sidewall of the cavity. So we offset the waveguide to 1/4 of the cavity length as shown in Figure 2.13.

As with the high-power coupler, our attempts to mesh the coupling aperture accurately in MAFIA resulted in errors for the coupling value. Also it was not determined until after the first high-power test that axial grooves on the endcaps affect the coupling to the diagnostic mode. This is due to the proximity of the diagnostic coupling aperture to one of the endcaps. The results from GdfidL include the modeling of the axial groove used for the second high-power test and agree with cold-tests as

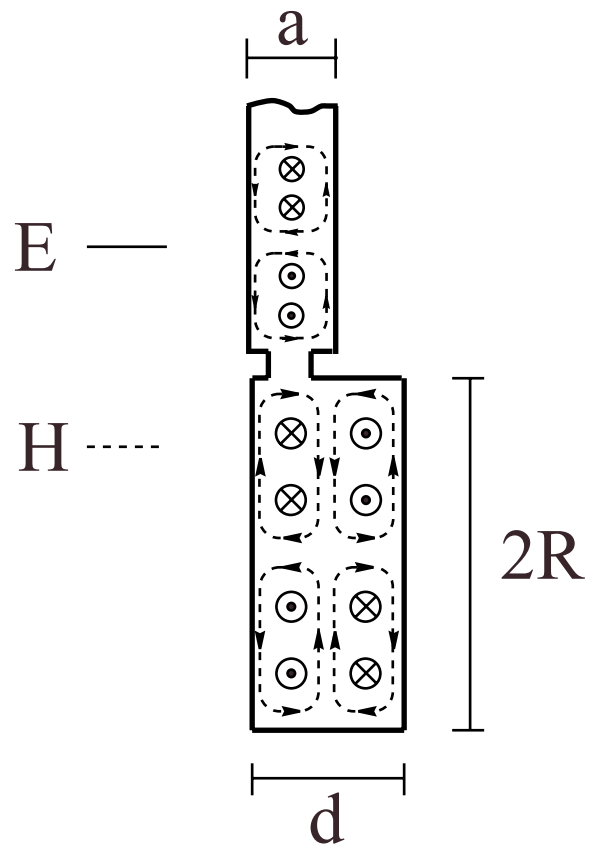


Figure 2.13: Cavity-waveguide coupling configuration to excite the  $TE_{012}$  mode for a circularly cylindrical cavity of radius  $R$  and length  $d$  and waveguide width  $a$ .

described in section 2.1.7.

Due to symmetry, it was only necessary to model 1/2 of the cavity-waveguide geometry as shown at the top of Figure 2.14. A close-up of the modelling of the coupling aperture is shown at the bottom of Figure 2.14. Figure 2.15 shows pictures of the electric and magnetic fields from a typical simulation run. Many simulation runs were used at different waveguide lengths  $D$  to determine the resonant frequency and the external  $Q$ . We used a mesh spacing of 0.31 mm. The data were fit to equation (2.10). The result is shown in Figure 2.16.

### 2.1.5 Endcaps

The cavity endcaps are designed to be removable so other materials and other surface preparations may be tested. Also, the endcaps are designed to be movable for cavity tuning. These two considerations along with the necessity of water-cooling (discussed in Section 2.1.6) lead us to the design shown in Figure 2.17. The endcaps are mounted onto pistons that contain a bellows, a vacuum flange, a differential screw and water pipes. The differential screw and the bellows allow for fine-adjustment of the cavity length.

In order to mount the endcaps, they must be brazed onto the pistons for each experiment. However, the bellows cannot be chemically cleaned because the small space between each of the folds does not allow for the easy flow of liquid. Therefore, the copper endcaps are mounted onto the stainless-steel pistons in a two-step process.

In the first step, the copper endcaps are brazed onto stainless-steel rings. This stainless-steel ring of the assembly is then cut to the correct dimensions for proper mounting onto the piston. In the second step, the endcap assembly is welded onto the stainless-steel piston. After a high-power test, the copper endcap is removed by cutting into the stainless-steel ring. Then the piston is re-machined to mount a new copper endcap for the next high-power test. Table 2.3 shows the steps for the assembly of the piston in detail.

In order to insert the endcaps into the cavity without mechanical problems, we need a small gap between the outer radius of the endcaps and the inner radius of the

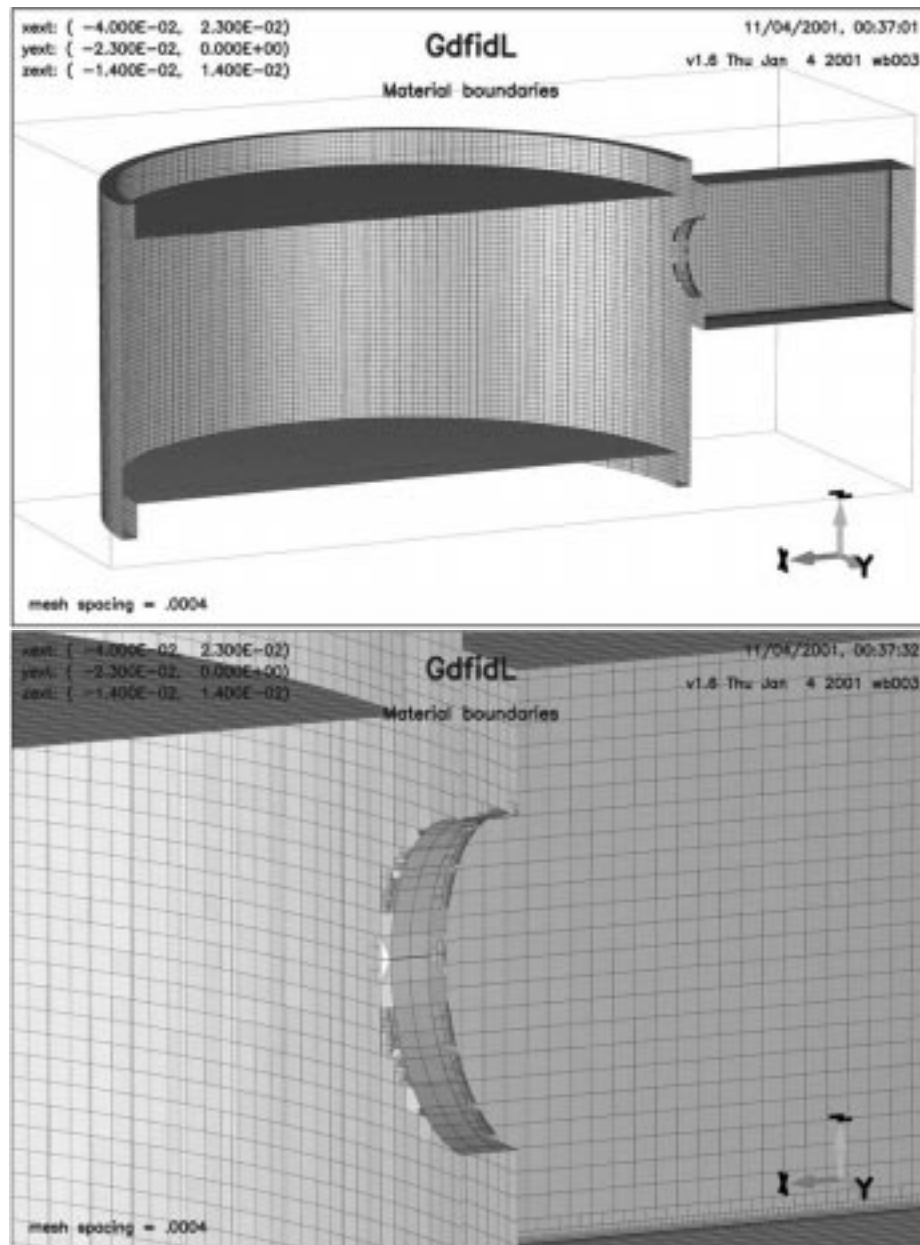


Figure 2.14: Geometry of diagnostic coupler modeled in GdfidL. Only 1/2 of the waveguide-loaded cavity structure is needed because of symmetry. A close-up of the diagnostic aperture is on the bottom.

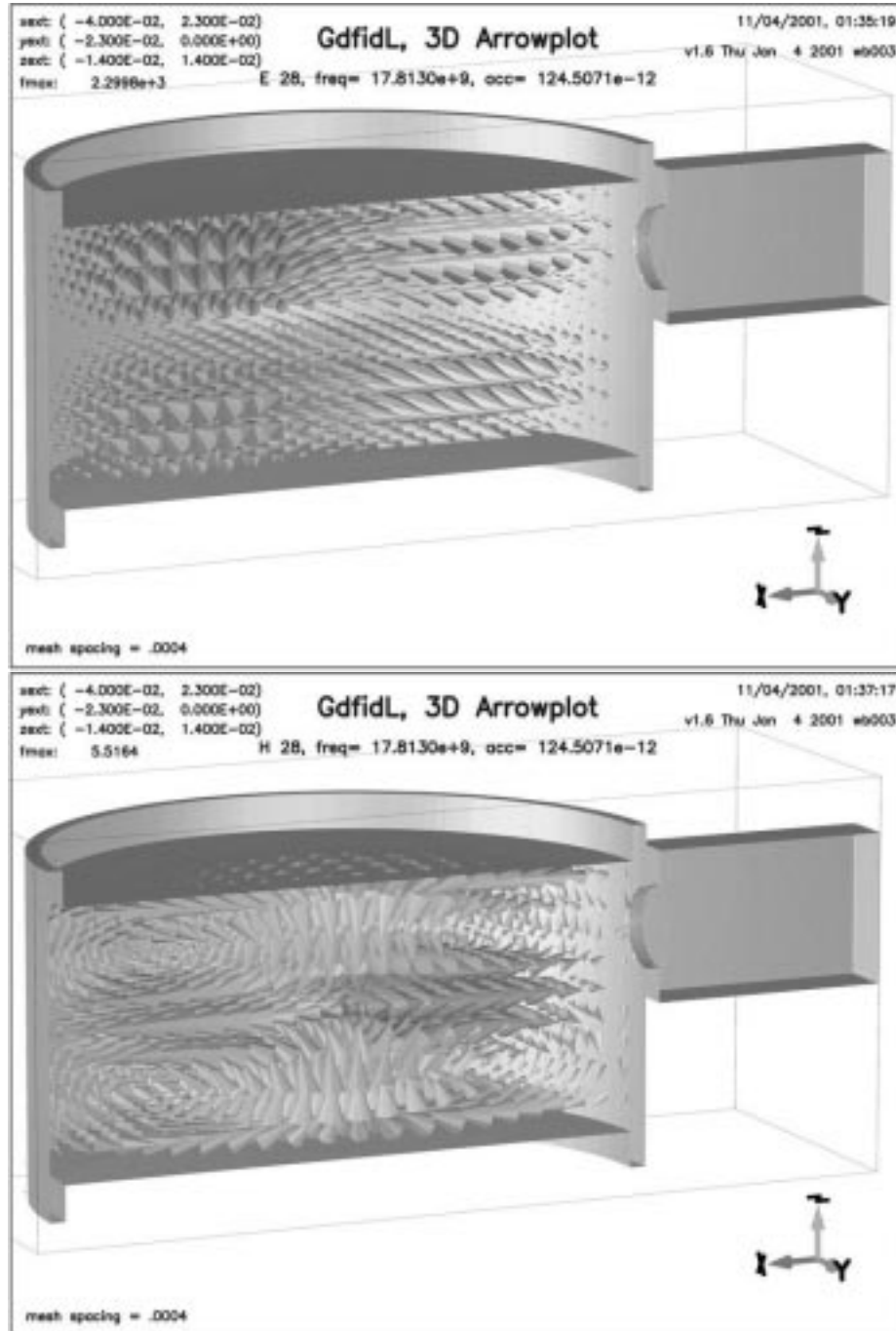


Figure 2.15: Field pattern of the  $TE_{012}$  mode modeled in GdfidL. The electric field is on the top and magnetic field is on the bottom.

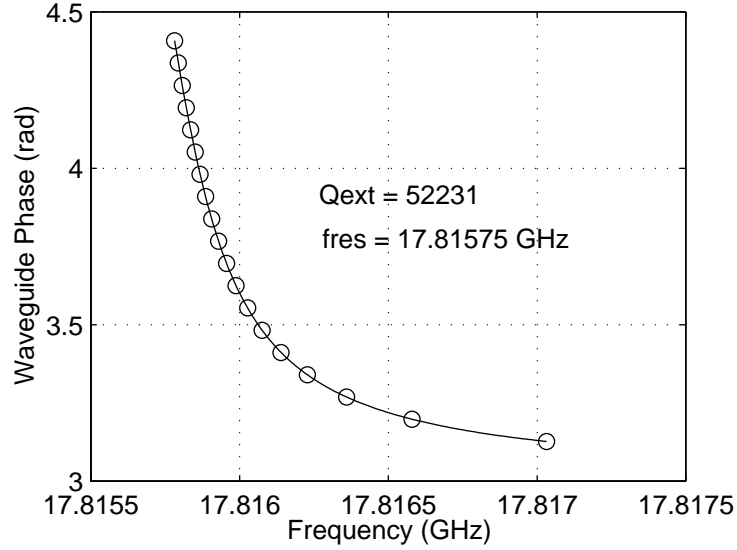


Figure 2.16: Determination of resonant frequency and  $Q_{ext}$  for the  $TE_{012}$  mode from equation (2.10) with a mesh spacing of 0.31 mm. Waveguide phase is  $k(\omega)D$ . The aperture has a radius  $R_a = 2.85$  mm and thickness  $d_a = 1.034$  mm.

#### STEP DESCRIPTION

- 1 Cooling channel and grooves machined on copper endcap
- 2 Surface of copper endcap machined to class-16 finish
- 3 Copper endcap brazed to stainless-steel ring
- 4 Stainless-steel ring assembly machined to correct dimensions
- 5 Surface of copper endcap diamond fly-cut to mirror finish
- 6 Surface of copper endcap chemically-etched for  
5 seconds for vacuum cleaning
- 7 Stainless-steel ring assembly welded to stainless-steel piston
- 8 RF spring gaskets placed in RF groove around  
circumference of copper endcap
- 9 Piston assemblies inserted into cavities and placed under vacuum

Table 2.3: Piston assembly and copper endcap surface preparation.

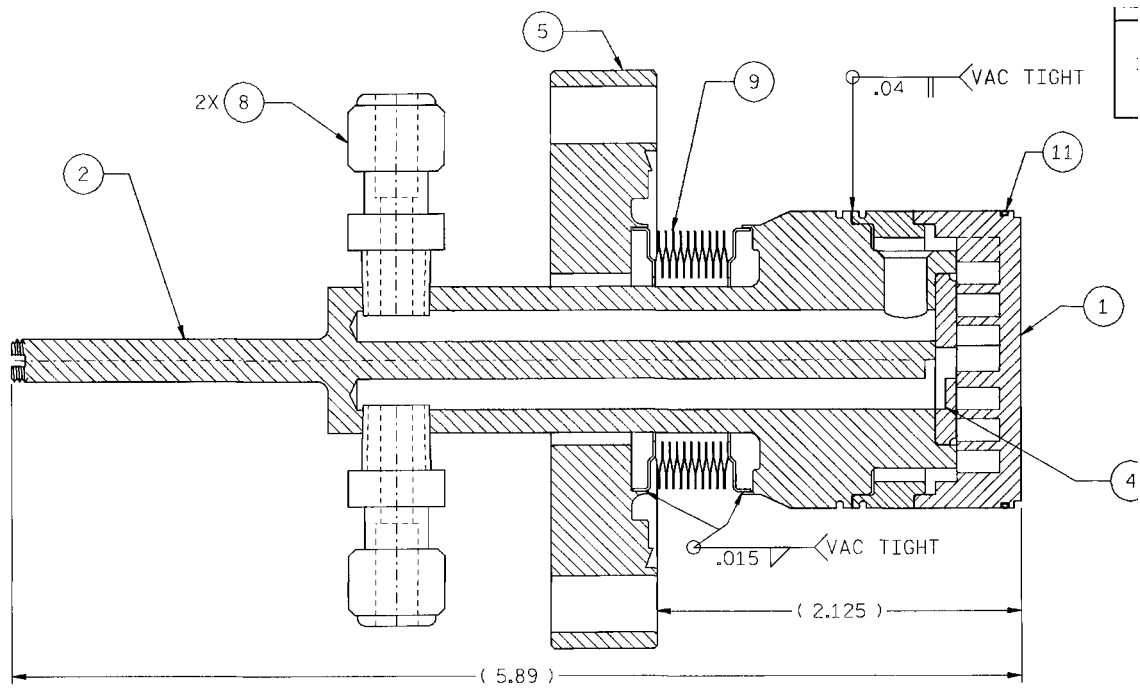


Figure 2.17: Assembly schematic of endcap and piston. 1. Copper endcap. 2. Part of differential screw assembly. 5. Vacuum flange. 8. Cooling pipe mounts. 9. Bellows. 11. Spring gasket housing.

cavity. For the first design discussed in [47], this gap was also used to remove the degeneracy between the  $TE_{011}$  mode and the  $TM_{111}$  mode. However, in that design we allowed the gap to be too long and RF breakdown occurred along the length of the piston as shown in Figure 2.18. From the pattern of the breakdown, it was determined that a coaxial  $TE_{31}$  mode was excited along the length of the piston. The average distance between the breakdown spots corresponded to a guided wavelength consistent with 11.424 GHz. This is also consistent with the fact that the nearest resonant mode that may be coupled from the high-power port is the  $TE_{311}$  mode.

To remedy this problem, we machined two grooves along the outer radius of the endcaps as shown in Figure 2.19. The groove on the face of the endcap is used to remove the degeneracies between the  $TE_{011}$  and  $TM_{111}$  modes as well as between the  $TE_{012}$  and  $TM_{112}$  modes. The smaller groove is used to house a gold-plated stainless-steel spring gasket from BalSeal (see Figure 2.20). When compressed the

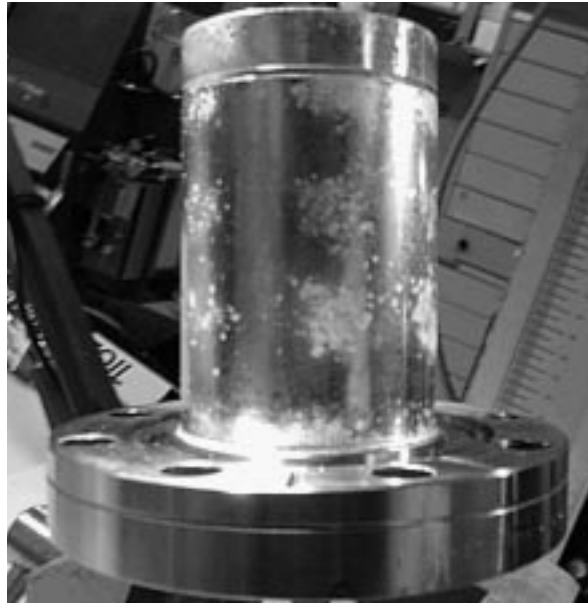


Figure 2.18: Picture of RF breakdown along endcap piston due to  $TE_{31}$  coaxial mode.

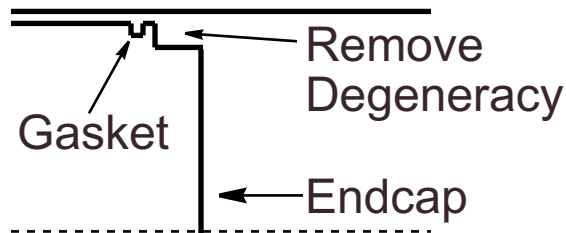


Figure 2.19: Close-up of endcap with grooves. Not to scale.

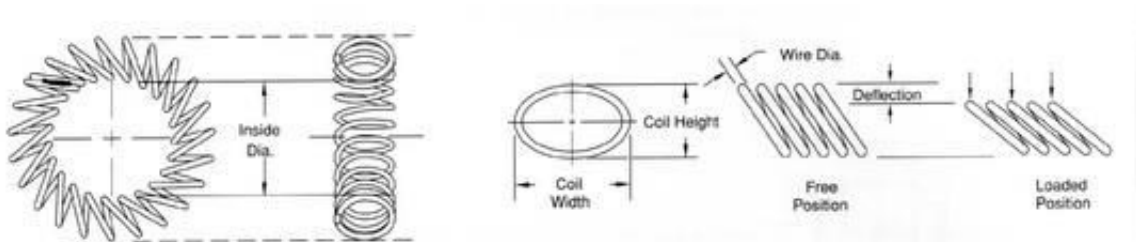


Figure 2.20: Spring gasket from BalSeal. An RF short is created when force is applied to the spring.

Mode	Freq (GHz) MAFIA	Freq (GHz) Nominal	$\Delta F$ (MHz) Nominal	$\Delta F$ (MHz) Main Mode	Q Nominal	Q MAFIA
TE <sub>011</sub>	11.438015	11.438156	-0.1	0.0	21944	21920
TM <sub>111</sub>	11.326234	11.438156	-111.9	-111.8	10760	7702
TM <sub>210</sub>	11.046129	11.100256	-54.1	-391.9	16296	12447
TM <sub>020</sub>	11.870313	11.931238	-60.9	432.3	16895	12582
TE <sub>311</sub>	11.975997	12.029013	-53.0	538.0	14052	11362
TE <sub>012</sub>	17.819734	17.820028	-0.3	0.0	21905	21881
TE <sub>611</sub>	17.969457	18.030973	-61.5	149.7	14821	12588
TM <sub>411</sub>	18.007711	18.200385	-192.7	188.0	13573	8871
TM <sub>112</sub>	17.625191	17.820028	-194.8	-194.5	13430	8764
TE <sub>312</sub>	18.033395	18.204921	-171.5	213.7	14866	9210
TM <sub>220</sub>	18.086097	18.193231	-107.1	266.4	16296	13705
TE <sub>021</sub>	17.092433	17.093202	-0.8	-727.3	34102	34066
TM <sub>030</sub>	18.585457	18.704386	-118.9	765.7	21154	13090
TE <sub>212</sub>	16.961036	17.103876	-142.8	-858.7	15199	9438
TM <sub>121</sub>	16.905671	17.093201	-187.5	-914.1	13153	8438

Table 2.4: 2D MAFIA simulation for endcaps with groove lengths of 0.99 mm. “Nominal” is the theoretical value without perturbations. Only modes that are within 1 GHz of the resonant frequencies of the TE<sub>011</sub> or the TE<sub>012</sub> modes are shown.

spring gasket becomes an RF short to stop coaxial modes from being excited along the length of the piston. Also, stainless-steel rings were brazed onto the inner radius of the cavity sidewall behind the spring gaskets to help damp any fields that may leak through them.

The gap between the endcap and the cavity sidewall is designed to be 0.1 mm. The spring gasket is estimated to contact the sidewall at approximately 0.4 mm away from the edge of the endcap groove. The endcap groove was initially designed to be 1.0 mm in radius and 0.99 mm in length. However, cold-tests (see Section 2.1.7) have shown that the TE<sub>012</sub> mode was not sufficiently isolated from other modes. Also, simulations from GdfidL after the first high-power test shows poor coupling to the TE<sub>012</sub> mode using endcaps with 0.99 mm grooves. The proper groove length was empirically determined to be 2.49 mm. Two-dimensional simulations of the cavity using MAFIA with these two different groove lengths are given in Tables 2.4–2.5.

Mode	Freq (GHz) MAFIA	Freq (GHz) Nominal	$\Delta F$ (MHz) Nominal	$\Delta F$ (MHz) Main Mode	Q Nominal	Q MAFIA
TE <sub>011</sub>	11.437957	11.438156	-0.2	0.0	21944	21915
TM <sub>020</sub>	11.673101	11.931238	-258.1	235.1	16895	8002
TE <sub>311</sub>	11.827942	12.029013	-201.1	390.0	14052	8675
TM <sub>111</sub>	11.025434	11.438156	-412.7	-412.5	10760	5552
TM <sub>210</sub>	10.897198	11.100256	-203.1	-540.8	16296	9095
TE <sub>012</sub>	17.819611	17.820028	-0.4	0.0	21905	21875
TE <sub>611</sub>	17.785366	18.030973	-245.6	-34.2	14821	9561
TM <sub>220</sub>	17.733733	18.193231	-459.5	-85.9	16296	10179
TM <sub>030</sub>	18.010282	18.704386	-694.1	190.7	21154	6604
TM <sub>411</sub>	17.338607	18.200385	-861.8	-481.0	13573	4835
TE <sub>312</sub>	17.158428	18.204921	-1046.5	-661.2	14866	3679
TE <sub>021</sub>	17.092316	17.093202	-0.9	-727.3	34102	34054
TM <sub>112</sub>	17.053051	17.820028	-767.0	-766.6	13430	7173

Table 2.5: 2D MAFIA simulation for endcaps with groove lengths of 2.49 mm. “Nominal” is the theoretical value without perturbations. Only modes that are within 1 GHz of the resonant frequencies of the TE<sub>011</sub> or the TE<sub>012</sub> modes are shown.

Of course, the coupling apertures were not taken into account in these simulations.

These two tables show only the modes that are within 1 GHz of the resonant frequencies of the TE<sub>011</sub> or the TE<sub>012</sub> modes. Notice that the degenerate modes TM<sub>111</sub> and TM<sub>112</sub> are more than 100 MHz away from the desired modes. Also, since the coupling to TM modes is weak due to the configuration of the waveguide couplers, only TE modes should be carefully considered.

The closest mode to the TE<sub>011</sub> mode is the TE<sub>311</sub> mode. According to the tables, the TE<sub>311</sub> mode is more than 300 MHz away and will not interfere with the desired mode.

The tables also show that the TE<sub>611</sub> and the TE<sub>312</sub> modes are the two closest TE modes that may interfere with the TE<sub>012</sub> mode. Although the TE<sub>611</sub> appears to be approximately 150 MHz higher for the endcaps with 0.99 mm groove lengths, the high-power coupling aperture actually decreases the resonant frequency of the TE<sub>611</sub> mode. This will be shown in more detail in section 2.1.7. This fact was discovered after the first high-power test. According to Table 2.5, the resonant frequency of

the  $TE_{611}$  mode is approximately 34 MHz lower than the resonant frequency of the  $TE_{012}$  mode for the endcaps with 2.49 mm groove lengths. However, the high-power coupling aperture lowers this frequency further and will eliminate the possibility of interference with the  $TE_{012}$  mode. Also, the  $TE_{312}$  is more than 600 MHz away. Hence, no modes are likely to interfere with the  $TE_{012}$  mode in this configuration.

A schematic of the full cavity assembly with the endcaps inserted is shown at the top of Figure 2.21. For completeness a sideview of the cavity in which the high-power coupler and the diagnostic coupler can both be seen is shown at the bottom of Figure 2.21.

### 2.1.6 Water-Cooling

Although a high temperature rise is desired for a pulsed heating experiment, we must remove the average heat that is applied to the cavity. This is necessary for a stable resonant frequency. Otherwise, the cavity tune will constantly shift from thermal expansion. In steady-state there is some power reflected from a cavity that is not matched ( $\beta \neq 1$ ). Taking account of this fact, the peak power dissipated in the cavity walls is [43, p. 163]

$$P_{diss} = \frac{4\beta}{(1 + \beta)^2} P_{peak}, \quad (2.14)$$

where  $P_{peak}$  is the peak RF power input to the cavity and  $\beta$  is the coupling coefficient. The total average power dissipated in the cavity walls is

$$P_{total} = \frac{4\beta}{(1 + \beta)^2} P_{peak} T_p f_{rep}, \quad (2.15)$$

where  $T_p$  is the pulse length of the RF and  $f_{rep}$  is the repetition rate of the RF source.

The cavity is cooled by contact with a turbulent flow of water. The water carries the heat away from the system as it is deposited by the RF source and places the system in thermal equilibrium. It is desirable to place the water as close to the heated surface as possible. In other words, the material we want to cool should be as thin as possible to keep the average temperature rise in the material low.

For any cooling situation, the temperature of the water must remain below the

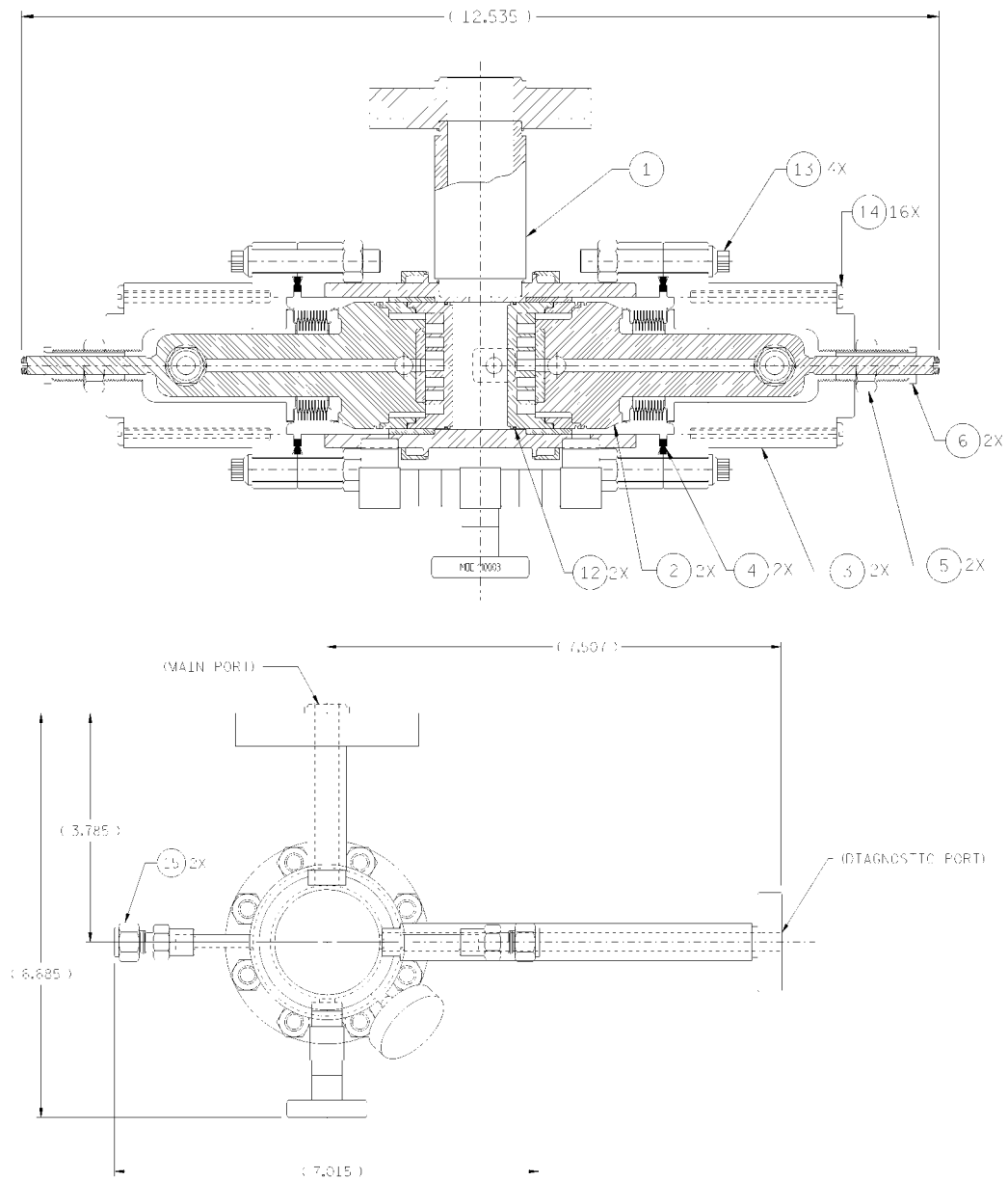


Figure 2.21: Assembly schematic of cavity with endcaps. The sideview of the cavity is shown on the bottom. 1. High-power port. 2. Endcap/Piston assembly. 3. Brace for differential screw assembly. 4. Vacuum gasket. 5. Differential screw locknut. 6. Differential screw. 15. Water-cooling pipes for cavity sidewall. All dimensions are in inches.

$\rho_w$	1.0 g/cm <sup>3</sup>
$c_{p,w}$	4.186 J/g · K
$\nu$	$1.006 \times 10^{-2}$ cm <sup>2</sup> /s
$k_w$	$5.95 \times 10^{-3}$ W/cm · K

Table 2.6: Parameters for water at room temperature.

boiling point. The average temperature rise of water from a known heat input is

$$\Delta T_w = \frac{P_{total}}{\rho_w c_{p,w} Q_w}, \quad (2.16)$$

where  $\rho_w$  is the density of water,  $c_{p,w}$  is the specific heat of water and  $Q_w$  is the flow rate of water. Some parameters of water are given in Table 2.6. It is more convenient to convert the flow rate to gallons per minute (gpm), since most commercial flow equipment use this unit. Using Table 2.6 we have

$$\Delta T_w [\text{K}] = \frac{P_{total} [\text{W}]}{264.1 Q [\text{gpm}]}. \quad (2.17)$$

$\Delta T_w$  must be less than approximately 70 K to keep the room-temperature water below the boiling point.

The heat transfer coefficient  $h$  [W/(cm<sup>2</sup> · K)] is the parameter that characterizes the amount of cooling available from the water flow. For turbulent water flowing in a tube,  $h$  can be parameterized as [38, eq.(9-10b)]

$$h = 0.023 \frac{k_w}{d_h} Re^{0.8} Pr^{0.33}, \quad (2.18a)$$

$$Re = \frac{d_h v}{\nu}, \quad (2.18b)$$

$$Pr = \frac{\rho_w \nu c_{p,w}}{k_w}, \quad (2.18c)$$

$$d_h = \frac{4A_h}{L_h}, \quad (2.18d)$$

where  $Re$  is the Reynold's number,  $Pr$  is the Prandtl number,  $d_h$  is the hydraulic

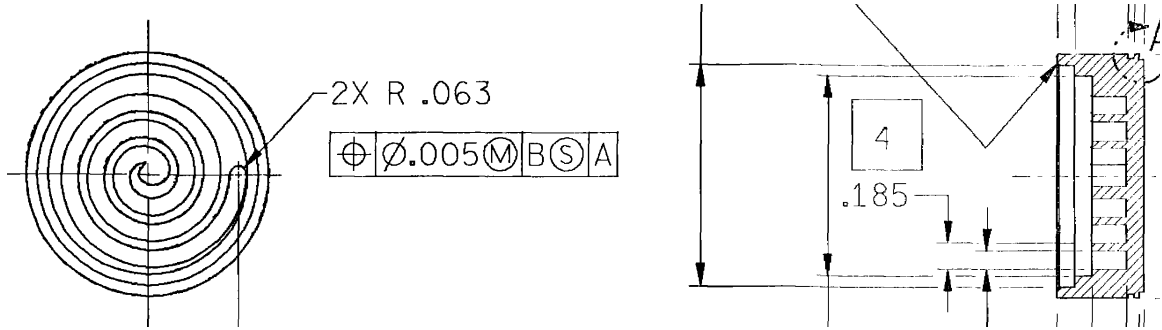


Figure 2.22: Schematic of the spiral cut into the back of the endcaps. The spiral becomes a rectangular tube of cross-section 0.125 inches by 0.25 inches.

diameter,  $v$  is the velocity of the water flow,  $\nu$  is the kinematic viscosity of water,  $k_w$  is the thermal conductivity of water,  $A_h$  is the cross-sectional area of the tube and  $L_h$  is the perimeter of the tube. Using the values in Table 2.6 we may write the heat transfer coefficient as

$$h [\text{W}/(\text{cm}^2 \cdot \text{K})] = 0.01 \frac{v [\text{cm}/\text{s}]^{0.8}}{d_h [\text{cm}]^{0.2}}. \quad (2.19)$$

The velocity of the water in the tube is given by the flow rate divided by the cross-sectional area. In our chosen units we get

$$v [\text{cm}/\text{s}] = \frac{63.09 Q [\text{gpm}]}{A_h [\text{cm}^2]}. \quad (2.20)$$

Figures 2.17 and 2.22 show the design for the water-cooling of the endcaps. A spiral is cut into the backs of the endcaps in order to keep the velocity of the water flow constant. Had we allowed the water to simply flow radially outward from the center of the endcap, the velocity of the water flow would decrease because of the increase in the cross-sectional area. According to equation (2.19),  $h$  would also decrease and the cooling would not be as effective.

Once the endcap is mated to the piston, the spiral becomes a long rectangular tube with cross-section 0.125 inches by 0.25 inches. For a pressure drop of 60 psi, the flow was measured to be 1.1 gpm. The flow parameters for the endcaps are given in Table 2.7.

$d_h$	0.42 cm
$A_h$	0.20 cm <sup>2</sup>
$\Delta P$	60 psi
$Q_w$	1.1 gpm
$v$	340 cm/s
$h$	1.3 W/(cm <sup>2</sup> · K)

Table 2.7: Flow parameters for water-cooling of endcaps.

$d_h$	0.36 cm
$A_h$	0.16 cm <sup>2</sup>
$\Delta P$	75 psi
$Q_w$	0.75 gpm
$v$	290 cm/s
$h$	1.2 W/(cm <sup>2</sup> · K)

Table 2.8: Flow parameters for water-cooling of the cavity body.

Figures 2.21 and 2.23 show the design for the water-cooling of the cavity body. The water flow splits and flows around the circumference of the cavity on both sides of the high-power coupler. The flow is in a rectangular tube with cross-section 0.1 inches by 0.25 inches. The flow parameters for the cavity body are given in Table 2.8.

Since the geometry for the cooling of the endcaps and the sidewall is complicated, it is necessary to solve for the temperature numerically. To simplify the problem, we will approximate the cooling of the endcaps as azimuthally symmetric. This will allow us to use two-dimensional finite element codes. The cooling for the sidewall is already azimuthally symmetric.

First, we need to modify the heat-diffusion equation to take advantage of this azimuthal symmetry. In steady-state, equation (3.9) becomes

$$-\vec{\nabla} \cdot (k \vec{\nabla} T) = g, \quad (2.21)$$

where we allow the thermal conductivity  $k$  to be spatially-dependent.  $T$  is the temperature and  $g$  is the heat per unit volume added to the system. In cylindrical

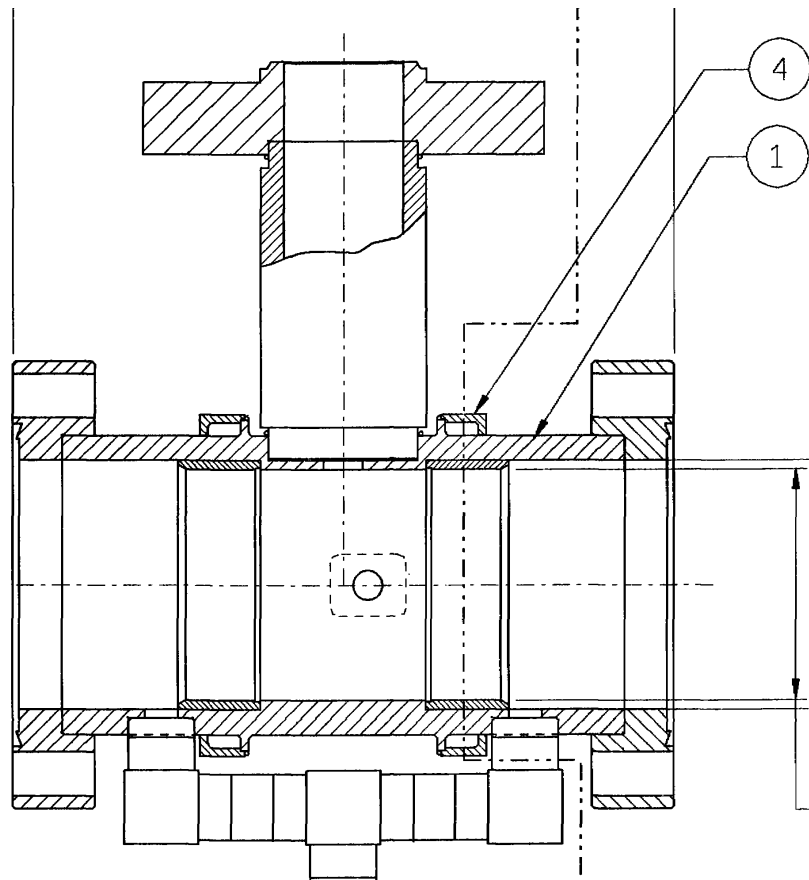


Figure 2.23: Schematic of the cooling tubes around the circumference of the cavity body. 4. Stainless-steel half-tube mated to a copper post to create a complete water tube of cross-section 0.1 inches by 0.25 inches.

coordinates this equation becomes

$$-\frac{1}{r} \frac{\partial}{\partial r} \left( r k \frac{\partial T}{\partial r} \right) - \frac{1}{r} \frac{\partial}{\partial \phi} \left( \frac{k}{r} \frac{\partial T}{\partial \phi} \right) - \frac{\partial}{\partial z} \left( k \frac{\partial T}{\partial z} \right) = g, \quad (2.22)$$

Since the heating is azimuthally symmetric we let  $\partial T / \partial \phi = 0$ . The heating equation finally becomes

$$-\frac{\partial}{\partial r} \left( k r \frac{\partial T}{\partial r} \right) - \frac{\partial}{\partial z} \left( k r \frac{\partial T}{\partial z} \right) = g r. \quad (2.23)$$

If we let  $k' = kr$ , then equation (2.23) is a two-dimensional cartesian heat-diffusion equation with a spatially-dependent thermal conductivity  $k'$ . Thus, we may solve a rotationally symmetric heating problem in steady-state using the two-dimensional heat-diffusion equation in cartesian coordinates.

The general boundary condition from equation (3.13) is written as

$$r k_i \hat{n}_i \cdot \vec{\nabla} T \Big|_{\vec{r}_i} + r h_i T \Big|_{\vec{r}_i} = r f_i(\vec{r}_i, t), \quad (2.24)$$

where  $i$  denotes the surface and  $h_i$  is the heat transfer coefficient for surface  $i$ . Basically, we use a two-dimensional code to solve for the heating by allowing

$$k_i \rightarrow k_i r, \quad h_i \rightarrow h_i r, \quad f_i \rightarrow f_i r. \quad (2.25)$$

For an isolated surface  $h_i = 0$  and  $f_i = 0$ . For a water-cooled surface  $f_i = 0$ . For a heated surface,  $h_i = 0$  and  $f_i = dP/dA$  where  $dP/dA$  is the heat flux.

For the cavity, the total power dissipated on the surface is

$$P_{total} = P_{side} + 2P_{end}, \quad (2.26)$$

where  $P_{side}$  is the power dissipated on the sidewall and  $P_{end}$  is the power dissipated on an endcap. The power dissipated on the sidewall is

$$P_{side} = \frac{1}{2} R_s \int_0^d |H_z(r = R)|^2 2\pi R dz = \frac{1}{2} \pi R d R_s H_0^2 J_0^2(x'_{01}), \quad (2.27)$$

and the power dissipated on an endcap is

$$P_{end} = \frac{1}{2} R_s \int_0^R |H_r(z=0)|^2 2\pi r dr = H_0^2 \frac{\pi^3 R_s R^4 J_0^2(x'_{01})}{2d^2 x_{01}'^2}, \quad (2.28)$$

where  $H_0$  is a field-strength constant to be determined. Substituting equations (2.27–2.28) into equation (2.26) and solving for  $H_0$  gives

$$H_0^2 = \frac{P_{total}}{R_s J_0^2(x'_{01}) \left[ \frac{1}{2} \pi d R + \frac{\pi^3 R^4}{d^2 x_{01}'^2} \right]}. \quad (2.29)$$

Hence the heat fluxes for the endcaps and the sidewall are

$$\left. \frac{dP}{dA} \right|_{end} = \frac{1}{2} R_s |H_r(z=0)|^2 = \frac{1}{2} \frac{\pi^2 R^2 P_{total}}{x_{01}'^2 d^2 J_0^2(x'_{01}) \left[ \frac{1}{2} \pi d R + \frac{\pi^3 R^4}{d^2 x_{01}'^2} \right]} J_1^2\left(\frac{x'_{01} r}{R}\right), \quad (2.30a)$$

$$\left. \frac{dP}{dA} \right|_{side} = \frac{1}{2} R_s |H_z(r=R)|^2 = \frac{1}{2} \frac{P_{total}}{\frac{1}{2} \pi d R + \frac{\pi^3 R^4}{d^2 x_{01}'^2}} \sin^2\left(\frac{\pi z}{d}\right). \quad (2.30b)$$

The cavity endcap is modeled in Figure 2.24. Since the endcap is axisymmetric, only half of the endcap is modeled. The heat flux is applied to the surface on the right and the water boundary conditions are applied along the fins. We will assume  $\beta = 1$  to obtain an upper bound on the temperature rise. Using the parameters given in Table 2.7 for  $P_{peak} = 10$  MW,  $T_p = 1.5$   $\mu$ s and  $f_{rep} = 60$  Hz we get the average temperature rise as shown in Figure 2.24. The maximum average temperature rise is approximately 14 K and it occurs at the location of the maximum heat flux. The temperature rise of the water is approximately 1 K.

The cavity sidewall is modeled in Figure 2.25. The stainless-steel half of the water tube is not modeled since its thermal conductivity is much lower than copper's. The heat flux is applied to the bottom surface around the center. Using the parameters given in Table 2.8 we get the average temperature rise as shown in Figure 2.25. The maximum average temperature rise is also approximately 14 K and it occurs at the location of the maximum heat flux. The temperature rise of the water is approximately 1.5 K.

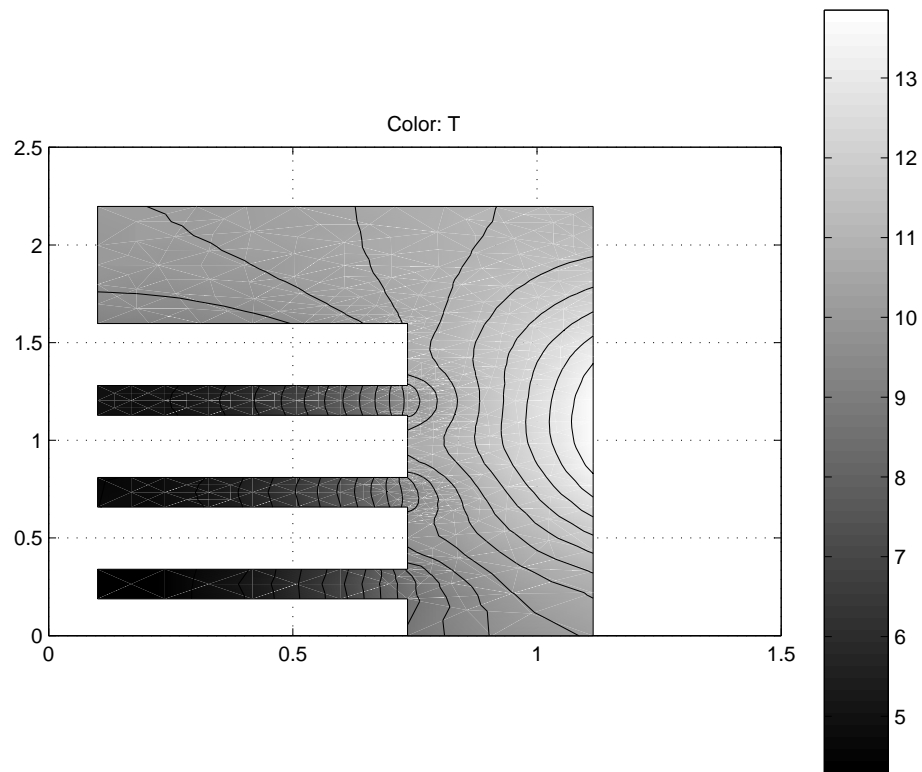


Figure 2.24: Average temperature rise on the cavity endcaps for  $P_{peak} = 10$  MW,  $T_p = 1.5 \mu\text{s}$  and  $f_{rep} = 60$  Hz. All dimensions are in cm.

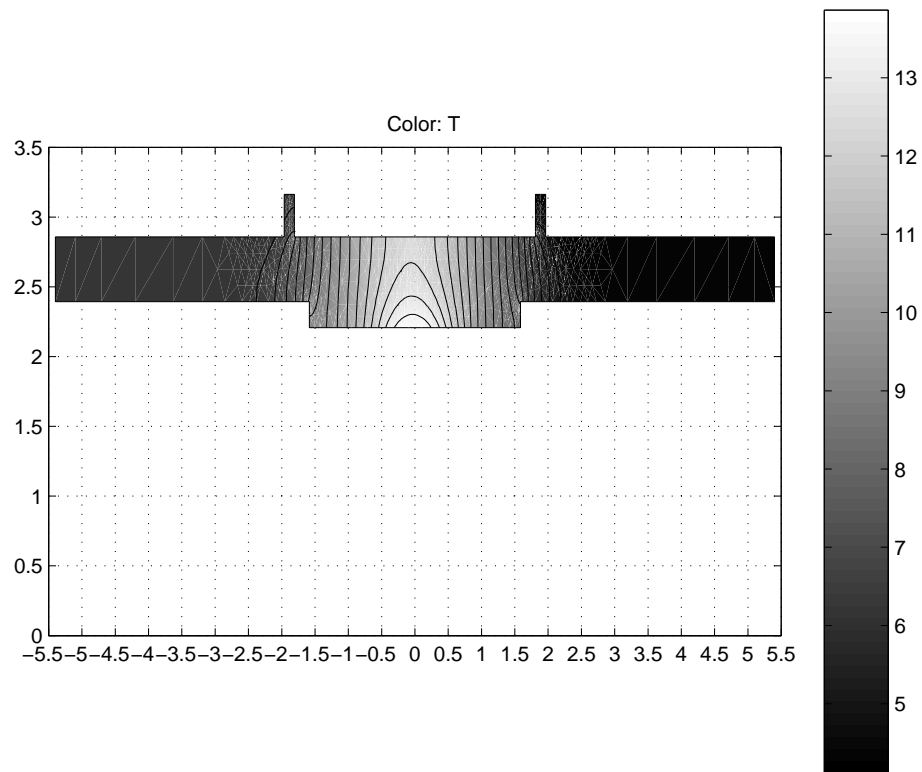


Figure 2.25: Average temperature rise on the cavity sidewall for  $P_{peak} = 10$  MW,  $T_p = 1.5 \mu\text{s}$  and  $f_{rep} = 60$  Hz. All dimensions are in cm.

If the cavity structure were completely made of the same material and the temperature rise was equal at all points, then the expansion may be computed from only the volume that contains the electromagnetic fields. When the length of the cavity structure increases, the pistons are pulled back because they are connected to the body. The pistons, however, will also expand the by same amount. The net increase is due to only the cavity volume itself. However, the pistons are mostly constructed from stainless-steel whose expansion is much less than copper's. Therefore, we expect a larger decrease in the resonant frequency as the cavity sidewall expands from heating. From equation (2.2) the sensitivity of the frequency to small changes in the cavity dimensions is

$$\frac{\partial f}{\partial R} = -2.7 \times 10^3 \text{ MHz/cm}, \quad \frac{\partial f}{\partial d} = -2.9 \times 10^3 \text{ MHz/cm}. \quad (2.31)$$

If we assume the maximum temperature rise of 14 K to be equal across the length of the cavity then the expansion would be

$$\Delta d = (1.67 \times 10^{-5} \text{ K}^{-1})(1.9 \text{ cm})(14 \text{ K}) = 0.4 \text{ } \mu\text{m},$$

$$\Delta R = (1.67 \times 10^{-5} \text{ K}^{-1})(0.5 \text{ cm})(14 \text{ K}) = 0.1 \text{ } \mu\text{m},$$

where the cavity sidewall is approximately 0.5 cm thick. This corresponds to a total decrease in frequency of approximately 1.5 MHz. Chapter 4 will show that the actual decrease in frequency is higher by a factor of 3.

### 2.1.7 Cold-Test Results

Three complete cavities were constructed. Figure 2.26 shows a picture of one such cavity with one of its endcaps sitting outside. The cavities are labeled from one to three to distinguish them. The third cavity is not used in any high-power tests, since there is a problem inserting the endcaps into the cavity. The spring gaskets used to cutoff the coaxial modes were caught in the hole left over from the brazing of stainless-steel rings in the cavity.

The first set of cold-tests were completed with endcaps that have 0.99 mm groove



Figure 2.26: Cavity body with endcap shown on the outside. The water-cooling pipes can be seen on the bottom of the cavity body.

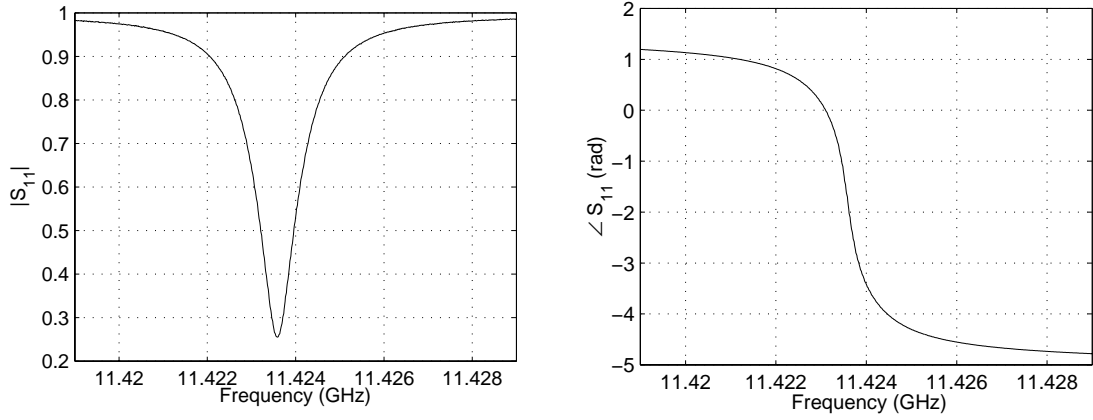


Figure 2.27: Magnitude and phase of the reflection coefficient for the  $\text{TE}_{011}$  mode of cavity 1.

Cavity	$\beta$	$Q_L$	$Q_{011}$	$Q_{\text{ext}}$	$Q_{\text{ext,sim}}$
1	1.65	7670	20350	12300	12830
2	1.69	7670	20600	12200	12830

Table 2.9: Measured parameters for the  $\text{TE}_{011}$  mode of cavities 1 and 2.

lengths. The second set of cold-tests were completed with endcaps that have 2.49 mm groove lengths.

### First Set

Data for the  $\text{TE}_{011}$  mode for cavities 1 and 2 were obtained with a HP8510C network analyzer using a WR-90 calibration kit. The data for cavity 1 is shown in Figure 2.27. Since the slope of the phase is negative, cavity 1 is over-coupled (see equation (A.143)). Using the method presented in Section A.4.4, we can fit to the data to determine  $\beta$ ,  $Q_L$  and  $Q_0$  for each cavity. The coupling mechanism for the  $\text{TE}_{011}$  mode is lossless. The results are given in Table 2.9. The data for cavity 2 is shown in Figure 2.28, and the results are also given in Table 2.9.

Figures 2.29–2.30 show the data for the  $\text{TE}_{012}$  mode for cavities 1 and 2 respectively. Because of mode-leakage through the high-power coupler, we must treat the system as a two-port cavity. However, notice there are nearby modes interfering

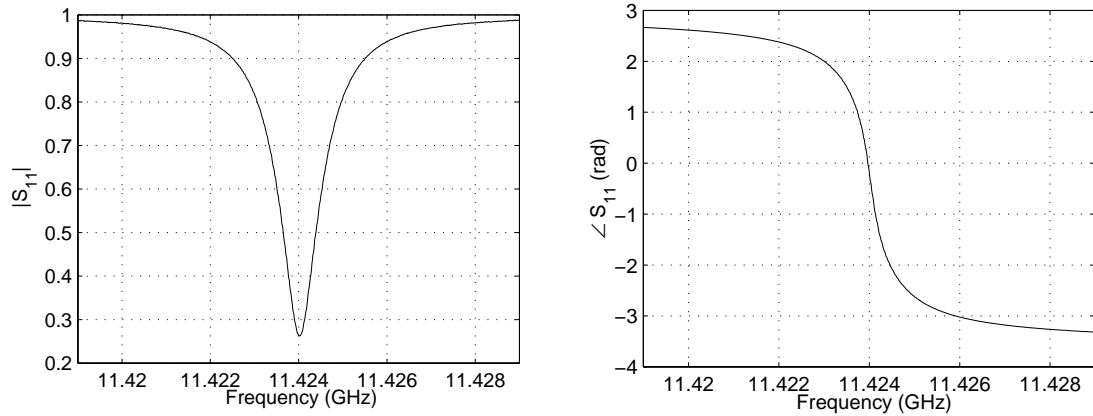


Figure 2.28: Magnitude and phase of the reflection coefficient for the  $TE_{011}$  mode of cavity 2.

with the diagnostic mode. The coupling for this mode is quite poor. Because of this problem, the diagnostic mode was not used for the first high-power test described in Chapter 4. The next section will discuss how this problem was resolved.

### Cold-test cavity

In order to study the problem with the diagnostic mode, we modified one of the first set of cavities that were built. The modified cavity allowed us to use endcaps with different groove lengths. Figure 2.31 shows a picture of the modified cavity. This modified cavity has a thicker aperture for the high-power coupler (2.064 mm) but the same aperture for the diagnostic coupler.

The cavity was modified such that when a flat circular plate is placed on each end of the cavity there would be no axial grooves on the endcaps. In order to use different groove lengths, we use copper endcaps with the specified grooves and copper spacer rings to push the endcaps back an equal amount to recover the proper cavity length. However, the frequencies are shifted higher due to the crushing of the spacer rings when pressure is applied to the endcaps for proper placement. Since the strain is approximately equal for all of the spacer rings, the longer rings will be crushed more and consequently cause a higher shift in the cavity resonant frequencies.

Table 2.10 lists the results for the  $TE_{011}$  mode. The external  $Q$ 's are different

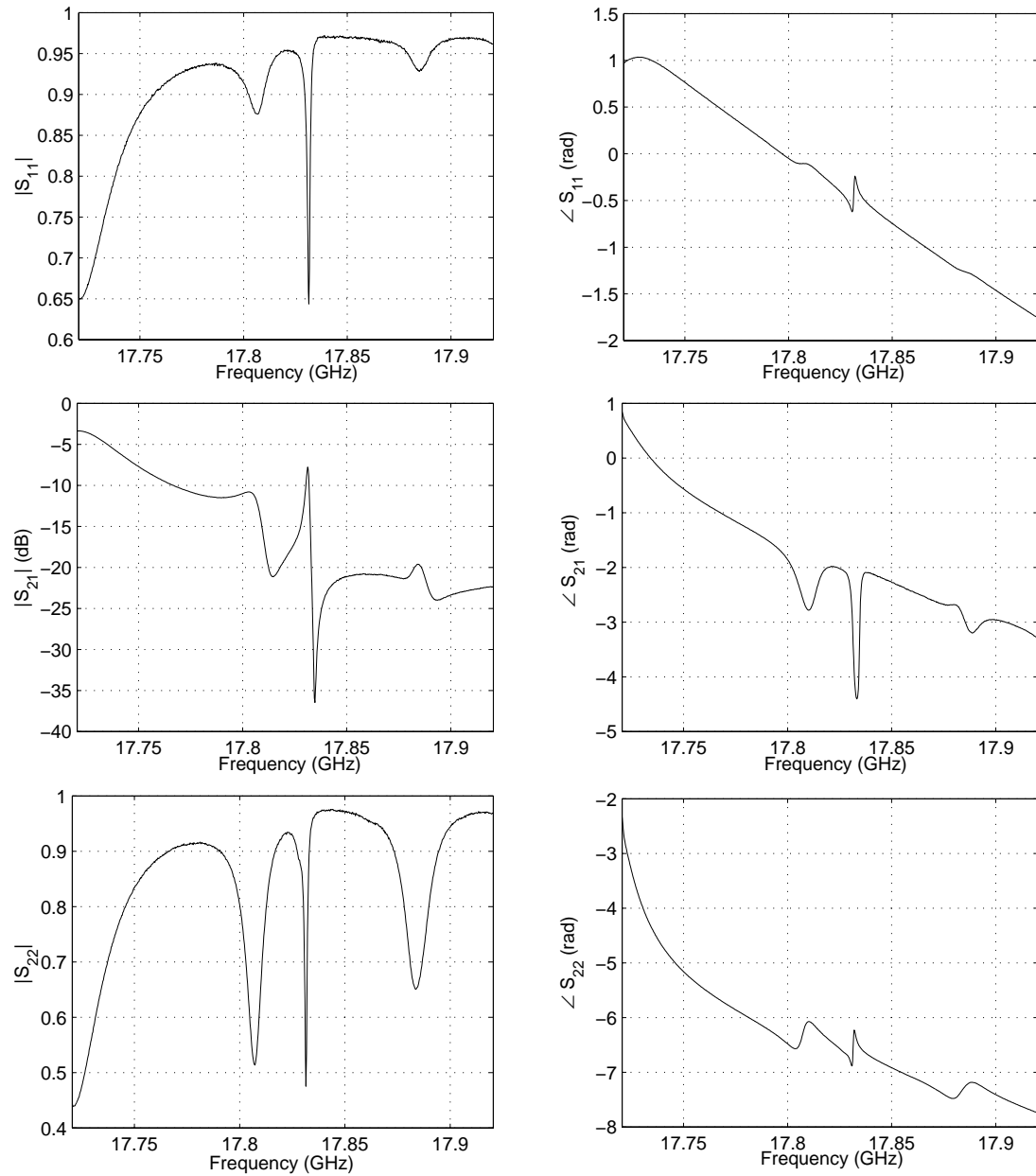


Figure 2.29: S-parameters for the  $TE_{012}$  mode of cavity 1. Port 1 is the diagnostic coupler, and port 2 is the high-power coupler.

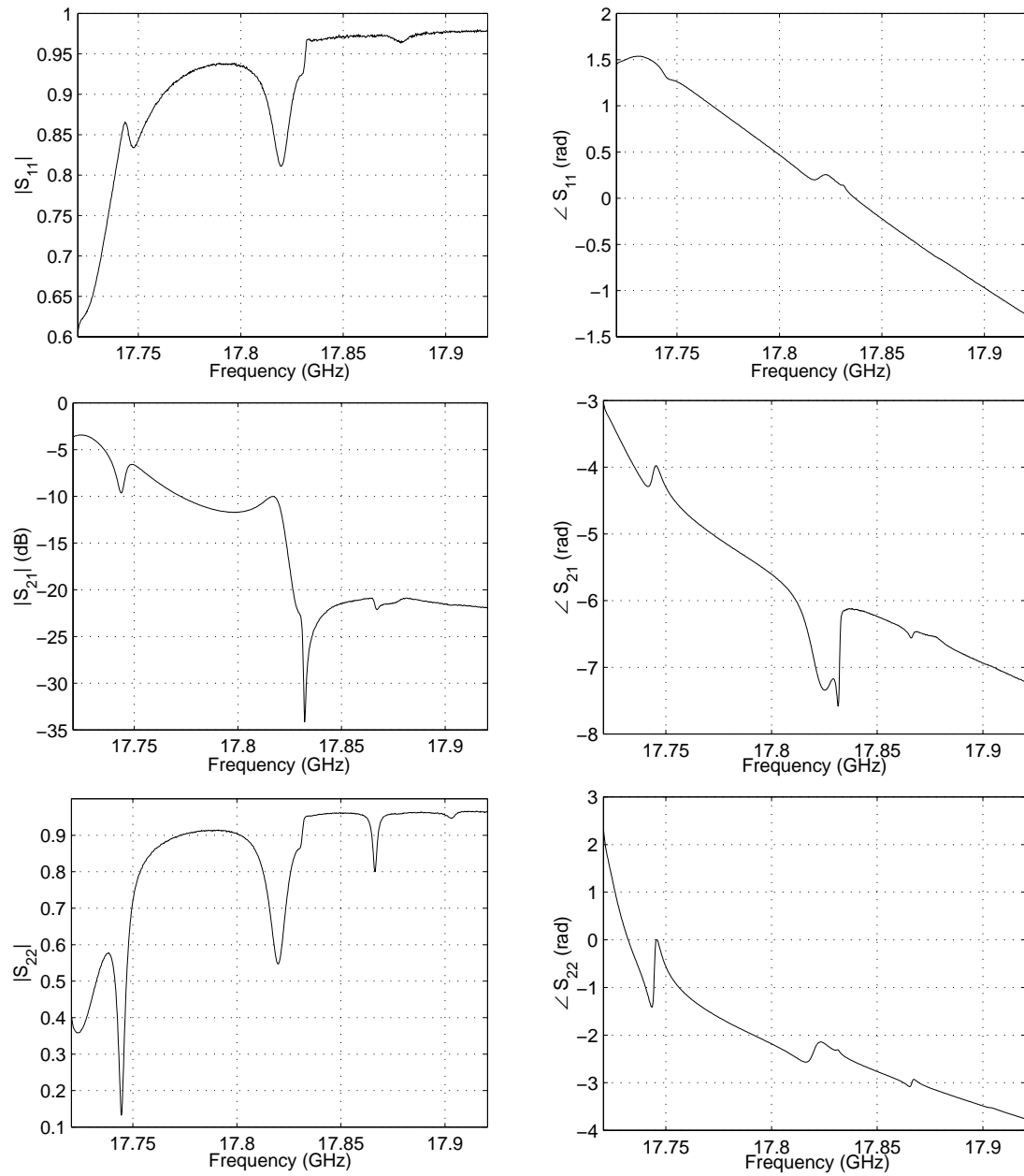


Figure 2.30: S-parameters for the TE<sub>012</sub> mode of cavity 2. Port 1 is the diagnostic coupler, and port 2 is the high-power coupler.

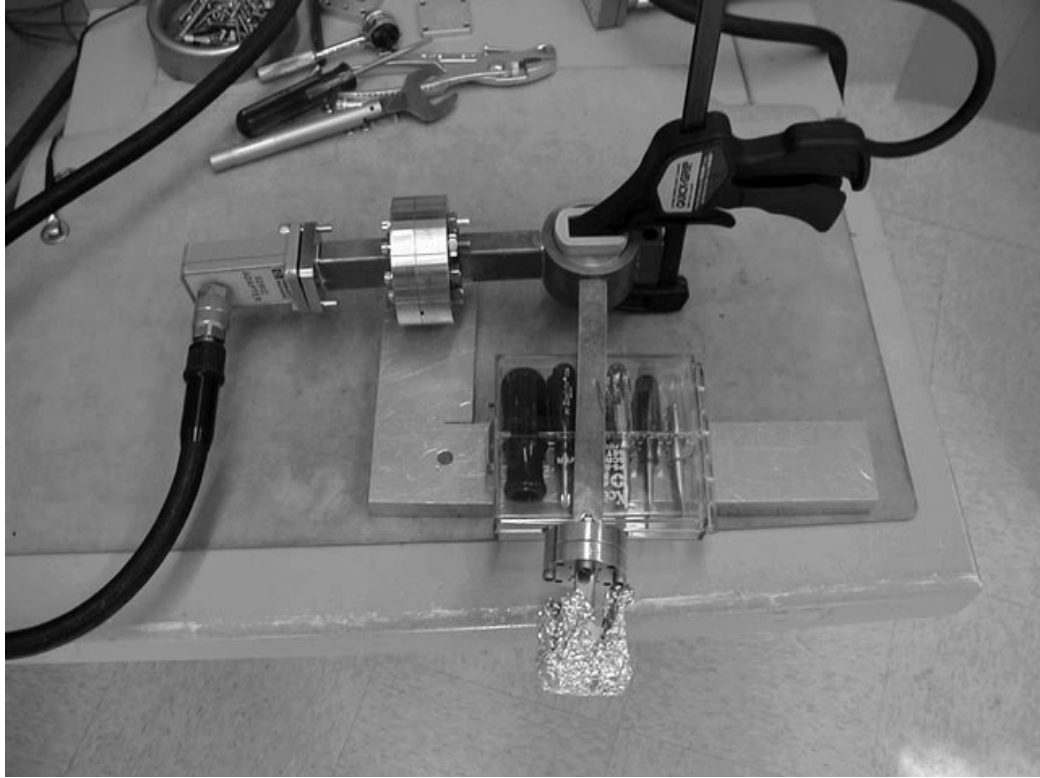


Figure 2.31: A picture of the modified cavity used to test endcaps with different groove lengths. A vice grip is used to hold the endcaps in the cavity.

Groove Length (mm)	Frequency (GHz)	$Q_0$	$Q_{\text{ext}}$	$Q_{\text{ext,sim}}$
0.0	11.42390	18750	15680	17030
0.99	11.45176	19070	15290	16400
2.49	11.48172	18870	14090	15220

Table 2.10: Measured parameters for the  $\text{TE}_{011}$  mode of modified cavity. Coupling aperture thickness  $d_a = 2.064$  mm.

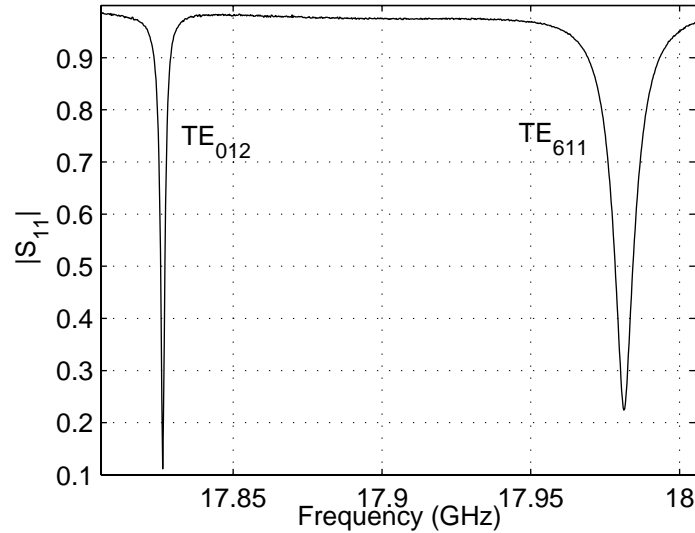


Figure 2.32:  $TE_{012}$  and  $TE_{611}$  modes with high-power coupling aperture taped. There are no axial grooves on the endcaps.

from those listed in Table 2.9 because the coupling aperture is thicker. The simulated results for the external Q's are also given in Table 2.10.

As previously shown in Figures 2.29–2.30, measurement of the  $TE_{012}$  mode must be treated as a two-port cavity due to leakage out the high-power coupling aperture. At these frequencies, the  $TE_{20}$  rectangular waveguide mode would be cutoff in a WR-62 waveguide. After adding a 6-inch WR-62 waveguide to the high-power coupler, no attenuation was measured in  $|S_{21}|$ . Hence the leakage of power occurs as a  $TE_{10}$  mode in the waveguide.

We may also cover the high-power coupling aperture from inside the cavity with copper tape to remove its effect on the fields in the cavity. Figure 2.32 shows this measurement with the high-power coupling aperture taped and with no axial grooves on the endcaps. Table 2.4 shows that the mode on the right is the  $TE_{611}$  mode. Table 2.11 gives the results of the Q measurements of the  $TE_{012}$  mode when the high-power coupling aperture is taped and with different axial groove lengths on the endcaps. The axial groove lengths have a significant effect on  $Q_{ext}$  for the  $TE_{012}$  mode. The close proximity of one of the endcaps to the diagnostic coupling aperture affects the scattering of the electromagnetic fields near the aperture.

Groove Length (mm)	Frequency (GHz)	$Q_0$	$Q_{\text{ext}}$	$Q_{\text{ext,sim}}$
0.0	17.82745	12672	16480	12660
0.99	17.89800	3060	3470	3620
2.49	17.96370	14610	48520	52230

Table 2.11: Measured parameters for the  $\text{TE}_{012}$  mode of modified cavity with high-power coupling aperture taped.

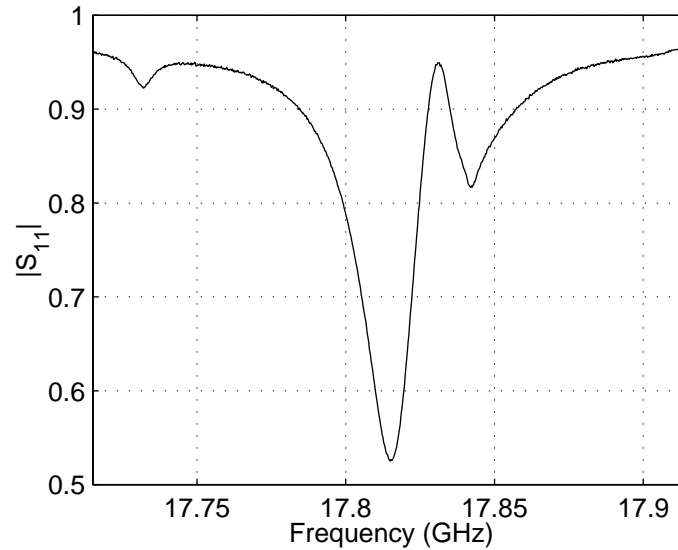


Figure 2.33: Reflection from the diagnostic port of  $\text{TE}_{012}$  mode with no axial grooves on endcaps and the copper tape removed from the high-power coupling aperture.

Using the measured resonant frequencies of the  $\text{TE}_{011}$  and the  $\text{TE}_{012}$  modes, equations (2.2) and (2.8) will give the actual cavity radius and length to be  $R = 2.216$  cm and  $d = 1.879$  cm. Using these values, the resonant frequency of the  $\text{TE}_{611}$  mode is predicted to be 17.980 GHz. This is in close agreement with the measured resonant frequency of 17.9813 GHz.

Figure 2.33 shows the reflection from the diagnostic port when the copper tape is removed from the high-power coupling aperture. There is obvious mode interference with the  $\text{TE}_{012}$  mode and most likely the  $\text{TE}_{611}$  mode. The high-power coupling aperture couples strongly to the  $\text{TE}_{611}$  mode and causes a downwards frequency shift. Using the Kroll-Yu method, GdfidL estimates this frequency shift to be approximately

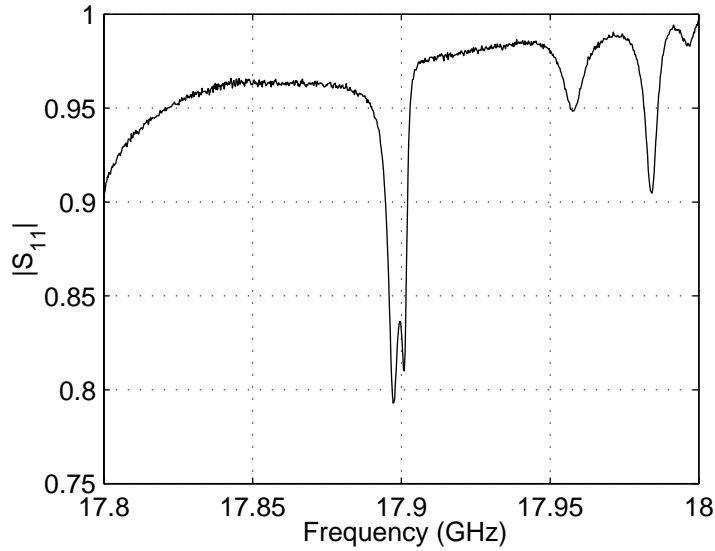


Figure 2.34: Reflection from diagnostic port of  $TE_{012}$  mode with 0.99 mm axial grooves on the endcaps.

230 MHz, but the measured shift is close to 150 MHz.

Figure 2.34 shows the reflection from the diagnostic port of the  $TE_{012}$  mode with 0.99 mm axial groove lengths on the endcaps. There is still mode interference and other parasitic modes exist. This picture is different from Figures 2.29–2.30 because the high-power coupling aperture has a different thickness. It is not known what causes the other parasitic modes to exist; however, it is quite clear that the  $TE_{012}$  mode is unsuitable in this configuration.

Figure 2.35 shows the reflection from the diagnostic port of the  $TE_{012}$  mode with 2.49 mm axial groove lengths on the endcaps. No parasitic modes exist within  $\pm 100$  MHz of the  $TE_{012}$  mode. A proper two-port measurement of the cavity using the methods described in Section A.4.4 gives the results shown in Table 2.12. A comparison of this method with the one described in Section A.4.3 will be described in Section 4.2.3. Notice that the external  $Q$  for the diagnostic port is lower as compared to the external  $Q$  when the high-power coupling aperture is taped. The high-power coupling aperture is large enough to affect the fields in the cavity and will change the scattering of the fields near the diagnostic coupling aperture.

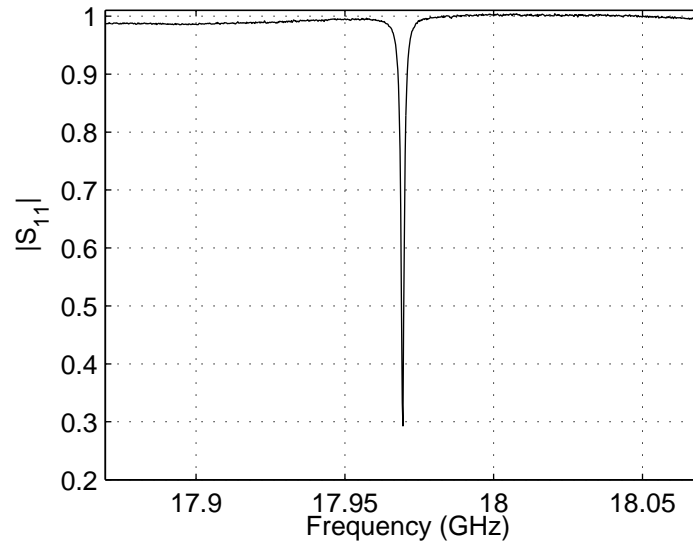


Figure 2.35: Reflection from diagnostic port of  $TE_{012}$  mode with 2.49 mm axial grooves on the endcaps.

$Q_L$	11450
$Q_0$	18920
$Q_{e1}$	31650
$Q_{e2}$	347000

Table 2.12: Two-port measurement of  $TE_{012}$  mode with 2.49 mm axial grooves on the endcaps.  $Q_{e1}$  is the external Q for the diagnostic port, and  $Q_{e2}$  is the external Q for the high-power port.

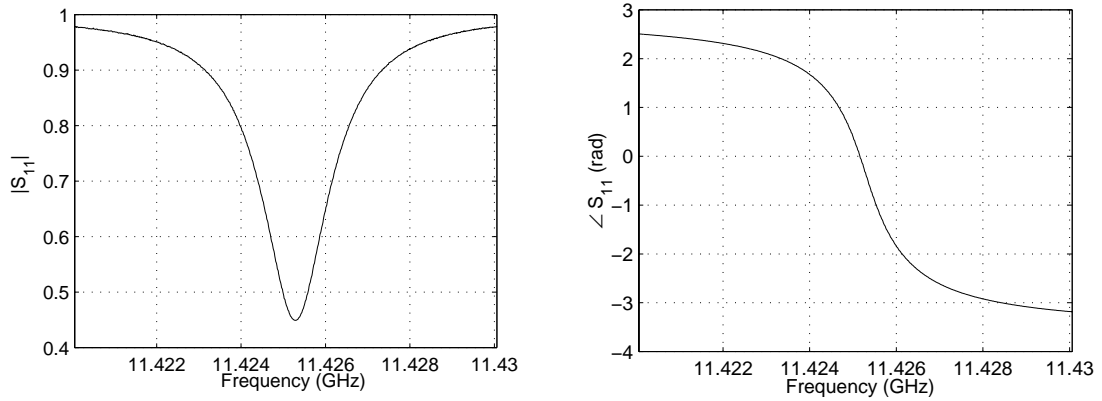


Figure 2.36: Magnitude and phase of the reflection coefficient for the  $TE_{011}$  mode of cavity 1 with 2.49 mm axial grooves on the endcaps.

$f_{\text{res}}$	11.42529 GHz
$Q_0$	17750
$Q_{\text{ext}}$	6850
$\beta$	2.59

Table 2.13: Cold-test results of  $TE_{011}$  mode for cavity 1 with 2.49 mm axial grooves on the endcaps.

### Second test

From the previous section, using endcaps with 2.49 mm axial grooves eliminates the interference with other modes. This design for the endcaps was used for the next high-power test.

Figure 2.36 shows the data for the  $TE_{011}$  mode in cavity 1. Table 2.13 lists the results of the  $Q$  measurement of this mode. The  $Q$ 's of this mode are lower as compared to the first cold-test presented in Table 2.9 because of the damage that occurred to the high-power coupling aperture from RF breakdown in the first high-power test.

Figure 2.37 shows the data for the  $TE_{012}$  mode. Table 2.14 lists the results of the  $Q$  measurement.

The slopes in the phases of the  $S_{11}$  and  $S_{22}$  signals are due to the length of waveguide attached to the cavity. Equations (A.161) represent a cavity with ports

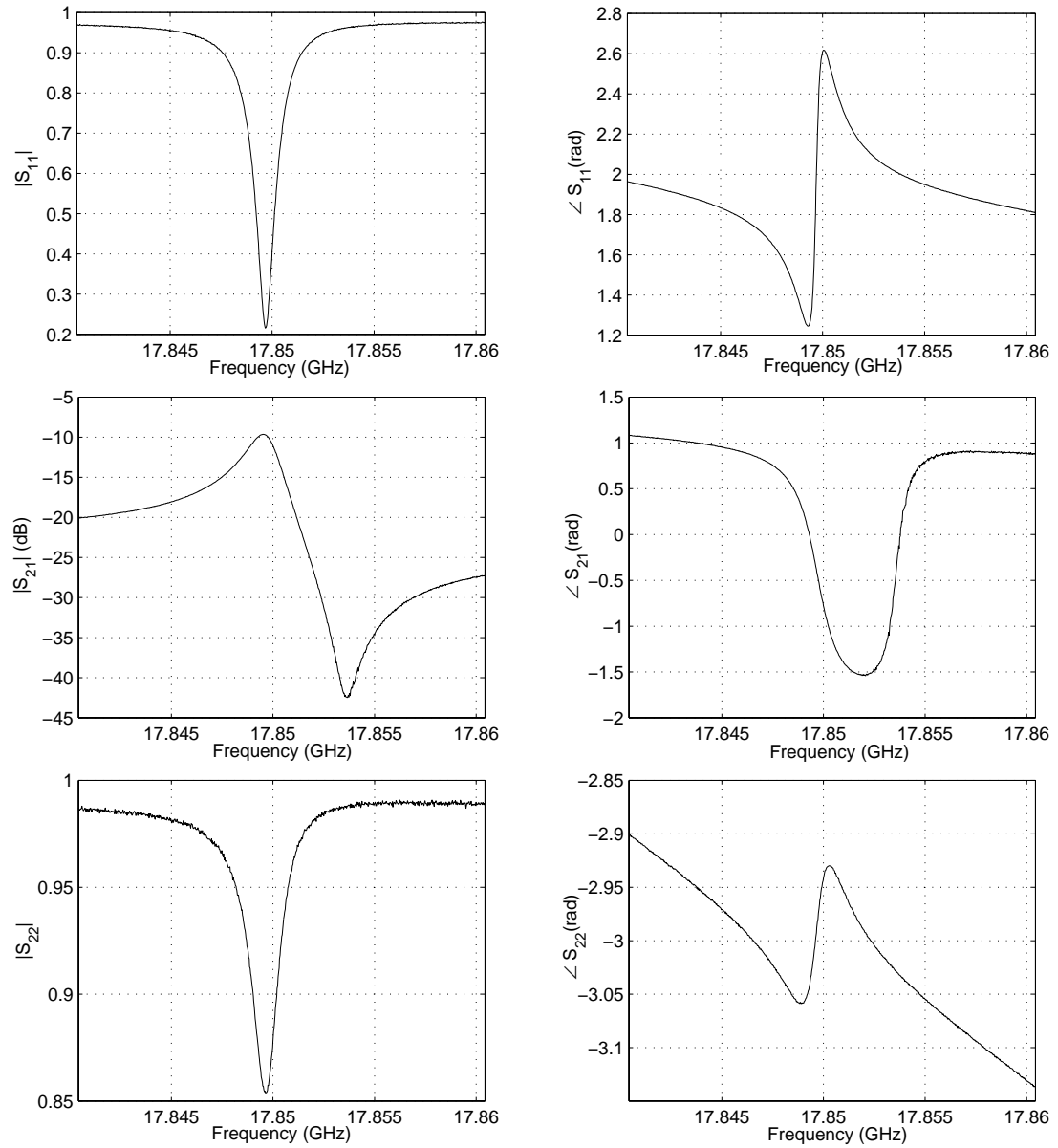


Figure 2.37: S-parameters for the TE<sub>012</sub> mode of cavity 1 with 2.49 mm axial grooves on the endcaps. Port 1 is the diagnostic coupler and port 2 is the high-power coupler.

$f_{\text{res}}$	17.85 GHz
$Q_0$	20380
$Q_{e1}$	28180
$Q_{e2}$	144500
$\beta_1$	0.72
$\beta_2$	0.14

Table 2.14: Cold-test results of  $\text{TE}_{012}$  mode for cavity 1 with 2.49 mm axial grooves on the endcaps.

that have zero length.

The asymmetry that occurs in  $S_{21}$  is due to transmission nulls from the interaction with other modes [24]. The phase of the transmission is defined with respect to the drive signal to the cavity. Using superposition of the modes in the cavity, the phase is only uniquely defined between  $0^\circ$  and  $180^\circ$ . For each mode, the phase of the transmission,  $S_{21}$ , undergoes a  $180^\circ$  phase shift when passing through the resonant frequency. At frequencies between two modes, one mode is above resonance and the other mode is below resonance. At a frequency in which the amplitude of the transmission for each mode is equal, the phase shift is almost  $180^\circ$  and a transmission null occurs. The interaction may be due to a mode that occurs several GHz away. However, the higher mode could not be found within the calibration limit of the network analyzer due to the  $\text{TE}_{20}$  cutoff limit in WR-62 waveguide at 19.04 GHz.

## 2.2 Klystron setup

Two different setups were used to conduct high-power tests with X-Band klystrons. Each experimental setup is required to protect the klystron from reflected power. The specifications require a maximum of 5 MW of reflected power back to the klystron output.

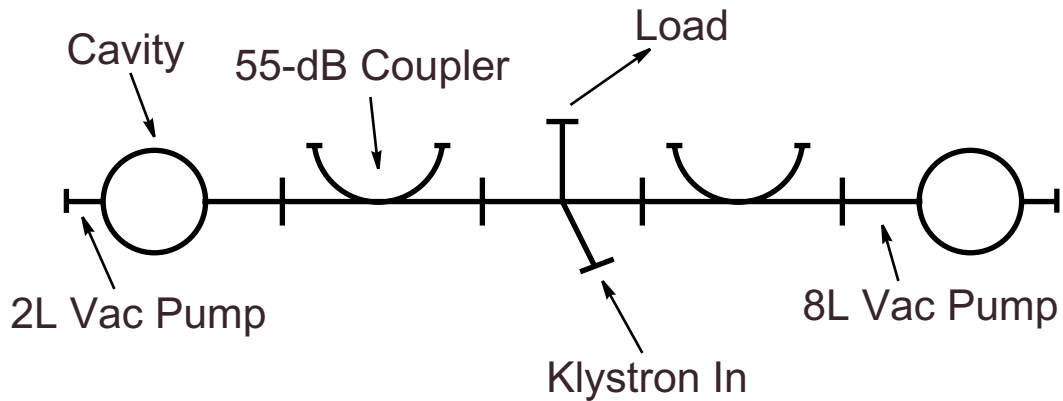


Figure 2.38: Schematic of the two-cavity setup for high power tests.

### 2.2.1 Two-cavity setup

In this particular setup, two cavities were connected to opposite sides of a magic-tee with a high-power load attached to the fourth arm. A schematic of this setup is shown in Figure 2.38. Due to the fill-time of the cavities, the reflected power will vary over the RF pulse length. Having two identical cavities on opposite arms of a magic-tee would ideally make the reflected power back to the klystron zero, since the phase difference between the arms is  $180^\circ$ . Since a high-power circulator does not exist at X-Band, this setup provides the maximum power to a cavity. Also, this setup allows us to test two sets of endcaps at the same time.

A picture of the setup that is to be attached to the klystron is shown in Figure 2.39. Figure 2.40 shows a close-up of one of the cavities. Each cavity has an 8 L/s vacuum pump-out port and a 55-dB directional coupler for measurements of the forward and reflected power to and from the cavity. There is also a 2 L/s vacuum pump-out port attached to the back of each cavity for pumping behind the spring gaskets of each piston.

In order to successfully put power into each cavity and protect the klystron, the resonant frequencies of each cavity must match. The differential screws were used to make large changes to the cavity frequencies, but were incapable of making fine adjustments due to backlash. Fine adjustments to the cavity frequencies were made

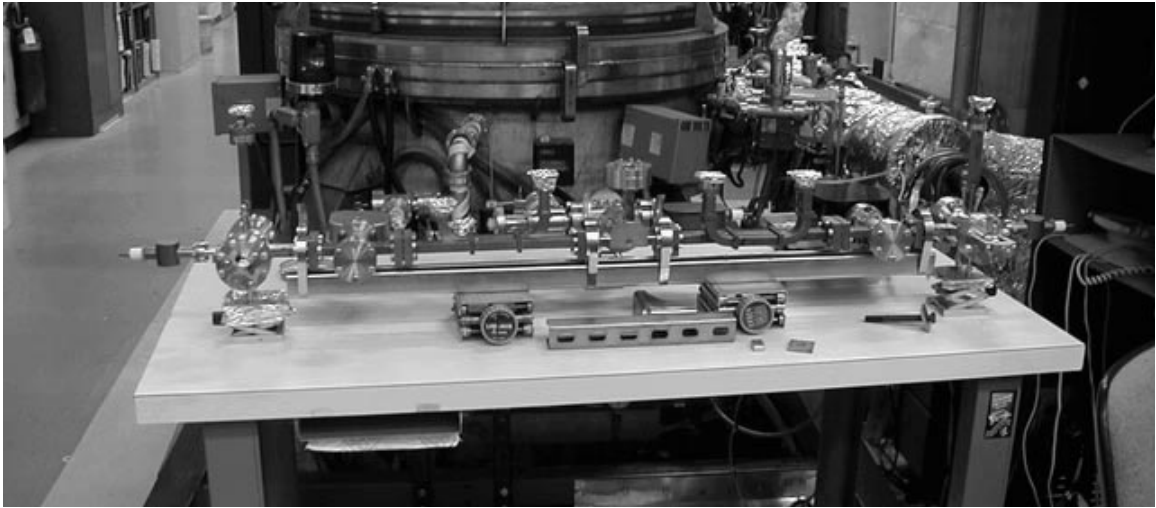


Figure 2.39: Picture of two-cavity setup with magic-tee, vacuum pump-out ports and 55-dB directional couplers attached.

by slight adjustments of the water flow to the endcaps. The flow to the cavity endcaps was easily adjusted with electric flow controllers that were operated with a computer. Hence, the cavities were matched in frequency under high-power due to thermal expansion.

It is not possible to reach the desired power level in the cavity immediately due to absorbed gases in copper. Normally the components are first placed under vacuum then baked out at high temperature (at least 400 °C) for a few days to remove the gases. However, the RF spring gaskets used to prevent the excitation of coaxial modes along the pistons cannot be baked at such a high temperature. They may lose their elastic properties causing their effectiveness as an RF short to deteriorate. Thus, the cavity body and the magic-tee were baked out separately at high temperature because they were new and were not handled in a clean environment. However, the endcaps did not go through a high-temperature bake-out. Afterwards, the components were assembled and attached to the klystron. After being placed under vacuum, the components were baked with heater tape at 150 °C for 3 days. This procedure removes some absorbed gas on the surface.

The klystron power level must be increased slowly as the high-power fields in the cavity and other waveguide components pull more gas out of the surface. This is

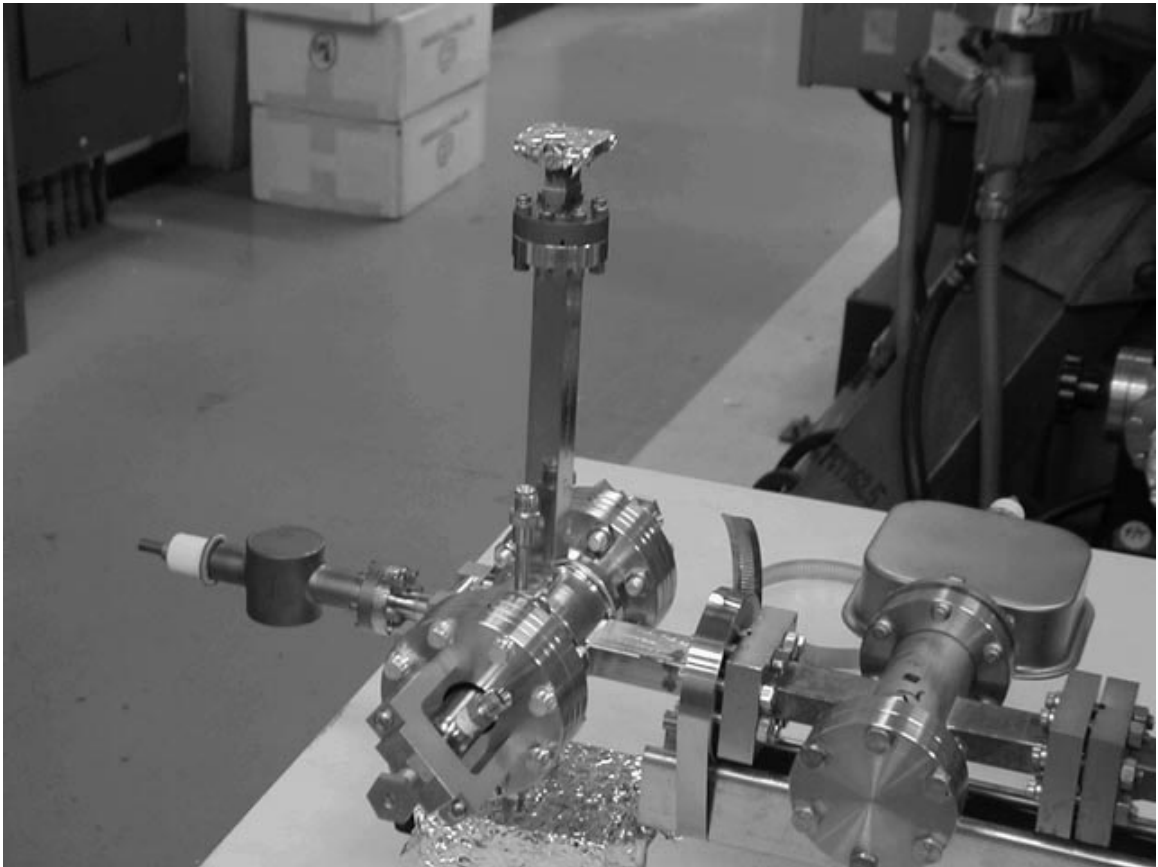


Figure 2.40: Close-up of one cavity of the two-cavity setup.

known as power conditioning. There are interlocks to shutdown the klystron when there is too much gas in the system. If this is not done, damage may result to the components due to RF breakdown. Over time, the gas is slowly removed and the power may be increased. As will be discussed in Chapter 4, RF breakdown at the high-power coupling aperture limited the amount of power that could be put into the cavity. At this point, gas is released violently and the cavity cannot be conditioned any further in a reasonable amount of time.

Periodic measurements were made of the cavity Q's by turning down the power on the klystron and measuring the reflected power from each cavity. The power was lowered so the Joule heating would not affect the cavity Q. The method described in Section A.4.2 was used. Each cavity had to be measured separately since the cavities are only matched in resonant frequency when the power input is high. However, the results from these measurements were far from agreement with measurements performed with a network analyzer. It was realized later that when the cavities are not matched to each other when their properties are measured, inconsistencies in the measurements will result. As a consequence, we decided to use only one cavity for the next high-power test.

### 2.2.2 One-cavity setup

In order to eliminate the problem of tuning cavity frequencies with respect to each other, we opted to use only one cavity in the next high-power test. This requires throwing more power away, since we must use more power dividers to protect the klystron from the reflected power from the cavity. Using two magic-tees as a 6-dB directional coupler, we reduce the maximum possible reflected power to the klystron by a factor of 16 down from its output power. A schematic of the setup is shown in Figure 2.41.

For a 50 MW klystron, the maximum power delivered to the cavity, ignoring losses in the waveguide, is 12.5 MW. Hence, the maximum reflected power back to the klystron is 3.125 MW. Since the maximum input power to the cavity is limited to 8.5 MW to 10 MW due to RF breakdown at the coupling aperture, the loss of input

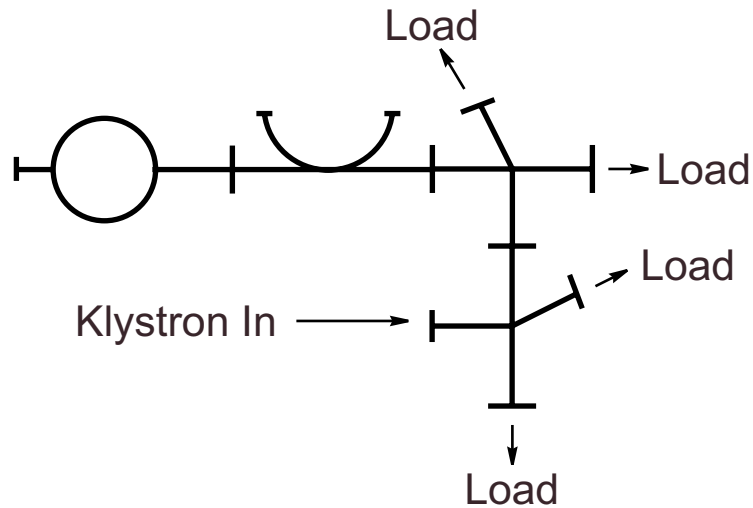


Figure 2.41: Schematic of the one-cavity setup for high-power tests.

power is not a hindrance.

In this setup, none of the components received a new high-temperature bake-out. Each component, except for the cavity pistons, received a high-temperature bake-out in the past and were handled cleanly since that time. After the components were assembled and attached to the klystron, the system was placed under vacuum and baked with heater tape at 150 °C for 4 days. The system was conditioned under high-power as described in the previous section.

## 2.3 Diagnostic setup

As discussed earlier, the diagnostic mode was fixed using a different groove length for the endcaps. This fix was performed after the first high-power test with two cavities. The diagnostic mode was used during the next high-power test with one cavity.

There are three items we want to measure in real-time: pulsed temperature rise, cavity  $Q$ , and pulse count. We want to measure the change in the cavity  $Q$  over time and correlate it with the number of pulses at which the cavity surface is subjected to a particular temperature rise.

### 2.3.1 Measurement of Pulsed Temperature Rise and Cavity Q

Pulsed temperature rise may be determined by measuring the change in cavity Q during a high-power pulse. Since the electrical resistivity is a function of temperature, the cavity Q will change when the cavity surface is heated. This means the coupling to the diagnostic mode will change. By measuring the change in the amplitude and phase of the reflected power from the diagnostic mode, we may indirectly determine the temperature rise on the surface of the cavity. Section 3.3.3 discusses this in more detail. A schematic of the setup to measure pulsed temperature rise and cavity Q is shown in Figure 2.42.

A low-power RF source excites the diagnostic mode into steady-state. A circulator is used to isolate the reflected signal from the input signal. Directional couplers with crystal detectors are placed on either side of the circulator to measure forward and reflected power. When the cavity is heated from a high-power pulse, the amplitude and phase of the reflected signal will change. A quadrature mixer is used to measure this signal. The oscilloscope measures the quadrature outputs, I and Q, from the mixer. As discussed in Section 3.3.3, the change in the cavity's resonant frequency and Q may be determined from the reflected signal. The temperature rise is then inferred.

Although the quadrature mixer can also measure reflected power, the crystal is used to tune the cavity mode in real time. The output from the mixer has to be added in quadrature after subtracting DC offsets in its outputs. Crystal detectors only measure magnitudes. The cavity is tuned by measuring the steady-state reflected power from the crystal detector. The frequency of the low-power source is varied until the reflected power is a minimum, which occurs at the resonant frequency of the cavity mode. Afterwards, a temperature rise measurement is taken with the quadrature mixer. Typical sensitivities of the crystals used are between approximately 500 to 700 mV/mW. Also, the input power to the quadrature mixer must be kept below -10 dBm to keep the phase imbalance between the I and Q outputs to a minimum, approximately 1.5°.



A waveguide low-pass filter is placed at the input to the cavity to protect the electronics from high-power harmonics from the klystron that may leak through the diagnostic coupler. These harmonics are not cutoff in the WR-42 hybrid waveguide. The forward and reflected high power from the cavity is also measured with crystal detectors attached to 55-dB directional couplers with additional attenuation added.

Certain subtleties of the circuit in Figure 2.42 must be understood. The circulator must have good isolation to prevent the forward power from interfering with the measurement of the reflected power from the cavity. The isolation of this circulator at 18 GHz is approximately 32 dB.

The steady-state reflection from the cavity with a coupling coefficient of  $\beta = 0.7$  is 16 dB below the input power. With an additional insertion loss of 2 dB for the circulator and directional coupler, the reflected signal will be approximately 14 dB above the input power that is transmitted through the isolation of the circulator. Thus this signal is easily measured and does not cause great error in the determination of the coupling coefficient of the cavity.

For the measurement of pulsed heating,  $Q_0$  of the cavity will fall and  $\beta$  will increase. This will result in a greater mismatch with more reflected power from the cavity. Thus, the steady-state reflection from the cavity when it is not heated from high power represents the lower limit of the power that may be measured. Due to the high isolation of the circulator, the forward power does not add appreciative error to the measurement of pulsed heating.

We would also like to know the cavity Q when the surface temperature rise is zero. This will allow us to determine the amount of Q degradation that will occur over time. An RF switch is used to allow the stored energy to drain from the cavity. The switch is triggered between high-power RF pulses. For  $f_{rep} = 60$  Hz, the switch would be triggered at 8.3 ms after an RF pulse. Since the temperature rise goes to zero on the order of 10's of  $\mu$ s (see Section 3.3.1), this will give us the amount of Q degradation over time. Also, by pre-triggering the oscilloscope with respect to the RF switch, the coupling coefficient of the cavity mode may be determined by measuring the steady-state reflected power as shown in Figure 2.43. These measurements are discussed in more detail in Chapter 4.

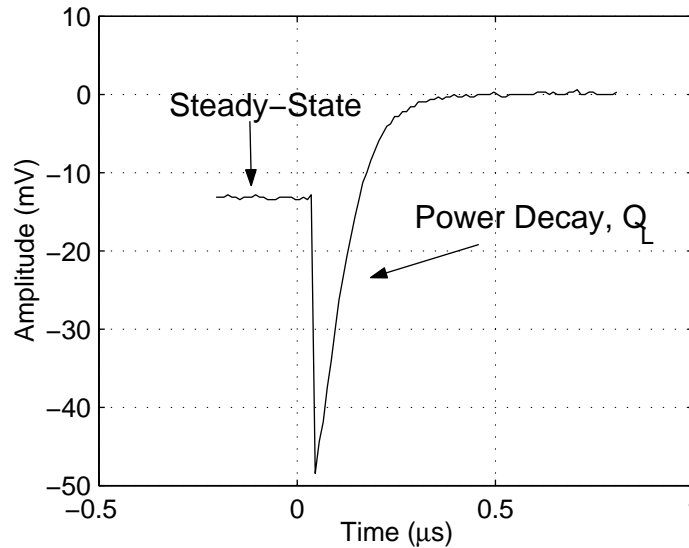


Figure 2.43: Example of reflected waveform from the cavity when the RF switch is opened. The spike occurs when the switch is opened.

### 2.3.2 Measurement of Pulse Count

We need an accurate count of the number of pulses applied to the cavity to determine the lifetime of the material at a particular temperature rise. We may measure pulse count easily with an 8-channel event counter.

We use the forward power port of the 55-dB directional coupler and digitize the square waveform. The height of the waveform is then binned into one of eight channels depending on a chosen reference voltage. This information is then passed to an 8-channel event counter. A computer periodically reads the event counter and stores the pulse count. Hence, the pulse counts may be stored at different power levels to distinguish between pulses at different temperature rises. Also, each time a temperature rise and  $Q$  measurement is taken, the pulse count is recorded. This allows us to correlate  $Q$ -degradation with the number of pulses applied at a particular temperature rise.

# Chapter 3

## Theory

As mentioned in Chapter 1, pulsed heating will induce stress on a metal surface. This stress can be evaluated using the *thermoelasticity equations* discussed further in later sections. The purpose of this chapter is to evaluate the temperature rise and stress induced by RF pulsed heating on the test device described in Chapter 2. Solutions to various simplified models of the test device will be discussed in detail. The dynamic electrical response of the test device will also be discussed, and, more specifically, how it applies to the measurement of the pulsed temperature rise on the metal surface.

### 3.1 Thermoelasticity

Usually problems of heat conduction and elasticity are solved assuming that they are uncoupled phenomena. However, when the storage of elastic energy is considered in irreversible thermodynamics [8] a coupling term arises in the familiar heat conduction equation

$$k\nabla^2 T + g = \rho c_\varepsilon \frac{\partial T}{\partial t} + (3\lambda + 2\mu)\alpha T_0 \frac{\partial e}{\partial t}, \quad (3.1)$$

where  $\lambda$  and  $\mu$  are the Lamé constants,  $e = \varepsilon_{xx} + \varepsilon_{yy} + \varepsilon_{zz}$  is the dilatation, and  $T_0$  is the ambient temperature in Kelvin. See Section 1.1 for the definition of the other symbols. The last term on the right of equation (3.1) is the term that couples heat diffusion to the elasticity equations. This coupling term arises from the fact that

some of the energy from the work done on the system to induce mechanical strain is dissipated as heat. Equation (3.1) along with equations (1.8–1.11) are known as the *thermoelasticity equations*.

The thermoelasticity equations were derived using linearization which assumes that not only are the strains small such that the system remains elastic but also the temperature rise  $\Delta T = T - T_0$  is small compared to the ambient temperature,  $\Delta T \ll T_0$ . Although the temperature rises in the pulsed heating experiment will not satisfy this requirement, the approximation will be good for the temperature ranges in which the system is elastic. When the stress induced by pulsed heating exceeds the yield strength of the material, then the equations of plasticity must be considered instead of the thermoelasticity equations. The theory of plasticity will be considered in more detail in later sections.

It is desirable to remove the coupling term from the heat diffusion equation in order to simplify the solutions. Once the coupling term is removed then the temperature may be found independently of the elasticity equations. The temperature becomes a known function and the stresses in the system may be found by substituting the temperature into the elasticity equations.

The strength of the coupling term can be approximated by considering the amount of energy used in creating strain that is dissipated as heat [9]. Consider the expansion of a long metal rod due to heating and ignore lateral contractions. The thermal energy density input through heat is

$$\Delta u_{thermal} = \rho c_\epsilon \Delta T. \quad (3.2)$$

Using Hooke's Law,  $\sigma = E\varepsilon$ , the work per unit volume necessary to compress the rod back to its original length from an expansion of  $\varepsilon = \alpha\Delta T$  is

$$\Delta u_{elastic} = \frac{1}{2}\sigma\varepsilon = \frac{1}{2}E\alpha^2\Delta T^2. \quad (3.3)$$

The ratio of these two energies is

$$\frac{\Delta u_{elastic}}{\Delta u_{thermal}} = \frac{E\alpha^2 \Delta T}{2\rho c_\varepsilon}. \quad (3.4)$$

For OFE copper heated to  $\Delta T = 100$  K, using the values given in Table 1.1, this ratio is  $5.0 \times 10^{-4}$ . This ratio is an upperbound on the energy dissipated as heat from the work done on the rod. The low value of this ratio demonstrates that the heat created from mechanical strain is much smaller than the heat input to create a moderate temperature rise. Thus, the coupling between the thermal system and the mechanical system is weak and may be safely ignored in a pulsed heating calculation.

To reinforce the physical argument given above, we will look at the coupling term in the heat diffusion equation more closely. Following the treatment given in [8, pp. 42–43], equation (3.1) may be written as

$$k\nabla^2 T + g = \rho c_\varepsilon \frac{\partial T}{\partial t} \left[ 1 + \delta \left( \frac{\lambda + 2\mu}{3\lambda + 2\mu} \right) \left( \frac{\partial e / \partial t}{\alpha \partial T / \partial t} \right) \right], \quad (3.5)$$

where

$$\delta = \frac{(3\lambda + 2\mu)^2 \alpha^2 T_0}{\rho^2 c_\varepsilon v_e^2}, \quad (3.6)$$

and  $v_e^2 = (\lambda + 2\mu)/\rho$ . The term proportional to  $\delta$  is the coupling term, and it is negligible compared to unity if

$$\frac{1}{3\alpha} \frac{\partial e / \partial t}{\partial T / \partial t} \ll \frac{1}{\delta} \left( \frac{\lambda + 2\mu/3}{\lambda + 2\mu} \right). \quad (3.7)$$

Using the values in Table 1.1 for OFE copper at a temperature of  $T_0 = 300$  K,  $\delta = 0.018$ . Using this value of  $\delta$  in equation (3.7) we arrive at the condition

$$\frac{1}{3\alpha} \frac{\partial e / \partial t}{\partial T / \partial t} \ll 37, \quad (3.8)$$

for OFE copper. If there are no sharp variations or discontinuities in the time history of the temperature distribution then we intuitively expect that the time rate of change of the dilatation is of the same order of magnitude as that of the temperature. If

this assumption is correct then equation (3.8) shows that the coupling term in the heat diffusion equation may be ignored. When the coupling term in equation (3.1) is ignored, the determination of stress is known as the *theory of thermal stresses*. The mechanical response of copper to RF pulsed heating falls under this condition and will be discussed in more detail in later sections.

In the sections to follow, the temperature distribution for the test device described in Chapter 2 will be solved first. It will also be shown how this information will be used to determine the measurable change in the electrical properties of the test device. Knowing the time history of the temperature distribution, the mechanical response of the test device will be solved and discussed afterwards.

## 3.2 Heat Conduction

The heat conduction equation for a homogeneous isotropic body will be restated here for convenience

$$\nabla^2 T(\vec{r}, t) + \frac{1}{k} g(\vec{r}, t) = \frac{1}{\alpha_d} \frac{\partial T(\vec{r}, t)}{\partial t} \quad \text{in volume V,} \quad (3.9)$$

where the thermal conductivity  $k$  and the thermal diffusivity  $\alpha_d = k/\rho c_\epsilon$  are constant.

The initial temperature distribution is given by

$$T(\vec{r}, 0) = F(\vec{r}). \quad (3.10)$$

The boundary conditions for equation (3.9) can be stated in three different forms. The *first* kind of boundary condition is a prescribed temperature at boundary  $S_i$ ,

$$T(\vec{r}_i, t) = f_i(\vec{r}_i, t), \quad (3.11)$$

where  $\vec{r}_i$  are the coordinates of surface  $S_i$ . The *second* kind of boundary condition is a prescribed heat flux on the surface,

$$k_i \hat{n}_i \cdot \vec{\nabla} T \Big|_{\vec{r}_i} = f_i(\vec{r}_i, t), \quad (3.12)$$

where  $\hat{n}_i$  is an outward pointing normal from surface  $S_i$  and  $k_i$  is the thermal conductivity at the surface. The *third* kind is a convective boundary condition,

$$k_i \hat{n}_i \cdot \vec{\nabla} T \Big|_{\vec{r}_i} + h_i T|_{\vec{r}_i} = f_i(\vec{r}_i, t), \quad (3.13)$$

where  $h_i$  is the *heat transfer coefficient* for surface  $S_i$ . This boundary condition is usually used for situations where liquid or gas is flowing across a surface and  $f_i = h_i T_\infty$  where  $T_\infty$  is the ambient temperature.  $h_i$  can be a function of position  $\vec{r}_i$ . The boundary conditions are most often written in the general form of equation (3.13) where the other types of boundary conditions are retrieved by setting  $k_i = 0$  or  $k$  and  $h_i = 0$  or  $h$ .

There are many methods available to evaluate the solution to equations (3.9–3.13) such as separation of variables, Fourier transforms and Laplace transforms. We will use the method of the Green's function throughout this chapter to solve heat conduction problems. This method reduces the partial differential equation to integrals which are easily evaluated numerically. This type of reduction is well-suited for temperature calculations of the conducting walls in resonant cavities due to RF power dissipation at the surface.

### 3.2.1 Green's Function Solutions

The general solution of equations (3.9–3.13) using Green's functions can be split into three terms [6]

$$T(\vec{r}, t) = T_{in}(\vec{r}, t) + T_g(\vec{r}, t) + T_{bc}(\vec{r}, t). \quad (3.14)$$

The first term is due to the initial conditions,

$$T_{in}(\vec{r}, t) = \int_V G(\vec{r}, t | \vec{r}', t' = 0) F(\vec{r}') dV', \quad (3.15)$$

where  $G(\vec{r}, t|\vec{r}', t')$  is the Green's function. The second term is due to the volumetric energy source,

$$T_g(\vec{r}, t) = \int_{t'=0}^t \int_V \frac{\alpha_d}{k} G(\vec{r}, t|\vec{r}', t') g(\vec{r}', t') dV' dt'. \quad (3.16)$$

The third term is due to the boundary conditions and has two different parts,

$$T_{bc}(\vec{r}, t) = -\alpha_d \int_{t'=0}^t \sum_{i=1}^s \int_{S_i} f_i(\vec{r}'_i, t') \hat{n}'_i \cdot \vec{\nabla} G \Big|_{\vec{r}'=\vec{r}'_i} ds'_i dt' \quad (\text{first kind}) \quad (3.17a)$$

$$= \alpha_d \int_{t'=0}^t \sum_{i=1}^s \int_{S_i} \frac{f_i(\vec{r}'_i, t')}{k_i} G(\vec{r}, t|\vec{r}'_i, t') ds'_i dt' \quad (\text{second or third kind}), \quad (3.17b)$$

where we must include all real physical boundaries. In general,  $0 \leq s \leq 6$ . Boundary conditions at  $x \rightarrow \pm\infty$  for semi-infinite or infinite bodies are not included. For example, a one-dimensional semi-infinite slab will have  $s = 1$ .

The Green's function  $G(\vec{r}, t|\vec{r}', t')$  is found from the following equation

$$\nabla^2 G + \frac{1}{\alpha_d} \delta(\vec{r} - \vec{r}') \delta(t - t') = \frac{1}{\alpha_d} \frac{\partial G}{\partial t} \quad t > t', \quad (3.18)$$

with initial condition

$$G(\vec{r}, t|\vec{r}', t') = 0 \quad t < t', \quad (3.19)$$

and boundary conditions

$$k_i \hat{n}'_i \cdot \vec{\nabla} G \Big|_{\vec{r}'_i} + h_i G \Big|_{\vec{r}'_i} = 0 \quad t > t'. \quad (3.20)$$

The Green's function for the heat conduction equation is due to a point source located at position  $\vec{r}'$  and turned on for one instant of time  $t'$ . The body is considered to be under homogeneous boundary conditions and zero initial condition. Because of causality, there is no response for times  $t < t'$ .

The power of the Green's function method lies with the fact that once  $G$  is found for a particular geometry for all homogeneous boundary conditions and zero initial

condition, then the temperature  $T$  may be found for any arbitrary source, boundary condition and initial condition for that geometry by integration (equations (3.14–3.17)). The differential equation (3.9) does not need to be solved again for different sources, boundary conditions or initial conditions. Although we must resort to other methods to solve for the Green's function, they are, fortunately, well-tabulated for common geometries [6, pp. 431–510]. More than one form of Green's functions may exist for a particular geometry and boundary condition to make calculations more convenient for short or long times and for steady-state solutions. Which Green's function to be used will depend on the particular problem being solved.

The Green's functions used in this chapter were derived assuming the specific heat and thermal conductivity are constant. It will be shown later that ignoring the temperature dependence of these parameters over the temperature range of interest introduces less than 2% relative error. However, the source term  $g(\vec{r}, t)$  is allowed to be temperature-dependent. This is necessary for an accurate calculation of temperature rise due to pulsed heating of copper.

### 3.2.2 1D Solution For Semi-Infinite Body

In anticipation of further results, we will consider a one-dimensional semi-infinite body subject to RF power dissipation at its surface due to a surface magnetic field (see Figure 3.1). We know that the power dissipated per unit area into a lossy conductor by a magnetic field tangential to the surface is given by [20, p. 339]

$$\left. \frac{dP}{dA} \right|_S = \frac{1}{2} R_s |H_{\parallel}|^2, \quad (3.21)$$

where  $R_s$  is the surface resistance given by equation (A.71). We also know from section A.3.1 that the tangential magnetic field decays into the conductor as  $e^{-z/\delta}$  where  $\delta$  is the skin-depth given by equation (A.68). Since the power dissipated in the  $z$ -direction must be normalized to one, the power dissipated per unit volume is

$$g(z, t) = \frac{dP(z, t)}{dA dz} = \frac{dP(t)}{dA} \frac{2}{\delta} e^{-2z/\delta} \quad z \geq 0. \quad (3.22)$$

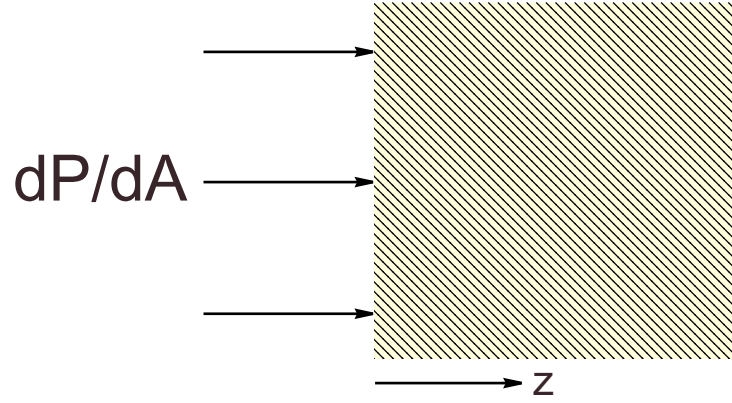


Figure 3.1: A one-dimensional semi-infinite slab in the  $z$ -direction with power per unit area being dissipated at the surface due to a magnetic field.

This heating problem is described by the following equation

$$\frac{\partial^2 T(z, t)}{\partial z^2} + \frac{g(z, t)}{k} = \frac{1}{\alpha_d} \frac{\partial T(z, t)}{\partial t} \quad 0 \leq z < \infty, \quad (3.23)$$

with initial and boundary conditions given by

$$T(z, t = 0) = T_0, \quad (3.24a)$$

$$\left. \frac{\partial T}{\partial z} \right|_{z=0} = 0. \quad (3.24b)$$

The Green's function for a semi-infinite slab with the boundary condition of a prescribed heat flux at the surface is [6, eq. X20.1]

$$G(z, t | z', t') = \frac{1}{\sqrt{4\pi\alpha_d(t-t')}} \left\{ \exp \left[ -\frac{(z-z')^2}{4\alpha_d(t-t')} \right] + \exp \left[ -\frac{(z+z')^2}{4\alpha_d(t-t')} \right] \right\}. \quad (3.25)$$

Substituting equations (3.22, 3.24 and 3.25) into equations (3.14–3.17) and using the known integral [6, eq. X20.4]

$$\int_0^\infty G(z, t | z', t') dz' = 1, \quad (3.26)$$

the temperature at all points  $z$  in the conductor is found to be

$$\begin{aligned}
T(z, t) &= T_0 + \frac{\alpha_d}{k} \int_0^t \int_0^\infty g(z', t') G(z, t|z', t') dz' dt' \\
&= T_0 + \frac{1}{\rho c_\varepsilon \sqrt{\pi \alpha_d}} \int_0^t \int_0^\infty dz' dt' \frac{dP(t')}{dA} \frac{1}{\delta} \frac{1}{\sqrt{t-t'}} \exp\left(-\frac{2z'}{\delta}\right) \\
&\quad \cdot \left\{ \exp\left[-\frac{(z-z')^2}{4\alpha_d(t-t')}\right] + \exp\left[-\frac{(z+z')^2}{4\alpha_d(t-t')}\right] \right\} dz' dt'.
\end{aligned} \tag{3.27}$$

For performing the integration over  $z'$  we will make use of [17, eq. 3.322.2]

$$\int_u^\infty \exp\left(-\frac{x^2}{4\beta} - \gamma x\right) dx = \sqrt{\pi\beta} e^{\beta\gamma^2} \operatorname{erfc}\left(\gamma\sqrt{\beta} + \frac{u}{2\sqrt{\beta}}\right), \tag{3.28}$$

and [17, eq. 3.323.2]

$$\int_{-\infty}^\infty \exp(-p^2 x^2 \pm qx) dx = \exp\left(\frac{q^2}{4p^2}\right) \frac{\sqrt{\pi}}{p} \quad p > 0, \tag{3.29}$$

where  $\operatorname{erfc}(x)$  is the complementary error function given by

$$\operatorname{erfc}(x) = \frac{2}{\sqrt{\pi}} \int_x^\infty e^{-t^2} dt. \tag{3.30}$$

By making a change of variables in equation (3.27) and using the above integrals with the identity

$$2 - \operatorname{erfc}(x) = \operatorname{erfc}(-x), \tag{3.31}$$

the temperature in the conductor is found to be

$$T(z, t) = T_0 + \frac{1}{\rho c_\epsilon} \int_0^t dt' \frac{dP(t')}{dA} \frac{1}{\delta} \exp \left[ \frac{4\alpha_d(t-t')}{\delta^2} \right] \cdot \left\{ e^{-2z/\delta} \operatorname{erfc} \left[ \frac{2}{\delta} \sqrt{\alpha_d(t-t')} - \frac{z}{2\sqrt{\alpha_d(t-t')}} \right] + e^{2z/\delta} \operatorname{erfc} \left[ \frac{2}{\delta} \sqrt{\alpha_d(t-t')} + \frac{z}{2\sqrt{\alpha_d(t-t')}} \right] \right\}. \quad (3.32)$$

This integral must be evaluated numerically.

A numerical example would prove valuable for understanding the basic process of heat diffusion due to pulsed heating. Let us assume a constant pulse of power is dissipated into the conductor due to a source resonating at a frequency of 11.424 GHz for a time  $t_p$

$$\frac{dP(t)}{dA} = \begin{cases} \frac{dP}{dA} & 0 \leq t \leq t_p \\ 0 & t > t_p. \end{cases} \quad (3.33)$$

Using the value given in Table 1.1 for electrical conductivity of pure copper, the skin-depth at this frequency is  $\delta = 0.62 \mu\text{m}$ . Figure 3.2 is a plot of the temperature rise  $\Delta T = T(z, t) - T_0$  normalized to the surface temperature at  $t = 1.0 \mu\text{s}$  in the conductor at various times for a pulse length of  $t_p = 1.0 \mu\text{s}$ . The value of the thermal constants were taken from Table 1.1. Notice that at all times the maximum temperature rise occurs on the surface.

One notable characteristic of heat diffusion is the *diffusion length* defined by the length  $D = \sqrt{\alpha_d t_p}$  over which the effect of the source decays on the order of  $1/e$  at time  $t_p$  (see equation (3.25)). It is analagous to the rms width of a gaussian curve. In the example worked out above,  $D = 10.8 \mu\text{m}$ , which is an order of magnitude larger than the skin-depth. This suggests that for a sufficiently long pulse, the decay of the surface magnetic field into the conductor has little effect on the temperature rise. In this regime the temperature rise is dominated by diffusion. We may let  $\delta \rightarrow 0$  with little loss of accuracy to simplify the calculation.

Let us look at the difference in surface temperature for the above example with

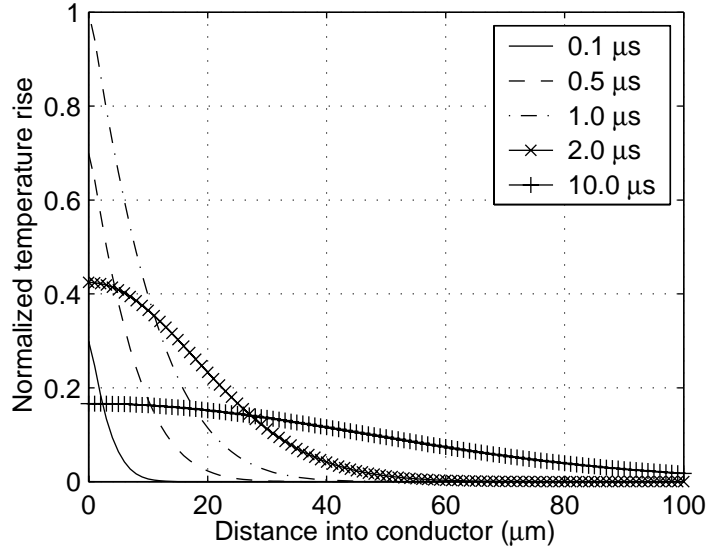


Figure 3.2: The temperature rise at various times in the conductor normalized to the surface temperature at  $t=1.0 \mu\text{s}$ . The source is on for  $1.0 \mu\text{s}$ .

the assumption  $\delta \rightarrow 0$ . On the surface,  $z = 0$ , equation (3.32) becomes

$$T(z = 0, t) = T_0 + \frac{2}{\rho c_\varepsilon} \int_0^t dt' \frac{dP(t')}{dA} \frac{1}{\delta} \exp\left[\frac{4\alpha_d(t-t')}{\delta^2}\right] \operatorname{erfc}\left[\frac{2}{\delta}\sqrt{\alpha_d(t-t')}\right]. \quad (3.34)$$

If we use the approximation [1, eq. 7.1.23]

$$\operatorname{erfc}(x) \approx \frac{1}{\sqrt{\pi} x e^{x^2}} \quad x \gg 1, \quad (3.35)$$

then the temperature on the surface is approximately

$$T(z = 0, t)|_{\delta \rightarrow 0} = T_0 + \frac{1}{\rho c_\varepsilon \sqrt{\pi \alpha_d}} \int_0^t \frac{dt'}{\sqrt{t-t'}} \frac{dP(t')}{dA}. \quad (3.36)$$

This is the same result as the 1D semi-infinite case with a prescribed surface heat flux

$$-k \left. \frac{\partial T}{\partial z} \right|_{z=0} = \frac{dP(t)}{dA}, \quad (3.37)$$

and zero volume energy generation,  $g(z, t) = 0$ . For a constant power input of length  $t$

$\delta$ ( $\mu\text{m}$ )	$\Delta T / (dP/dA)$ ( $\times 10^{-8}$ K/(W/m <sup>2</sup> ))	Relative Error (%)
0.0	3.0350	0.00
0.62	2.9589	2.57
1.0	2.9135	4.17
2.0	2.7986	8.45
5.0	2.4910	21.8
10.0	2.0868	45.4
20.0	1.5562	95.0

Table 3.1: Normalized temperature rise at the surface for various skin-depths compared to no skin-depth. Diffusion length is 10.8  $\mu\text{m}$ .

the surface temperature is simply

$$T(z = 0, t) = T_0 + \frac{dP}{dA} \frac{2\sqrt{t}}{\rho c_\varepsilon \sqrt{\pi \alpha_d}}. \quad (3.38)$$

If the power dissipation is due to a constant surface magnetic field

$$\frac{dP}{dA} = \frac{1}{2} R_s |H_{\parallel}|^2, \quad (3.39)$$

then we arrive at equation (1.4).

Table 3.1 compares the solutions from equations (3.32) and (3.36) for various values of  $\delta$  with a constant power input of time  $t_p = 1.0 \mu\text{s}$  as before. Intuitively, the calculated temperature rise with a finite skin-depth will be lower than with no skin-depth since the power is dissipated over a finite volume. The table shows that the error due to ignoring the skin-depth is 2.6%. If the copper material were at an ambient temperature of 800 K, then the electrical conductivity would be  $1.9 \times 10^7$  S. This corresponds to a skin-depth of 1.1  $\mu\text{m}$  resulting in less than 5% error in the calculation of the surface temperature rise. By ignoring the skin-depth, the calculation of temperature rise due to pulsed heating is simplified when we allow the prescribed surface heat flux to be temperature-dependent.

In the temperature range of interest ( $\Delta T < 500$  K), we have shown that the variation of skin-depth due to temperature introduces less than 5% error in the calculation

T (K)	$c_p$ (J/kg·K)	k (W/m·K)	$\alpha_d$ ( $\times 10^{-4}$ m <sup>2</sup> /s)	$\Delta T/(dP/dA)$ ( $\times 10^{-8}$ K/(W/m <sup>2</sup> ))
300	385.2	401	1.163	3.035
350	392.6	396	1.127	3.025
400	398.6	393	1.102	3.013
500	407.7	386	1.058	3.007
600	416.7	379	1.016	3.002

Table 3.2: Thermal data of pure copper for various temperatures with the corresponding surface temperature rise for a constant power input for time  $t = 1.0 \mu\text{s}$ .

of temperature rise. This is an upper bound on the error since a more accurate calculation would take account of the temperature dependence of the electrical conductivity. Before we conjecture that equation (3.36) should be used to calculate the temperature rise of the cavity described in Chapter 2, we should also investigate the error due to ignoring the temperature dependence of the thermal parameters.

Table 3.2 contains values of the thermal parameters of pure copper for various temperatures [31]. Although the specific heat at constant strain,  $c_\epsilon$ , is best approximated with the specific heat at constant volume,  $c_v$ , data is more easily obtained for the specific heat at constant pressure,  $c_p$ . For temperatures larger than room temperature, the difference between these two values is less than 1% [54, p. 23].

Table 3.2 also shows the normalized temperature rises calculated from equation (3.38) for a constant power input of  $t = 1.0 \mu\text{s}$ . At an ambient temperature of 600 K, the error in ignoring the temperature dependence of the thermal parameters is 1.1%. This error is also an upper bound since the calculation assumes the thermal parameters are held constant at their values.

In conclusion, for the temperature range of interest to pulsed heating, we may ignore the temperature dependence of the thermal parameters. We may also ignore the effect of the skin-depth for sufficiently long pulses. We have also shown that the temperature rise is maximum on the surface for a prescribed surface heat flux. In the next section, we will demonstrate that for short times the effect of diffusion in lateral directions for two or three dimensions is negligible. Once this fact is shown, then equation (3.36) may be used to calculate the surface temperature rise at all points in

the cavity due to pulsed heating. This is an important simplification when we allow the prescribed heat flux to vary with temperature since the electrical conductivity will vary significantly over the temperature range of interest.

### 3.2.3 Heat Conduction in Two Dimensions

In this section, the geometry of the test cavity described in Chapter 2 will be taken into account when calculating the temperature rise on the surface due to pulsed heating. We will demonstrate that for short times every point on the surface of the cavity behaves like a one-dimensional semi-infinite slab. We will consider the endcaps and the cylindrical sidewall separately.

#### Cavity Endcaps

If we are only interested in the temperature at the surface, then for short times we may treat a piece of metal with sufficient thickness as a semi-infinite slab. For the times we are interested in, the example provided in the previous section may be used for guidance. In that particular case, the source is on for  $t = 1.0 \mu\text{s}$  corresponding to a diffusion length of  $D = 10.8 \mu\text{m}$ . By referring to Figure 3.2, we see that even at  $t = 10.0 \mu\text{s}$  the temperature rise at a distance of  $100 \mu\text{m}$  into the conductor is negligible. We may safely conclude that a piece of metal with a thickness an order of magnitude larger than this distance for the time scale we are interested in can be treated as a semi-infinite slab. The cavity endcaps have a solid thickness of  $3 \text{ mm}$  before the cooling channels on the back are reached, so their approximation as semi-infinite slabs is a good one.

Since the cavity of radius  $R$  and length  $d$  is operated in the  $\text{TE}_{011}$  mode, the surface magnetic field on the endcaps at  $z = 0$  and  $z = d$  is purely radial (see equations (A.34))

$$|H_{||}| = A_{TE} \frac{\pi R}{dx_{11}} J_1 \left( \frac{x_{11} r}{R} \right) |h_{011}|, \quad (3.40)$$

where  $A_{TE}$  is given by equation (A.36) and  $h_{011}$  is the expansion coefficient for the magnetic field in the cavity for mode  $\text{TE}_{011}$ . We used the identity  $J_0'(x) = -J_1(x)$  and  $x_{11}$  is the first zero of  $J_1$ . To reduce the clutter, we will define a constant  $C_1$  such

that

$$|H_{\parallel}| \equiv C_1 J_1 \left( \frac{x_{11} r}{R} \right). \quad (3.41)$$

To determine the temperature rise on the endcaps, we will only look at the endcap located at  $z = 0$ . The heating of the endcap at  $z = d$  will be identical.

The calculation of the temperature rise is set up as follows:

$$\frac{1}{r} \frac{\partial}{\partial r} \left( r \frac{\partial T}{\partial r} \right) + \frac{\partial^2 T}{\partial z^2} = \frac{1}{\alpha_d} \frac{\partial T}{\partial t} \quad 0 \leq r \leq R, \quad 0 \leq z < \infty, \quad (3.42)$$

where  $z$  is now the distance into the conductor. The initial condition is

$$T(r, z, t = 0) = T_0, \quad (3.43)$$

and the boundary conditions are

$$\left. \frac{\partial T}{\partial r} \right|_{r=R} = 0, \quad (3.44)$$

and

$$-k \left. \frac{\partial T}{\partial z} \right|_{z=0} = \frac{dP}{dA} = \frac{1}{2} R_s |H_{\parallel}|^2. \quad (3.45)$$

The Green's function for this geometry is given by [6, eq. R02.1 and X20.1]

$$G(r, z, t | r', z', t') = \frac{1}{\pi R^2} \frac{1}{\sqrt{4\pi\alpha_d(t-t')}} \left[ 1 + \sum_{m=1}^{\infty} e^{-\alpha_d \beta_m^2 (t-t')/R^2} \frac{J_0\left(\frac{\beta_m r}{R}\right) J_0\left(\frac{\beta_m r'}{R}\right)}{J_0^2(\beta_m)} \right] \cdot \left\{ \exp \left[ -\frac{(z-z')^2}{4\alpha_d(t-t')} \right] + \exp \left[ -\frac{(z+z')^2}{4\alpha_d(t-t')} \right] \right\}, \quad (3.46)$$

where the constants  $\beta_m$  are the  $m$ -th zeros of  $J_1$ . By substituting equation (3.46) into equations (3.14–3.17) and using the result [6, eq. R02.12 and eq. X20.4]

$$\int_0^{\infty} \int_0^R G(r, z, t | r', z', t') 2\pi r' dr' dz' = 1, \quad (3.47)$$

the temperature is found to be

$$T(r, z, t) = T_0 + \frac{\alpha_d}{k} \int_0^t \int_0^R G(r, z, t | r', z' = 0, t') \frac{1}{2} R_s |H_{||}|^2 2\pi r' dr' dt'. \quad (3.48)$$

We are only interested in the temperature at the surface, so using equations (3.46) and (3.41) in equation (3.48) we have

$$T(r, z = 0, t) = T_0 + \frac{C_1^2 R_s}{\rho c_\varepsilon R^2 \sqrt{\pi \alpha_d}} \int_0^t \int_0^R dr' dt' \frac{1}{\sqrt{t-t'}} r' J_1^2 \left( \frac{x_{11} r'}{R} \right) \cdot \left[ 1 + \sum_{m=1}^{\infty} e^{-\alpha_d \beta_m^2 (t-t')/R^2} \frac{J_0 \left( \frac{\beta_m r}{R} \right) J_0 \left( \frac{\beta_m r'}{R} \right)}{J_0^2(\beta_m)} \right]. \quad (3.49)$$

We shall integrate over  $r'$  first. Using the integral [17, eq. 6.521.1]

$$\int_0^1 x J_\nu^2(\alpha x) dx = \frac{1}{2} J_{\nu+1}^2(\alpha) \quad \text{for } J_\nu(\alpha) = 0, \quad \nu > -1, \quad (3.50)$$

and the identity [17, eq. 8.473.1]

$$J_2(x) = \frac{2}{x} J_1(x) - J_0(x), \quad (3.51)$$

we get

$$\int_0^R r' J_1^2 \left( \frac{x_{11} r'}{R} \right) dr' = \frac{1}{2} R^2 J_0^2(x_{11}). \quad (3.52)$$

By defining the constants  $K_m$  to be

$$K_m \equiv \int_0^R r' J_1^2 \left( \frac{x_{11} r'}{R} \right) J_0 \left( \frac{\beta_m r'}{R} \right) dr', \quad (3.53)$$

and using equation (3.52) we have for the surface temperature

$$T(r, z = 0, t) = T_0 + \frac{C_1^2 R_s}{\rho c_\varepsilon R^2 \sqrt{\pi \alpha_d}} \cdot \int_0^t \frac{dt'}{\sqrt{t-t'}} \left[ \frac{1}{2} R^2 J_0^2(x_{11}) + \sum_{m=1}^{\infty} e^{-\alpha_d \beta_m^2 (t-t')/R^2} \frac{K_m J_0\left(\frac{\beta_m r}{R}\right)}{J_0^2(\beta_m)} \right]. \quad (3.54)$$

The constants  $K_m$  must be numerically evaluated. Using the integral [17, eq. 3.361.1]

$$\int_0^u \frac{e^{-qx}}{\sqrt{x}} dx = \sqrt{\frac{\pi}{q}} \operatorname{erf}(\sqrt{qu}), \quad (3.55)$$

the surface temperature is finally written as

$$T(r, z = 0, t) = T_0 + \frac{C_1^2 R_s}{\rho c_\varepsilon \sqrt{\pi \alpha_d}} \cdot \left[ J_0^2(x_{11}) \sqrt{t} + \sqrt{\frac{\pi}{\alpha_d}} \frac{1}{R} \sum_{m=1}^{\infty} \frac{K_m J_0\left(\frac{\beta_m r}{R}\right)}{\beta_m J_0^2(\beta_m)} \operatorname{erf}\left(\frac{\sqrt{\alpha_d \beta_m^2 t}}{R}\right) \right]. \quad (3.56)$$

If diffusion in the transverse direction is negligible for short times, then we may use equation (3.38) to determine the temperature at each point on the surface. Using equations (3.39) and (3.41) in equation (3.38) gives

$$T(r, z = 0, t) = T_0 + \frac{C_1^2 R_s}{\rho c_\varepsilon \sqrt{\pi \alpha_d}} J_1^2\left(\frac{x_{11} r}{R}\right) \sqrt{t}. \quad (3.57)$$

We will compare equation (3.57) to (3.56) to test this assumption.

The first 10 values of  $\beta_m$  are given in Table 3.3 along with the corresponding values of  $K_m$  for the cavity radius  $R = 2.2075$  cm. We shall first test if the 10 values of  $\beta_m$  given in Table 3.3 are sufficient for good accuracy in the calculation of temperature rise with equation (3.56). If equation (3.57) is sufficient to calculate the surface temperature, then we expect both equations to predict the same location for the maximum temperature rise. According to equation (3.57), this maximum occurs

m	$\beta_m$	$K_m (\times 10^{-10} \text{ m}^2)$
1	3.83171	69617.5
2	7.01559	-71123.5
3	10.17347	-2639.27
4	13.32369	496.108
5	16.47063	-161.447
6	19.61586	67.5956
7	22.76008	-32.9761
8	25.90367	17.8601
9	29.04683	-10.4483
10	32.18968	6.48206

Table 3.3: The first 10 values of  $\beta_m$  and  $K_m$  for radius  $R = 2.2075$  cm.  $x_{11} = \beta_1$ .

Equation	$\Delta T / (C_1^2 R_s)$ ( $\times 10^{-9} \text{ K} / (\text{W} / \text{m}^2)$ )
1-D	5.14038
2-D, m=9	5.14037
2-D, m=10	5.14016

Table 3.4: Temperature rise for 1-D and 2-D equations at position  $r = 1.0607$  cm for time  $t = 1.0 \mu\text{s}$ .

at

$$r = R \frac{x'_{11}}{x_{11}}, \quad J'_1(x'_{11}) = 0. \quad (3.58)$$

Since  $x'_{11} = 1.84118$ , the maximum temperature rise occurs at  $r = 1.0607$  cm. Table 3.4 gives the calculated temperature rises at this point. The relative error between the temperature rises listed in Table 3.4 is less than 0.01%.

Figure 3.3 plots the temperature rises from equations (3.56) and (3.57). Figure 3.4 plots the relative error between the calculations. As the two previous figures show, the relative error over the region of interest is less than 1% up to a time of  $t = 1.0$  ms. The relative error increases towards the center of the endcap because the one-dimensional solution predicts a temperature rise close to zero. In the case of pulsed heating we are only interested in times on order of  $1 \mu\text{s}$ . Therefore, equation (3.36) is sufficient to calculate the surface temperature rise on the cavity endcaps due to pulsed heating.

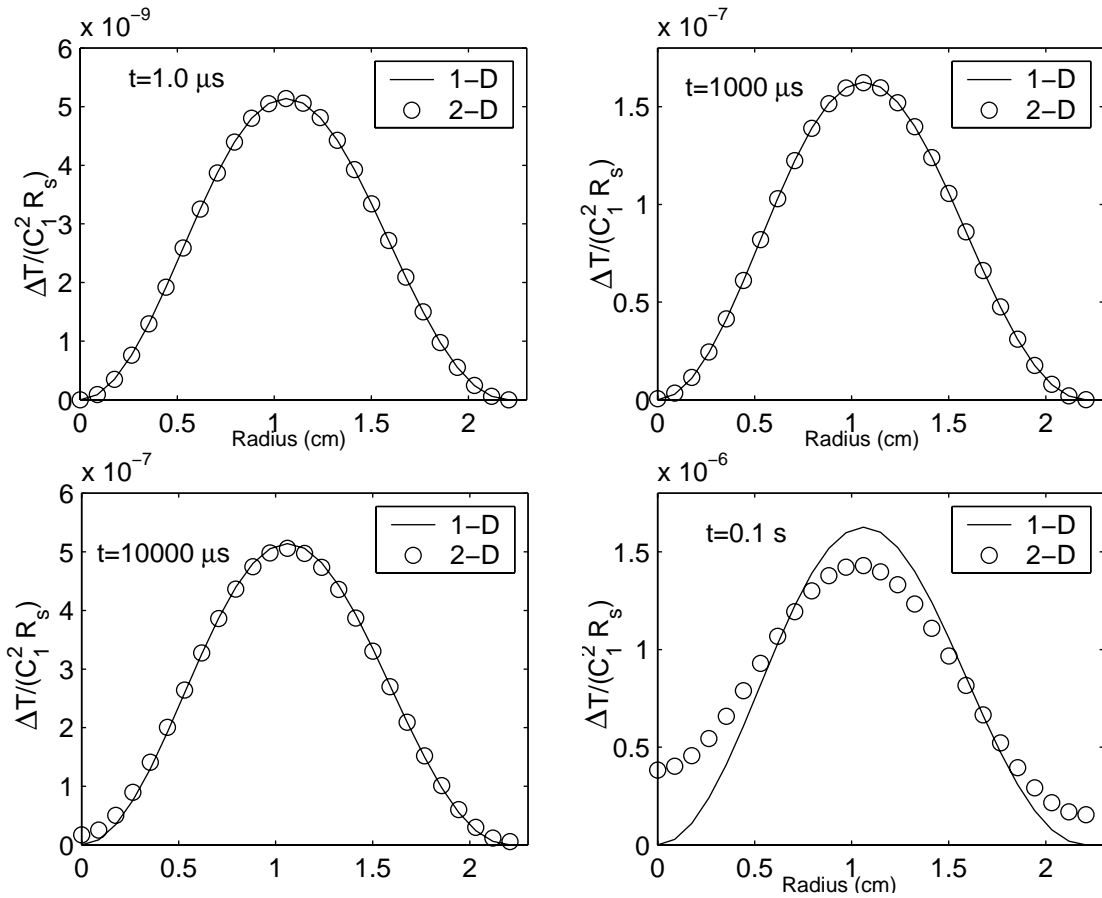


Figure 3.3: 1-D and 2-D temperature rises for various times.

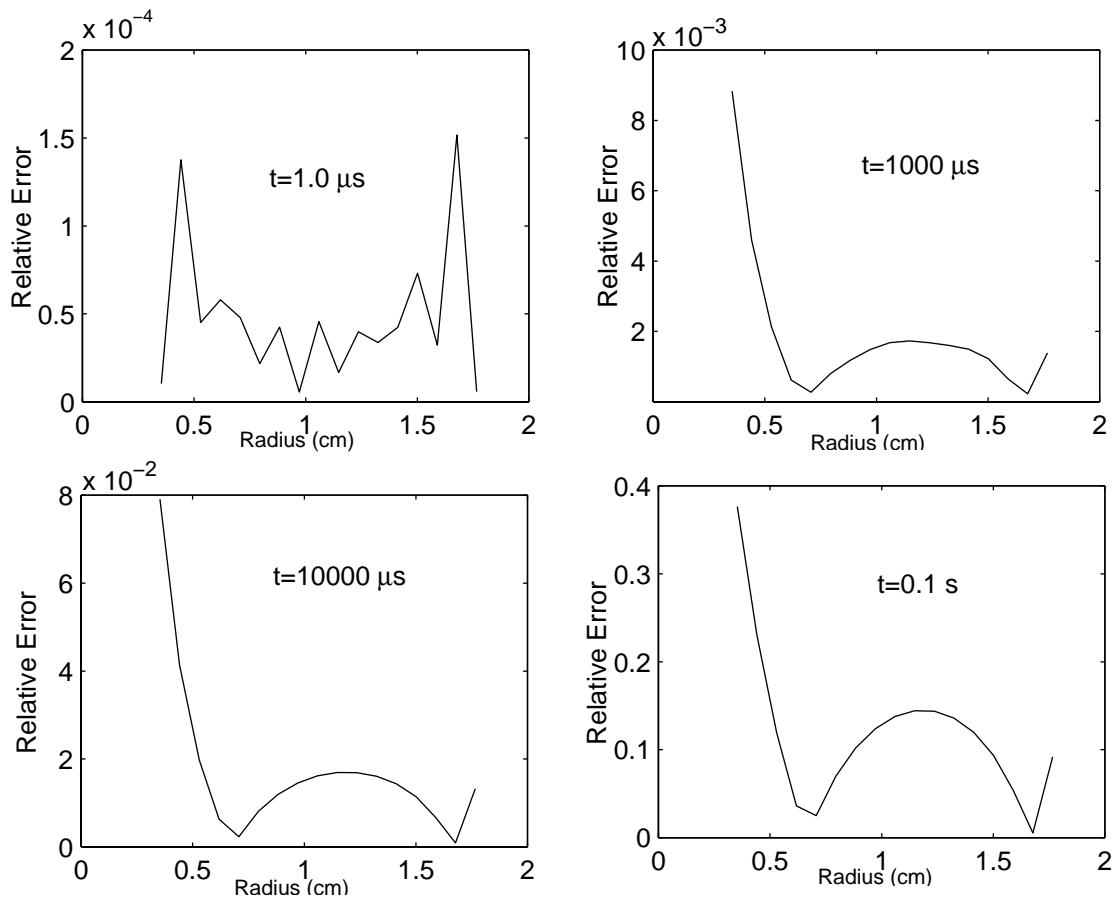


Figure 3.4: Relative error between 1-D and 2-D temperature rises for various times.

### Cavity Sidewall

In the last section, we showed that for times less than 1 ms lateral diffusion is not important for a smoothly varying power density over a flat surface. From this result, we also expect that lateral diffusion along the cavity axis is not important for calculating the temperature rise on the surface of the cylindrical sidewall of the cavity. Since the surface magnetic field varies as  $\sin(\pi z/d)$ , the power density is also a smoothly varying function. However, the cavity sidewall is not a flat surface. We must test the effect of the curvature of the surface on the temperature rise.

Since we only care about the curvature of the cavity surface, we may simplify the analysis by using an infinite hollow cylinder with a constant power input on the surface. The problem is formulated as follows:

$$\frac{\partial^2 T}{\partial r^2} = \frac{1}{\alpha_d} \frac{\partial T}{\partial t}, \quad R \leq r < \infty, \quad (3.59)$$

with initial condition

$$T(r, t = 0) = T_0, \quad (3.60)$$

and boundary condition

$$-k \left. \frac{\partial T}{\partial r} \right|_{r=R} = \frac{dP}{dA}. \quad (3.61)$$

We are only interested in the temperature on the surface. For  $\alpha_d(t - t')/R^2 \ll 1$ , the Green's function for this geometry is [6, eq. R20.3]

$$G(r = R, t | r' = R, t') = \frac{1}{2\pi R^2} \left[ \frac{R}{\sqrt{\pi \alpha_d (t - t')}} - \frac{1}{2} + \frac{3}{4} \sqrt{\frac{\alpha_d (t - t')}{\pi R^2}} \right]. \quad (3.62)$$

Using equations (3.14–3.17) and the fact that [6, eq. R20.6]

$$\int_R^\infty G(r, t | r', t') 2\pi r' dr' = 1, \quad (3.63)$$

the temperature at the surface is found to be

$$\begin{aligned} T(r = R, t) &= T_0 + \frac{\alpha_d}{k} \int_0^t \frac{dP}{dA} G(R, t | R, t') 2\pi R dt' \\ &= T_0 + \frac{dP}{dA} \frac{2\sqrt{t}}{\rho c_\varepsilon \sqrt{\pi \alpha_d}} \left[ 1 - \frac{\sqrt{\pi \alpha_d}}{4R} \sqrt{t} + \frac{\alpha_d}{4R^2} t \right]. \end{aligned} \quad (3.64)$$

In order for the above equation to be accurate we need  $t \ll R^2/\alpha_d = 3$  s, which is sufficient for the time range we are interested in. By comparing equation (3.64) with equation (3.38), we see that the first term corresponds to a one-dimensional semi-infinite slab. The last two terms are the corrections due to the curvature of the surface. We find that the first-order correction due to the curvature will cause a 1% relative error to occur at time

$$t = \frac{16R^2}{10201\pi\alpha_d}. \quad (3.65)$$

For the cavity radius  $R = 2.2075$  cm, this corresponds to a time of  $t = 1.5$  ms. Since the temperature rise due to pulsed heating occurs on the order of  $1 \mu\text{s}$ , we may ignore the effect of the curvature of the walls.

Based on the analysis in this section and in the previous section, we may use equation (3.36) to calculate the surface temperature rise at every point in the cavity. In the next section, we will allow the power density  $dP/dA$  to be temperature-dependent. By using equation (3.36) the analysis is greatly simplified.

### 3.3 Pulsed Heating of Test Cavity

In this section, we will consider the pulsed heating of the surface of the test cavity as it fills with energy from an RF pulse. The test cavity of radius  $R$  and length  $d$  resonates in the  $\text{TE}_{011}$  mode. The magnetic field in the cavity is given in Chapter 2. On the surface of the endcap, the magnetic field is

$$|H_r| = |h_{011}(t)| A_{TE}^{011} \frac{\pi R}{dx_{11}} J_1 \left( \frac{x_{11} r}{R} \right), \quad (3.66)$$

$Q_0$	21900
$Q_{\text{ext}}$	17110
$Q_L$	9605
$\beta$	1.28
$P_{\text{in}}$	10 MW
$t_p$	1.0 $\mu\text{s}$

Table 3.5: Cavity design parameters from Chapter 2.

where  $h_{011}(t)$  is the magnetic expansion coefficient found from equation (A.102). Similarly, the magnetic field on the surface of the cavity sidewall is

$$|H_z| = |h_{011}(t)| A_{TE}^{011} \sin\left(\frac{\pi z}{d}\right) |J_0(x_{11})|, \quad (3.67)$$

with the normalization

$$A_{TE}^{011} = \sqrt{\frac{2}{\pi d}} \frac{c x_{11}}{\omega_{011} R^2 |J_0(x_{11})|}, \quad (3.68)$$

and angular resonant frequency

$$\omega_{011} = c \sqrt{\left(\frac{x_{11}}{R}\right)^2 + \left(\frac{\pi}{d}\right)^2}. \quad (3.69)$$

For the test cavity with radius  $R = 2.2075$  cm and length  $d = 1.9$  cm, the resonant frequency of the  $TE_{011}$  mode is  $f_{011} = 11.438$  GHz. However, as described in Chapter 2, the coupling iris reduces the resonant frequency to  $f_{011} = 11.424$  GHz.

Equation (3.36) will be used to determine the temperature rise on every point of the surface of the test cavity. Before we include the temperature dependence of the parameters, we will find the temperature rise due to constant cavity parameters as a point of comparison to later results. We will use the data in Table 3.5 throughout this section.

### 3.3.1 Constant Cavity Parameters

Since  $Q_0 \gg 1$  and is held constant in this section, we may use equation (A.107) for the expansion coefficient of the magnetic field in the cavity. Using this coefficient with the condition  $dP/dA = (1/2)R_s |H_{\parallel}|^2$  in equation (3.36) gives the surface temperature on the endcap as

$$T(r, t) = T_0 + \sqrt{\frac{\pi}{\alpha_d \mu_0 \rho c_\epsilon J_0^2(x_{11})}} \frac{8c^2}{\omega_{011}^3 Q_{ext} R^2 d^3} J_1^2\left(\frac{x_{11}r}{R}\right) \cdot \int_0^t \frac{dt'}{\sqrt{t-t'}} \left[1 - \exp\left(-\frac{\omega_{011}t'}{2Q_L}\right)\right]^2. \quad (3.70)$$

If we introduce the easily-computed Dawson's integral [46, pp. 259-261]

$$F(x) = e^{-x^2} \int_0^x e^{t^2} dt, \quad (3.71)$$

then the surface temperature on the endcap can be written as

$$T(r, t) = T_0 + \sqrt{\frac{\pi}{\alpha_d \mu_0 \rho c_\epsilon J_0^2(x_{11})}} \frac{16c^2}{\omega_{011}^3 Q_{ext} R^2 d^3} J_1^2\left(\frac{x_{11}r}{R}\right) \cdot \left[ \sqrt{t} - 2\sqrt{\frac{2Q_L}{\omega_{011}}} F\left(\sqrt{\frac{\omega_{011}t}{2Q_L}}\right) + \sqrt{\frac{Q_L}{\omega_{011}}} F\left(\sqrt{\frac{\omega_{011}t}{Q_L}}\right) \right]. \quad (3.72)$$

Similarly, the surface temperature on the cavity sidewall is

$$T(z, t) = T_0 + \frac{16c^2 x_{11}^2}{\pi^{3/2} \mu_0 \rho c_\epsilon \sqrt{\alpha_d} \omega_{011}^3 Q_{ext} R^4 d} \sin^2\left(\frac{\pi z}{d}\right) \cdot \left[ \sqrt{t} - 2\sqrt{\frac{2Q_L}{\omega_{011}}} F\left(\sqrt{\frac{\omega_{011}t}{2Q_L}}\right) + \sqrt{\frac{Q_L}{\omega_{011}}} F\left(\sqrt{\frac{\omega_{011}t}{Q_L}}\right) \right]. \quad (3.73)$$

If we consider an RF pulse that is on up to time  $t = t_p$ , then for time  $t > t_p$ , the expansion coefficient for the magnetic field is found from equation (A.109) with

$P_{in} = 0$ . Using continuity at  $t = t_p$  we have

$$h_{011}(t) = -jQ_L \sqrt{\frac{8P_{in}}{\mu_0 Q_{ext} \omega_{011}}} \left[ \exp\left(\frac{\omega_{011} t_p}{2Q_L}\right) - 1 \right] \exp\left(-\frac{\omega_{011} t}{2Q_L}\right), \quad t > t_p. \quad (3.74)$$

For  $t > t_p$ , the integral from equation (3.70) is written as

$$\int_0^{t_p} \frac{dt'}{\sqrt{t-t'}} \left[ 1 - \exp\left(-\frac{\omega_{011} t'}{2Q_L}\right) \right]^2 + \int_{t_p}^t \frac{dt'}{\sqrt{t-t'}} \left[ \exp\left(\frac{\omega_{011} t_p}{2Q_L}\right) - 1 \right]^2 \exp\left(-\frac{\omega_{011} t'}{Q_L}\right) \quad (3.75)$$

Therefore, for time  $t > t_p$ , the surface temperature in the cavity is found by replacing the terms in brackets in equations (3.72–3.73) with the following terms

$$\left\{ \left[ \sqrt{t} - \sqrt{t-t_p} \right] - 2\sqrt{\frac{2Q_L}{\omega_{011}}} \left[ F\left(\sqrt{\frac{\omega_{011} t}{2Q_L}}\right) - e^{-\frac{\omega_{011} t_p}{2Q_L}} F\left(\sqrt{\frac{\omega_{011} (t-t_p)}{2Q_L}}\right) \right] \right. \\ \left. + \sqrt{\frac{Q_L}{\omega_{011}}} \left[ F\left(\sqrt{\frac{\omega_{011} t}{Q_L}}\right) + \left(1 - 2e^{-\frac{\omega_{011} t_p}{2Q_L}} + e^{-\frac{\omega_{011} t_p}{Q_L}}\right) F\left(\sqrt{\frac{\omega_{011} (t-t_p)}{Q_L}}\right) \right] \right\}. \quad (3.76)$$

Using the values given in Table 3.5, the point of maximum surface temperature rise for the endcaps and the cavity sidewall is plotted in Figure 3.5 as a function of time. Notice that the maximum temperature rise occurs at a time slightly larger than  $t_p$ . This occurs because there is still stored energy in the cavity when the RF pulse turns off. Even when the RF is off, power is dissipated in the cavity walls. Figure 3.6 is a plot of the surface temperature rise for each surface as a function of position at the time of maximum temperature rise.

### 3.3.2 Temperature-Dependent Parameters

We now allow the surface heat flux,  $dP/dA$ , to vary with temperature due to the dependence of the electrical resistivity,  $\rho_{res}$ , on temperature. The electrical resistivity is the reciprocal of the electrical conductivity,  $\sigma$ . Not only will the surface resistance,  $R_s$  vary with temperature due to its dependence on the square root of the resistivity

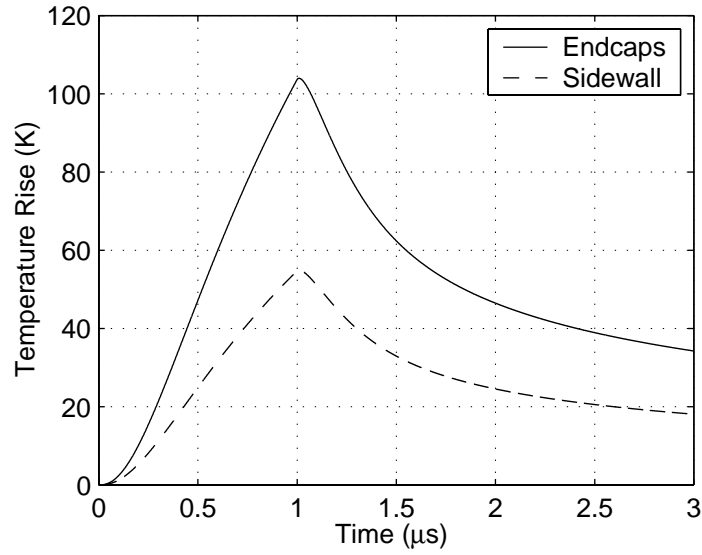


Figure 3.5: Point of maximum temperature rise for endcaps ( $r = 1.0607$  cm) and cavity sidewall ( $z = 0.95$  cm) as a function of time using the values from Table 3.5.

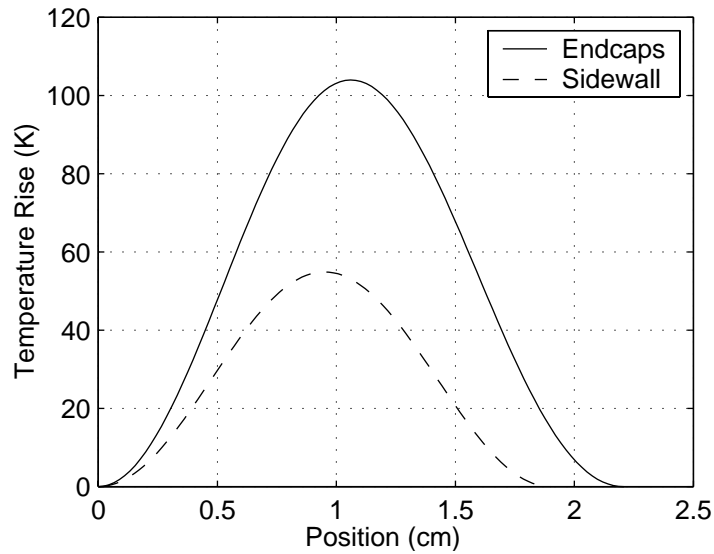


Figure 3.6: Surface temperature rise of endcaps ( $J_1^2$ ) and cavity sidewall ( $\sin^2$ ) as a function of position at the time of maximum temperature rise.

T (K)	$\rho_{\text{data}}$ ( $\times 10^{-8} \Omega \cdot \text{m}$ )	$\rho_{\text{fit}}$ ( $\times 10^{-8} \Omega \cdot \text{m}$ )	Relative Error (%)
273	1.543	1.528	0.99
293	1.678	1.668	0.59
298	1.712	1.703	0.52
300	1.725	1.717	0.46
400	2.402	2.418	0.68
500	3.090	3.120	0.95
600	3.792	3.821	0.76
700	4.514	4.522	0.18
800	5.262	5.223	0.74

Table 3.6: Data for temperature dependence of electrical resistivity for pure copper [31] along with the linear fit and the relative error.

(see equation (A.71)), but so will the magnetic field. The magnetic field varies with the unloaded cavity Q and this quantity varies as  $1/R_s$  (see equations (A.73), (A.102), (A.104) and (A.107)).

The resistivity varies linearly with temperature and the data for pure copper is given in Table 3.6 [31, p. 12-43] The fit to the data using the linear least-squares method is given by

$$\rho_{\text{res}}(T) = 7.012 \times 10^{-11} T - 3.865 \times 10^{-9} (\Omega \cdot \text{m}), \quad 273\text{K} \leq T \leq 800\text{K}. \quad (3.77)$$

A plot of this fit is shown in Figure 3.7. The fit at the data points is also given in Table 3.6 along with the relative error. The table shows that the error is less than 1% over the desired temperature range.

Putting the temperature dependence into equation (3.36) gives

$$\begin{aligned} T(\vec{r}, t) &= T_0 + \frac{1}{\rho c_\epsilon \sqrt{\pi \alpha_d}} \int_0^t \frac{dt'}{\sqrt{t-t'}} \frac{dP(t', T)}{dA} \\ &= T_0 + \frac{1}{2\rho c_\epsilon \sqrt{\pi \alpha_d}} \int_0^t \frac{dt'}{\sqrt{t-t'}} R_s(T) |H_{\parallel}(\vec{r}, t', T)|^2, \end{aligned} \quad (3.78)$$

where  $\vec{r}$  denotes position along the surface of the cavity. Because temperature is

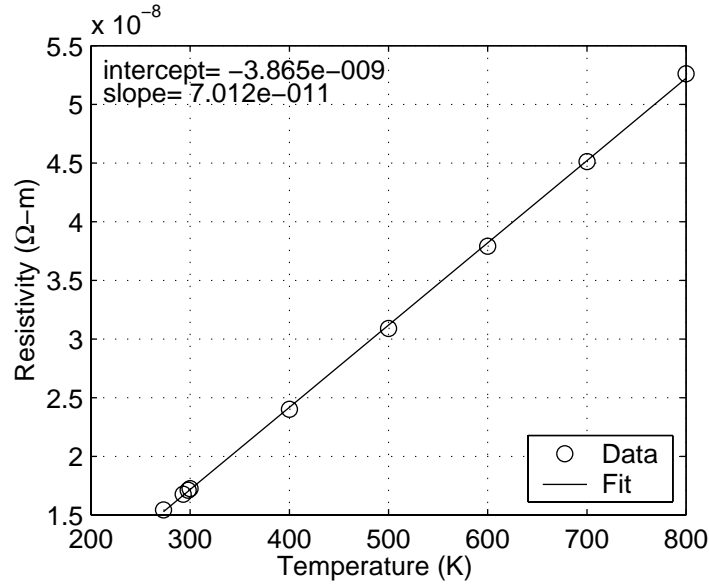


Figure 3.7: A plot of the linear fit of the electrical resistivity to temperature.

on the right-hand side of equation (3.78), we must solve an integral equation. In the literature, this equation is known as a nonlinear Volterra equation of the second kind [33, eq. (4.1)]

$$f(t) = g(t) + \int_0^t K(t, t', f(t')) dt', \quad (3.79)$$

where  $K$  is called the *kernel*. Inspection of equation (3.78) shows that a singularity occurs at  $t' = t$ . Since the kernel is singular, the equation is best written as [33, eq. (8.1)]

$$f(t) = g(t) + \int_0^t p(t, t') K(t, t', f(t')) dt', \quad (3.80)$$

where  $p(t, t')$  represents the singular part of the kernel that has been separated from the original kernel. In our case

$$p(t, t') = \frac{1}{\sqrt{t - t'}}. \quad (3.81)$$

There are numerical procedures known as *product integration methods* [33, Ch. 8] that can be used to solve equation (3.80). For the case of equation (3.81), the solution

may be found with [33, eqs. (8.15–8.16)]

$$F_n = g(t_n) + \sum_{j=0}^{n-1} w_{nj} K(t_n, t_j, F_j), \quad n = 1, 2, \dots, \quad (3.82)$$

where  $F_n$  is the approximation for  $f(t_n)$  and

$$w_{nj} = 2 \left( \sqrt{t_n - t_j} - \sqrt{t_n - t_{j+1}} \right). \quad (3.83)$$

The method used to derive equation (3.82) is essentially Euler's method, so the error is approximately

$$|F_n - f(t_n)| = O(h), \quad (3.84)$$

where  $h$  is the stepsize. Since we only need to know the temperature rise due to pulsed heating to within a few percent, we do not need high accuracy. Hence, equation (3.82) is suitable for our needs. If more accuracy is desired, then we may use a technique known as *Richardson's extrapolation* [33, pp. 133–134]. Richardson's extrapolation combines solutions to equation (3.82) with different stepsizes in such a way as to reduce the error to  $O(h^p)$  where  $p > 1$ .

Using equations (3.66–3.68) and (A.71), the kernels for the cavity endcaps and sidewall are

$$K_{end}(r, t, t', T) = \sqrt{\frac{\mu_c}{2\pi\alpha_d}} \frac{\pi c^2}{\rho c_\epsilon \omega_{011}^{3/2} R^2 d^3 J_0^2(x_{11})} J_1^2\left(\frac{x_{11}r}{R}\right) \sqrt{\rho_{res}(T)} |h_{011}(t', T)|^2, \quad (3.85)$$

$$K_{wall}(z, t, t', T) = \sqrt{\frac{\mu_c}{2\pi\alpha_d}} \frac{c^2 x_{11}^2}{\pi \rho c_\epsilon \omega_{011}^{3/2} R^4 d} \sin^2\left(\frac{\pi z}{d}\right) \sqrt{\rho_{res}(T)} |h_{011}(t', T)|^2, \quad (3.86)$$

where  $\rho_{res}$  is given by equation (3.77) and  $h_{011}$  is found from equation (A.102). Notice that the right-hand side of equations (3.85–3.86) do not depend on  $t$ .  $t$  is kept on the left-hand side of these equations as a placeholder to prevent confusion when they are substituted into equation (3.82).

The magnitude of the magnetic field in the cavity depends on the unloaded Q, so

we must calculate its variation with temperature. According to equation (A.73), the unloaded Q for the TE<sub>011</sub> mode is

$$\begin{aligned} \frac{1}{Q_{011}(T)} &= \frac{1}{\sqrt{2\mu_c\omega_{011}}} \int_{S_w} dS \sqrt{\rho_{res}(T(\vec{r}))} \left| \vec{H}_{011}(\vec{r}) \right|^2 \\ &= \frac{1}{\sqrt{2\mu_c\omega_{011}}} (A_{TE}^{011})^2 \left[ \frac{4\pi^3 R^2}{d^2 x_{11}^2} \int_0^R \sqrt{\rho_{res}(T(r))} J_1^2\left(\frac{x_{11}r}{R}\right) r dr \right. \\ &\quad \left. + 2\pi R J_0^2(x_{11}) \int_0^d \sqrt{\rho_{res}(T(z))} \sin^2\left(\frac{\pi z}{d}\right) dz \right]. \end{aligned} \quad (3.87)$$

We now see that we must know the temperature before calculating the unloaded Q and the magnetic field. However, the temperature depends on the magnetic field. For this reason, equation (3.82) is desirable since the temperature at time  $t_n$  depends only on quantities determined for time up to  $t_{n-1}$ . The procedure consists of finding the temperature at time  $t_n$  using the magnetic field for times up to  $t_{n-1}$ . Then the unloaded Q and the magnetic field is updated using this temperature. Of course, this process is repeated until the final timestep is reached.

The magnetic expansion coefficient  $h_{011}(t) = \tilde{h}_{011}(t)e^{-j\omega t}$  is found from equation (A.102), where  $\omega$  is the angular drive frequency. For a numerical solution, we need to split the real and imaginary parts of  $\tilde{h}$ , which will result in two coupled first-order differential equations. Defining  $\tilde{h} = \tilde{h}_R + j\tilde{h}_I$  we have

$$\frac{d\tilde{h}_R}{dt} = \frac{1}{\omega} \frac{1 + \frac{1}{Q_{011}}}{2 + \frac{1}{Q_{011}}} \left[ M \frac{d\tilde{h}_I}{dt} - \omega N \tilde{h}_R + W \tilde{h}_I \right], \quad (3.88a)$$

$$\begin{aligned} \frac{d\tilde{h}_I}{dt} &= \left[ \frac{1}{\omega} \frac{1 + \frac{1}{Q_{011}}}{2 + \frac{1}{Q_{011}}} M^2 + \omega \frac{2 + \frac{1}{Q_{011}}}{1 + \frac{1}{Q_{011}}} \right]^{-1} \\ &\cdot \left[ \left( \frac{1 + \frac{1}{Q_{011}}}{2 + \frac{1}{Q_{011}}} MN - W \right) \tilde{h}_R - \left( \frac{1}{\omega} \frac{1 + \frac{1}{Q_{011}}}{2 + \frac{1}{Q_{011}}} MW + \omega N \right) \tilde{h}_I \right. \\ &\quad \left. - \frac{1}{1 + \frac{1}{Q_{011}}} \sqrt{\frac{8P_{in}\omega_{011}^3}{\mu_0 Q_{ext}}} \right], \end{aligned} \quad (3.88b)$$

where

$$M = \frac{\omega}{Q_{011}} + \frac{\omega_{011}}{Q_{ext} \left(1 + \frac{1}{Q_{011}}\right)}, \quad (3.89a)$$

$$N = \frac{\omega}{Q_{011}} + \frac{\omega_{011}}{Q_{ext}}, \quad (3.89b)$$

$$W = \frac{\omega_{011}^2}{1 + \frac{1}{Q_{011}}} - \omega^2. \quad (3.89c)$$

Many methods exist to numerically solve equations (3.88–3.89). We will use the Runge-Kutta method of order four [11, p. 297]. With this method, we may obtain the solution to the magnetic field one timestep at a time.

We will test our algorithm with the results from the last section by setting  $\rho_{res}$  to be constant at its room temperature value. Using the values from Table 3.5, the magnetic field found from equations (3.88–3.89) should match that found from equations (A.107) and (3.74). The fields in the cavity are initially zero, so  $\tilde{h}_{011}(t = 0) = 0$ . Also we assume that we drive the cavity at the measured resonance,  $\omega = \omega_{011}/\sqrt{1 + 1/Q_{011}}$ . Remember that the resonant frequency of a lossy cavity is shifted slightly. Figure 3.8 compares the solutions for the expansion coefficient of the magnetic field. The error between the two solutions at the time of maximum field is less than 0.01%.

When calculating the temperature rise with the new algorithm, the timestep used must be larger than an RF period. By adhering to this limit, we avoid any ambiguity about the value of  $Q_{011}$  throughout the integration. For a resonant frequency of 11.424 GHz the RF period is approximately 0.1 ns. We will use a timestep of 1 ns. Figure 3.9 compares the solutions for the temperature rise of the cavity endcaps and sidewall of the new algorithm with equations (3.72–3.73) and (3.76). Figure 3.10 shows the absolute error for the temperature rise of the endcaps. The absolute error for the cavity sidewall is similar. The relative error between the two maximum temperature rises is less than 0.05%. Therefore, this algorithm may be confidently used to calculate the temperature rise from pulsed heating with variable  $\rho_{res}$ .

Figure 3.11 compares the temperature rise on the endcaps for variable  $\rho_{res}$  (see

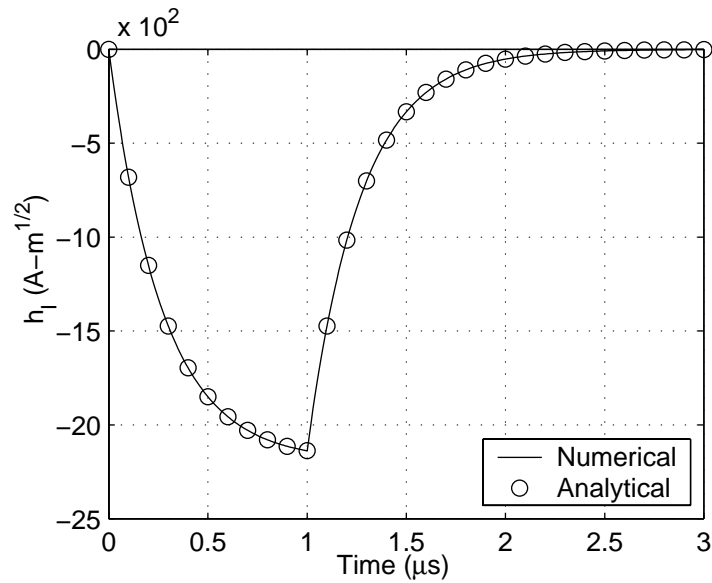


Figure 3.8: Comparison of the expansion coefficient of the magnetic field from equations (3.88–3.89) with equations (A.107) and (3.74) for constant  $\rho_{res}$ .

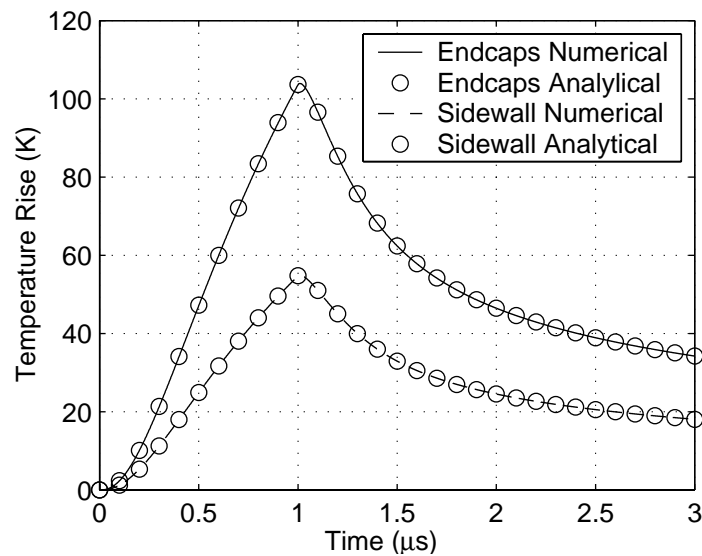


Figure 3.9: Comparison of the temperature rise for the cavity endcaps and sidewall from the new algorithm with the analytical solution from the last section.

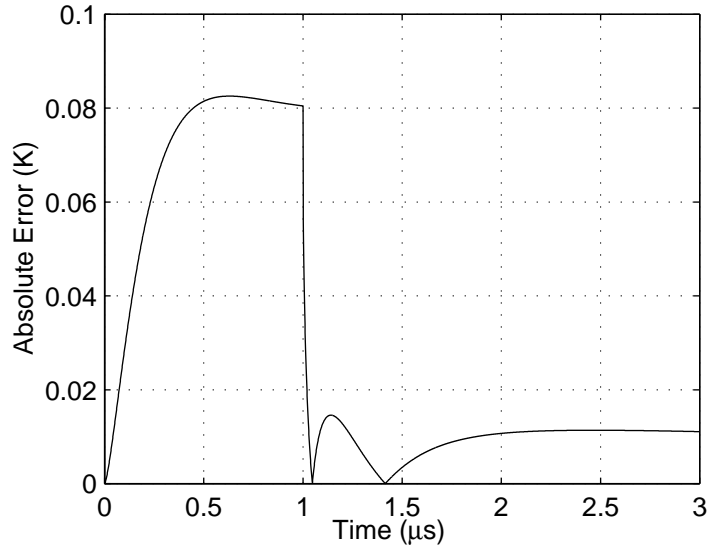


Figure 3.10: Absolute error in the temperature rise of the cavity endcaps between the new algorithm and the analytical solution from the last section.

equation (3.77)) as compared to constant  $\rho_{res}$ . The maximum temperature rise on the endcaps is greater by 10.3 K. This corresponds to a difference of approximately 10%. Figure 3.12 displays the comparison of temperature rises for the cavity sidewall. The difference in maximum temperature rise is only 1.5 K. The difference is smaller than for the endcaps because the temperature rise is smaller and the electrical resistivity does not change as much. Figure 3.13 shows the change of  $Q_{011}$  as the cavity heats and then cools. In this case,  $Q_{011}$  drops by approximately 12%.

### 3.3.3 Measurement of Pulsed Temperature Rise

In Chapter 2, we discussed the implementation of a steady-state low-power  $TE_{012}$  mode in the cavity to measure the change in  $Q$ 's and the temperature rise of the surface. A change in the resonant frequency and unloaded  $Q$  of this mode will result in a change in the amplitude and phase of the reflected signal as measured from the diagnostic port. In this section we will show what a typical signal will look like. Also, we will demonstrate how to extract the change in  $Q$  and the temperature rise of the surface from this reflected signal. The design parameters for the  $TE_{012}$  mode are

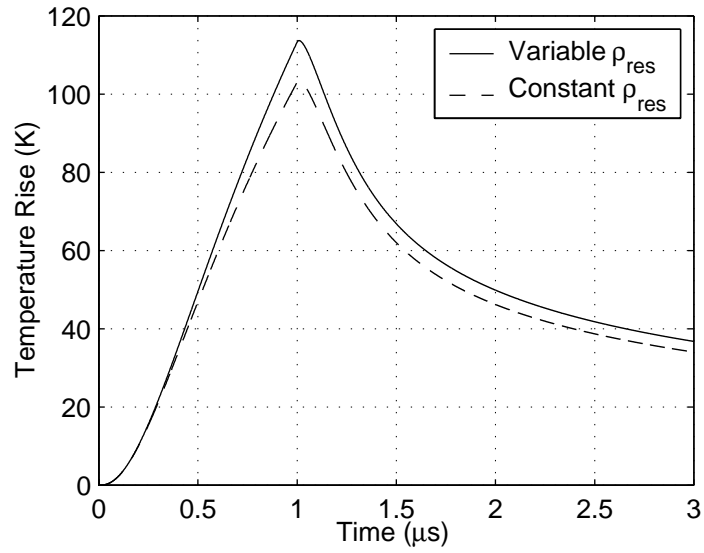


Figure 3.11: Comparison of variable  $\rho_{res}$  with constant  $\rho_{res}$  on the temperature rise of the cavity endcaps.

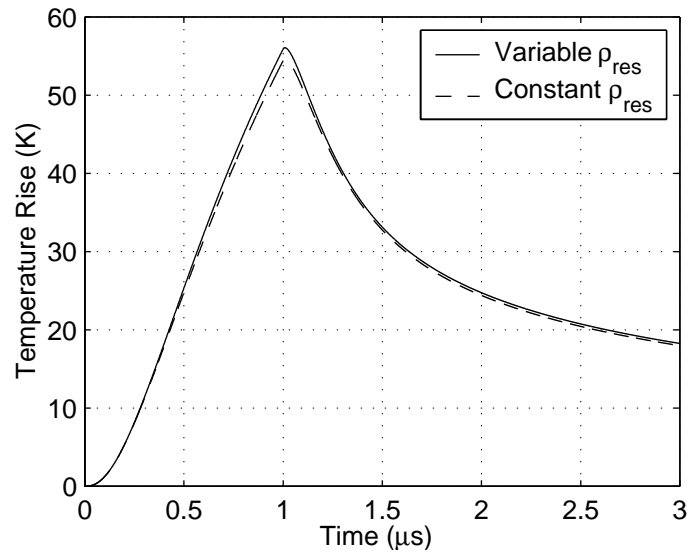


Figure 3.12: Comparison of variable  $\rho_{res}$  with constant  $\rho_{res}$  on the temperature rise of the cavity sidewall.

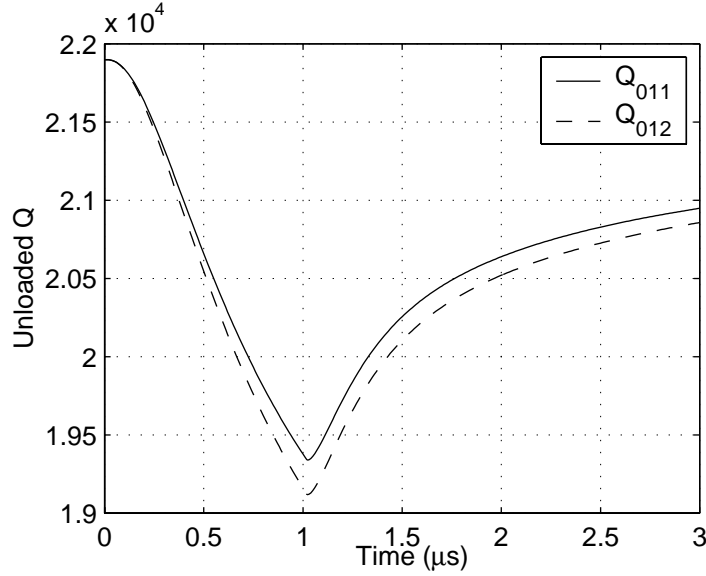


Figure 3.13: Change in  $Q_{011}$  and  $Q_{012}$  due to heating of cavity.

given in Table (3.7).

### Typical cavity response

In the previous section we discovered that the unloaded  $Q$  for the  $TE_{011}$  mode changes due to the heating of the surface. Likewise, the unloaded  $Q$  for the  $TE_{012}$  will also change according to (see equation (A.73))

$$\begin{aligned}
 \frac{1}{Q_{012}(T)} &= \frac{1}{\sqrt{2\mu_c\omega_{012}}} \int_{S_w} dS \sqrt{\rho_{res}(T(\vec{r}))} \left| \vec{H}_{012}(\vec{r}) \right|^2 \\
 &= \frac{1}{\sqrt{2\mu_c\omega_{012}}} (A_{TE}^{012})^2 \left[ \frac{16\pi^3 R^2}{d^2 x_{11}^2} \int_0^R \sqrt{\rho_{res}(T(r))} J_1^2\left(\frac{x_{11}r}{R}\right) r dr \right. \\
 &\quad \left. + 2\pi R J_0^2(x_{11}) \int_0^d \sqrt{\rho_{res}(T(z))} \sin^2\left(\frac{2\pi z}{d}\right) dz \right], \tag{3.90}
 \end{aligned}$$

where the magnetic field for the  $TE_{012}$  mode is given in Chapter 2. The change in  $Q_{012}$  due to the temperature rise derived in the last section is also shown in Figure 3.13. In this case the unloaded  $Q$  drops by approximately 13%. Note that it is a coincidence

$Q_0$	21880
$Q_{e1}$	21880
$Q_{e2}$	100000
$Q_L$	9860
$\beta_1$	1.0
$\beta_2$	0.22
$f_{012}$	17.81 GHz

Table 3.7: Cavity design parameters for the  $TE_{012}$  mode from Chapter 2.

due to the geometry of the cavity that the values for the unloaded  $Q$ 's of the  $TE_{011}$  and  $TE_{012}$  modes are close.

To find the change in the reflected signal from the diagnostic port, we must use equation (A.125). The  $TE_{012}$  mode is driven in steady-state with a low-power frequency generator at its measured angular resonant frequency,  $\omega_{012}/\sqrt{1+1/Q_{012}}$ , through the diagnostic port which will be labeled as port one. Thus,  $d\tilde{V}_1^+/dt = 0$  and  $\tilde{V}_2^+ = 0$ . Before the cavity heats up due to a high-power pulse in the  $TE_{011}$  mode, the reflected signal from the diagnostic port is initially

$$\left. \frac{\tilde{V}_1^-}{\tilde{V}_1^+} \right|_{t=0} = \left. \frac{V_{1\lambda}\tilde{e}_\lambda}{\tilde{V}_1^+} \right|_{t=0} - 1 = \frac{2Q_{L,012}}{Q_{e1}} \left( 1 + j\frac{1}{Q_{012}} \right). \quad (3.91)$$

Likewise with the previous section, we must split equation (A.125) into real and imaginary parts and use a Runge-Kutta method of order four to solve the coupled first-order differential equations that ensue. Let  $V_{1\lambda}\tilde{e}_\lambda/\tilde{V}_1^+ = a + jb$ , then equation (A.125) becomes

$$\frac{da}{dt} = \frac{A}{\omega} \left[ M\frac{db}{dt} - a\omega N + bW + \frac{2\omega\omega_{012}}{Q_{e1}} \right], \quad (3.92a)$$

$$\frac{db}{dt} = \left[ \frac{A}{\omega}M^2 + \frac{\omega}{A} \right]^{-1} \left[ a(AMN - W) - b \left( \frac{A}{\omega}MW + \omega N \right) - \frac{2\omega_{012}}{Q_{e1}}AM + \frac{2\omega\omega_{012}}{Q_{e1}Q_{012}} \right] \quad (3.92b)$$

where

$$A = \frac{1 + \frac{1}{Q_{012}}}{2 + \frac{1}{Q_{012}}}, \quad (3.93a)$$

$$M = \frac{\omega}{Q_{012}} + \frac{\omega_{012}}{1 + \frac{1}{Q_{012}}} \left( \frac{1}{Q_{e1}} + \frac{1}{Q_{e2}} \right), \quad (3.93b)$$

$$N = \frac{\omega}{Q_{012}} + \omega_{012} \left( \frac{1}{Q_{e1}} + \frac{1}{Q_{e2}} \right), \quad (3.93c)$$

$$W = \frac{\omega_{012}^2}{1 + \frac{1}{Q_{012}}} - \omega^2. \quad (3.93d)$$

Using the change in  $Q_{012}$ , the reflected signal from the diagnostic port will change according to

$$\frac{\tilde{V}_1^-(t)}{\tilde{V}_1^+} = \frac{V_{1\lambda}\tilde{e}_\lambda(t)}{\tilde{V}_1^+} - 1 = [a(t) - 1] + jb(t). \quad (3.94)$$

Using the parameters in Tables 3.5 and 3.7, the magnitude and phase of the reflected signal from the diagnostic port is shown in Figure 3.14. Notice that the amplitude and phase of the reflected signal reach an extremum some time after the high-power pulse turns off and the unloaded Q's reach a minimum. The time at which these extrema occur are on order of the fill-time after the pulse turns off (see equation (A.106)).

The phase shift in the reflected signal arises from the change in the cavity's resonant frequency due to the change in its unloaded Q. If we look more closely at equation (A.125), we notice that the *measured* angular resonant frequency of the cavity is

$$\omega_0 = \frac{\omega_{012}}{\sqrt{1 + \frac{1}{Q_{012}}}}. \quad (3.95)$$

Initially, we drive the cavity at this resonant frequency, so the term

$$\frac{\omega_{012}^2}{1 + \frac{1}{Q_{012}}} - \omega^2, \quad (3.96)$$

is zero. However, as  $Q_{012}$  changes during the heating of the cavity, this term will differ

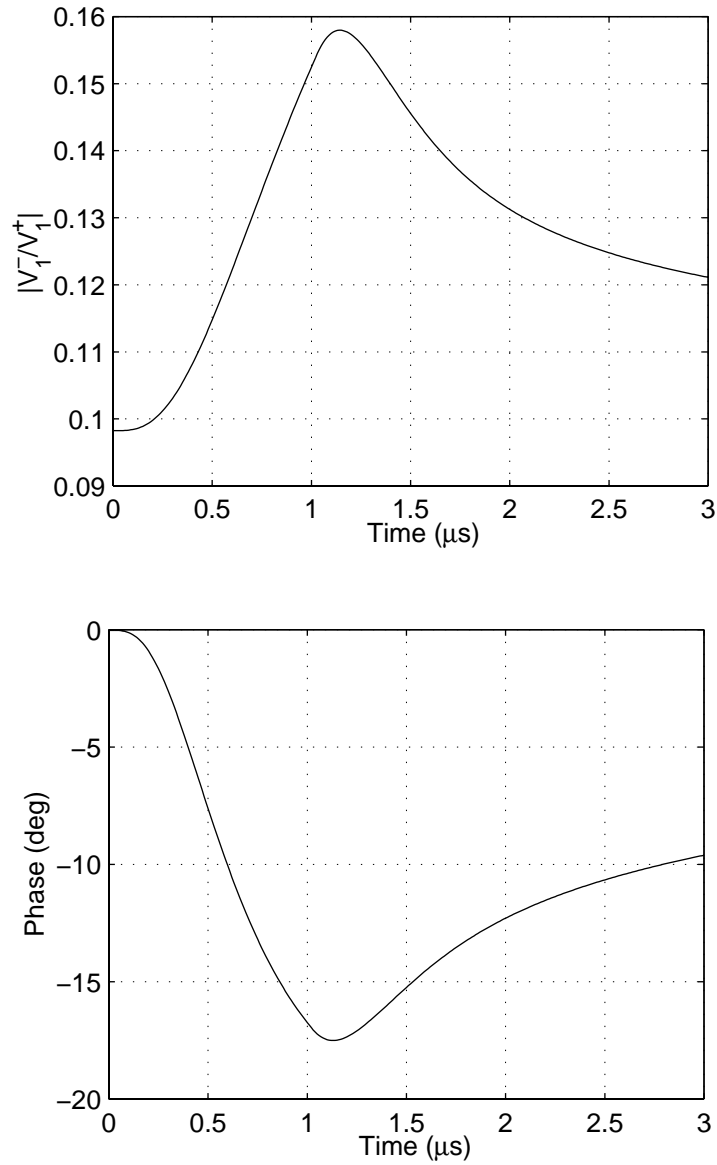


Figure 3.14: Magnitude and phase of reflected signal from diagnostic port due to the change in  $Q_{012}$  from pulsed heating.

from zero. It is the change in this term that results in a phase shift of the reflected signal. Of course, the amplitude of the signal changes because a change in unloaded  $Q$  results in a change in coupling to the cavity mode.

### Measuring temperature rise

Figure 3.14 shows the typical response of the  $TE_{012}$  mode to pulsed heating. In this section, we will show how to determine the temperature rise on the surface from the measurement of the amplitude and phase of the reflected signal.

The first step involves extracting the change in unloaded  $Q$  from the reflected signal. However, we must also allow for a change in  $\omega_{012}$  from the deformation of the surface of the cavity due to heating. This effect is difficult to predict since the heating is high enough to cause the deformation to be nonlinear. Fortunately, this effect can be easily measured and it is predicted to be small. Looking back at equation (A.125), we split it into real and imaginary parts and solve the resulting equations in terms of  $Q_{012}(t)$  and  $\omega_{012}(t)$

$$\begin{aligned}
Q_{012}^2 \left[ \frac{\omega_{012}}{Q_{e||}} \frac{db}{dt} - 2\omega \frac{da}{dt} + b(\omega_{012}^2 - \omega^2) - a \frac{\omega\omega_{012}}{Q_{e||}} + \frac{2\omega\omega_{012}}{Q_{e1}} \right] \\
+ Q_{012} \left[ \omega \left( \frac{db}{dt} - \frac{da}{dt} \right) - (a+b)\omega^2 - a \frac{\omega\omega_{012}}{Q_{e||}} + \frac{2\omega\omega_{012}}{Q_{e1}} \right] \\
+ \omega \frac{db}{dt} - a\omega^2 = 0, \quad (3.97a)
\end{aligned}$$

$$\begin{aligned}
aQ_{012}^2\omega_{012}^2 + \omega_{012} \left[ \frac{Q_{012}^2}{Q_{e||}} \left( \frac{da}{dt} + b\omega \right) + Q_{012} \left( b \frac{\omega}{Q_{e||}} - \frac{2\omega}{Q_{e1}} \right) - \frac{2\omega}{Q_{e1}} \right] \\
+ Q_{012}^2 \left( 2\omega \frac{db}{dt} - a\omega^2 \right) + Q_{012} \left[ \omega \left( \frac{da}{dt} + \frac{db}{dt} \right) + (b-a)\omega^2 \right] \\
+ \omega \frac{da}{dt} + b\omega^2 = 0, \quad (3.97b)
\end{aligned}$$

where

$$\frac{1}{Q_{e||}} = \frac{1}{Q_{e1}} + \frac{1}{Q_{e2}}. \quad (3.98)$$

Equations (3.97) may be solved using algorithms that find solutions of nonlinear systems of equations [11, pp. 543–576].

We will test this method. First we will use the unloaded Q change shown in Figure 3.13 given by the temperature rise found in section 3.3.2. Next we will introduce a fictitious frequency shift of 100 kHz that occurs at the end of the pulse

$$\omega_{012} = \begin{cases} \omega_{012}(t=0) + \frac{\Delta\omega}{t_p}t & t \leq t_p \\ \omega_{012}(t=0) + \frac{\Delta\omega}{t_p}(2t_p - t) & t_p < t \leq 2t_p \\ \omega_{012}(t=0) & t > 2t_p, \end{cases} \quad (3.99)$$

where  $\Delta\omega = 2\pi(100 \text{ kHz})$ . This frequency shift is about 10% of the Q-bandwidth for the TE<sub>012</sub> mode. The amplitude and phase of the reflected signal due to changes in  $Q_{012}$  and  $\omega_{012}$  are shown in Figure 3.15. After solving equations (3.97) with the data shown in Figure 3.15, the change in  $Q_{012}$  and  $\omega_{012}$  is plotted in Figure 3.16 along with their relative errors.

Once the value of  $Q_{012}$  as a function of time is extracted from the reflected signal, we may indirectly approximate the maximum temperature rise of the surface. We will use equation (3.90) to determine the temperature rise in the cavity. Since  $Q_{012}$  is a global parameter of the cavity, we must make some assumptions.

The first assumption is that the temperature rise on the endcaps and the cavity sidewall have a functional dependence which ignores the variation of the electrical resistivity. At first glance, this approximation may seem to have large error, because Section 3.3.2 showed that the variation of the electrical resistivity caused a 10% increase in the maximum temperature rise on the endcaps. However, the overall error is smaller and acceptable, because the variation of the electrical resistivity is taken into account in equation (3.90). Thus, we model the temperature on the endcaps and cavity sidewall as

$$T(r) = T_0 + \frac{\Delta T_{r,\max}}{J_1^2(x'_{11})} J_1^2\left(\frac{x_{11}r}{R}\right), \quad (3.100a)$$

$$T(z) = T_0 + \Delta T_{z,\max} \sin^2\left(\frac{\pi z}{d}\right), \quad (3.100b)$$

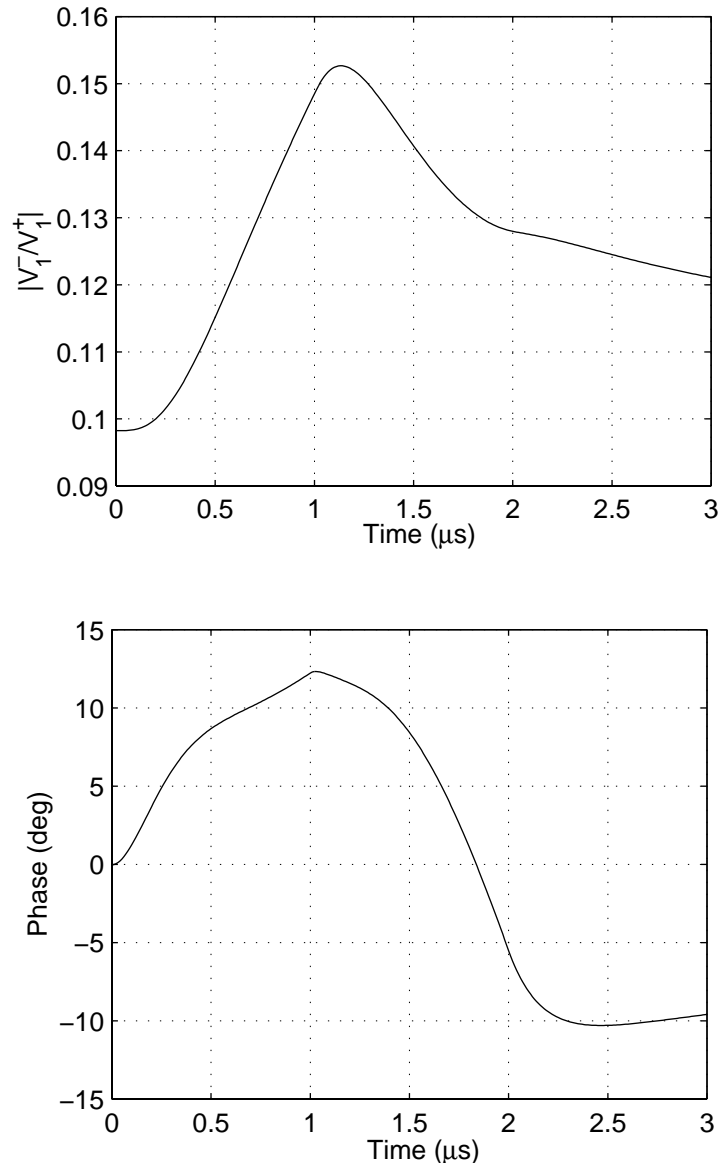


Figure 3.15: Magnitude and phase of reflected signal from diagnostic port due to the change in  $Q_{012}$  from pulsed heating and the fictitious change in  $\omega_{012}$ .

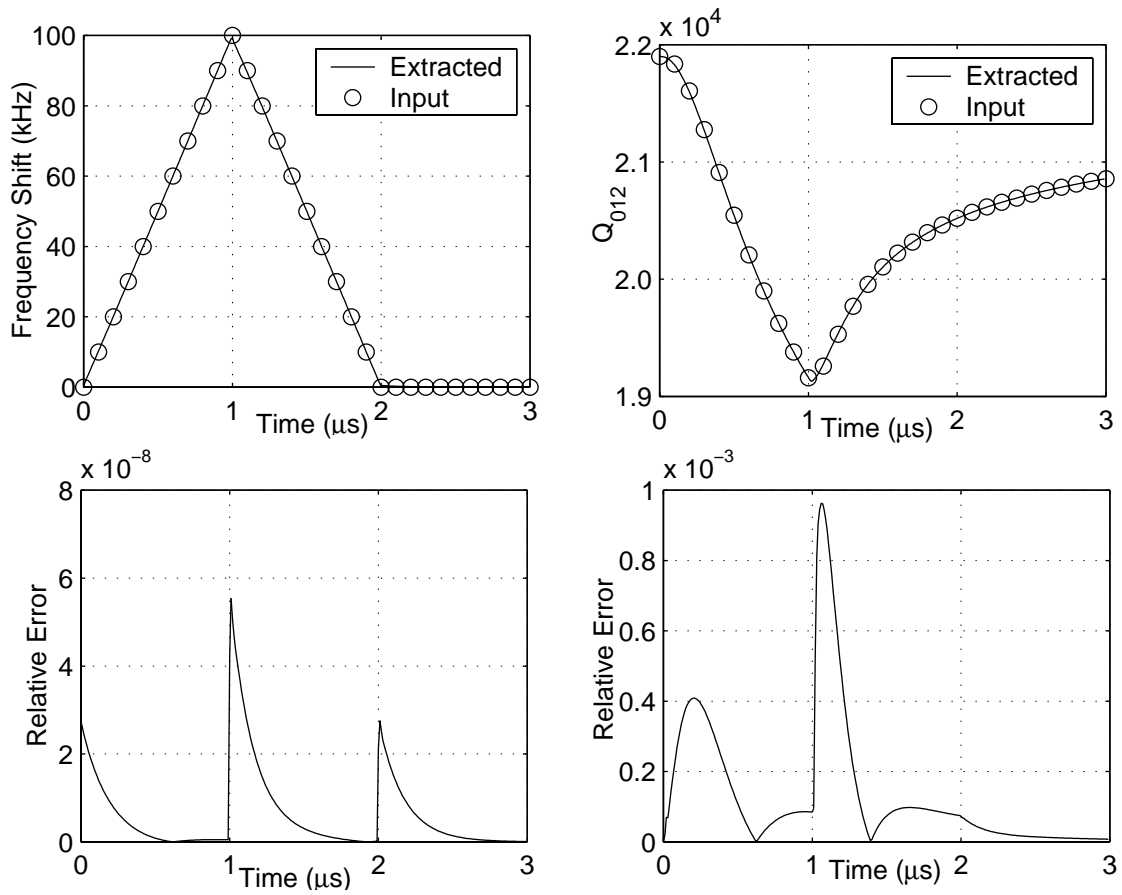


Figure 3.16: Extracted  $Q_{012}$  and  $\omega_{012}$  from the reflected signal data in Figure 3.15. Their relative errors are shown beneath.

where the term  $J_1^2(x'_{11})$  is used for normalization.

The second assumption is the ratio between the maximum temperature rise on the endcaps to the maximum temperature rise on the cavity sidewall. Our simulations show this ratio to be approximately 2. Fortunately, the temperature determined using equation (3.90) is not sensitive to this ratio since  $Q_{012}$  is approximately 8 times more sensitive to changes on the endcap than on the cavity sidewall. So we let  $\Delta T_{r,\max} = 2\Delta T_{z,\max}$ .

Using these assumptions and equation (3.77) in equation (3.90) we have

$$\begin{aligned} \frac{\sqrt{\mu_c \omega_{012}}}{Q_{012} (A_{TE}^{012})^2} - \frac{16\pi^3 R^2}{d^2 x_{11}^2} \int_0^R dr r J_1^2\left(\frac{x_{11}r}{R}\right) \sqrt{a_1 \left[ \frac{\Delta T_{r,\max}}{J_1^2(x'_{11})} J_1^2\left(\frac{x_{11}r}{R}\right) + T_0 \right] + a_2} \\ - 2\pi R J_0^2(x_{11}) \int_0^d dz \sin^2\left(\frac{2\pi z}{d}\right) \sqrt{a_1 \left[ \frac{1}{2} \Delta T_{r,\max} \sin^2\left(\frac{\pi z}{d}\right) + T_0 \right] + a_2} = 0, \end{aligned} \quad (3.101)$$

where

$$a_1 = 7.012 \times 10^{-11} \Omega \cdot \text{m/K}, \quad a_2 = -3.865 \times 10^{-9} \Omega \cdot \text{m}. \quad (3.102)$$

$\omega_{012}$  will be taken as a constant in equation (3.101) since its variation is slight.  $\Delta T_{r,\max}$  may be found by solving equation (3.101) by iteration where the integrals are computed numerically. We may simulate this procedure by using the value of  $Q_{012}$  found in the previous section. The results are plotted in Figure 3.17.

This procedure will always systematically underestimate the actual temperature rise since the assumed temperature ignores the variation of the electrical resistivity. However, the relative error in this case is less than 3%. This error will increase for higher temperature rises. For example, for a temperature rise of 250 K, the relative error is less than 5%. This is an acceptable error. The change in relative error due to the approximation that the ratio of the maximum temperature rise on the endcaps to the maximum temperature rise on the cavity sidewall is 2 is also slight. From simulations, the ratio varies from 1.9 to 2.4 over the temperature range of room temperature to the melting point of copper. Over this entire range, the relative error

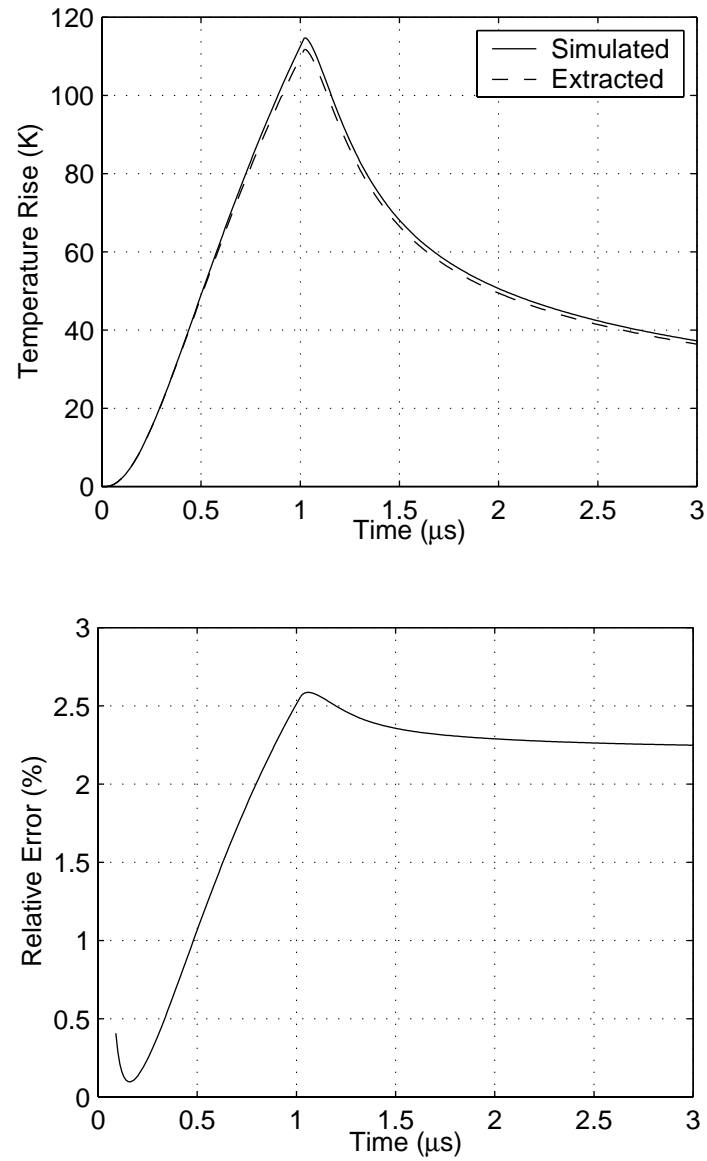


Figure 3.17: The extracted temperature rise of the cavity endcaps from  $Q_{012}$  simulated data and the relative error.

changes at most by 1%.

# Chapter 4

## Results

In this chapter, we will discuss the results obtained from two high-power tests on OFE copper using the cavities described in Chapter 2. The first high-power test used the two-cavity setup described in Section 2.2.1. In the second high-power test, we used the one-cavity setup described in Section 2.2.2.

### 4.1 First Test

A picture of the test setup is shown in Figure 4.1. We used an XL-3 50 MW klystron for the high-power RF source. Although the tube is capable of producing 1.5  $\mu$ s pulses, we were limited to 1.25  $\mu$ s pulses due to rounding of the RF pulse by the modulator. The repetition rate is 60 Hz.

We experienced extensive RF breakdown at the coupling irises and were required to surround the cavity structures with 2-inch lead bricks. Because of this breakdown, we limited the input power to each cavity to 8.5 MW and accumulated pulses at this setting. The vacuum in the cavities was approximately between  $10^{-9}$  Torr and  $10^{-8}$  Torr.

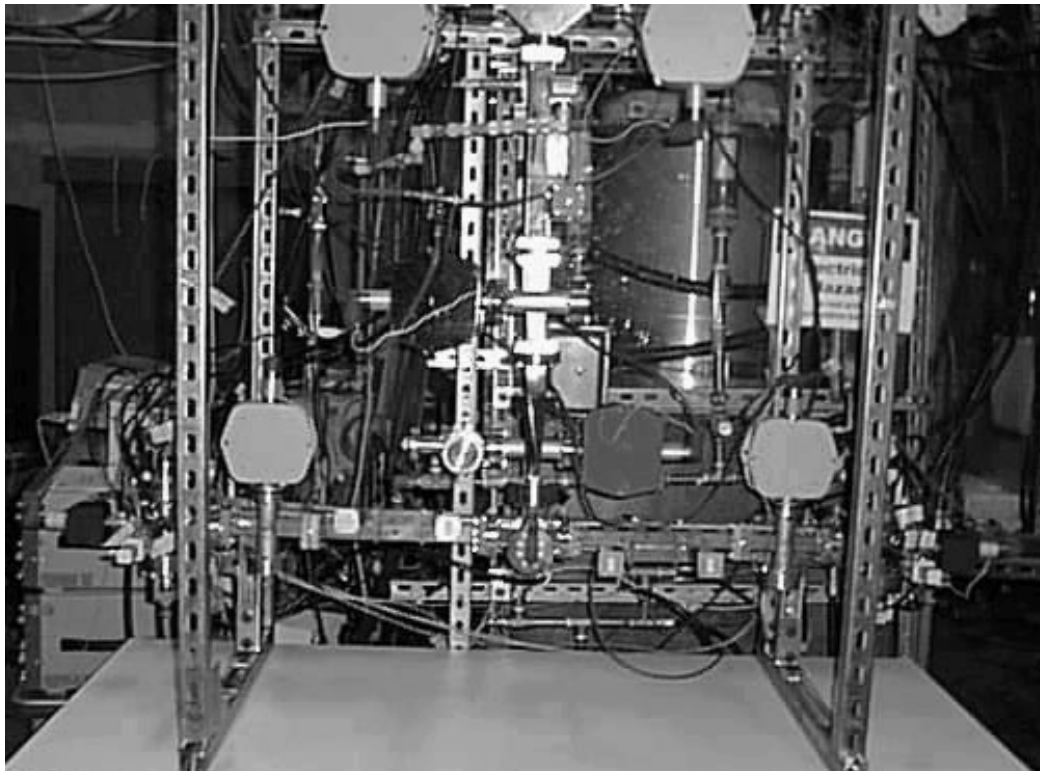


Figure 4.1: A picture of the two-cavity setup attached to the klystron. The XL-3 klystron is seen in the background. The cavities are on the left and right of the setup in the lower part of the picture.

### 4.1.1 Run-Up Procedure

As described in Section 2.2, the input power to the cavities must be raised slowly due to outgasing from the copper surface and RF breakdown. The entire experimental run occurred over a two-month period. It took approximately two weeks to reach 8.5 MW to each cavity. Although the power to each cavity could eventually be raised over time, we decided to stay at one power level for two reasons. First, the amount of time required to raise the power further became prohibitive. Second, it was desirable to accumulate high-power pulses at one temperature rise to minimize the effects of cyclic fatigue from multiple stress levels. We stayed at 8.5 MW because we considered calculated temperature rises over 100 K to be interesting.

During the experiment, the cavities were tuned to each other in such a way that their resonant frequencies would match after thermal expansion due to average heating. Using equation (2.15) with  $\beta = 1.7$ ,  $P_{peak} = 8.5$  MW,  $T_p = 1.25$   $\mu$ s and  $f_{rep} = 60$  Hz, the total power dissipated in the cavities is approximately 595 W. This assumes the RF pulse is a flat-top. Looking at Figure 4.4, the input pulse is actually rounded. Therefore, this approximation represents an upper-bound on the average temperature rise.

Following the discussion in Section 2.1.6, the maximum temperature rise due to average heating on the endcap surface is calculated to be approximately 10 K. The maximum temperature rise due to average heating on the cylindrical sidewall is approximately 9 K. The cavity frequencies decreased around 4 MHz at full power giving a ratio of 6.7 kHz/W. According to equation (2.31), the sensitivity of the cavity resonant frequency to length changes in the radial or axial direction is approximately  $-7$  MHz for every 25  $\mu$ m increase in dimensions. Cavity 2 shifts an additional 400 kHz more than cavity 1 due to average heating which represents a change of less than 10%. This may be due to small differences in the flow of water to each cavity.

### 4.1.2 Measurement of RF Power

As described in Section 2.2, attached to the high-power coupler of each cavity is a 55-dB directional coupler. Directional couplers allow the measurement of forward and

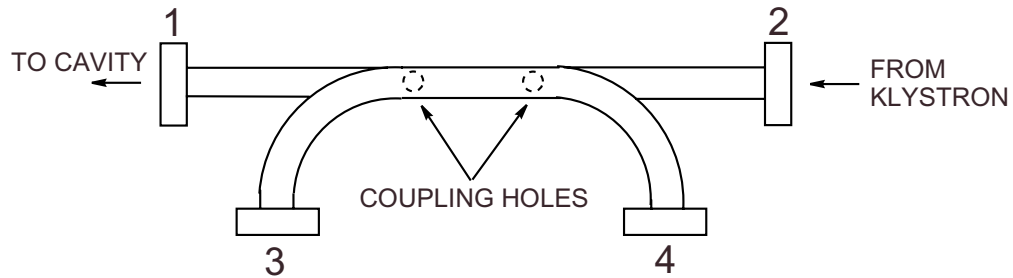


Figure 4.2: Schematic of a 55-dB directional coupler. Port 1 is connected to the input of the test cavity and Port 2 is the input from the klystron.

reflected power from the cavity by coupling a small amount of power to a side-coupled waveguide. In this case, the amount of coupling is small enough such that the loss of power to the cavity is less than 0.1 dB. A schematic of a directional coupler is shown in Figure 4.2.

Power is coupled to the coupling arm of the directional coupler through apertures cut along the broad wall of the waveguide. Looking at Figure 4.2, the length between the coupling holes of the directional coupler is chosen such that most of the power coupled to port 4 is from port 1 and most of the power coupled to port 3 comes from port 2. For a 55-dB directional coupler, the isolation between ports 1 and 3 and ports 2 and 4 is approximately 90 dB. Since these couplers are to be operated under vacuum for high power, ports 3 and 4 have RF vacuum windows that are matched at 11.424 GHz.

Forward power measurements are important for two reasons. First, using the formulas presented in Section 3.3, knowledge of the input power to each cavity allows us to calculate the maximum temperature rise on the surface. Second, as discussed in Section A.4.2, the coupling coefficient to each cavity may be determined in conjunction with the measurement of reflected power from the cavity.

The forward power to each cavity is measured at port 3 of the directional coupler with the use of a crystal detector. Depending on the detector, the maximum power a crystal detector can measure without damage is approximately +10 dBm. Since 8.5 MW corresponds to 99.3 dBm, we must add additional attenuation to the

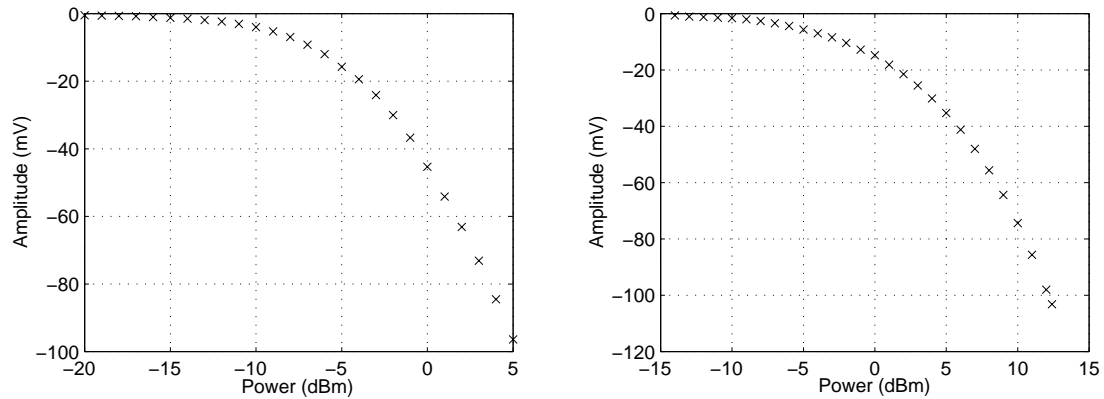


Figure 4.3: Crystal detector calibrations for the forward power (left) and the reflected power (right) for cavity 1.

directional couplers. The additional attenuation comes from cross-guide couplers, which are waveguide-couplers that behave similarly to directional couplers, and coaxial attenuators. The coaxial attenuators are added after using waveguide-to-coaxial adapters. 16 GHz low-pass waveguide filters are also added to the cross-guide couplers to eliminate higher harmonics of the klystron frequency.

The parameters of the above components used in the experiment were measured with a HP8510C network analyzer. Since the network analyzer cannot measure over 100 dB of attenuation with reasonable accuracy due to noise, the components must be measured separately. When the network analyzer is calibrated with isolation and averaging, the error in the measurement of the coupling of the directional coupler is  $\pm 0.2$  dB. The same error occurs with the measurement of the cross-guide couplers with coaxial attenuators attached. Adding the errors in quadrature, the total error for the measurement of forward power is  $\pm 0.3$  dB. This error is systematic because all measurements of forward power will have the same discrepancy.

There is also random error in the measurement of forward power. The output voltage of the crystal detectors is calibrated with a known RF power close to the frequency at which a measurement is taken. Figure 4.3 shows the calibration curves for the crystal detectors used to measure the forward and reflected power to cavity 1. The amplitude of the waveforms are converted to power using cubic interpolation of the crystal calibrations. The noise from the klystron modulator adds a random

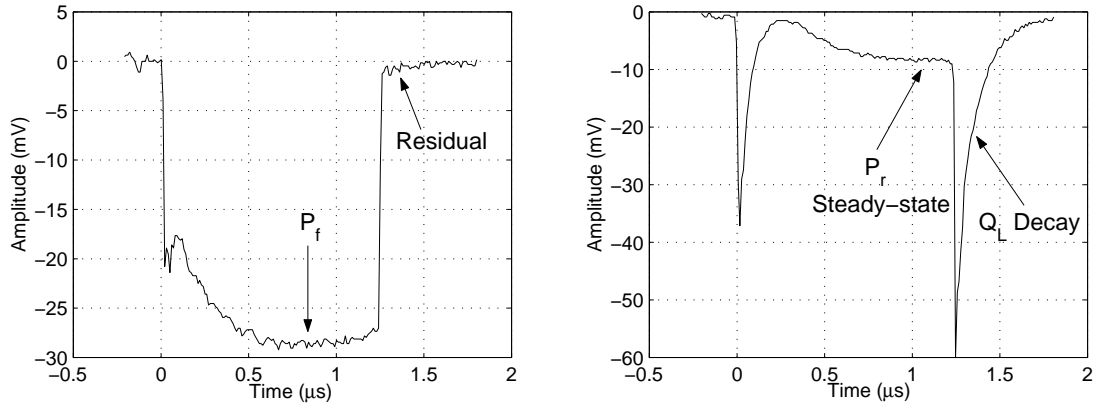


Figure 4.4: Forward and reflected high-power waveforms for cavity 1 from the first high-power test.  $P_f$  and  $P_r$  are the forward and reflected powers measured in steady-state respectively. “Residual” is the residual forward power after the RF pulse turns off due to mismatches along the waveguide line.

error of approximately 0.5 mV to the output of the detector. This error in voltage is converted to an error in power using the calibration curves for the crystal detectors. The error will depend on the crystal amplitude. Since the power in units of dBm varies logarithmically with crystal voltage, smaller voltages will result in larger errors in power.

A typical forward power waveform is shown on the left of Figure 4.4. Notice that the forward power waveform is not a perfect square wave. This is due to the mixing of the reflected power from the cavities with the forward power. This mixing will be explained in more detail in Section 4.1.3. However, notice that there seems to be an exponential filling time to reach full power. Since saturation occurs at approximately 5 filling-times, the filling time for this process is approximately  $0.6 \mu\text{s}/5 = 0.12 \mu\text{s}$ . This is in rough agreement with the filling-time of  $0.14 \mu\text{s}$  for the cavities at the end of the high-power test. It will also be shown later in Section 4.1.3 that this has negligible effects on the measurement of the coupling coefficient and loaded  $Q$  for each cavity.

The reflected power from each cavity is measured at port 4 of the directional couplers. A typical reflected waveform is shown on the right of Figure 4.4. The first peak in the figure occurs when the RF turns on and the second peak occurs when the RF turns off. The measurement of reflected power is important for two reasons.

Cavity	Initial $Q_0$	Final $Q_0$	Initial $Q_L$	Final $Q_L$
1	$20350 \pm 520$	$14360 \pm 300$	$7670 \pm 110$	$5010 \pm 50$
2	$20610 \pm 530$	$16810 \pm 260$	$7670 \pm 110$	$5010 \pm 50$

Cavity	Initial $\beta$	Final $\beta$	Initial $Q_{ext}$	Final $Q_{ext}$
1	$1.65 \pm .06$	$1.87 \pm .05$	$12320 \pm 520$	$7690 \pm 260$
2	$1.69 \pm .06$	$2.36 \pm .07$	$12220 \pm 530$	$7140 \pm 250$

Table 4.1: Cavity Q measurements of cavity 1 and 2 using a HP8510C network analyzer before and after the first high-power test. The change in  $Q_{ext}$  is due to the increase in size of the high-power coupling apertures.

First, the reflected power waveform is needed to determine the resonant frequency of each cavity. The amplitude of the steady-state part of the waveform before the RF pulse turns off is at a minimum at the resonant frequency of the cavity. Second, the coupling coefficient and the loaded Q for each cavity can be measured from this waveform.

As with the measurement of forward power, there are systematic and random errors involved with the measurement of reflected power. Although cross-guide couplers are also used, the total systematic error is  $\pm 0.2$  dB. We are using less attenuation to measure the steady-state part of the reflected waveform more accurately. Of course, the random errors in power will vary with crystal amplitude.

### 4.1.3 High-Power Results

Table 4.1 gives the values of the cavity Q's measured with a HP8510C network analyzer before the start of the high-power test. Using the values given in Table 4.1 with an 8.5 MW, 1.25  $\mu$ s pulse in the equations presented in Section 3.3.2 gives a temperature rise of 120 K  $\pm 10$  K. The error in the calculated temperature rise comes from the range of input power due to systematic error, 8.5 MW  $\pm 0.6$  MW. At this power level, the error is dominated by systematics. Consequently, the temperature rise on the cylindrical sidewall is 60 K  $\pm 5$ K (see Section 2.1.2).

The experiment was run at the temperature rise of 120 K for  $5.6 \times 10^7$  pulses. Afterwards, the cavities were removed from the test setup and their Q's were measured

with a network analyzer. The results are given in Table 4.1. Both the unloaded and the external Q's are lower than their initial values for each cavity. These changes are explained in Section 4.1.5.

The coupling coefficient  $\beta$  and loaded Q of each cavity were determined throughout the experiment by measuring the forward and reflected power to and from each cavity in the time domain. The typical shape of these waveforms is shown in Figure 4.4. The amplitudes of these waveforms are converted to power using the known calibrations of the crystal detectors.

The coupling coefficient is essentially determined by the ratio of the reflected to forward power in steady-state. Steady-state occurs near the end of the RF pulse when the cavities have been filled with energy longer than 5 fill-times. When the RF pulse turns off, the power decays out of each cavity exponentially at a rate proportional to  $1/Q_L$ .  $Q_L$  is found by fitting this decay curve to an exponential. These measurement points are shown in Figure 4.4. Refer to Section A.4.2 for more background on these measurements.

### Measurement of Coupling Coefficient

The coupling coefficient for each cavity is determined by measuring the forward and reflected power in steady-state at the points indicated by  $P_f$  and  $P_r$  in Figure 4.4 respectively. Using equation (A.133) and assuming the cavity is filled by the end of the pulse ( $t \rightarrow \infty$ ), the reflected power is simply

$$P_r = \left( \frac{\beta - 1}{\beta + 1} \right)^2 P_f. \quad (4.1)$$

Using the parameters in Table 4.1 with a pulse length of 1.25  $\mu\text{s}$  shows that the error in the assumption  $t \rightarrow \infty$  is less than 0.1%. Solving this equation for  $\beta$  gives

$$\beta = \frac{1 \pm \sqrt{\frac{P_r}{P_f}}}{1 \mp \sqrt{\frac{P_r}{P_f}}}, \quad (4.2)$$

where the upper sign is for  $\beta > 1$  and the lower sign is for  $\beta < 1$ . Since the height of the second peak in the reflected waveform is higher than the height of the first peak,  $\beta > 1$  (see Section A.4.2).

We also discussed earlier the fact that the forward power is not a perfect square-wave. In the analysis used in Section A.4.2, we assumed  $\tilde{V}_1^+$  is constant. Looking at Figure 4.4, we may model the waveform as filling from some initial power level to the final desired power level. We will assume that the filling-time is equal to that of the cavities at the end of the high-power test. Thus we write

$$\frac{\tilde{V}_1^+}{\tilde{V}_{1,0}^+} = A_1 + A_2 (1 - e^{-t/\tau}), \quad (4.3)$$

where  $\tilde{V}_{1,0}^+$  is the desired voltage ( $\propto \sqrt{P}$ ),  $\tau$  is the filling-time, and  $A_1$  and  $A_2$  are ratios such that  $A_1 + A_2 = 1$ . In Figure 4.4, the rounding of the input power occurs over a range of 2 dB corresponding to 80% of full power. Hence,  $A_1 = 0.8$  and  $A_2 = 0.2$ . If we drive the cavity at its resonant frequency and use equation (4.3) in equation (A.129) with the continuity condition  $\tilde{V}_1^- = \tilde{V}_C - \tilde{V}_1^+$ , then the reflected power normalized to the forward power is

$$\left| \frac{\tilde{V}_1^-}{\tilde{V}_{1,0}^+} \right|^2 = \left| \frac{\beta - 1}{\beta + 1} - \frac{2\beta}{\beta + 1} e^{-t/\tau} - A_2 \frac{\omega}{Q_{ext}} t e^{-t/\tau} \right|^2. \quad (4.4)$$

This result is similar to the case where  $\tilde{V}_1^+$  is constant except for the last term on the right-hand side of equation (4.4). Using the final values given in Table 4.1 at the time where  $\beta$  is measured ( $t = T_p = 1.25 \mu\text{s}$ ) we find that the last term is smaller by three orders of magnitude than the first two dominant terms. Therefore, the effect of the rounding of the forward power on the measurement of  $\beta$  is negligible.

Before a measurement is done, the power from the klystron must be decreased below approximately 2 MW to each cavity to minimize the effects of pulsed heating on the cavity Q and the coupling coefficient. Also, the power must be high enough for the signal to have sufficient amplitude for reasonable error. However, at this power the cavities are no longer matched to each other. The consequence of this fact will

	Cavity 1	Cavity 2
$\beta_{low}$	$1.73 \pm .04$	$2.51 \pm .09$
$\beta_{nom}$	$1.79 \pm .04$	$2.68 \pm .11$
$\beta_{high}$	$1.85 \pm .05$	$2.87 \pm .12$
$\beta_{freq}$	$1.87 \pm .05$	$2.36 \pm .07$

Table 4.2: Measurement of coupling coefficients for cavities 1 and 2 in the time and frequency-domain at the end of the high-power test. The range of  $\beta$  is due to systematic errors in the measurement of power where  $\beta_{nom}$  is the nominal value. The errors listed for each value is due to random errors.  $\beta_{freq}$  is the value measured in the frequency-domain.

be shown later in this section.

The oscilloscope used to measure these waveforms, LeCroy 9314M, adds a small DC-offset to the signal amplitude that should be subtracted. Although the errors in the measurement of forward and reflected power due to noise depends on the crystal amplitude, all measurements were taken at roughly the same power level resulting in a constant error. Hence, for cavity 1, the average error in the measurement of forward power due to noise is approximately 0.1 dB. Likewise, the average error in the measurement of reflected power is 0.35 dB. For cavity 2, the average error in the measurement of forward power is 0.2 dB and the average error in the measurement of reflected power is also 0.2 dB. The variation in these errors is due to the different sensitivities of the crystal detectors.

We will compare the measurements in the time-domain for cavities 1 and 2 at the end of the high-power test with the measurements done in the frequency-domain. Table 4.2 presents the range of values measured for the coupling coefficient of cavities 1 and 2. The three different measured values of  $\beta$  in the time-domain for each cavity are due to the extreme ranges of the systematic errors in the measurement of forward and reflected power. The error given for each value of the coupling coefficients is due to random errors. The systematic errors dominate. Although the discrepancy between the accepted or nominal value for  $\beta$  in the time-domain and the value measured in the frequency-domain is approximately 4% for cavity 1 and 14% for cavity 2, the range of  $\beta$  due to errors in the time-domain is consistent with the measurement in

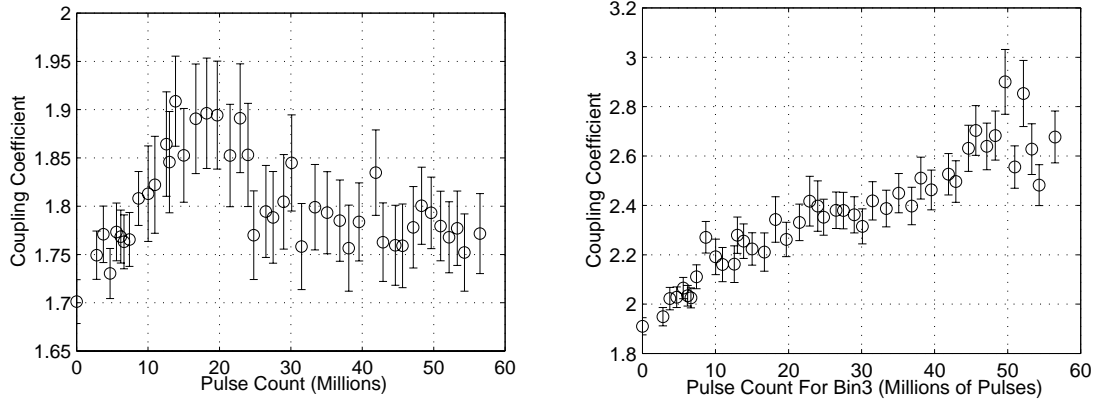


Figure 4.5: Variation of the nominal value of  $\beta$  for cavity 1 (left) and cavity 2 (right) as a function of pulse count at a 120 K temperature rise on the endcap surfaces. The errors shown are due to random errors only.

the frequency-domain.

The measurement of  $\beta$  as a function of pulse count for each cavity is shown in Figure 4.5. As described in Section 2.3.2, the pulse count is determined by digitizing the forward power waveform and binning it by power level into an event counter. Looking at Figure 4.5, we see that  $\beta$  increases quickly for both cavities in the first 10 to 20 million pulses. If damage is occurring on the surface of the cavity in the form of surface roughening and cracks, we expect  $Q_0$  to decrease due to the increase in electrical resistivity of the surface. Since  $\beta = Q_0/Q_{ext}$ , this suggests that  $Q_{ext}$  is decreasing in this pulse range since  $Q_0$  cannot increase. This is in agreement with the decrease in  $Q_{ext}$  presented in Table 4.1. The decrease in  $Q_{ext}$  is due to the increase in size of the coupling aperture of each cavity and is discussed in more detail in Section 4.1.5.

After 20 million pulses, there is a decreasing trend in  $\beta$  for cavity 1. This indicates a decrease in the value of  $Q_0$ . According to Table 4.1,  $Q_0$  for cavity 1 decreases by almost 30%, but Figure 4.5 shows only a 10% decrease in  $\beta$  starting at 20 million pulses. Also,  $Q_{ext}$  decreased by almost 40% according to frequency-domain measurements. This shows that  $Q_{ext}$  for cavity 1 likely decreased over the entire pulse range, competing with the degradation of  $Q_0$ .

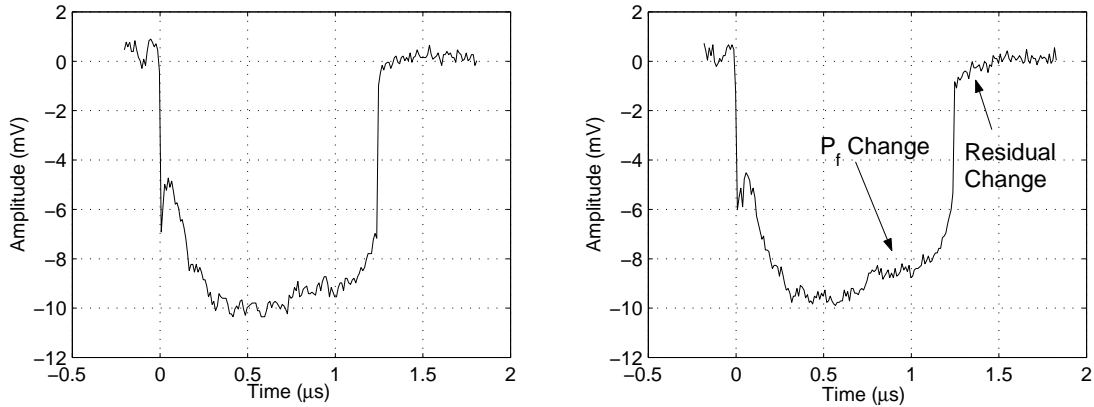


Figure 4.6: Forward power waveforms for cavity 2 at 32 million pulses (left) and at 56 million pulses (right). A change is visible in the region where  $P_f$  is measured and also in the “Residual” power.

Notice that for cavity 2,  $\beta$  generally increases over the entire pulse range. According to Table 4.1, cavity 2 suffered a 18% degradation in  $Q_0$  with over 40% degradation in  $Q_{ext}$ . This fact combined with Figure 4.5 indicates that the degradation in  $Q_{ext}$  dominated the change in  $Q_0$ , since  $Q_0$  is only expected to decrease over time. After 20 million pulses the variation in  $\beta$  is slight until after 40 million pulses have been reached. This suggests that in this region  $Q_0$  began to degrade while  $Q_{ext}$  did not degrade as much. However, after 40 million pulses there appears to be another sharp rise in  $\beta$ . Although this may be due to another sharp change in  $Q_{ext}$ , it is more likely due to additional measurement error.

Figure 4.6 shows forward power waveforms for cavity 2 recorded at 32 million pulses and at 56 million pulses when the experiment was stopped. There is an obvious difference in the shapes of these two waveforms. There is an ambiguity of the measurement of forward power depending on what point in the waveform the measurement is taken. This problem stems from the fact that the cavities are not matched to each other during the measurement process.

Ideally, the asymmetric magic-tee used to split the input power to the two cavities will cause the reflected power from the cavities to go to a load. From symmetry, this occurs only if the up-and-back transmission length between the klystron and each cavity represent a  $180^\circ$  phase shift between their fields and if the cavities have

identical properties. Even an ideal magic-tee with the correct phase shift at the correct frequency will not prevent reflected power going back to the klystron if the cavities are not matched to each other. In our case, the cavities not only become increasingly mismatched over time as shown in Figure 4.5, but one is driven off-resonance while the properties of the other cavity is measured.

The output cavity of the klystron is grossly over-coupled to provide high bandwidth for its output signal. Hence, the klystron is not matched to the magic-tee. The difference between the reflected power from the cavities will go to the klystron and reflect back to be split by the magic-tee again. This signal will interfere with the output power from the klystron. This causes a change in the actual forward power to each cavity and is not simply a measurement problem.

From the data, it appears that only cavity 2 is affected by this problem. Mismatches between the cavity and the magic tee will cause a slight detuning of the cavities. Hence, a measurement of  $\beta$  will occur slightly off-resonance causing the measured  $\beta$  to move farther away from 1 than the actual value. It is likely that a stronger mismatch occurred on the side with cavity 2 over time than on the side with cavity 1. Figure 4.5 indeed shows that the measured value of  $\beta$  for cavity 2 is higher than compared to the measurement in the frequency domain.

Overall, each cavity suffered extensive degradation in their values of  $Q_0$  and  $Q_{ext}$ . Although damage most likely occurred to the coupling aperture of each cavity over the entire pulse range, it would appear that the damage became less extensive over time due to the slower variation of  $\beta$  in the last half of the experiment. This corroborates the fact that RF breakdown became less of a problem at this power level over time. In the last half of the experiment there was no measurable outgassing and the disruption of the forward and reflected waveforms due to RF breakdown occurred less frequently. As will be discussed in Section 4.1.6, we know that breakdown occurred at the coupling apertures of each cavity.

After 20 million pulses it appears that degradation of  $Q_0$  for each cavity dominated the change in  $\beta$ . Cavity 1 suffered a greater degradation in  $Q_0$ , causing  $\beta$  to eventually decrease over time. However, the degradation of  $Q_0$  for cavity 2 was not enough to overcome the change in  $Q_{ext}$  and only caused  $\beta$  to increase less swiftly.

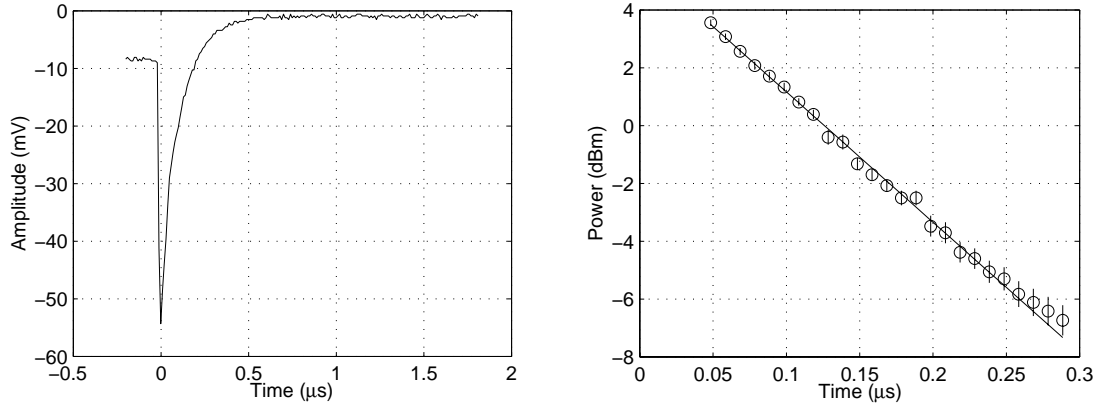


Figure 4.7: Reflected waveform from cavity 1 at the end of the first high-power test. The fit of the waveform using linear least-squares is on the right.

The measurement of loaded  $Q$ ,  $Q_L$ , for each cavity combined with the measurement of  $\beta$  isolates the values of  $Q_0$  and  $Q_{ext}$ . However, the problem with the mismatched cavities described earlier also affected the results for  $Q_L$ . As will be described in the next section, this made it difficult to conclude how  $Q_0$  degraded over time for each cavity.

### Measurement of Cavity $Q$

The loaded  $Q$  of each cavity can be determined from the reflected waveform using the method described in section A.4.2. The decay of the power leaking out of the cavity after the RF is turned off is fit to an exponential to find the loaded  $Q$ . As an example, the reflected waveform for cavity 1 on the right of Figure 4.4 will be analyzed in detail. A close-up of this waveform is shown in Figure 4.7. As with the measurement of  $\beta$ , the DC-offset in the oscilloscope is subtracted first. Then the amplitude is converted to power by interpolation of the crystal calibration curve. The first few points near the peak of the amplitude are ignored, because the crystal may not accurately represent the spike that occurs when the RF is shut off. The points near zero amplitude are also ignored due to the large error in the conversion to power.

	Cavity 1	Cavity 2
$Q_{L,time}$	$6910 \pm 110$	$7180 \pm 70$
$Q_{L,freq}$	$5010 \pm 50$	$5010 \pm 50$

Table 4.3: Comparison of measurement of  $Q_L$  for cavities 1 and 2 in the time and frequency-domain at the end of the first high-power test.

From equation (A.136), the reflected power is parameterized as

$$P_r = A \exp\left(-\frac{\omega_0 t}{Q_L}\right), \quad (4.5)$$

where  $A$  is a constant. Since energy is simply decaying out of the cavity after the RF turns off, the rounding of the forward power waveform has no effect on the measurement of  $Q_L$ .

The amplitude of the crystal detector is converted to power in dBm, so it is useful to convert equation (4.5) to dBm

$$P_r[\text{dBm}] = B - 10(\log e)\frac{\omega_0}{Q_L}t, \quad (4.6)$$

where  $B$  is a constant. This equation may be fit using linear least-squares. The fit is shown on the right of Figure 4.7. The results of the fit are presented in Table 4.3 along with the result for cavity 2. The error in the fit is due to the assumed error of approximately 0.5 mV in determining the amplitude because of noise. The systematic error due to the calibration of the 55-dB directional couplers is ignored since the determination of absolute power is not necessary.

The discrepancies between the measurements of  $Q_L$  in the time and frequency-domains for cavities 1 and 2 are 38% and 43% respectively. These discrepancies are likely due to the mismatch of the cavities with respect to each other and the mismatch of the klystron output cavity to the magic-tee. As with the measurement problem of the coupling coefficient, a portion of the reflected power from each cavity will reach the klystron output cavity due to the mismatch of the test cavities. Although the RF is off, the klystron output cavity will fill and emit power using the reflected power

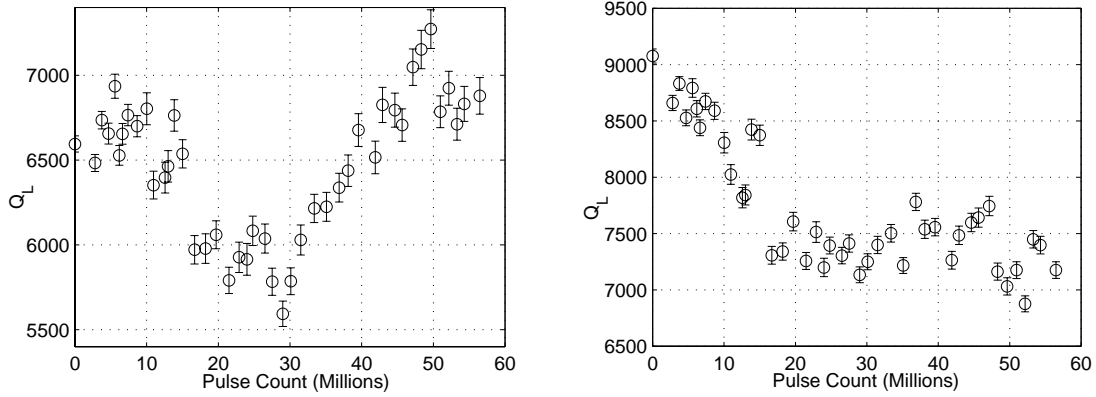


Figure 4.8:  $Q_L$  for cavity 1 (left) and cavity 2 (right) as a function of pulse count for a 120 K temperature rise on the endcap surfaces.

from the test cavities as an input. This can be seen in the forward power waveform in Figure 4.4 as residual power after the RF pulse turns off. The level of residual power changes over time as the properties of the cavities change as can be seen in Figure 4.6. The emitted power from the klystron output cavity will have a characteristic decay due to its loaded  $Q$ . This emitted power will travel back to the cavities and fill them causing them to re-emit power. Hence, the overall measured reflected power from each cavity will involve the mixing of characteristic decays of both test cavities and the klystron output cavity.

Figure 4.8 shows the measurement of  $Q_L$  for each cavity versus pulse count. Notice that there are large discrepancies between the measurements in the time and frequency-domain even at the beginning of the high-power test when the cavities were almost identical. This is due to the fact that one cavity is driven half a  $Q$ -bandwidth off resonance while the properties of the other cavity is measured. Both cavities show a degradation in  $Q_L$  for the first 30 million pulses. However,  $Q_L$  increases in cavity 1 after 30 million pulses almost back to its beginning value at the end of the high-power test. Since we know that  $Q_{ext}$  must be decreasing over time due to the increase in size of the coupling aperture,  $Q_0$  would have to increase in order for  $Q_L$  to increase. This is the opposite of what we expect to occur from surface damage. We believe these measurements do not correctly reflect the change in the properties of the cavities over time because of the interference that results from the measurement of reflected power

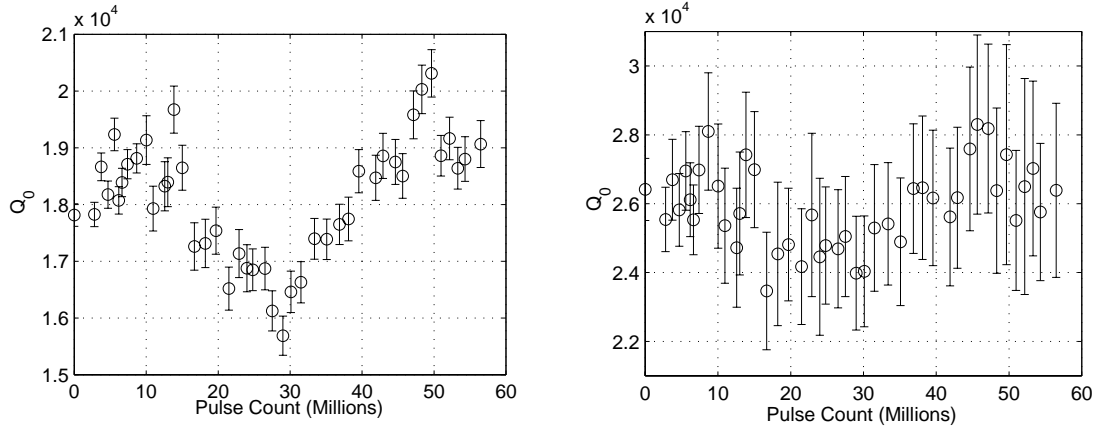


Figure 4.9:  $Q_0$  for cavity 1 (left) and cavity 2 (right) as a function of pulse count for a 120 K temperature rise on the endcap surfaces.

due to the mismatch of the cavities with respect to each other.

Figure 4.9 shows the value of  $Q_0 = Q_L(1 + \beta)$  for each cavity versus pulse count. The discrepancies between the measurement of  $Q_0$  in the time and frequency-domain at the end of the high-power test are large (30% for cavity 1 and 60% for cavity 2.) The estimation of the errors do not account for such large discrepancies. Also, both cavities display behavior that is contrary to what we expect to occur during damage. Figure 4.9 shows that  $Q_0$  for cavity 1 increases after 30 million pulses and  $Q_0$  for cavity 2 did not change much during the entire pulse range. We only expect  $Q_0$  to decrease.

In conclusion, measurements of the properties of the cavities in the frequency-domain conducted at the beginning and end of the data taking run show degradation in both  $Q_0$  and  $Q_{ext}$  for both cavities. The measurements of  $\beta$  in the time-domain are consistent with measurements taken with a network analyzer when the systematic errors due to the calibration of the couplers are considered. Hence, Figure 4.5 seems to be a good indication of the change in the properties of the cavities over time. This is reasonable since the mismatch of the test cavities and the klystron will change the actual forward power to each cavity. This will change the steady-state reflected power from each cavity by the same ratio and should not affect the determination of  $\beta$ . However,  $Q_L$  is determined by fitting an exponential to the decay of power out of

each cavity after the RF pulse turns off. Due to the mismatches of the test cavities and the klystron described above, the characteristic decays from each test cavity and the klystron output cavity will be mixed. The measurement of  $Q_L$  will be affected and the large discrepancies between the time and frequency domains indicate that the measurement of  $Q_L$  in the time domain is unreliable. Hence, the variation of  $Q_0$  and  $Q_{ext}$  over time cannot be properly isolated.

#### 4.1.4 Endcap Removal

At the end of the high-power test, the vacuum in the cavities was broken with a nitrogen purge. The cavity properties were measured with a network analyzer; the results are given in Table 4.1. The pistons with the endcaps attached were removed from the cavities, and the endcaps were carefully removed from the pistons using a lathe (see Section 2.1.5). The surface of the endcaps were protected with a ceramic cover at all times, and all parts were handled with gloves and covered with aluminum foil that was cleaned for vacuum. Afterwards, the surfaces of the endcaps were inspected visually and with a scanning electron microscope. The inner cross-section of one endcap was also inspected. See Table 2.3 for the preparation of the surfaces of the copper endcaps for the high-power test.

Each endcap is labeled uniquely with a three character designation. The first character is the cavity number. The second character is  $L$  or  $R$  whether the endcap is on the left or the right side of the cavity looking from the high-power coupler. The last character is the test number. For the first high-power test, the endcaps are labeled  $1L1$ ,  $1R1$ ,  $2L1$  and  $2R1$ . For the second high-power test, the endcaps are  $1L2$  and  $1R2$ .

#### 4.1.5 Visual Inspection of Copper Endcap Surface

Each copper endcap is made from polycrystalline OFE copper. This means the structure at the surface is made from crystal grains whose lattices are oriented in a generally random direction with respect to each other. This is not completely true due to the nature of how the copper material was formed, but it is a good approximation for our

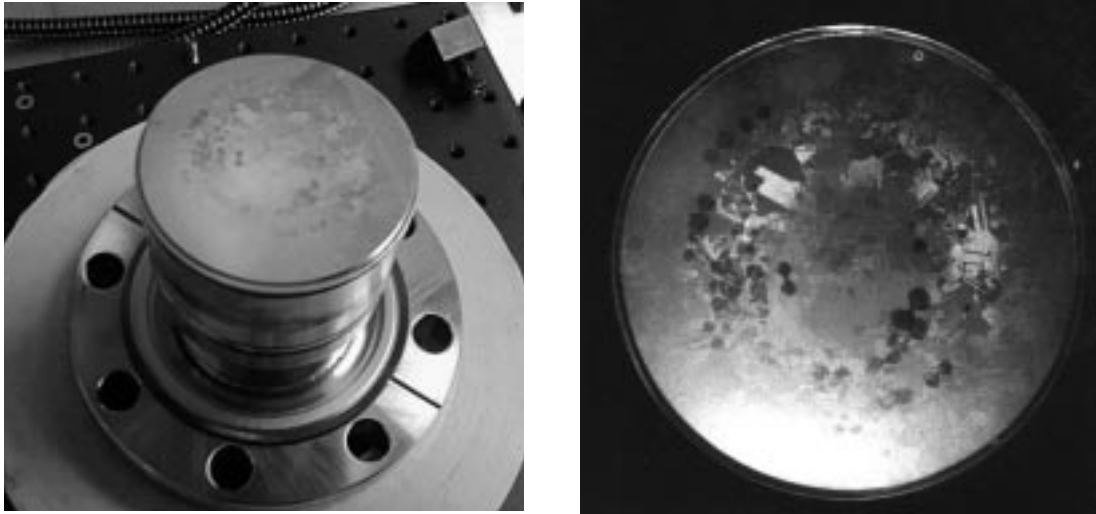


Figure 4.10: Picture of endcap 2L1. A change in the crystal grains is visible even in the region where the temperature rise was lower by 10% as explained in the next section. The tarnish from the sputtering of copper is on the lower part of the endcap.

study. The intersections of these grains are known as *grain boundaries*.

A visible change in the surface of all four endcaps is obvious with the naked eye. Figure 4.10 shows endcap 2L1 still attached to a piston as well as a snapshot from the top. In both of these pictures an obvious change in the crystal grains is visible in the region where the temperature rise is maximum, which is approximately half-way between the center and the outer radius of the endcap. In this area in which there is high-amplitude cyclic straining, steps may form in crystal grain boundaries with height differences on the order of  $\mu\text{ms}$  [7, p. 126]. This would change the direction of light specularly reflected from the surface, which will cause a contrast between the grains in the fatigued area compared to the rest of the surface.

### **Tarnish**

Also visible is a tarnish of the surface. The tarnish is thicker at the outer radius and at the azimuth closest to the high-power coupling aperture. The next section will show that the tarnish is due to copper globules. These copper globules were sputtered onto the surface of the endcaps from fatigue damage and RF breakdown that occurred at the high-power coupling aperture. Because these copper globules may add to the

surface roughness of the cavity, we cannot conclude that the degradation in  $Q_0$  shown in Table 4.1 is completely due to cracks from pulsed heating. However, the table also shows that the aperture for cavity 2 changed more than cavity 1 yet cavity 1 suffered a larger  $Q$  degradation. This would indicate there is no direct correlation between the amount of aperture damage and the amount of  $Q$  degradation.

### Multipacting

Also visible on the endcap surface are black patches that appear on the half of the endcap that is closest to the coupling aperture. We believe these patches are due to multipacting since they occur mostly in pairs. Since the magnetic field is radial at the endcap surface, electrons emitted from the surface will orbit around the magnetic field lines. At the time that the electron comes back to the surface to cause another electron to be emitted, the magnetic field goes through  $180^\circ$  phase shift to allow the next emitted electron to travel on a reverse trajectory. Thus one electron must complete an orbit in one-half of an RF period. This restricts the energy of the electrons.

If we assume a perfectly semi-circular orbit for the electron, then equating the centripetal force with the force from the magnetic field gives

$$H = \frac{m_e v}{\mu e r_e}, \quad (4.7)$$

where  $m_e$  is the mass of the electron,  $v$  is the electron's velocity and  $r_e$  is the radius of its orbit around the magnetic field. Since the orbit must be completed in one-half of an RF period

$$v = \frac{\pi r_e}{\frac{T_{RF}}{2}} = 2\pi r_e f_{RF}, \quad (4.8)$$

where  $T_{RF}$  is the RF period and  $f_{RF}$  is the RF frequency. Thus the strength of the magnetic field must be

$$H = \frac{2\pi f_{RF} m_e}{\mu e}. \quad (4.9)$$

For  $f_{RF} = 11.424$  GHz,  $H = 0.32$  MA/m. Using the initial values given in Table 4.1 with an 8.5 MW, 1.25  $\mu$ s pulse, the maximum magnetic field on the surface of the

endcap is 0.47 MA/m. This is in good agreement with the previous result considering that the actual orbit of the electron will not be perfectly circular. The azimuthal electric field will affect the electron trajectory, thus affecting the required magnetic field.

On average, the distance between each pair of patches on the surface is approximately 2 mm which gives  $r_e = 1$  mm. If we continue to use the assumption that the orbit is perfectly semi-circular, then equation (4.8) gives a kinetic energy of 15 keV for the electron. It is possible for the electron to receive such energy from the azimuthal electric field. The maximum electric field occurs at the same radius in the cavity as the surface magnetic field on the endcap, but in the middle of the cavity at  $z=0$ . For the above parameters, the maximum field strength is approximately 260 MV/m. Therefore, the electron with an orbital radius of 1 mm will experience an electric field strength of approximately 40 MV/m at its maximum excursion from the surface of the endcap. However, a perpendicular electric field is required on the endcap for an electron to be emitted from the surface. A perfect  $TE_{011}$  mode will only have azimuthal electric fields. It is likely that a tilt of the surface of the endcap due to a misalignment of the vacuum flanges of the piston and the cavity caused a small perpendicular component of the electric field to occur on the surface.

According to a GdfidL simulation in the time-domain, the maximum magnetic field on the endcap closest to the azimuth of the high-power coupling aperture is approximately 5% higher than on the spot diametrically opposite of it. Since multipacting only occurs over a small range of energies, this may explain why dark patches are only seen on one half of the endcap. That half of the endcap is the half closest to the high-power coupling aperture.

#### 4.1.6 Damage to High-Power Coupling Aperture

In Figure 4.11, we see the high-power coupling aperture of cavity 1 after the first high-power test. The magnetic field is in the up-down direction of the picture and the electric field is in the left-right direction near the aperture. The aperture is rounded in the direction of the magnetic field, which suggests the damage is due to heating.



Figure 4.11: A picture of the high-power coupling aperture of cavity 1 after the first high-power test. Near the aperture, the magnetic field is in the up-down direction and the electric field is in the left-right direction. The aperture has been rounded in the up-down direction, and pitting has occurred to the left and the right of the aperture.

According to simulations using HFSS [2], which solves for the fields in steady-state, the magnetic field at the edge of the aperture is approximately 0.7 MA/m for an input power of 8.5 MW. The maximum magnetic field on the endcap at this power is approximately 0.5 MA/m. Therefore the temperature rise is almost twice as high on the coupling aperture than on the endcap. The electric field on the aperture is approximately 85 MV/m, which is sufficient to cause RF breakdown.

A likely explanation of the damage to the coupling aperture is fatigue due to pulsed heating. As cracks develop in the aperture region, the heating will increase due to the larger electrical resistivity. The increased heating will cause more cracks to develop and increase the size of cracks that already exist. Eventually, local melting will result. Metal will evaporate and spray from these cracks [23, Ch. 7]. The aperture increased in size on the cavity side which explains the drop in external  $Q$  shown in Table 4.1.

Although the copper endcaps were the main test pieces of the pulsed heating experiment, the damage that occurred at the high-power coupling apertures sets another limit. It shows that a temperature rise of approximately 250 °C will cause extensive damage after 50 million pulses. The damage occurred before this time, but we could not accurately assess the time at which the damage became significant as

shown in Figure 4.11.

### 4.1.7 Internal Cross-Section

Endcap 2L1 was cut along a diameter and polished to view the cross-section. Magnified scans were taken at the center of the endcap and in the region in which the maximum temperature rise occurred. No cracks were found in the center of the endcap where the temperature rise is close to zero. Less than 10 cracks are visible in the region of maximum temperature rise at magnifications up to 1000, and only 2 cracks are longer than 10  $\mu\text{m}$ . Figure 4.12 shows both of these cracks. These cracks were first created at the surface and then propagated internally, because higher stresses and strains occur at the surface than in the interior of the metal [22, p. 66]. Once cracks nucleate at the surface, stress is amplified near the crack tips leading to further crack propagation. However, only a few cracks will actually propagate internally to cause fracture as compared to the amount of cracks that are nucleated at the surface. As will be shown in Section 4.1.8, many cracks do occur on the surface as compared to internal cracks.

The crystal lattice structure of copper is face-centered cubic. This configuration contains 12 slip planes, which are planes at which the atoms can move most easily along one another in the lattice. Microcracks nucleate due to slip processes and lie predominantly along slip planes [7, p. 59]. Slip occurs when the shear stress along a slip plane is above a critical value[49, Sec. 6.2.3]. Slip may be seen as striations on the surface and some examples will be shown in Section 4.1.8. In the case of the copper endcaps, the normal stress axis occurs parallel to the surface; therefore, the maximum shear stress occurs along a plane inclined at  $45^\circ$  to the copper surface as shown in Figure 4.13. For polycrystalline copper, only grains that have slip planes oriented close to this angle will show slip if the stress is large enough.

Notice in Figure 4.12 that the two large cracks begin propagating at roughly  $45^\circ$  to the surface within the first few  $\mu\text{m}$  into the surface. This is known as Stage I crack propagation where cracks will propagate along the slip plane. Stage II crack

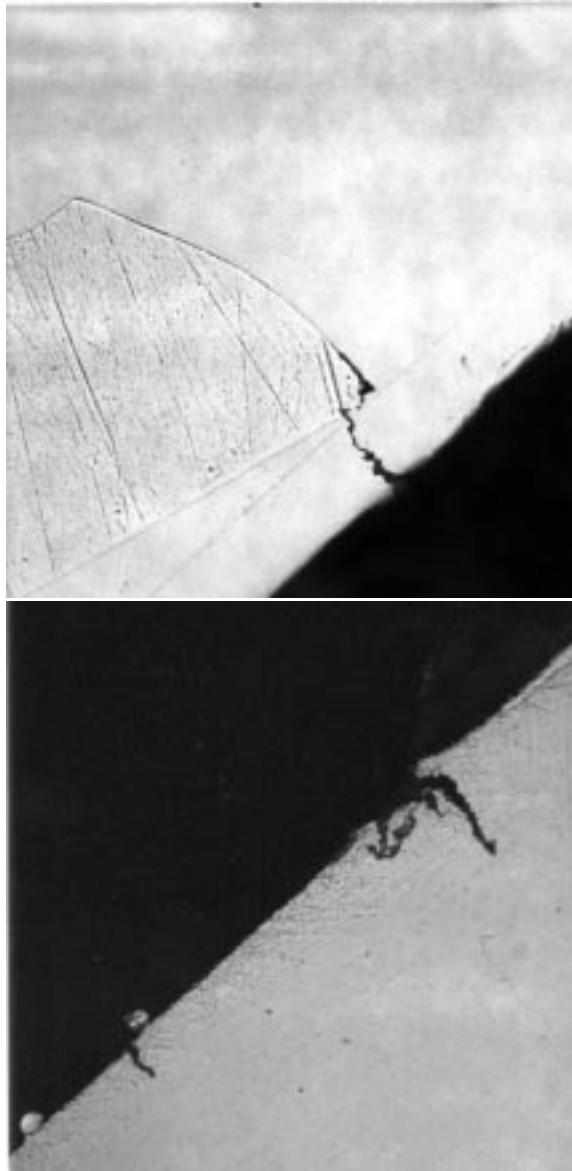


Figure 4.12: An internal cross-section of endcap 2L1 in the region of maximum temperature rise on the surface. The endcap surface is the boundary between the white and black regions of the pictures. The crack on the top propagated  $25\ \mu\text{m}$  into the surface before reaching an internal grain boundary. The crack on the bottom propagated  $15\ \mu\text{m}$  into the surface.

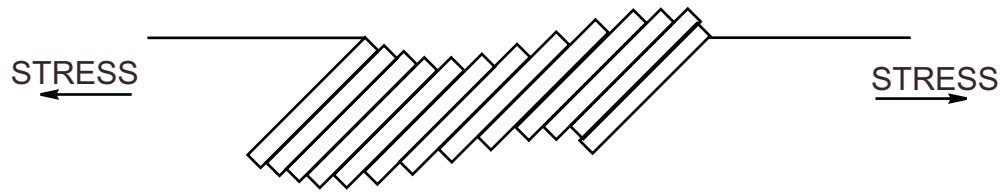


Figure 4.13: A schematic of the creation of intrusions and extrusions on the surface due to fatigue slip bands. The slip bands are at an interior angle of  $45^\circ$  due to stress in the lateral direction.

propagation occurs when the cracks propagate perpendicular to the surface and perpendicular to the stress axis [7, p. 60], which is also shown to occur in Figure 4.12. Fracture of specimens occur due to the propagation of Stage II cracks. Since the depth of the copper endcaps is 3 mm and the longest crack shown is  $25\ \mu\text{m}$ , fracture would not occur for some time but may be inevitable at this stress level.

#### 4.1.8 Scanning Electron Microscope Inspection of Copper Endcap Surface

Each endcap was inspected with a scanning electron microscope (SEM) using secondary scattering with a 5 kV beam. First, scans were taken along a random diameter of each endcap. Cracks are only visible in the region where the maximum heating occurred at a radius of 10.6 mm. The thickness of this region is approximately 4 to 5 mm for each endcap. No other damage is visible on the surface except at the region where the fields scattered from the diagnostic coupling aperture. This only occurred on endcaps 1R1 and 2R1 because they are nearest to the diagnostic coupling aperture.

Second, scans were taken around the region of maximum heating at different magnifications. One such region is shown on the left of Figure 4.14. Numerous cracks are visible on the surface of endcap 1L1. The bumps that occur on the surface are due to copper globules being sputtered onto the endcaps from the coupling aperture. For comparison, the center of the endcap is shown on the right of Figure 4.14. No cracks are visible in the center where the temperature rise is close to zero. A few close-ups

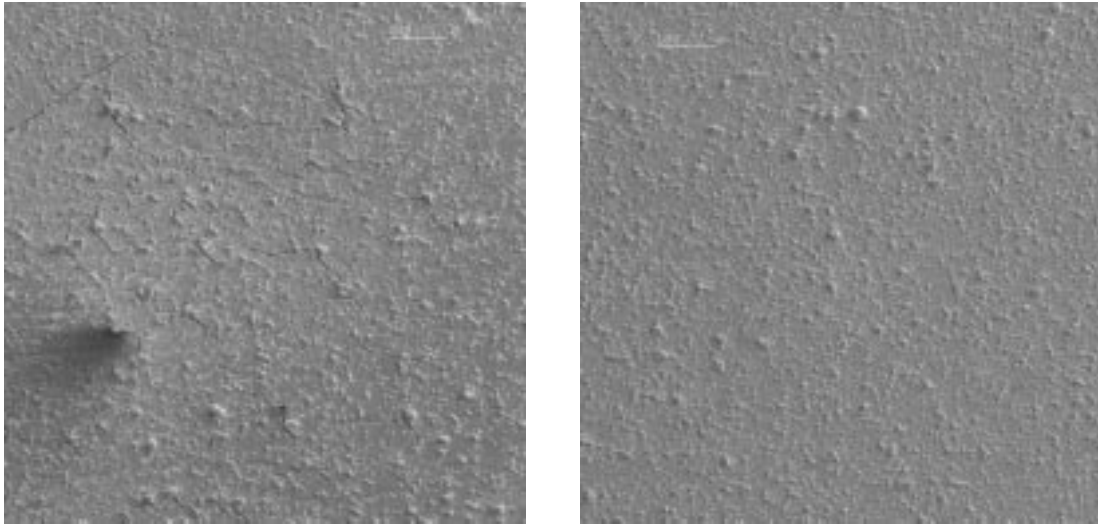


Figure 4.14: Comparison snapshot of a region of maximum temperature rise on the left and a region of zero temperature rise on the right for endcap 1L1. The length scale is  $100.7 \mu\text{m}$ .

of some of the cracks are shown in Figure 4.15. The copper globules sputtered on the surface are most dense near the outer radius where no cracks are visible. This suggests that the copper globules are not responsible for the nucleation of cracks on the surface.

As mentioned earlier, some crystal grains will show signs of slip if they have the proper orientation. Figure 4.16 shows an example of these *slip bands* as striations on the surface. Slip bands are created from stress relaxation of the surface due to plastic deformation, which results in surface intrusions and extrusions as shown schematically in Figure 4.13. Surface intrusions create a notch effect for possible nucleation of microcracks as demonstrated on the right of Figure 4.16 [7, p. 60]. In general, crack propagation along the surface is perpendicular to fatigue striations [22, p. 95].

Figure 4.17 demonstrates another instance of slip bands in which the grain boundary is evident where the slip bands suddenly stop. On the right of the figure is a close-up of some of these slip bands in which some cracks are also evident at the base of the slip bands.

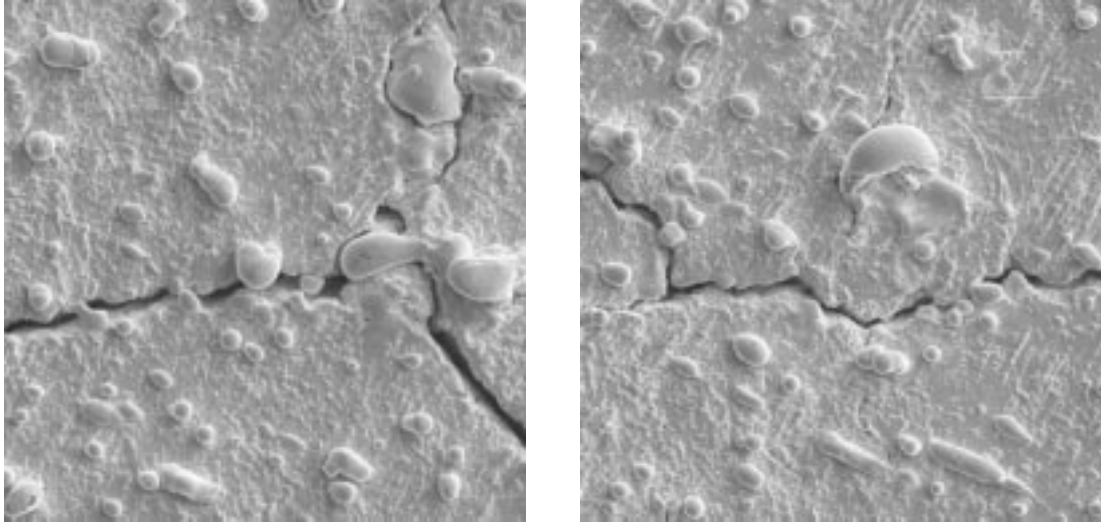


Figure 4.15: Two close-ups of cracks appearing on the left of Figure 4.14. The length scale is  $10\ \mu\text{m}$ .

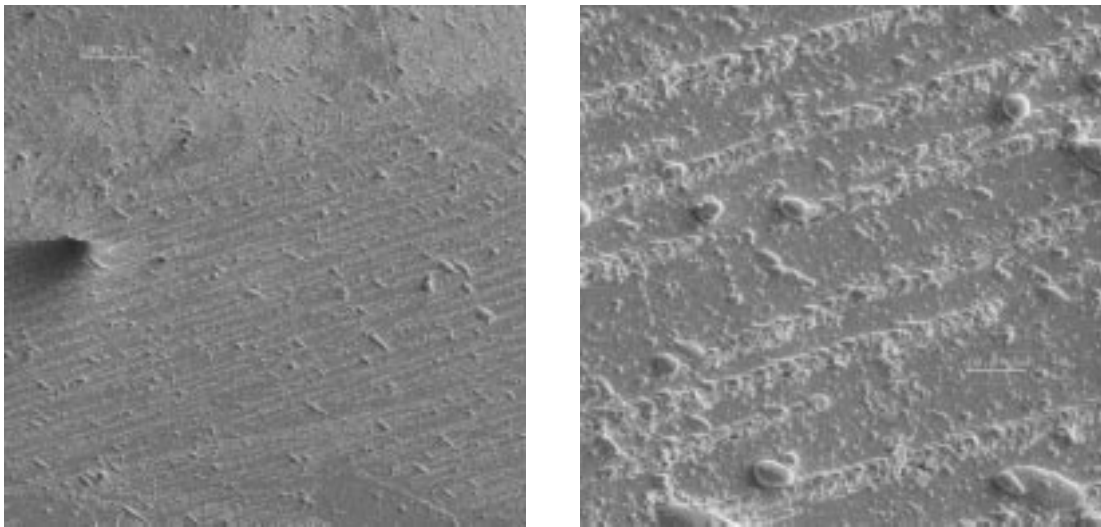


Figure 4.16: Fatigue slip bands on a particular crystal grain in the area of maximum temperature rise on endcap 2R1. The picture on the right is a close-up of these slip bands in which some microcracks are evident at the base of the slip bands. The scale is  $100.7\ \mu\text{m}$  on the left and  $10.1\ \mu\text{m}$  on the right.

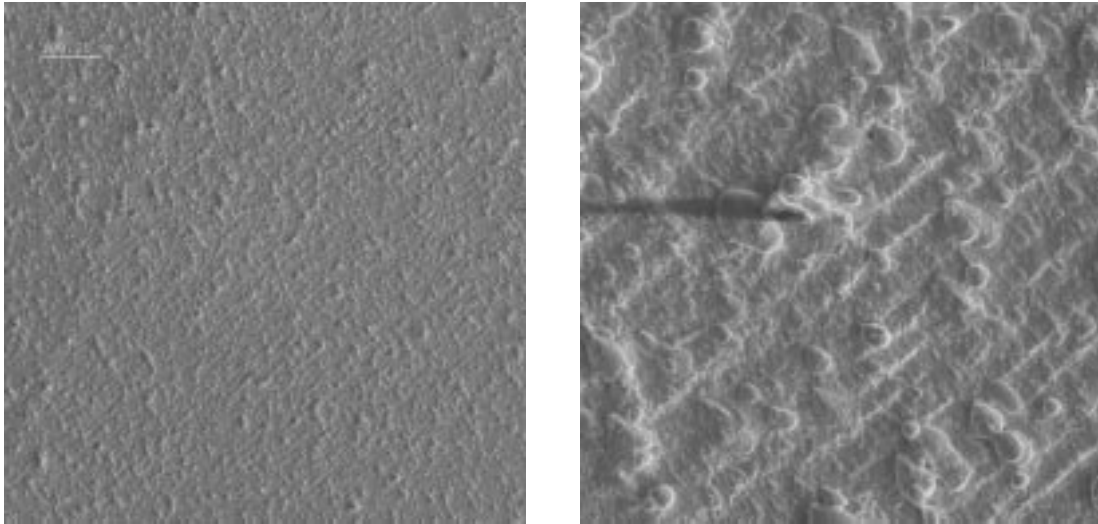


Figure 4.17: Fatigue slip bands on a particular crystal grain in the area of maximum temperature rise on endcap 2R1. A grain boundary is evident at the left of the picture on the left where the slip bands suddenly stop. The picture on the right is a close-up of these slip bands in which some microcracks are evident at the base of the slip bands. The length scale is  $100.7 \mu\text{m}$  on the left and  $10.1 \mu\text{m}$  on the right.

Other than slip bands, another common site for crack nucleations are grain boundaries [22, p. 67]. Usually cracks nucleate because grain boundaries are obstacles against slip bands if the neighboring grain is incompatible with the slip plane. Hence, grain boundaries can be seen at the point where slip bands suddenly stop. Figure 4.18 shows such an example. The transition between the whitening caused by slip bands and the rest of the surface is the grain boundary. Figure 4.19 shows two close-ups of grain-boundary cracks.

Figure 4.20 is another example of cracks along grain boundaries. In the picture on the left, the transition between the area with whitening from the slip bands and the area without the slip bands is clear. A close-up of the grain-boundary crack is on the right. Notice that the striations of the slip bands end at the crack. Grain boundaries act as natural barriers for slip bands, because the neighboring grains usually have incompatible orientations to allow slip bands to propagate across the boundary. The enhanced stress from this incompatibility may lead to crack nucleation at the grain boundary. Appendix B contains more examples of cracks along grain boundaries.

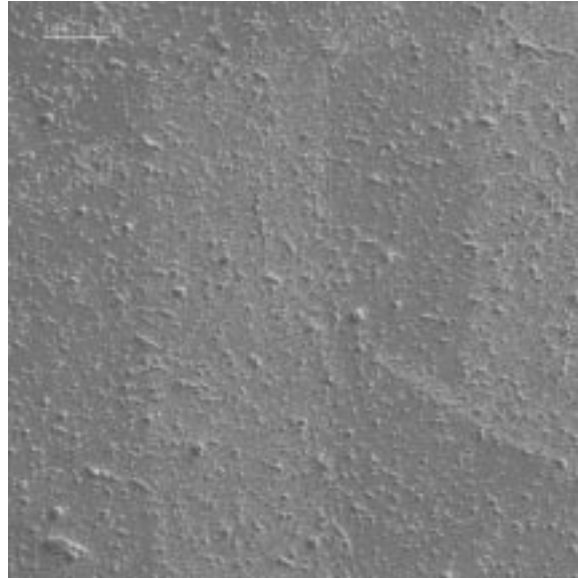


Figure 4.18: Instance of cracks occurring along grain boundaries on endcap 1L1. The length scale is  $100.7 \mu\text{m}$ .

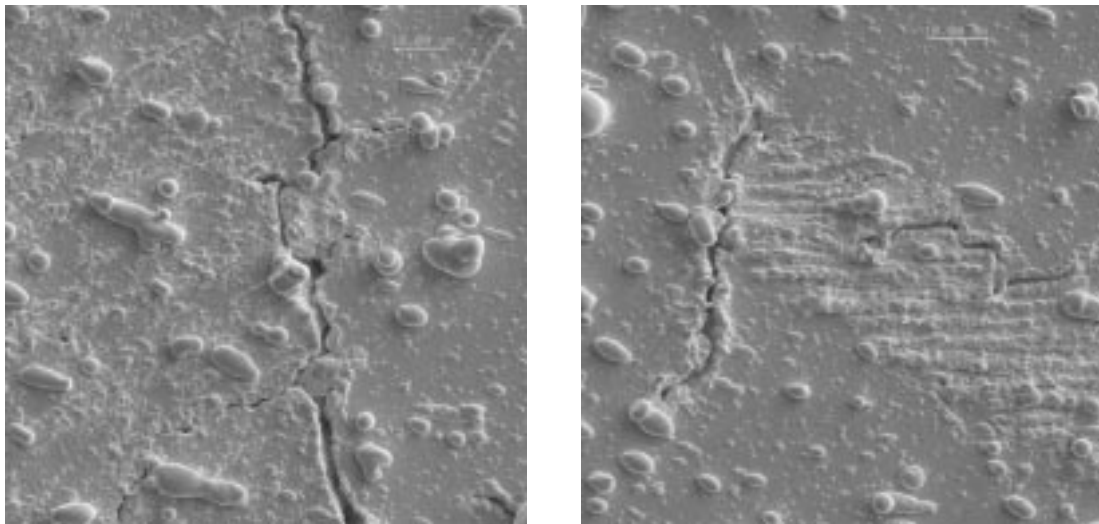


Figure 4.19: Two close-ups of cracks appearing in Figure 4.18. On the left, the crack occurs between an area with slip bands and an area with no such structure. On the right, cracks not only occur along a grain boundary near the top, but also along the slip bands. The length scale is  $10 \mu\text{m}$ .

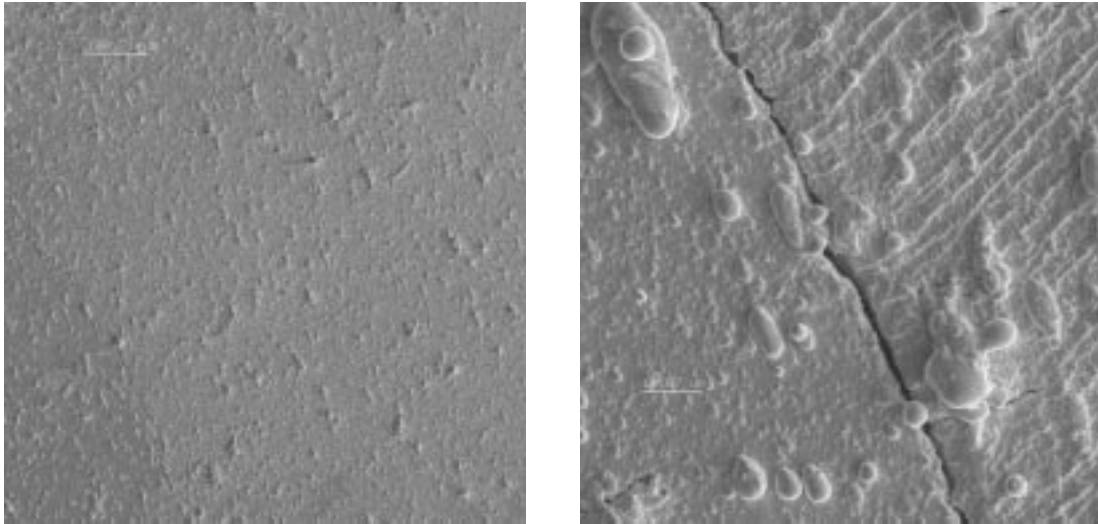


Figure 4.20: Grain-boundary cracks on endcap 2R1 in the area of maximum temperature rise. The grain boundary is the transition where the whitening due to slip bands stop. A close-up of one crack is on the right where the grain boundary is clear. The length scales are  $100.7 \mu\text{m}$  and  $10.1 \mu\text{m}$  respectively.

It is not obvious that all cracks occur along grain boundaries or as a result of surface relaxation due to slip. Figure 4.21 shows one example in which several microcracks are present in random directions. Figure 4.22 shows some close-ups of these cracks.

Scans were completed along random diameters of each endcap at the same magnification. Each snapshot corresponded to an area approximately  $0.9 \text{ mm}$  by  $0.9 \text{ mm}$ . If a snapshot showed damage in the form of fatigue slip bands or surface roughening, then an arbitrary value 1.2 was assigned. If that area contained at least one crack, then a value of 1 was assigned. If the area showed no signs of damage, then a value of 0 was assigned. Figure 4.23 shows the results of these scans.

In general, the scans indicate that surface roughening from fatigue is a precursor for crack nucleation, because most of the regions containing cracks are within the regions of surface roughness. Also, the bands generally surround the expected area of maximum temperature rise at the radius of  $10.6 \text{ mm}$ . The widths of these regions are listed in Table 4.4. The variation in the widths of damage reported in Table 4.4 among each endcap is due to the location of the scanned diameter with respect to the

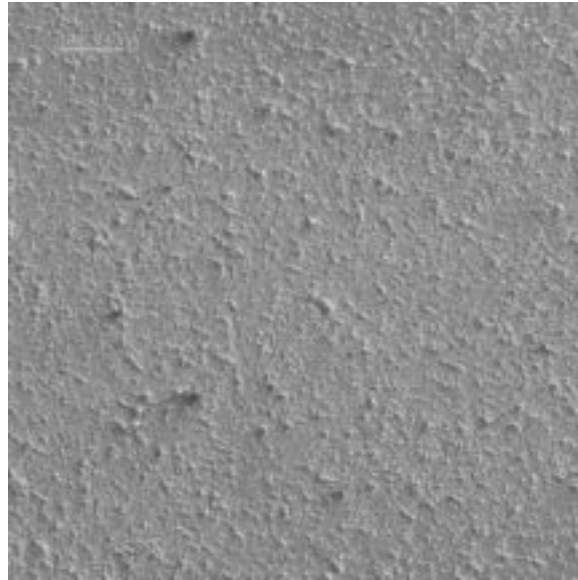


Figure 4.21: Cracks occurring in area of maximum temperature rise on endcap 1L1. No obvious signs of slip bands or grain boundaries are evident. The length scale is  $100.7 \mu\text{m}$ .

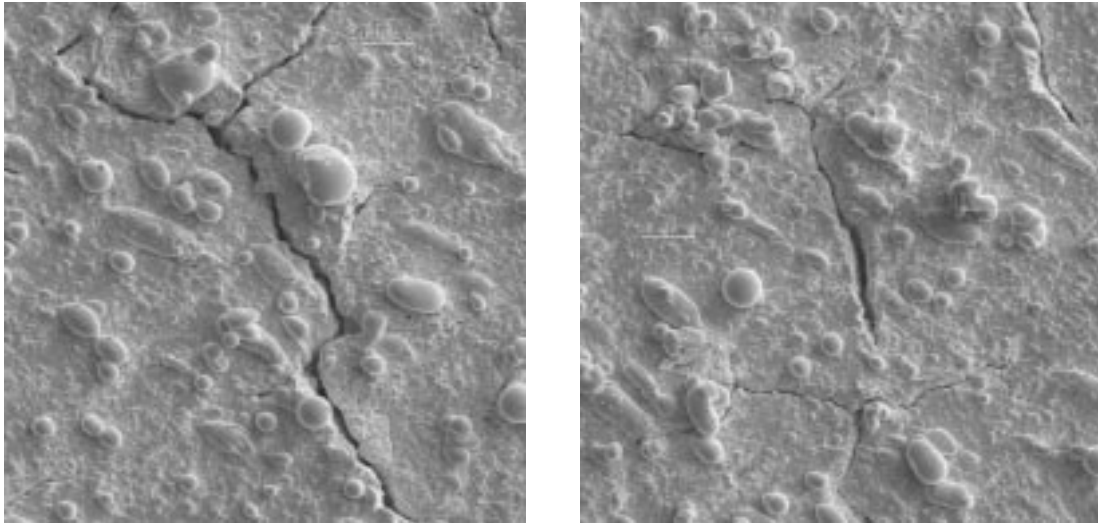


Figure 4.22: Close-ups of two cracks from Figure 4.21. The scale is  $10.1 \mu\text{m}$ .

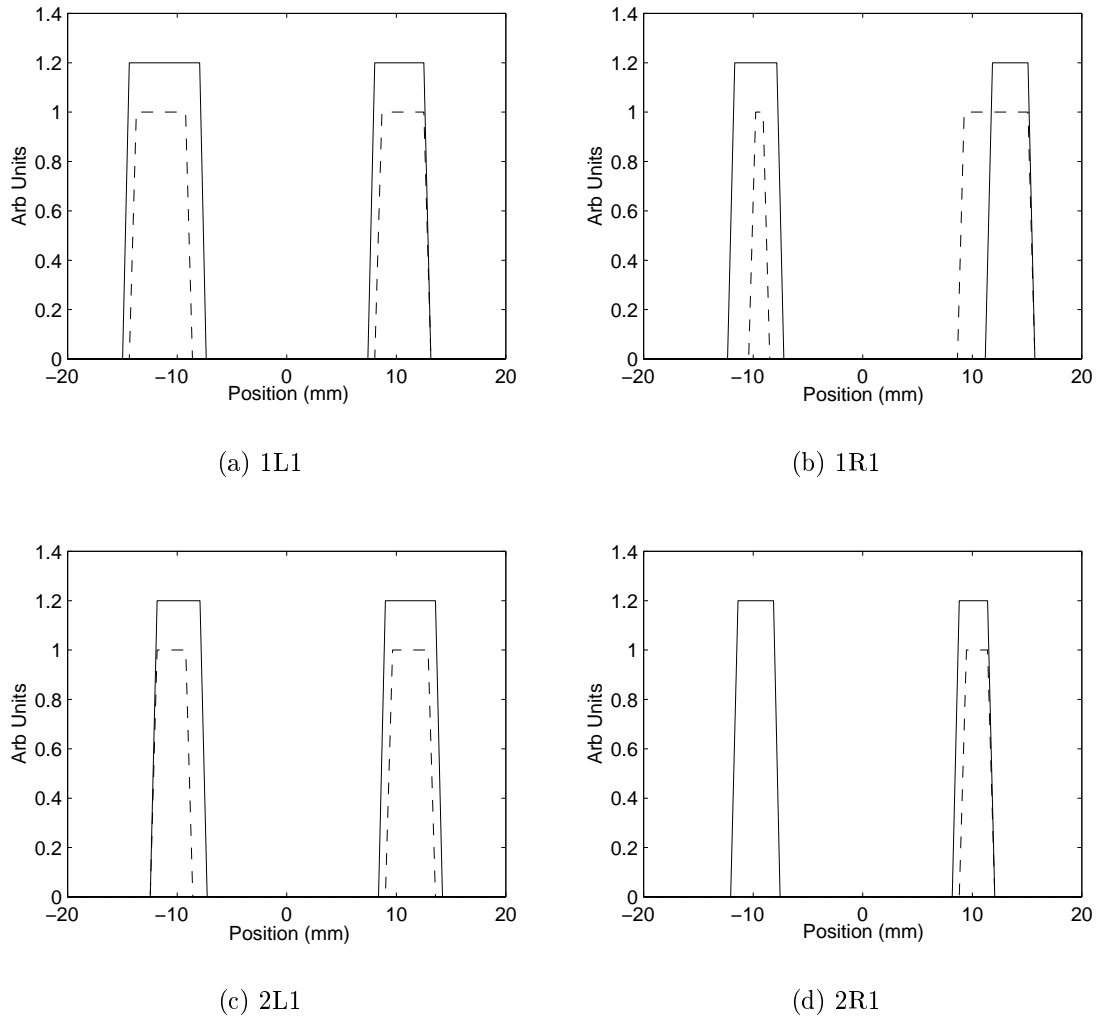


Figure 4.23: Random scans along diameters of each endcap. The solid line corresponds to regions of surface roughening and the dotted line is for regions that contain cracks on the surface.

Region	1L1 (mm)		1R1 (mm)		2L1 (mm)		2R1 (mm)	
Roughness	6.4	4.5	3.8	3.2	3.9	4.6	3.2	2.6
Cracks	5.1	3.8	0.7	5.8	2.6	3.2	0	1.9

Table 4.4: Widths of regions of surface roughening and cracks for each endcap from first high-power test.

Endcap	Average Radius (mm)	Standard Deviation (mm)
1L1	10.4	1.3
1R1	11.3	0.9
2L1	10.5	1.4
2R1	11.1	1.1

Table 4.5: Average radius and standard deviation of the distribution of crack positions shown in Figure 4.24 for each endcap.

azimuth of the high-power coupling aperture. The widths are generally larger when the scanned diameter is closer to the aperture. This feature is largely explained by the higher temperature rise in this area which is discussed later.

Endcap 1R1 contains an example in which cracks are visible outside regions of surface roughening. This is a scan along one random diameter and is not indicative of a general pattern. It is possible that signs of surface roughening or slip bands were not obvious in this region due to the clutter from the sputtered copper globules on the surface. The random scans taken along the other endcaps do indicate a general pattern that cracks occur within the region of surface roughening.

Figure 4.24 shows the positions at which higher magnification scans were taken of cracks on the endcaps. Zero degrees is the approximate azimuth of the plane of the high-power coupling aperture. These scans were taken of some of the cracks present. They do not represent every crack that occurs on the surface of the endcaps. In fact, these scans are in areas where the crack density seemed largest when compared to other regions along the radius. This was determined simply by looking at the number of cracks present in different regions at the same magnification. The distribution shown for endcap 2L1 is limited because it is the first endcap that was investigated with an SEM. By the time techniques were improved in scanning the other endcaps, 2L1 was already cut to look at its cross-section. Table 4.5 shows the average radius and standard deviation of the distribution of cracks shown in Figure 4.24 for each endcap.

Notice that the distribution of cracks shown in these plots are more dense near zero degrees. From a GdfidL simulation in the time-domain, the magnetic field on

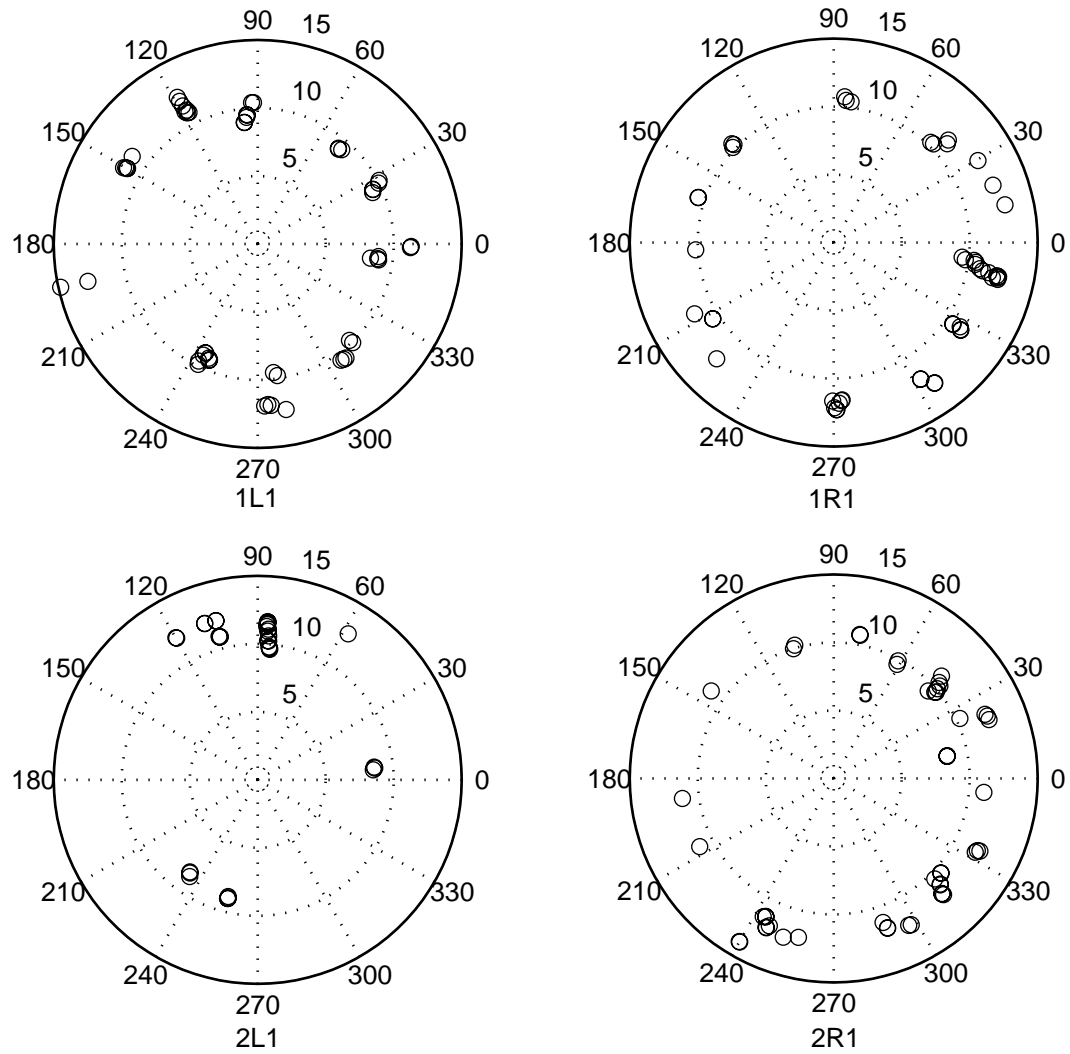


Figure 4.24: Positions of cracks in the densest areas on the copper endcaps. The radius is in mm. The azimuth of the high-power coupling aperture occurs at  $0^\circ$ .

the endcap at  $180^\circ$  is approximately 5% lower than the field at  $0^\circ$ . The field at  $0^\circ$  is equal to the estimation given by equation (A.115). Hence the temperature rise is approximately 10% lower at  $180^\circ$  than expected. A difference in temperature of 10 K to 15 K can make a large difference in the number of cracks that are visible.

For documentation purposes, additional pictures of damage to the endcap surfaces are presented in Appendix B.

## 4.2 Second Test

Only one cavity is used in this test setup for the second experimental run. The diagnostic mode was used in this run to measure pulsed temperature rise and changes in cavity Q. We used the same XL-3 50 MW klystron from the previous run for the high-power RF source. However, a different test area was used in this experiment due to space availability. The main difference of this test area, which will be shown in the next sections, was the proximity of the modulator to the test setup. The modulator caused electrical noise on the waveforms of the measured forward and reflected high power to the cavity.

The cavity chosen for this experimental run is cavity 1 from the previous run. Since the high-power coupling aperture has already been processed with high power, it was conjectured that the run-up time for RF processing would be shorter and the sputtering of copper onto the endcaps would be less. The vacuum in the cavity throughout the run is  $10^{-9}$  Torr.

### 4.2.1 Run-Up Procedure

The run-up procedure used in this experimental run is similar to the one described in Section 4.1.1. In this situation, only one week was needed to reach full power. Due to an error in the calibration of the cross-guide couplers used in the measurement of forward power, the input power to the cavity is 7.3 MW instead of the desired 8.5 MW. At this power level, not much RF breakdown occurred within the cavity as compared to the previous run.

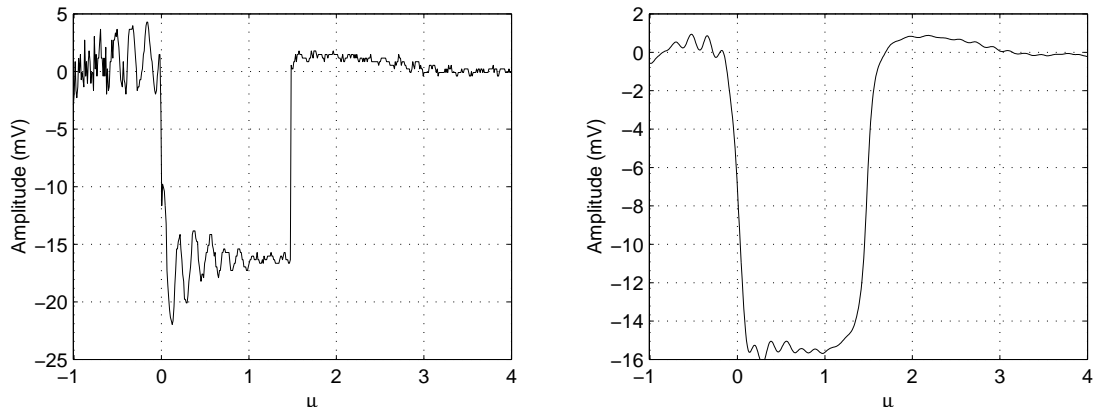


Figure 4.25: Forward power waveform for  $TE_{011}$  mode measured with a crystal detector. The waveform on the right has been low-pass filtered with an FFT using a cut-off frequency of 3 MHz.

#### 4.2.2 Measurement of RF Power

The technique of measuring the forward and reflected high power to and from the cavity is described in Section 4.1.2. As noted previously, the additional noise on the waveforms due to the proximity of the modulator to the test setup has made the measurements more difficult using crystal detectors. Typical examples of these waveforms are shown in Figures 4.25–4.26.

The forward and reflected power to the cavity were measured with cross-guide couplers attached to a 55-dB directional coupler. The systematic error described in Section 4.1.2 was reduced to  $\pm 0.2$  dBm due to improved measurement techniques with the network analyzer. The forward arm had two cross-guide couplers attached so that forward power could be measured with both a crystal detector and a peak-power analyzer. The noise from the modulator did not affect the peak-power analyzer. The reflected power was measured with a cross-guide coupler and a crystal detector.

The noise from the modulator shows a predictable pattern on the waveforms as shown on the left of Figures 4.25–4.26. It has two effects on the results. The first effect is the obvious ripple that occurs along the steady-state value of power. The second effect is the change in the amplitude of the zero baseline. It does not occur at zero volts on the oscilloscope. To determine the actual power, the ripple must either be removed by using the mean value of the ripple or by using a low-pass filter on a

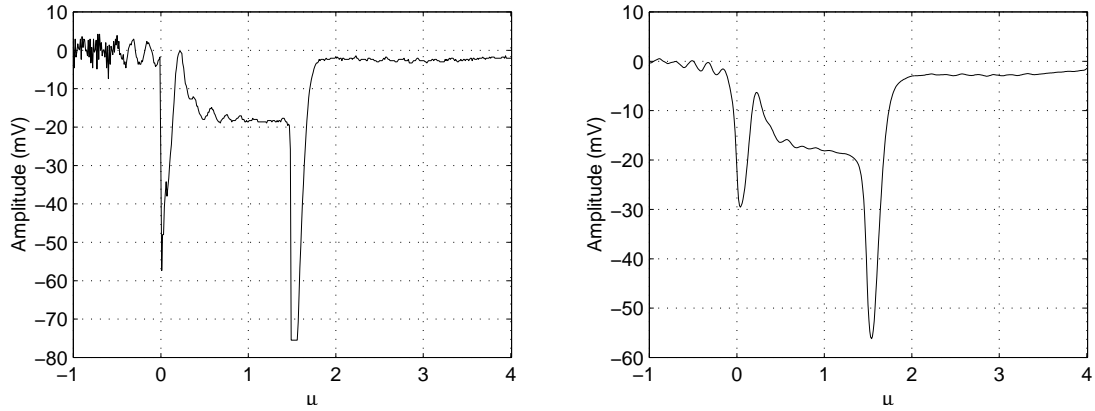


Figure 4.26: Reflected power waveform for  $TE_{011}$  mode measured with a crystal detector. The waveform on the right has been low-pass filtered with an FFT using a cut-off frequency of 5 MHz.

Initial $Q_0$	Final $Q_0$	Initial $Q_{ext}$	Final $Q_{ext}$	Initial $Q_L$	Final $Q_L$
$17750 \pm 360$	$16870 \pm 310$	$6850 \pm 220$	$6200 \pm 180$	$4940 \pm 40$	$4530 \pm 40$
Initial $\beta$	Final $\beta$				
$2.59 \pm .07$	$2.72 \pm .06$				

Table 4.6: Cavity Q measurements of  $TE_{011}$  mode of cavity 1 using a HP8510C network analyzer before and after the second high-power test. The resonant frequency is 11.425 GHz. The errors are due to errors from fits to the data.

Fourier transform of the waveform to reduce the effects of the ripple. The right side of Figures 4.25–4.26 shows an example in which the ripples are removed with Fourier transforms. Although a peak power analyzer was used to independently determine the forward power, the waveforms measured with the crystal detectors are important for determining the coupling coefficient and Q of the  $TE_{011}$  mode of the cavity.

### 4.2.3 High-Power Results

Table 4.6 shows the values of the cavity Q for the  $TE_{011}$  mode before the start of the high-power test. Table 4.7 shows the values of the cavity Q for the  $TE_{012}$  mode before the start of the high-power test. The results from using both methods described in Sections A.4.3–A.4.4 are shown in the table for consistency. In the “Loss Subtract”

Method	Initial $Q_0$	Final $Q_0$	Initial $Q_L$	Final $Q_L$
Loss Subtract	$20760 \pm 240$	$19200 \pm 230$	$10940 \pm 100$	$10260 \pm 100$
Loss Fit	$20380 \pm 360$	$18570 \pm 320$	$10940 \pm 140$	$10140 \pm 120$
Method	Initial $Q_{1,ext}$	Final $Q_{1,ext}$	Initial $Q_{2,ext}$	Final $Q_{2,ext}$
Loss Subtract	$27140 \pm 470$	$25880 \pm 470$	$157000 \pm 6300$	$147500 \pm 5900$
Loss Fit	$28180 \pm 850$	$26920 \pm 910$	$144500 \pm 5400$	$130800 \pm 5100$
Method	Initial $\beta_1$	Final $\beta_1$	Initial $\beta_2$	Final $\beta_2$
Loss Subtract	$0.77 \pm .01$	$0.74 \pm .01$	$0.13 \pm .005$	$0.13 \pm .005$
Loss Fit	$0.72 \pm .02$	$0.69 \pm .02$	$0.14 \pm .005$	$0.14 \pm .005$

Table 4.7: Cavity Q measurements of TE<sub>012</sub> mode of cavity 1 using a HP8510C network analyzer before and after the second high-power test. “Loss Subtract” is based from the method described in Section A.4.3 and “Loss Fit” is the method described in Section A.4.4. The resonant frequency is 17.85 GHz.

method listed in Table 4.7, the loss in the coupling in each port is determined by measuring the value of the reflection far from resonance. In the case of lossless coupling, the reflection should be close to 1. For lossy coupling, the reflection will reach steady-state at a value less than 1 due to the loss of power from the coupling mechanism. This value can be subtracted from the measurement to determine the actual coupling to the cavity.

In the course of the experiment, we discovered that the RF properties for the TE<sub>012</sub> were sensitive to small changes in the resonant frequency. During the experiment, the cavity is tuned such that under high power the resonant frequency is approximately 17.85 GHz. Since measurements were also obtained in the time-domain under low power in which the resonant frequency of the TE<sub>012</sub> increased to approximately 17.856 GHz, the properties of this mode were also characterized at this frequency after the completion of the high-power test. These measurements are given in Table 4.8.

Both methods for determining Q are within 5% of each other; therefore, both methods are consistent. We will use the results from the “Loss Fit” method, since they involve fitting data with the real and imaginary parts of the measured S-parameters. The “Loss Subtract” method only considers the magnitude of the S-parameters and is not fit to the data.

Method	$Q_0$	$Q_L$	$Q_{1,ext}$	$Q_{2,ext}$
Loss Fit	$17860 \pm 320$	$10140 \pm 130$	$26820 \pm 940$	$186000 \pm 10000$
Method	$\beta_1$	$\beta_2$		
Loss Fit	$0.67 \pm .02$	$0.10 \pm .005$		

Table 4.8: Cavity Q measurements of TE<sub>012</sub> mode of cavity 1 using a HP8510C network analyzer after the second high-power test. The resonant frequency is 17.856 GHz.

The differences in the properties of the TE<sub>012</sub> mode due to small changes in frequency are likely due to the proximity of the diagnostic coupling aperture to one of the endcaps. Since this mode is driven asymmetrically, small changes to the cavity length can cause a large shift in the mode’s RF properties because it changes the symmetry of the fields. A similar effect is noticed with a small change in the length of the endcap grooves to remove mode degeneracies as reported in Section 2.1.7.

Using the values given in Tables 4.6–4.7 with an 7.3 MW, 1.5  $\mu$ s pulse in the equations presented in Section 3.3.2 gives a temperature rise of 82 K  $\pm$ 3 K. The error in the calculated temperature rise comes from the range of input power due to systematic error, 7.3 MW  $\pm$ 0.3 MW. At this power level, the error is dominated by systematics. Consequently, the temperature rise on the cylindrical sidewall is calculated to be 73 K  $\pm$ 3 K. The temperature rise along the sidewall is no longer 1/2 that of the endcaps due to the differences in the resistivities described below.

The experiment was run at the temperature rise of 82 K for  $8.6 \times 10^7$  pulses. Afterwards, the cavity was removed from the test setup and its Q was measured with a network analyzer. The results are given in Tables 4.6–4.7. Just as with the first high-power test, both the unloaded and the external Q’s are lower than their initial values. These changes are explained in Section 4.2.4.

Since the surfaces of the endcaps are cut to a mirror-finish and the cavity sidewall has had damage from a previous high-power test, we expect the resistivities to be different on these surfaces. By separating the resistivities on the endcaps and the sidewall and using equation (A.73) for the Q’s of the TE<sub>011</sub> and TE<sub>012</sub> modes, the

Test	$\rho_{end}$ ( $\times 10^{-8} \Omega \cdot \text{m}$ )	$\rho_{wall}$ ( $\times 10^{-8} \Omega \cdot \text{m}$ )
Initial	$1.73 \pm .11$	$5.1 \pm .7$
Final	$2.20 \pm .13$	$4.7 \pm .7$

Table 4.9: Electrical resistivities of the endcaps and cavity sidewall before and after the second high-power test. This assumes the resistivities are constant across the surface. The reported errors are due to errors in the determination of  $Q$  for each mode.

different resistivities of the endcaps,  $\rho_{end}$ , and the sidewall,  $\rho_{wall}$ , are given by

$$\rho_{end} = A \left( \frac{\omega_{012}^{5/2}}{Q_{012}} - \frac{\omega_{011}^{5/2}}{Q_{011}} \right)^2, \quad (4.10a)$$

$$\rho_{wall} = B \left( \frac{\omega_{012}^{5/2}}{Q_{012}} - \frac{4\omega_{011}^{5/2}}{Q_{011}} \right)^2, \quad (4.10b)$$

$$A = \frac{\mu d^6}{72\pi^4 c^4}, \quad (4.10c)$$

$$B = \frac{\mu R^6}{18 (x'_{01})^4 c^4}, \quad (4.10d)$$

where  $R$  is the radius of the cavity and  $d$  is its length. Using the fitted  $Q$ 's given in Tables 4.6–4.7 the electrical resistivities of the endcaps and the sidewall are given in Table 4.9. The theoretical resistivity at room temperature for pure copper is  $1.717 \times 10^{-8} \Omega \cdot \text{m}$ , which is close to the initial value measured for the endcaps. If the resistivity is constant along the endcap surface after the high-power test, then the resistivity increased by 27%. This is a lower bound on the resistivity change.

The values given in Table 4.9 so far assume that the resistivity is constant along each of the surfaces. This is a good approximation before the high-power test; however, after the test the damage to the endcaps shown in Sections 4.2.4–4.2.5 indicate that the resistivity will be different within a band around the area of maximum temperature rise. The maximum temperature rise occurs at a radius  $r = .4805R$ . Letting  $\rho_{end,1}$  be the resistivity inside the band of damage,  $r = .4805R \pm r_b$ , and  $\rho_{end,2}$  the

$r_b$ (mm)	$\rho_{end,1}$ ( $\times 10^{-8} \Omega \cdot \text{m}$ )	$\rho$ change %
1.0	$5.0 \pm 1.0$	186
1.5	$3.8 \pm 0.6$	117
2.0	$3.2 \pm 0.5$	87
2.5	$3.0 \pm 0.4$	72
3.0	$2.8 \pm 0.3$	62
3.5	$2.7 \pm 0.3$	57
4.0	$2.7 \pm 0.3$	55

Table 4.10: Electrical resistivities of the endcaps in the band of damage after the second test.  $\rho_{end,2} = 1.73 \times 10^{-8} \Omega \cdot \text{m}$ .  $\rho_{wall} = 4.7 \times 10^{-8} \Omega \cdot \text{m}$ .

resistivity along the rest of the endcap we have

$$\rho_{end,1} = \frac{1}{D^2} \left[ A \left( \frac{\omega_{012}^{5/2}}{Q_{012}} - \frac{\omega_{011}^{5/2}}{Q_{011}} \right) + \left( D - \frac{1}{2} R^2 J_0^2(x'_{01}) \right) \sqrt{\rho_{end,2}} \right]^2, \quad (4.11a)$$

$$\rho_{wall} = B \left( \frac{\omega_{012}^{5/2}}{Q_{012}} - \frac{4\omega_{011}^{5/2}}{Q_{011}} \right)^2, \quad (4.11b)$$

$$A = \sqrt{\frac{\mu d^3 R^2 J_0^2(x_{11})}{2 \cdot 12\pi^2 c^2}} \quad (4.11c)$$

$$B = \frac{\mu R^6}{18c^4 (x'_{01})^4}, \quad (4.11d)$$

$$D = \frac{1}{2} r_{hi}^2 [J_1^2(y_{hi}) - J_0(y_{hi})J_2(y_{hi})] - \frac{1}{2} r_{lo}^2 [J_1^2(y_{lo}) - J_0(y_{lo})J_2(y_{lo})], \quad (4.11e)$$

$$y_{lo} = \frac{x'_{01} r_{lo}}{R}, \quad y_{hi} = \frac{x'_{01} r_{hi}}{R}, \quad (4.11f)$$

$$r_{lo} = .4805R - r_b, \quad r_{hi} = .4805 + r_b, \quad (4.11g)$$

where we approximate  $\rho_{end,2}$  as the initial value before the high-power test. Table 4.10 lists the resistivities after the high-power tests assuming different sizes of the band of damage around the area of maximum temperature rise. The band of damage discussed in Section 4.2.4 has an approximate width between 7 to 8 mm. Thus,

$\beta_{nom}$	$2.16 \pm .04$
$\beta_{low}$	$2.08 \pm .04$
$\beta_{high}$	$2.25 \pm .04$
$\beta_{freq}$	$2.72 \pm .06$

Table 4.11: Measurement of  $\beta$  at the end of the second high-power test in the time and frequency domains. The range of values in the time-domain are due to the systematic errors in the measurement of power.

Table 4.10 indicates that the resistivity in the area of maximum damage along the endcap increased between 25% and 60%. The resistivity of the sidewall changed less than 8%. The width of damage on the endcaps corresponds to a range of temperature rise from 65 K to 82 K.

Since the temperature rise is proportional to the square-root of electrical resistivity, the temperature is expected to increase over time as the copper surface becomes degraded from fatigue damage. With these resistivity increases, the maximum temperature rise on the endcaps increased between 10% to 25% to between 90 K and 105 K. Over time, the resistivity is expected to increase due to further damage from an increased temperature rise, which leads to thermal runaway.

### Measurement of Coupling Coefficient and Cavity Q of TE<sub>011</sub> Mode

The same procedure described in Section 4.1.3 is used to measure and calculate the coupling coefficient and cavity Q's for the TE<sub>011</sub> mode of the cavity. The only difference occurs with the determination of the coupling coefficient from noisy data. The noise on the waveforms is reduced by low-pass filtering the waveform's Fourier transforms as shown in Figures 4.25–4.26.

As described previously, the coupling coefficient is determined by using equation (4.2). The reflected power is measured at its steady-state value just before the input RF pulse turns off. Table 4.11 compares the measurement of the coupling coefficient made in the time-domain at the end of the high-power test with the measurement made in the frequency-domain after the high-power test. The range of values of the measurement in the time-domain is due to the systematic error in the

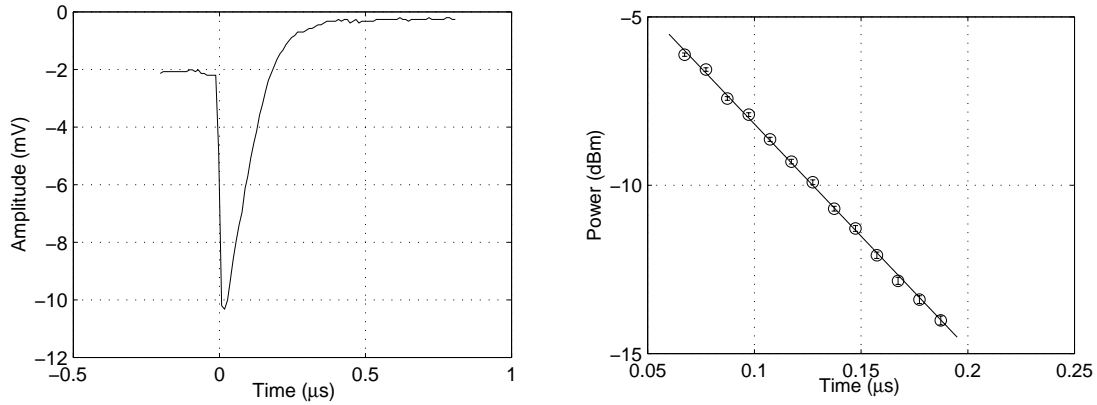


Figure 4.27: Reflected waveform from  $TE_{011}$  mode at the end of the second high-power test. The fit of the waveform using linear least-squares is on the right.

measurement of power of  $\pm 0.2$  dB. The random error is due to the residual noise left on the waveforms after the use of Fourier transforms to filter the noise. Although the random error in the measurement of power depends on the amplitude of the voltage measured on the oscilloscope with crystal detectors, the amplitude is measured at a consistent value throughout the experiment. Hence, the average random error of the measurement of forward and reflected power for the determination of  $\beta$  is 0.1 dB. As shown in Table 4.11, systematic error dominates the measurement of  $\beta$ . The discrepancy between the nominal values of  $\beta$  in the time and frequency domains is 20%.

The measurement of loaded  $Q$  involves the same procedure as with the first high-power test. No Fourier transforms are necessary to reduce the noise since the signal-to-noise ratio is large for this measurement. Equation (4.6) is used to fit to the decay of the power out of the cavity when the RF input pulse turns off. The waveform of the last data set is shown on the left of Figure 4.27 along with its fit using linear least-squares on the right (see equation (4.6)). A comparison of the measurements of the loaded  $Q$  in the time and frequency domains at the end of the high-power test is given in Table 4.12. The discrepancy between the measured values is 3%.

Figure 4.28 shows the results of the measurements of  $\beta$  and loaded  $Q$  for the  $TE_{011}$  mode of the cavity over the course of the high-power test. The pulse count was measured with an event counter as described in Section 2.3.2. After 15 million

$Q_{L,time}$	$4680 \pm 40$
$Q_{L,freq}$	$4530 \pm 40$

Table 4.12: Measurement of  $Q_L$  in the time and frequency domains at the end of the second high-power test. The errors are due to errors from the fit to the data.

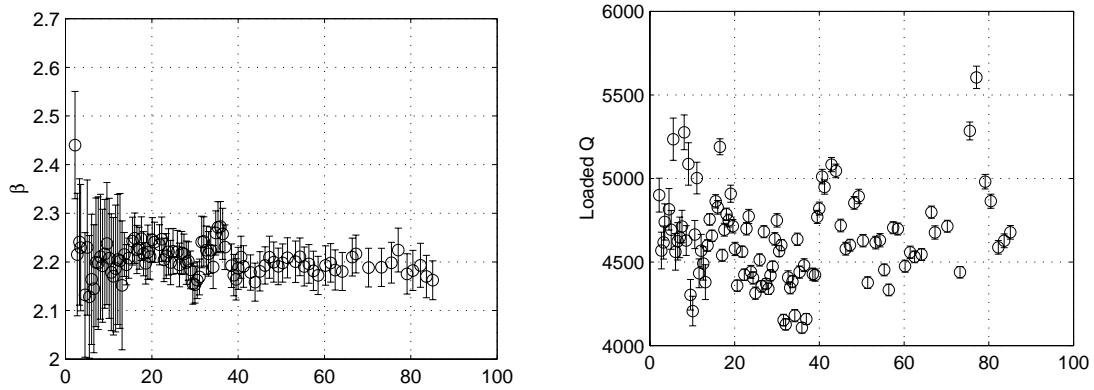


Figure 4.28: Measurement of  $\beta$  and loaded  $Q$  of the  $TE_{011}$  mode during the second high-power test.

pulses, the random error was reduced by decreasing the attenuation of reflected power measured by the crystal detector at the risk of destroying the detector over time. The increased amplitude output by the detector increased the signal-to-noise ratio, thus the error in the determination of  $\beta$  decreased from  $\pm 0.2$  to  $\pm 0.04$ .

The measurement of  $\beta$  over time indicates that the coupling to the  $TE_{011}$  mode remained mostly constant. The frequency-domain measurements listed in Table 4.6 are in agreement with this conclusion. However, the discrepancy between these two measurements is 20% and are not consistent with each other when including systematic and random errors.

Table 4.6 indicates the loaded  $Q$  for the  $TE_{011}$  mode decreased by 8%. Although the measurement of  $Q_L$  over time is in rough agreement with this small change, it is difficult to discern any pattern due to the scatter of the data.

At 40 and 78 million pulses, there is a sharp change in the measured values of  $Q_L$ . This occurred at the time the cross-guide couplers from the branch of the 55-dB directional coupler used to measure forward power were removed to re-calibrate

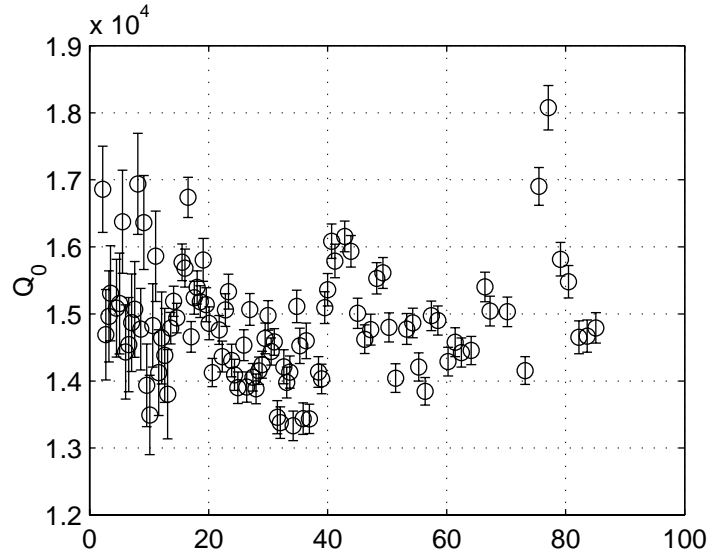


Figure 4.29: Measurement of  $Q_0$  during the second high-power test.

the attenuation factor. They were placed back in their original position afterwards. Interestingly,  $Q_L$  is determined only from the measurement of reflected power. This suggests the existence of a standing-wave in the coupling arm of the directional coupler, which is depicted as branches 3 and 4 in Figure 4.2. Each time the forward cross-guide couplers are replaced, the match looking into the couplers change. This will change the strength of the standing-wave and affect the measurement of forward and reflected power.

Figure 4.29 shows the measurement of unloaded  $Q$  of the  $TE_{011}$  mode determined by  $Q_0 = Q_L(1 + \beta)$ . Due to the scatter of data from the measurement of  $Q_L$ , it is also difficult to discern a general pattern in the value of  $Q_0$  over time. Table 4.6 indicates that  $Q_0$  decreased by 5% which is in rough agreement with the data scatter shown in Figure 4.29. However, there is a discrepancy in the measured values of  $Q_0$  due to the discrepancy in the measured values of  $\beta$ .

Table 4.6 also indicates that  $Q_0$  and  $Q_{ext}$  decreased by roughly the same percentage. This explains the somewhat constant value measured for  $\beta$ . Therefore,  $Q_0$  and  $Q_{ext}$  degraded at roughly the same rate.

The drop in  $Q_{ext}$  is due to damage to the high-power coupling aperture, which

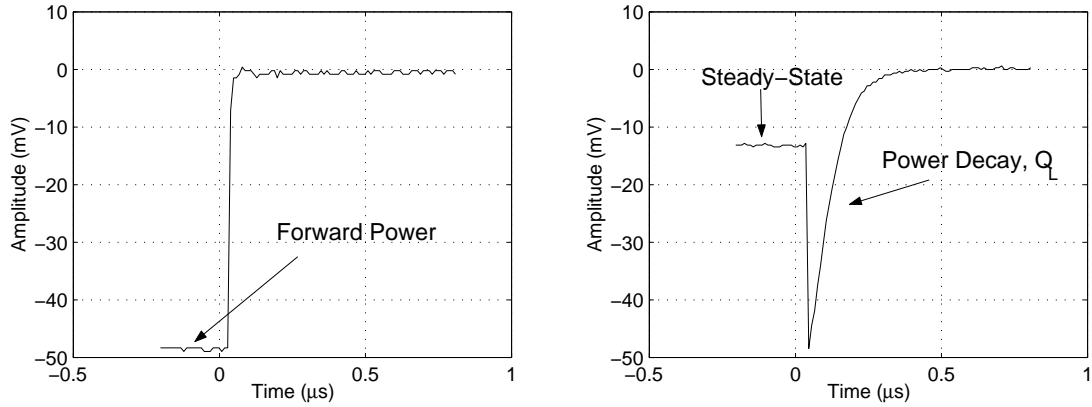


Figure 4.30: Forward and reflected waveforms from  $TE_{012}$  mode using crystal detectors.

effectively increased the diameter of the coupling hole. However, the damage is not as extensive as with the first high-power test because of the lower power and decreased field enhancement. The drop in  $Q_0$  is due to the increase in electrical resistivity of the surface of the endcaps discussed earlier.

### Measurement of Coupling Coefficients and Cavity Q of $TE_{012}$ Mode

The coupling coefficients and cavity Q of the  $TE_{012}$  mode were measured with the setup shown in Figure 2.42. The details of this setup is described in Section 2.3.1.

The forward and reflected waveforms measured with the crystal detectors and quadrature mixer do not suffer from modulator noise since they are measured between klystron pulses. Typical waveforms from the crystal detectors are shown in Figure 4.30. The acquisition of these waveforms were triggered near the low-power RF pulse turn-off such that  $\beta$  and  $Q_L$  may be determined from the same trace.

Referring to Section A.4.3, we may use equation (A.154) to find the coupling coefficient to the diagnostic port of the  $TE_{012}$  mode in the time-domain. Assuming the cavity is filled by the end of the pulse ( $t \rightarrow \infty$ ), the reflected power is simply

$$P_r = (\gamma - 1)^2 P_f, \quad \gamma = \frac{2\beta_1}{1 + \beta_1 + \beta_2}. \quad (4.12)$$

	$\beta_{1,time}$	$\beta_{1,freq}$
Hot	$0.65 \pm .005$	$0.69 \pm .02$
Cold	$0.61 \pm .005$	$0.67 \pm .02$

Table 4.13: Measurement of  $\beta_1$  of TE<sub>012</sub> mode assuming  $\beta_2 = .14$  for the “Hot” case and  $\beta_2 = 0.10$  for the “Cold” case. “Hot” corresponds to  $f_{res} = 17.850$  GHz and “Cold” corresponds to  $f_{res} = 17.856$  GHz.

Hence the coupling coefficient for the diagnostic port is

$$\beta_1 = \frac{\gamma}{2 - \gamma}(1 + \beta_2). \quad (4.13)$$

The value of  $\beta_1$  depends on the value of  $\beta_2$ . Since  $\beta_2$  cannot be measured directly in the time-domain while the cavity is undergoing a high-power test, its value must be assumed from an initial measurement conducted in the frequency-domain. Fortunately the value of  $\beta_2$  changes only slightly during the experiment because this port is weakly-coupled.

Table 4.13 shows a comparison of the measurements of  $\beta_1$  in the time and frequency domains at the end of the high-power test. The random errors in the time-domain are due to  $\pm 0.2$  mV fluctuations which correspond to an approximate error of  $\pm 0.05$  dB at the steady-state value of power.  $\beta_1$  was measured at two different high-power levels, because it was noticed that the RF properties of the TE<sub>012</sub> mode were sensitive to small changes in resonant frequency. The “Hot” case shown in Table 4.13 occurs while the TE<sub>011</sub> mode is excited at full power corresponding to a resonant frequency of 17.850 GHz for the TE<sub>012</sub> mode. When the RF power was reduced to perform measurements of the properties of the TE<sub>011</sub> mode, another set of measurements were taken for the TE<sub>012</sub> mode while at a resonant frequency of 17.856 GHz. This corresponds to the “Cold” case shown in the table. The discrepancies for either case between the time and frequency domains is less than 10%.

Figure 4.31 shows the measurement of  $\beta_1$  for both “Hot” and “Cold” cases over the course of the high-power test. Since the values of  $\beta_2$  are approximately constant throughout the experiment, we assume their final values given in Tables 4.7–4.8.

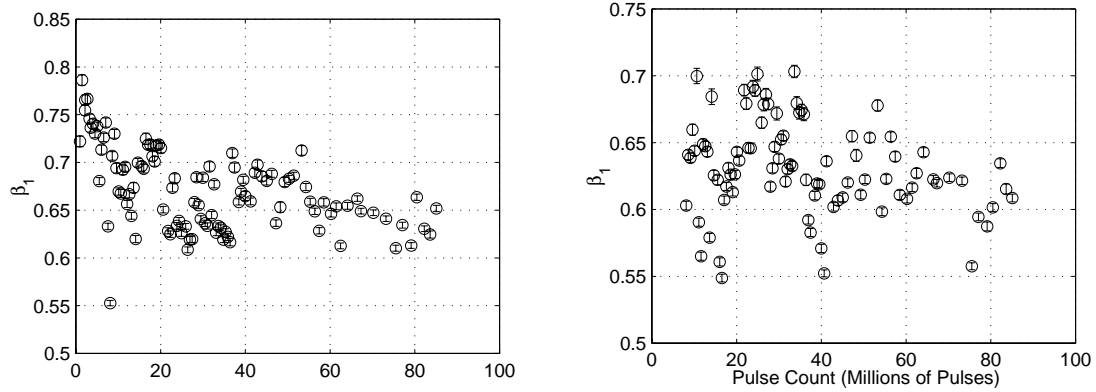


Figure 4.31: Measurement of  $\beta_1$  during the high-power test for both “Hot” (left) and “Cold” (right) cases.

The scatter in the data is partly due to vibrations of the endcaps from the flow of cooling water, because the endcaps were mounted on bellows that act like springs. The vibrations are seen as fluctuations in the steady-state value of reflected power from the  $TE_{012}$  mode and only occur when water flows through the cooling channels on the back of the endcaps. The resonant frequency fluctuates on the order of 50 kHz, corresponding to length changes of less than  $0.1 \mu\text{m}$ .

Although there is a large scatter in the data, there is a general pattern of decreasing  $\beta_1$  over time. This is in agreement with the measurements in the frequency domain. This is also expected from  $Q_0$  degradation due to fatigue damage on the surface of the endcaps, which will be shown in Section 4.2.5. Although there is some degradation in  $Q_{ext,1}$  due to damage to the diagnostic coupling aperture, there is more degradation of  $Q_0$  resulting in an overall decrease in  $\beta_1$ . Since the  $TE_{012}$  mode is weakly-coupled to the high-power coupler, a small change in  $Q_{ext,2}$  has little effect on  $\beta_2$ .

Table 4.14 shows a comparison between the measurements of  $Q_L$  in the time and frequency domains for both “Hot” and “Cold” cases. The discrepancy for either case is less than 17%. The results, however, are inconsistent with each other. Figure 4.32 shows the measurement of  $Q_L$  for both “Hot” and “Cold” cases over the course of the high-power test. Although there is a large scatter in the data, the average of the data points suggests a discrepancy of approximately 20% in the measurements of  $Q_L$  in the time and frequency domains. However, there is general decreasing trend in the

	$Q_{L,time}$	$Q_{L,freq}$
Hot	$8450 \pm 60$	$10140 \pm 120$
Cold	$9000 \pm 80$	$10140 \pm 130$

Table 4.14: Measurement of  $Q_L$  of TE<sub>012</sub> mode. “Hot” corresponds to  $f_{res} = 17.850$  GHz and “Cold” corresponds to  $f_{res} = 17.856$  GHz.

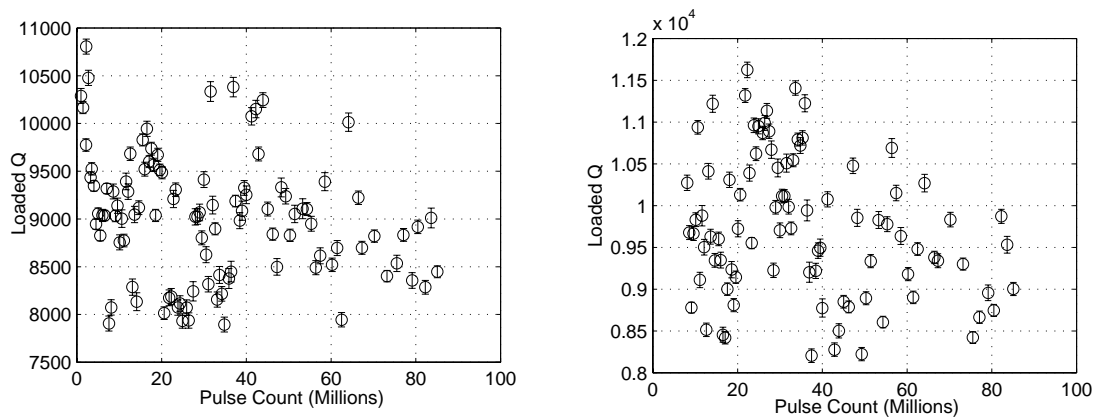


Figure 4.32: Measurement of  $Q_L$  during the high-power test for both “Hot” (left) and “Cold” (right) cases.

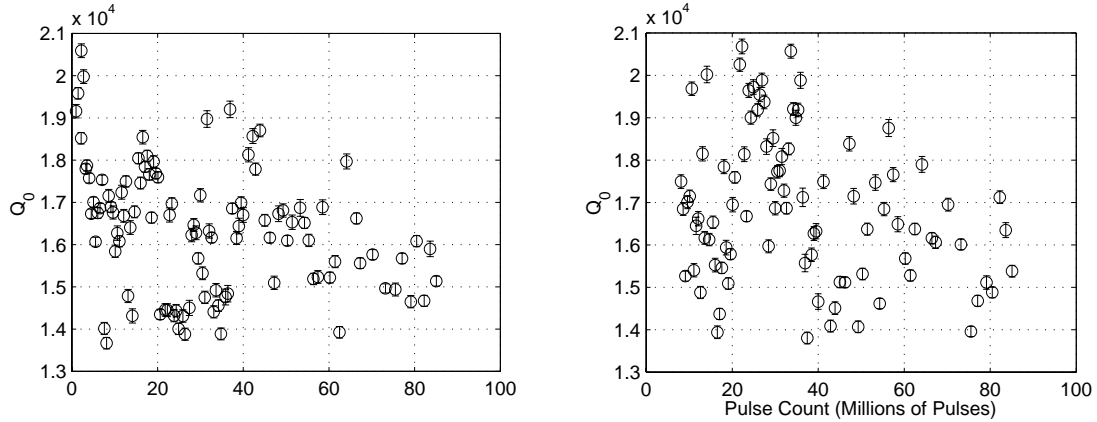


Figure 4.33: Measurement of  $Q_0$  during the high-power test for both “Hot” (left) and “Cold” (right) cases.

value of  $Q_L$  that is in agreement with Table 4.7.

The inconsistency of these results could be due to two factors. The first is the vibration of the endcaps due to water cooling discussed earlier. The second may be due to the leakage of power out the high-power coupler. Although this is nominally accounted for in  $\beta_2$ , this assumes a matched load. There may be reflections from the magic-tees and the klystron output cavity that could influence this measurement.

Figure 4.33 shows the measurement of  $Q_0$  for both “Hot” and “Cold” cases over the course of the high-power test determined by  $Q_0 = Q_L(1 + \beta_1 + \beta_2)$ . The final values given in Tables 4.7–4.8 were used for  $\beta_2$ . Due to the discrepancies and data scatter from the measurement of  $\beta_1$  and  $Q_L$ , the determination of  $Q_0$  suffers from the same problems. However, a general decreasing trend in the value of  $Q_0$  exists in agreement with Table 4.7. This is also in agreement with the expectation of a degrading  $Q_0$  due to fatigue damage on the surface of the endcaps which will be shown in Section 4.2.5.

### Measurement of Pulsed Temperature Rise

Using the experimental setup described in Section 2.3, the maximum pulsed temperature rise on the surface of the copper endcaps may be inferred from the measurement of the change in  $Q_{012}$  due to the heating from a high-power RF pulse. By measuring the magnitude and phase of the reflected power from the  $TE_{012}$  mode using the

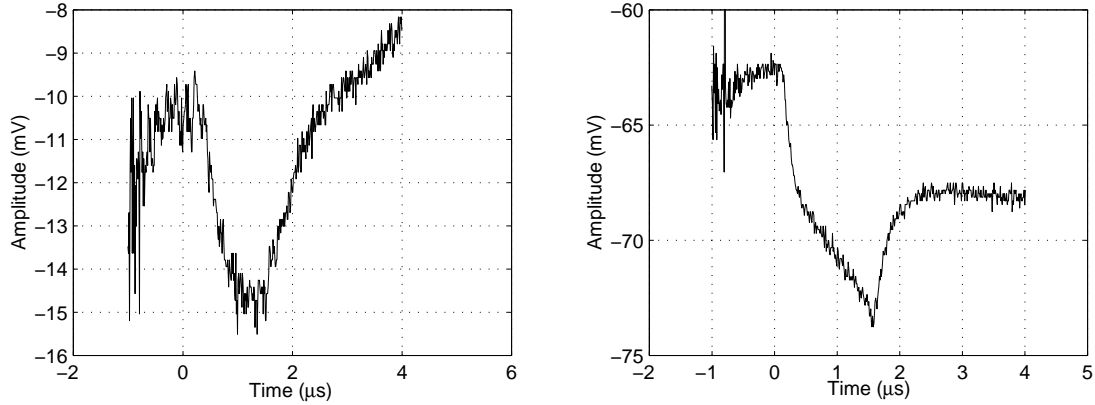


Figure 4.34: Quadrature outputs from quadrature mixer during a typical measurement of reflected power from  $TE_{012}$  mode.

quadrature mixer, the change in  $Q_{012}$  can be determined from equations (3.97).

The quadrature outputs labeled I and Q from the mixer for a typical measurement are shown in Figure 4.34. A constant DC-offset occurs in each output channel due to leakage of power from the LO channel in the mixer. This offset must be subtracted from the outputs first.

The mixer was calibrated inline by replacing the cavity with a signal generator phase-locked to the generator that provides the LO power to the mixer. By measuring the output amplitude of the mixer at known power levels into the intervening cables and other components, the mixer output is easily correlated to the output power from the cavity. By offsetting the frequency of the test generator from the LO generator, the amplitude of the sine wave that occurs at the difference in frequency can be measured. This procedure removes any ambiguities due to phase in the calibration setup. By measuring the forward power to the cavity with a calibrated crystal detector, the reflection coefficient is known. The phase is determined by taking the inverse tangent of the ratio of the I and Q outputs. As long as the input RF power to the mixer is below a certain level, the phase imbalance between the two outputs is less than  $2^\circ$ .

Using the described calibration procedure, the magnitude of the reflection coefficient is shown in Figure 4.35 along with the theoretical prediction based on a calculated 82 K maximum temperature rise on the endcap. The measured and theoretical prediction for the phase shift assuming no change in  $\omega_{012}$  due to thermal expansion is

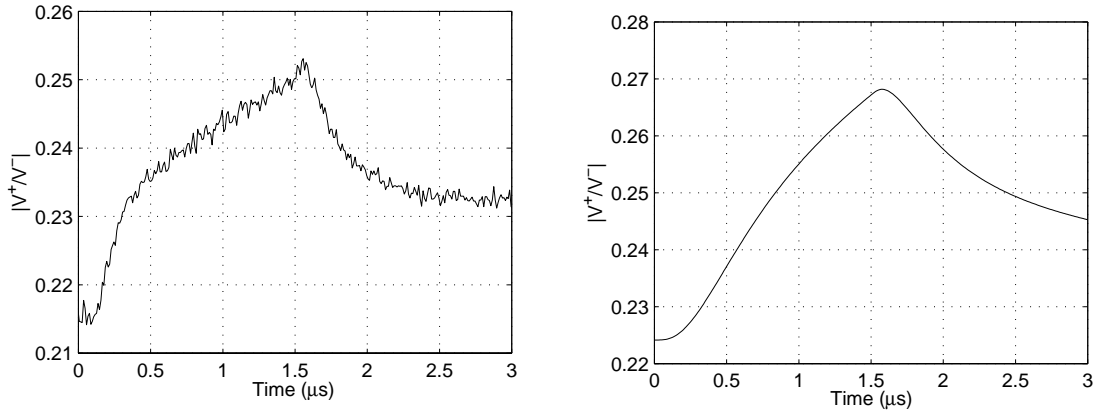


Figure 4.35: Measured and theoretical reflection coefficients from  $TE_{012}$  mode. Theoretical prediction is based on an 82 K calculated maximum temperature rise on the endcap.

shown in Figure 4.36. Notice that the measured reflected power has an initial large jump in the signal at the beginning of the RF pulse. Also, the reflected power flattens out instead of decaying back to its initial value. This is due to a long-time effect on the heating of the endcap that will be discussed later. This same effect applies to the measured phase as well.

Since equations (3.97) require the derivatives of the real and imaginary parts of the reflected power, the data must be smoothed because of the modulator noise. The signals are Fourier transformed and a low-pass filter is applied. The derivatives are obtained by multiplying the Fourier transforms by the frequency and inverting the convolutions back to the time domain.

Using the above procedure, the change in the unloaded cavity  $Q$  for the  $TE_{012}$  mode is determined using equations (3.97). It is also found from these equations that no measureable change occurs in  $\omega_{012}$  due to thermal expansion. The change in resonant frequency is only due to the change in  $Q$ . The measured change in  $Q_{012}$  using the waveforms depicted earlier is shown in Figure 4.37 along with the theoretical prediction using an 82 K calculated maximum temperature rise on the endcaps.

The initial measured value of  $Q_{012}$  is not equal to the value given in Table 4.7. This value depends on the initial steady-state response of the cavity. From the measurements of  $\beta$  described in an earlier section, it is known there is variation of the

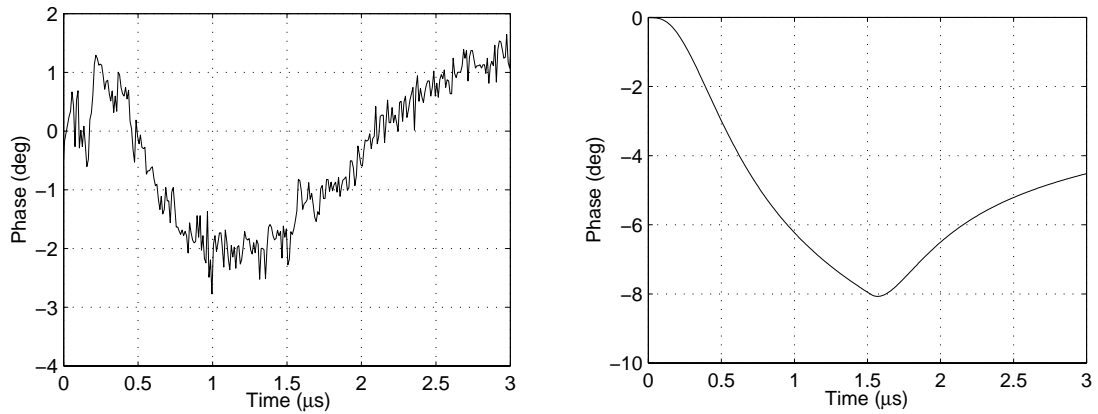


Figure 4.36: Measured and theoretical prediction in the change of phase of reflected power from  $TE_{012}$  mode. Theoretical prediction is based on 82 K calculated maximum temperature rise on the endcap.

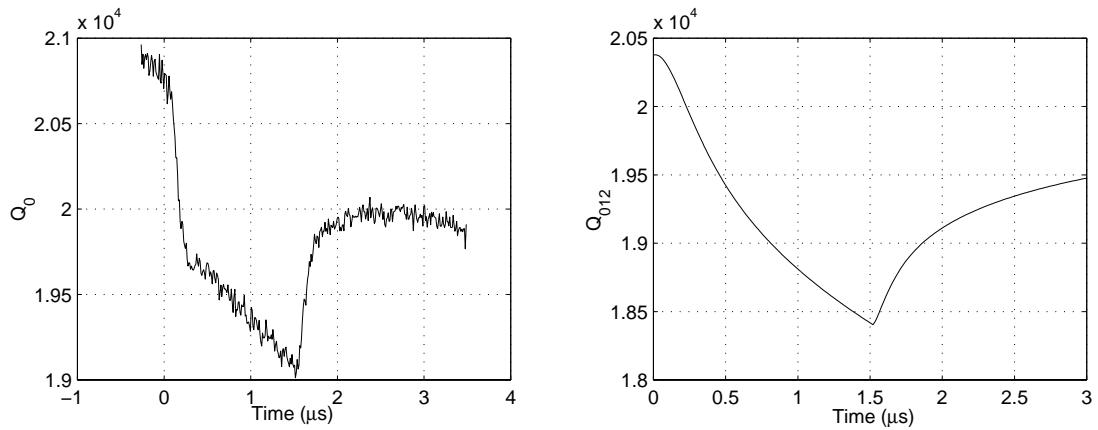


Figure 4.37: Measured and theoretical prediction of change in  $Q_{012}$  during a high-power pulse. Theoretical prediction is based on a 82 K maximum temperature rise on the endcap.

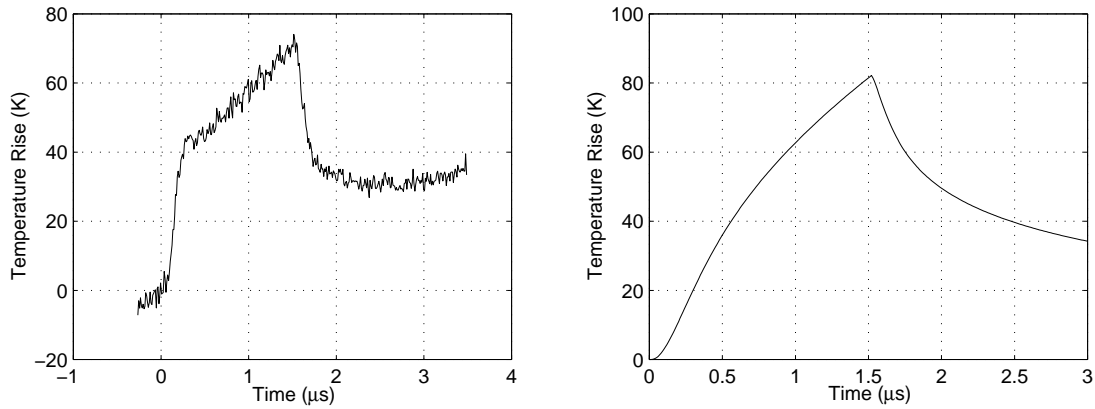


Figure 4.38: Measured and theoretical prediction of maximum temperature rise on the endcaps during a high-power pulse. Theoretical prediction is based on a 7.3 MW power input into the  $TE_{011}$  mode.

steady-state reflected power due to vibrations of the endcaps from the flow of cooling water. These same vibrations cause the DC levels of the mixer output to fluctuate. A correct estimate of the temperature rise on the endcap requires the initial value of  $Q_{012}$  to be accurate. Therefore, each measurement of the change in  $Q_{012}$  is corrected by subtracting the DC offsets. This is easily accomplished by making the initial value of  $Q_{012}$  equal to the value given in Table 4.7.

Using the measured value of  $Q_{012}$  in equation (3.101), the maximum temperature rise on the endcaps over time is inferred. Using the waveforms depicted earlier, Figure 4.38 shows the measured maximum temperature rise on the endcap along with the theoretical prediction based on an input power of 7.3 MW into the  $TE_{011}$  mode. Due to residual noise left on the waveforms, the random error associated with the measurement of temperature rise amounts to approximately 3%. In this case, the temperature rise is  $72 \pm 3$  K. The error in the resistivity of the endcaps reported in Table 4.9 corresponds to a systematic error of 3% in the determination of maximum temperature rise. Therefore the full range for the measured temperature rise is 66 K to 78 K. This is consistent with the calculated temperature rise of 82 K.

The measurement of maximum temperature rise on the endcaps for the first 20 million pulses of the high-power test is shown in Figure 4.39. The data is shown only for the first 20 million pulses since the response of the quadrature mixer degraded

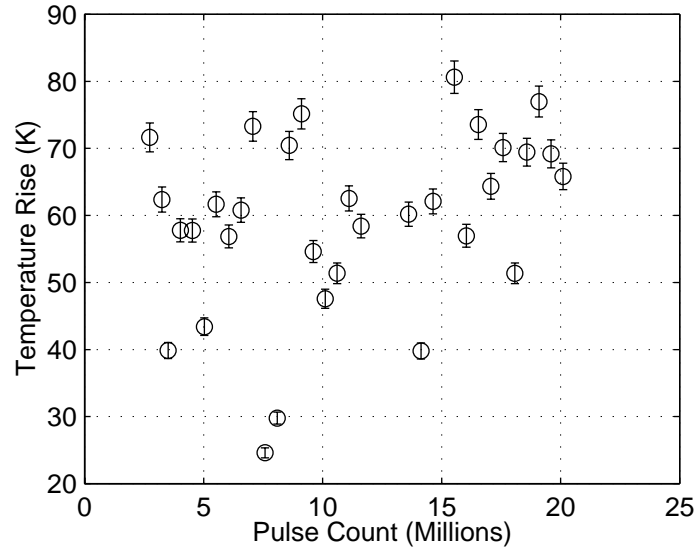


Figure 4.39: Measurement of maximum pulsed temperature rise on the endcaps for the first 20 million pulses of the second high-power test.

over time due to high input power levels during the measurement of  $\beta$  and  $Q_L$  for the  $TE_{012}$  mode. The diodes in the mixer output were damaged and their sensitivities were significantly diminished. This was not noticed initially since the raw outputs of the mixer are offset in phase. The result is a drop in signal amplitude from the same input power. If unchecked, the overall effect is a measured decline in pulsed temperature rise over time. The data show that the average temperature rise changed slowly from between 60 to 70 K to approximately 40 K at the end of the data taking run. Therefore, the calibration for the device was invalidated for the last 60 million pulses.

Although there is data scatter in the measurement of temperature rise, an eyeball average shows the temperature rise is between 60 K to 70 K with a general increase over time. However, the same initial  $Q_{012}$  given in Table 4.7 was always used. Ideally, the initial Q used should be the one measured over time as discussed previously. The data scatter in that measurement prevented any accurate assessment of the pulsed temperature rise.

Another possible error in the measurement of pulsed temperature rise is from long-term effects of pulsed heating. Figure 4.40 shows the evolution of this effect over

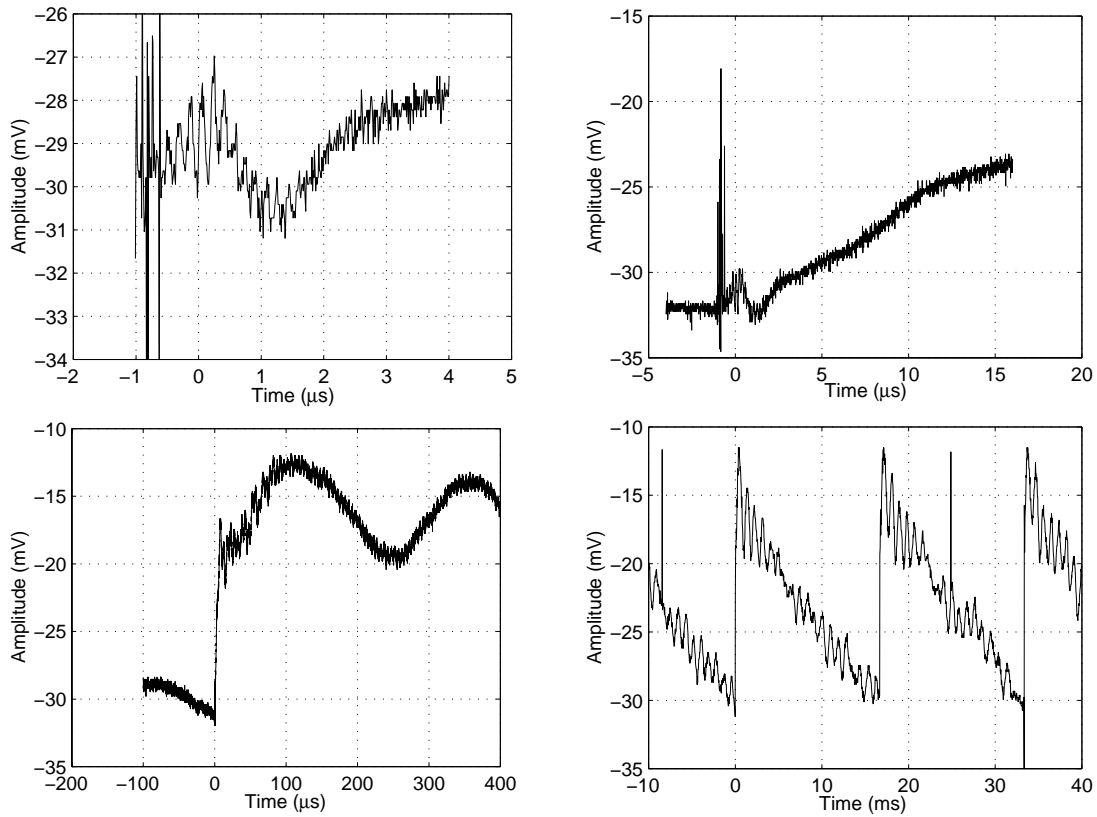


Figure 4.40: Evolution of long-time effect on measurement of pulsed temperature rise on wider time scales on one of the outputs of the quadrature mixer.

larger time scales on one of the outputs from the quadrature mixer. This effect occurs on both outputs of the quadrature mixer. A large ramp in the signal occurs after the RF pulse turns off at  $1.5 \mu\text{s}$ . A sinusoidal response occurs in the signal with a period of approximately  $250 \mu\text{s}$  corresponding to a frequency of  $4 \text{ kHz}$ . This response decays in time until another RF pulse occurs  $16.6 \text{ ms}$  later, which is the repetition rate of the klystron.

This signal response is likely due to stress waves that are launched at the surface of the endcap due to shock from pulsed heating of the surface. Since the endcaps are mounted on bellows, these stress waves cause the endcap positions in the cavity to vibrate. This is a likely conclusion because the signal disappears when the high-power RF is switched off. Also, this signal depends on the mode response of the cavity. Figure 4.41 shows the disappearance of the signal when  $\text{TE}_{012}$  mode is driven

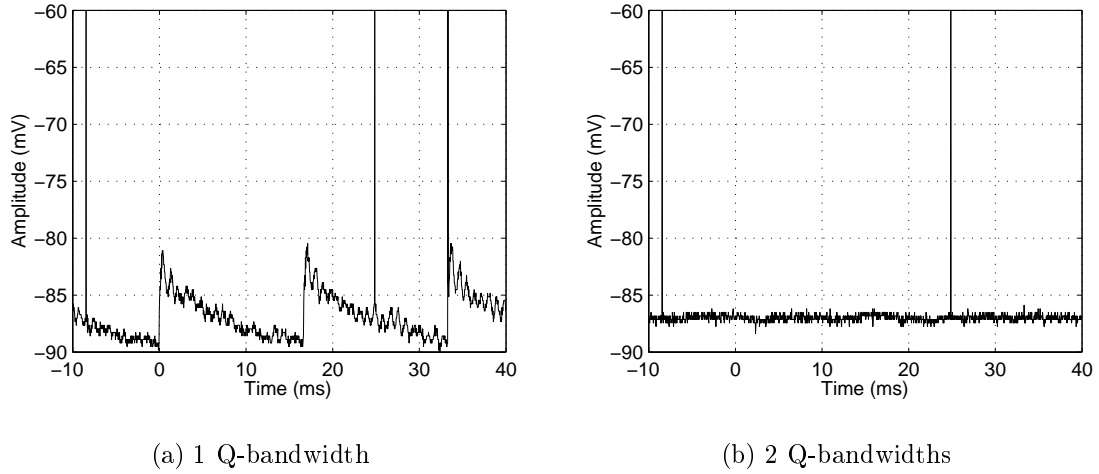


Figure 4.41: The response of the  $TE_{012}$  to stress waves disappears when cavity is driven more than 2 Q-bandwidths from its resonant frequency.

more than approximately 2 Q-bandwidths away from the mode's resonant frequency. The two spikes that occur in the plots are due to the RF switch that triggers between klystron pulses for the measurement of  $\beta_1$  and  $Q_L$ .

This signal response is the reason why the change in the reflected power to the  $TE_{012}$  mode does not return to zero after the klystron RF pulse switches off. A large signal spike occurs at this time. Also, at the beginning of the RF pulse, the signal is decaying from the previous klystron pulse. The signal from the heating of the surface of the endcap is convoluted with the response of the cavity mode to shock waves. This may explain why the initial cavity Q must be corrected. Also, the measurement of the overall Q change may also be influenced by this response which will cause an error in the determination of pulsed temperature rise.

#### 4.2.4 Visual Inspection of Copper Endcap Surface

As with the first high-power test, a visual change in the grains of both endcaps is obvious with the naked eye. Figure 4.42 shows the surface of each endcap after the high-power test. The band of damage occurs in the area of maximum temperature rise with a width between 6 and 8 mm. The width of the damage is wider near the azimuth

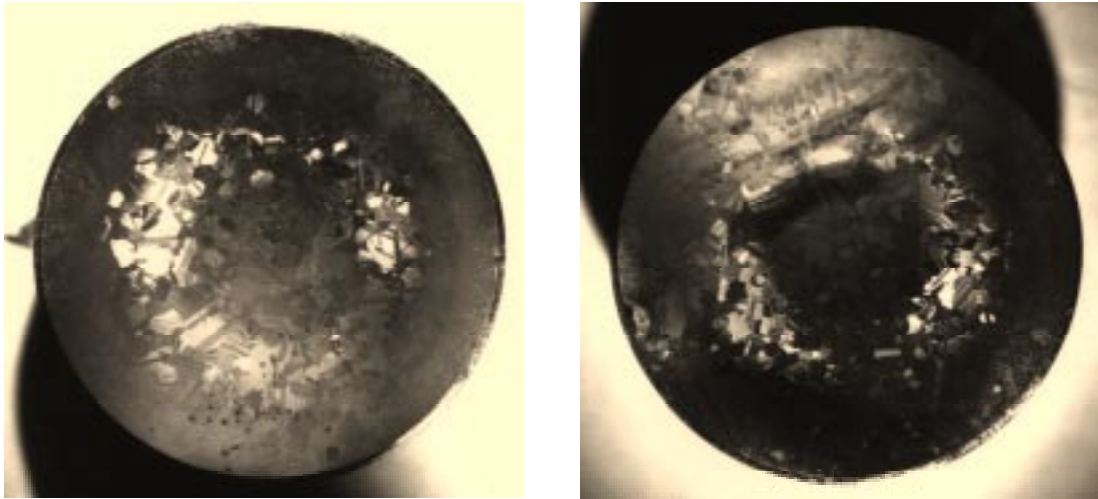


Figure 4.42: Surfaces of endcap 1L2 (left) and 1R2 (right) after high-power test. The position of the high-power coupling aperture relative to the pictures is the top of endcap 1L2 and top-left of endcap 1R2.

of the high-power coupling aperture. The surface magnetic field is approximately 5% higher there than at the point diametrically opposite of it. This corresponds to a higher temperature rise of approximately 10%. Notice at the far point that the band of damage is not visible.

The visual change across the surface is microscopically due to a change in the height of the grains. Grain growth occurs due to plastic deformation. The grains cannot expand laterally due to the constraint of the material, but they are allowed to expand from the free surface into vacuum.

There is some tarnish on the surface near the azimuth of the high-power coupling aperture. It will be shown in the next section that this tarnish is due to copper globules sputtered onto the surface from fatigue damage and RF breakdown at the high-power coupling aperture. However, the amount of copper sputtered is much less than the first high-power test due to a lower input power. Hence, it is reasonable to conclude that most of the resistivity change reported in Section 4.2.2 is due to fatigue damage. The fatigue damage will be more closely examined in the next section.

Another noticeable difference from the first high-power test is the absence of multipacting on the endcap surfaces. The surface magnetic field is approximately 15%

less than the first high-power test and is not sufficient to cause multipacting on the surface. Multipacting occurs over a small range of electron energies. In the first high-power test as reported in Section 4.1.5, multipacting only occurred over half of the surface due to variation of the magnetic field. The variation in that case is only 5% and is already sufficient to cease multipacting on the other half of the endcap. This is consistent with absence of multipacting in the second high-power test.

#### 4.2.5 Scanning Electron Microscope Inspection of Copper Endcap Surface

Just as described in Section 4.1.8, the two copper endcaps from the high-power test were examined with a scanning electron microscope (SEM) using secondary-scattering with a 5 kV electron beam. A scan along a diameter of each endcap was completed, and damage in the form of fatigue slip bands and cracks only occurred in the region of maximum temperature rise. The amount of cracking occurring on the endcaps is much less prevalent than with the endcaps from the first high-power test. This result is attributed to the lower pulsed temperature rise in this experimental run.

The results from this experimental run indicate that cracks only occur along grain boundaries. Grain boundaries are clearly seen between areas that contain fatigue slip bands and areas that do not have them. Figure 4.43 shows such a case in which a crack clearly occurs along a grain boundary in the area of maximum temperature rise of endcap 1R2. Cracks tend to nucleate at grain boundaries due to incompatibility of slip from one grain to the next. Incompatible slip will increase the local stress at a grain boundary.

Another example of this is given in Figure 4.44 where a crack develops along a grain boundary due to fatigue slip bands along one side. Also, multiple slip bands are seen to occur at different angles. This is due to multiple slip in which the applied shear stress will act along multiple slip planes [18, p. 29]. This can occur when the crystal axes of the grain are such that the applied shear stress is greater than a critical value on more than one slip system.

As a point of comparison, the picture on the left of Figure 4.45 shows a region

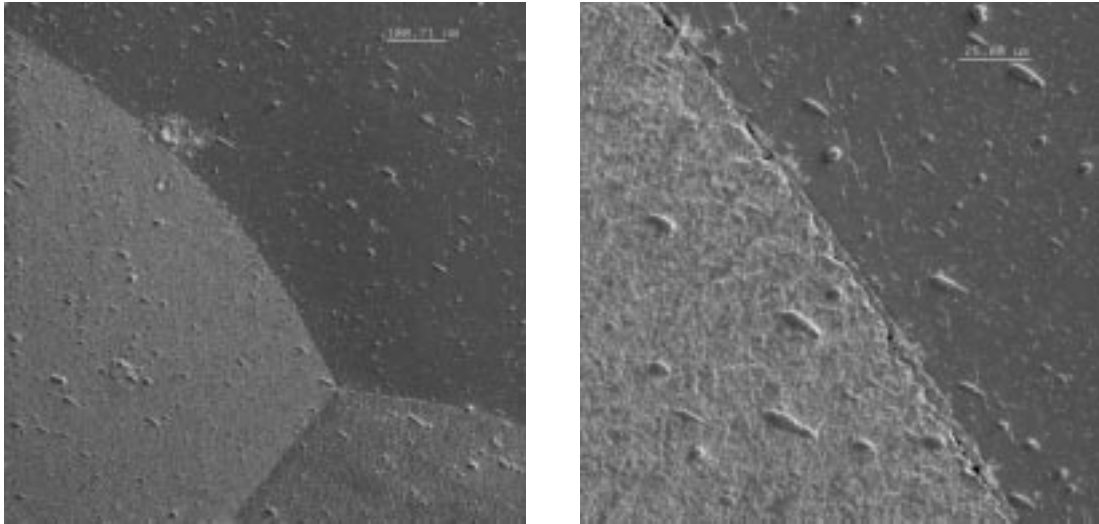


Figure 4.43: Grain-boundary cracks on endcap 1R2 in the area of maximum temperature rise. The grain boundary is the transition where the whitening due to slip bands stop. A close-up of one crack is on the right where the grain boundary is clear. The length scales are  $100.7 \mu\text{m}$  and  $25.0 \mu\text{m}$  respectively.

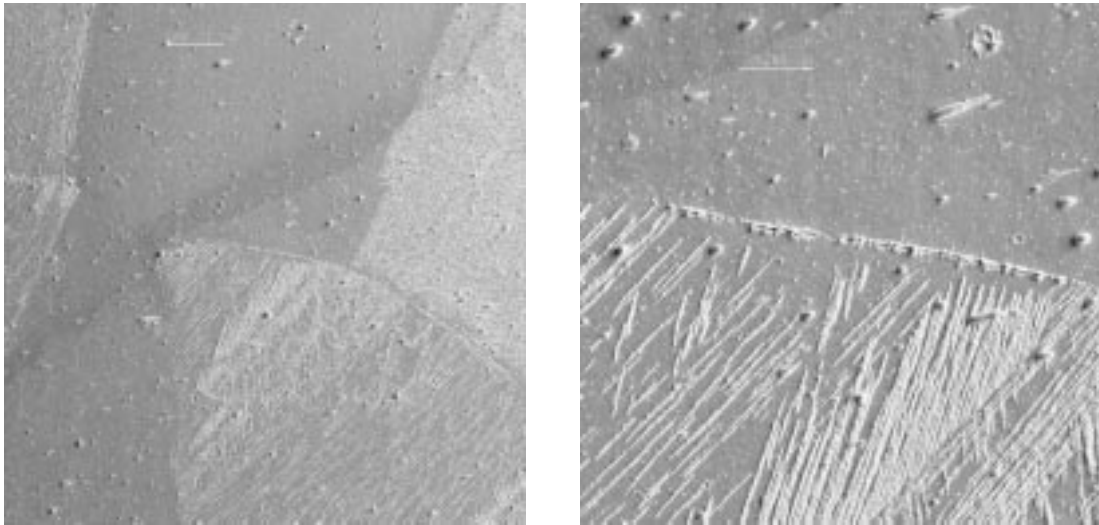


Figure 4.44: Grain-boundary crack on endcap 1R2 in the area of maximum temperature rise. A close-up of one crack is on the right where the grain boundary is clear. Multiple fatigue slip bands are also visible at different angles with one set more dense than the other. The length scales are  $100.7 \mu\text{m}$  and  $25.0 \mu\text{m}$  respectively.

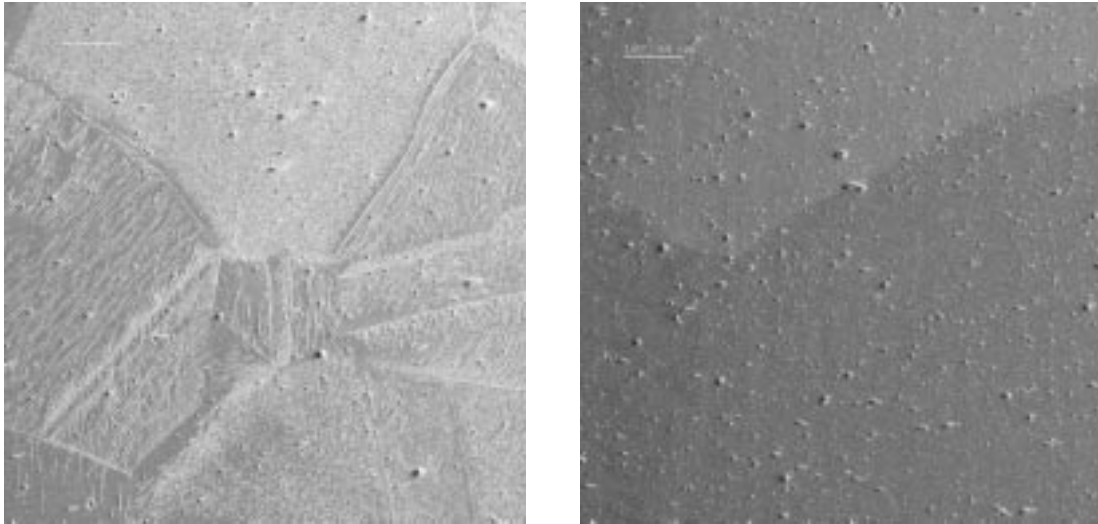


Figure 4.45: A comparison between a region in the area of maximum temperature rise on endcap 1R2 (left) and the center of the endcap in which the temperature rise is close to zero (right). The length scale is  $100.7\ \mu\text{m}$ .

in the area of maximum temperature rise of endcap 1R2 that shows a multitude of fatigue slip bands including grains with multiple slip. On the right is a region near the center of the endcap in which the pulsed temperature rise is close to zero. A grain boundary is evident from the change in contrast in the picture; however, no fatigue slip bands or cracks occur in this area. Also notice that by comparing these pictures to Figure 4.14 the amount of copper globules on the surface is much less than with the first high-power test. This supports the conclusion that the resistivity change is due to surface roughening and cracks on the surface of the endcaps.

Similar results are found on the surface of endcap 1L2. Figure 4.46 shows one such example where a crack occurs along a grain boundary.

In this experimental run, more fatigue bands and less cracks have occurred on the surface as compared to the first high-power test. This is expected to occur for small plastic strain. For higher amounts of plastic strain, the number of stress cycles spent causing fatigue slip bands decreases. More cycles are spent in crack nucleation and propagation.

For documentation purposes, additional pictures of the damage on endcaps 1L2 and 1R2 are shown in Appendix B.

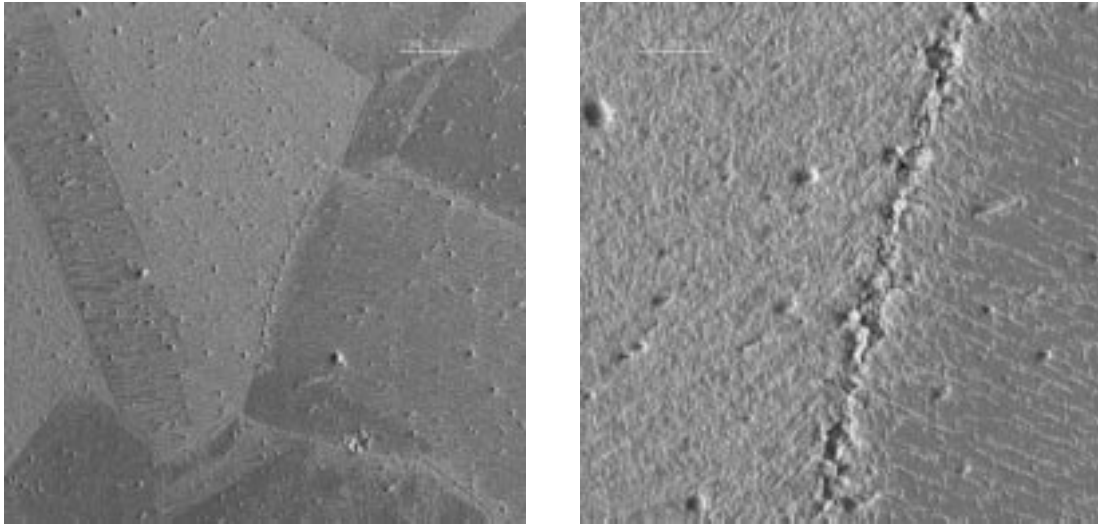


Figure 4.46: Grain-boundary crack for endcap 1L2 in the area of maximum temperature rise. A close-up of one crack is on the right where the grain boundary is clear. The scales are  $100.7\ \mu\text{m}$  and  $25.0\ \mu\text{m}$  respectively.

As with the first high-power test, a scan along a random diameter of each endcap at constant magnification was completed. Each snapshot covered an area approximately  $0.9\ \text{mm}$  by  $0.9\ \text{mm}$  in size. If a snapshot showed damage in the form of fatigue slip bands or surface roughening, a value of 1.2 was assigned. If a crack occurred in the area, a value of 1 was assigned. If no damage existed, a value of 0 was assigned. Figure 4.47 shows the results of these scans.

The plots show that surface roughening and slip bands occur around the area of maximum temperature rise at the radius  $10.6\ \text{mm}$ . The offset that occurs in the plot for endcap 1L2 is due to an offset of  $2\ \text{mm}$  of the scanned diameter from the center of the endcap. The center of the endcap was approximated at the time the diameters were scanned and determined more precisely afterwards. The small amount of cracks that were found do support the conclusion that surface roughening and slip bands are precursors to crack nucleation which corroborates the findings from the first high-power test. The widths of the regions of surface roughening and cracks are given in Table 4.15.

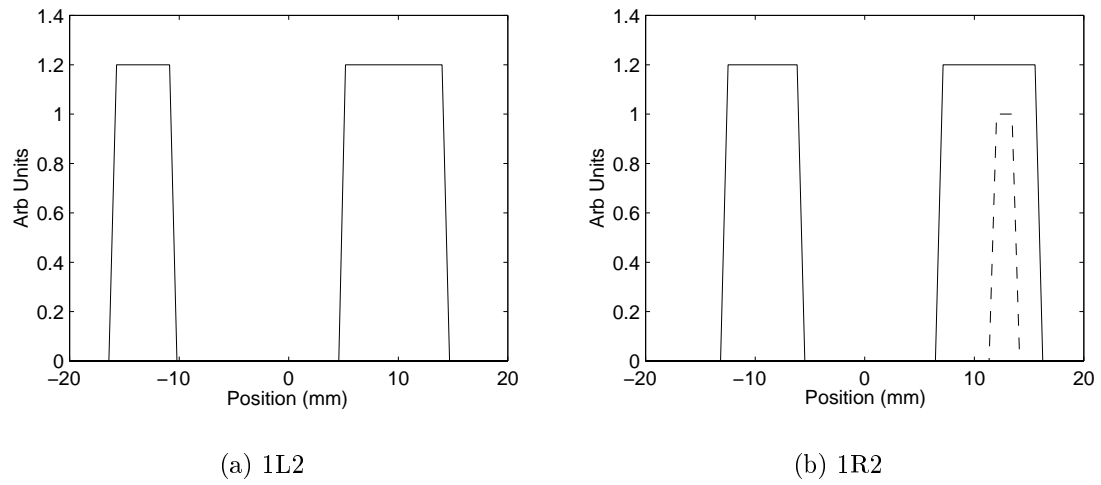


Figure 4.47: Random scans along diameters of each endcap. The solid line corresponds to regions of surface roughening and the dotted line is for regions that contain cracks on the surface.

Region	1L2 (mm)		1R2 (mm)	
	Roughness	4.8	8.8	6.3
Cracks	0.0	0.0	0.0	1.4

Table 4.15: Widths of regions of surface roughening and cracks for endcaps 1L2 and 1R2.

# Chapter 5

## Conclusion

In the previous chapters, we have described the design and execution of an experiment to study the effects of pulsed heating on the surface of OFE copper. The damage that results from pulsed heating will impact future designs of high-energy particle accelerators.

We have demonstrated that the cyclic stress induced by pulsed heating beyond the yield stress of fully-annealed OFE copper results in damage to the surface in the form of surface roughening and cracks. The two experiments have shown such damage to occur at 56 million pulses at a calculated  $120 \pm 10$  K temperature rise on the surface and at 86 million pulses at a calculated temperature rise of  $82 \pm 3$  K on the surface. The measurements of pulsed temperature rise are in reasonable agreement with the calculations for the second high-power test. From the destruction of the high-power coupling aperture, we also know that 56 million pulses at a temperature rise of approximately 250 K will create enough cracks to cause local melting of the surface. Cracks cause the electrical resistivity of the surface to increase; consequently, the temperature rise increases for the same applied power density.

Since the cavity Q depends on the electrical resistivity of the surface, surface roughening and cracks that ensue will degrade the RF properties of a device long before catastrophic damage like melting and copper sputtering occur. The numbers given above are not thresholds for damage to occur. The lifetime of a material damaged from cyclic fatigue will in general follow a power-law parameterization as

given in equation (1.25).

The threshold for damage from pulsed heating is not known. From the data reported above, a design for an accelerator must be well below these temperature rises for a reasonable lifetime. The prediction given in Chapter 1 for a threshold of 40 ° temperature rise is not too conservative. It is commonly known that cyclic fatigue is highly dependent on the preparation of the surface. The light chemical etch performed on the surface for vacuum preparation may significantly reduce the lifetime of the material. Grain boundaries are primary sites for crack nucleation, and the etching of material within the grain boundaries can increase the stress concentration in that area. However, the two high-power tests already conducted followed standard procedures for the preparation of the copper surface. These tests are indicative of the danger that pulsed heating poses for future accelerator designs.

Some possibilities exist for increasing the lifetime of accelerators for these same temperature rises. One is to look for material with good electrical conductivities and high yield strengths. Glidcop is one example. It has the same electrical conductivity as copper, yet its yield strength when fully annealed is six times that of OFE copper's. The yield strength determines the point at which applied stress causes plastic deformation. A higher yield strength will increase the material's tolerance to higher temperature rises.

Another possibility is to operate at a lower ambient temperature. Due to lower electrical resistivity and higher thermal conductivity, using OFE copper at liquid nitrogen temperature ( $T=77$  K), the temperature rise from pulsed heating may be reduced by a factor of 2 for the same applied power density to the surface.

Third, the copper surface may be coated with diamond with a thickness on the order of the heat diffusion length [32]. Diamond has a higher thermal conductivity than copper and will act as a heat sink for the fast temperature rises from pulsed heating. This heat sink may reduce the temperature rise on the surface of copper by a factor of 2 or 3.

This experiment has shown that pulsed heating is an important limit to achievable acceleration gradients for future accelerators. Due to the dependence of surface preparation on material lifetime, this experiment was more of a test of the process

of building accelerators than just a test of the material itself. Many tests should be performed at different power levels and with different surface preparations before a definite conclusion is made.

# Appendix A

## Resonant Cavities

Resonant cavities are devices in which electromagnetic fields resonate in a space enclosed by good conducting walls. The theory describing resonant cavities is well-known and can be found in numerous references on electricity and magnetism and microwave circuits [14, 20, 28, 39, 45, 57]. The equations describing resonant cavities will be derived in this chapter under a formalism adapted from [28, 57] that allows easy computation of the heating of the conducting walls in the cavity.

### A.1 Maxwell's Equations

The description of resonant cavities begins with Maxwell's equations

$$\vec{\nabla} \times \vec{E} = -\frac{\partial \vec{B}}{\partial t}, \quad (\text{A.1a})$$

$$\vec{\nabla} \times \vec{H} = \frac{\partial \vec{D}}{\partial t} + \vec{J}, \quad (\text{A.1b})$$

$$\vec{\nabla} \cdot \vec{D} = \rho_{chg}, \quad (\text{A.1c})$$

$$\vec{\nabla} \cdot \vec{B} = 0, \quad (\text{A.1d})$$

where  $\vec{E}$  is the electric field,  $\vec{H}$  is the magnetic field,  $\vec{D}$  is the electric displacement,  $\vec{B}$  is the magnetic induction,  $\vec{J}$  is the current density and  $\rho_{chg}$  is the charge density. Since we are interested in the fields in vacuum enclosed by perfectly conducting walls

where there are no external charges and no external currents we have

$$\rho_{chg} = 0, \quad (\text{A.2a})$$

$$\vec{J} = 0, \quad (\text{A.2b})$$

$$\vec{D} = \varepsilon_0 \vec{E}, \quad (\text{A.2c})$$

$$\vec{B} = \mu_0 \vec{H}, \quad (\text{A.2d})$$

where  $\varepsilon_0$  is the electric permittivity of vacuum and  $\mu_0$  is the magnetic permeability of vacuum. Using the above conditions, Maxwell's equations take the form

$$\vec{\nabla} \times \vec{E} = -\mu_0 \frac{\partial \vec{H}}{\partial t}, \quad (\text{A.3a})$$

$$\vec{\nabla} \times \vec{H} = \varepsilon_0 \frac{\partial \vec{E}}{\partial t}, \quad (\text{A.3b})$$

$$\vec{\nabla} \cdot \vec{E} = 0, \quad (\text{A.3c})$$

$$\vec{\nabla} \cdot \vec{H} = 0. \quad (\text{A.3d})$$

If we take the *curl* of both sides of equation (A.3a) we get

$$\begin{aligned} \vec{\nabla} \times \vec{\nabla} \times \vec{E} &= \vec{\nabla} \left( \vec{\nabla} \cdot \vec{E} \right) - \nabla^2 \vec{E} = -\nabla^2 \vec{E} \\ &= -\mu_0 \frac{\partial}{\partial t} \vec{\nabla} \times \vec{H} = -\mu_0 \varepsilon_0 \frac{\partial^2 \vec{E}}{\partial t^2}, \end{aligned} \quad (\text{A.4})$$

where we have used equations (A.3b) and (A.3c). Since the speed of light in vacuum is given by  $c = 1/\sqrt{\mu_0 \varepsilon_0}$  equation (A.4) becomes

$$\nabla^2 \vec{E} - \frac{1}{c^2} \frac{\partial^2 \vec{E}}{\partial t^2} = 0. \quad (\text{A.5})$$

Similarly if we take the *curl* of both sides of equation (A.3b) and substitute equations (A.3a) and (A.3d) into the result we arrive at

$$\nabla^2 \vec{H} - \frac{1}{c^2} \frac{\partial^2 \vec{H}}{\partial t^2} = 0. \quad (\text{A.6})$$

When we include the boundary conditions that the tangential electric field and the normal magnetic field must vanish on the surface of a perfect conductor we get

$$\left[ \nabla^2 - \frac{1}{c^2} \frac{\partial^2}{\partial t^2} \right] \begin{Bmatrix} \vec{E}(\vec{r}, t), \\ \vec{H}(\vec{r}, t) \end{Bmatrix} = 0 \quad \text{in volume V,} \quad (\text{A.7a})$$

$$\hat{n} \times \vec{E}(\vec{r}, t) = 0 \quad \text{on surface S,} \quad (\text{A.7b})$$

$$\hat{n} \cdot \vec{H}(\vec{r}, t) = 0 \quad \text{on surface S,} \quad (\text{A.7c})$$

where  $\hat{n}$  is the unit normal on the surface pointing out of the cavity volume into the conductor. Equation (A.7a) is known as the vector Helmholtz equation and can be used to solve for either  $\vec{E}$  or  $\vec{H}$ . Once one field is found, the other can be found from Maxwell's equations.

If we consider the cavity in steady-state oscillation at the angular frequency  $\omega$  then the fields may be assumed to have a harmonic time-dependence of  $e^{-j\omega t}$  where  $j = \sqrt{-1}$ . Using this assumption in equation (A.7a) we get

$$[\nabla^2 + k^2] \begin{Bmatrix} \vec{E}(\vec{r}) \\ \vec{H}(\vec{r}) \end{Bmatrix} = 0, \quad (\text{A.8a})$$

$$k = \omega/c, \quad (\text{A.8b})$$

where  $k$  is known as the wavenumber. Maxwell's equations have been reduced to an eigenvalue equation with eigenvalue  $k$  and eigenfunctions  $\vec{E}$  and  $\vec{H}$ . This fact suggests that we may expand the electromagnetic fields in cavities in terms of modes with eigenvalue  $k$ .

## A.2 Expansion of Electromagnetic Fields in Cavities

Kurokawa [27] is credited to be the first to do a full treatment of the problem of expansion of electromagnetic fields in cavities. A similar treatment will be shown here adapted from [20, 28, 57].

### A.2.1 Basis Functions

We will enumerate the modes in a cavity with index  $\lambda$  which have eigenvalues  $k_\lambda$  and eigenfrequencies  $\omega_\lambda = k_\lambda c$ . For the electric field we will choose basis functions  $\vec{E}_\lambda$  and expansion coefficients  $e_\lambda$ . Likewise for the magnetic field we have basis functions  $\vec{H}_\lambda$  and expansion coefficients  $h_\lambda$ . The total fields are now written as

$$\vec{E}(\vec{r}, t) = \sum_{\lambda} \vec{E}_\lambda(\vec{r}) e_\lambda(t), \quad (\text{A.9a})$$

$$\vec{H}(\vec{r}, t) = \sum_{\lambda} \vec{H}_\lambda(\vec{r}) h_\lambda(t). \quad (\text{A.9b})$$

The basis functions  $\vec{E}_\lambda$  are chosen such that they are real and orthonormal. The orthogonality of the basis functions can be shown for non-degenerate modes with  $\lambda \neq \lambda'$ :

$$\begin{aligned} (k_\lambda^2 - k_{\lambda'}^2) \int dV \vec{E}_\lambda \cdot \vec{E}_{\lambda'} &= \int dV \left[ \vec{E}_\lambda \cdot \nabla^2 \vec{E}_{\lambda'} - \vec{E}_{\lambda'} \cdot \nabla^2 \vec{E}_\lambda \right] \\ &= \int dV \vec{\nabla} \cdot \left[ \vec{E}_\lambda \times (\vec{\nabla} \times \vec{E}_{\lambda'}) - \vec{E}_{\lambda'} \times (\vec{\nabla} \times \vec{E}_\lambda) \right] \\ &= \int dS \hat{n} \cdot \left[ \vec{E}_\lambda \times (\vec{\nabla} \times \vec{E}_{\lambda'}) - \vec{E}_{\lambda'} \times (\vec{\nabla} \times \vec{E}_\lambda) \right] \\ &= \int dS \left[ (\vec{\nabla} \times \vec{E}_{\lambda'}) \cdot (\hat{n} \times \vec{E}_\lambda) - (\vec{\nabla} \times \vec{E}_\lambda) \cdot (\hat{n} \times \vec{E}_{\lambda'}) \right] \\ &= 0, \end{aligned} \quad (\text{A.10})$$

where we have used equations (A.7b) and (A.8a) and the vector identity

$$\vec{\nabla} \cdot (\vec{f} \times \vec{g}) = \vec{g} \cdot (\vec{\nabla} \times \vec{f}) - \vec{f} \cdot (\vec{\nabla} \times \vec{g}). \quad (\text{A.11})$$

If degenerate modes exist then they may be orthogonalized using the Gram-Schmidt orthogonalization procedure [40, pp. 928–935]. Hence, we have the condition

$$\int dV \vec{E}_\lambda(\vec{r}) \cdot \vec{E}_{\lambda'}(\vec{r}) = \delta_{\lambda, \lambda'}. \quad (\text{A.12})$$

The basis functions for the magnetic field are defined according to

$$\vec{\nabla} \times \vec{E}_\lambda = k_\lambda \vec{H}_\lambda, \quad (\text{A.13a})$$

$$\vec{\nabla} \times \vec{H}_\lambda = k_\lambda \vec{E}_\lambda, \quad (\text{A.13b})$$

which are also orthonormal

$$\begin{aligned} \int dV \vec{H}_\lambda(\vec{r}) \cdot \vec{H}_{\lambda'}(\vec{r}) &= \frac{1}{k_\lambda k_{\lambda'}} \int dV (\vec{\nabla} \times \vec{E}_\lambda) \cdot (\vec{\nabla} \times \vec{E}_{\lambda'}) \\ &= \frac{1}{k_\lambda k_{\lambda'}} \int dV \vec{\nabla} \cdot [\vec{E}_{\lambda'} \times (\vec{\nabla} \times \vec{E}_\lambda)] \\ &\quad + \frac{1}{k_\lambda k_{\lambda'}} \int dV \vec{E}_{\lambda'} \cdot (\vec{\nabla} \times \vec{\nabla} \times \vec{E}_\lambda) \\ &= \frac{1}{k_\lambda k_{\lambda'}} \int dS \hat{n} \cdot [\vec{E}_{\lambda'} \times (\vec{\nabla} \times \vec{E}_\lambda)] + \frac{k_\lambda}{k_{\lambda'}} \int dV \vec{E}_{\lambda'} \cdot \vec{E}_\lambda \\ &= \frac{1}{k_\lambda k_{\lambda'}} \int dS (\hat{n} \times \vec{E}_{\lambda'}) \cdot (\vec{\nabla} \times \vec{E}_\lambda) + \frac{k_\lambda}{k_{\lambda'}} \delta_{\lambda, \lambda'} \\ &= \delta_{\lambda, \lambda'}. \end{aligned} \quad (\text{A.14})$$

Using the above orthogonality conditions, the expansion coefficients can be determined as

$$e_\lambda(t) = \int dV \vec{E}_\lambda(\vec{r}) \cdot \vec{E}(\vec{r}, t), \quad (\text{A.15a})$$

$$h_\lambda(t) = \int dV \vec{H}_\lambda(\vec{r}) \cdot \vec{H}(\vec{r}, t). \quad (\text{A.15b})$$

It is proven in [28] that these basis functions form a complete set.

### A.2.2 Cavity Modes

We will only be considering cylindrical waveguides and cavities whose axes lie along  $\hat{z}$  (see Figure A.1), so it will be convenient to separate the perpendicular and longi-

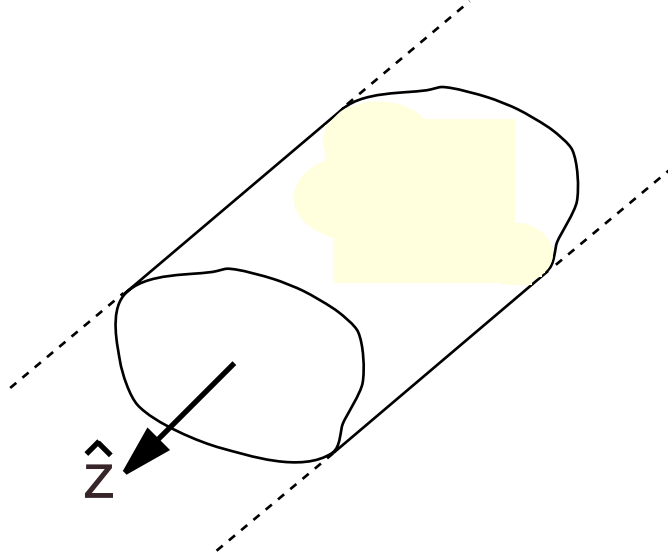


Figure A.1: Cylindrical waveguide of arbitrary cross-section with axis along  $\hat{z}$ .

tudinal components of the fields as follows

$$\vec{E}_\lambda = \vec{E}_{\lambda\perp} + \hat{z}E_{\lambda z}, \quad (\text{A.16a})$$

$$\vec{H}_\lambda = \vec{H}_{\lambda\perp} + \hat{z}H_{\lambda z}. \quad (\text{A.16b})$$

Using the definition of the basis functions (equations (A.13)) and the following vector identity

$$\vec{f} \times (\vec{\nabla} \times \vec{g}) = \vec{\nabla} (\vec{f} \cdot \vec{g}) - (\vec{g} \cdot \vec{\nabla}) \vec{f} - (\vec{f} \cdot \vec{\nabla}) \vec{g} - \vec{g} \times (\vec{\nabla} \times \vec{f}), \quad (\text{A.17})$$

we get the following relation

$$\begin{aligned}
\hat{z} \times (\vec{\nabla} \times \vec{E}_\lambda) &= \hat{z} \times (\vec{\nabla} \times \vec{E}_{\lambda\perp}) + \hat{z} \times (\vec{\nabla} \times \hat{z} E_{\lambda z}) \\
&= \vec{\nabla} (\hat{z} \cdot \vec{E}_{\lambda\perp}) - (\hat{z} \cdot \vec{\nabla}) \vec{E}_{\lambda\perp} + \vec{\nabla} [\hat{z} \cdot (E_{\lambda z} \hat{z})] - (\hat{z} \cdot \vec{\nabla}) E_{\lambda z} \hat{z} \\
&= k_\lambda \hat{z} \times \vec{H}_\lambda \\
&= k_\lambda \hat{z} \times \vec{H}_{\lambda\perp}.
\end{aligned} \tag{A.18}$$

If we define  $\vec{\nabla}_\perp \equiv \vec{\nabla} - \hat{z} \partial / \partial z$  and use the fact that  $\hat{z} \cdot \vec{\nabla} = \partial / \partial z$  we arrive at the following useful relation

$$-\frac{\partial \vec{E}_{\lambda\perp}}{\partial z} + \vec{\nabla}_\perp E_{\lambda z} = k_\lambda \hat{z} \times \vec{H}_{\lambda\perp}. \tag{A.19}$$

Similarly, the procedure may be repeated for the magnetic field and we get

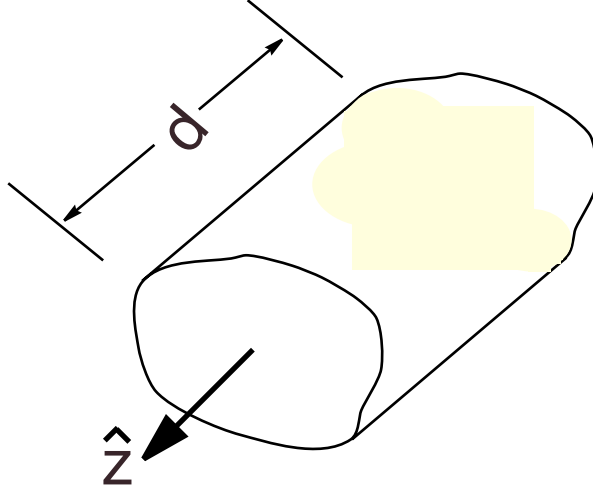
$$-\frac{\partial \vec{H}_{\lambda\perp}}{\partial z} + \vec{\nabla}_\perp H_{\lambda z} = k_\lambda \hat{z} \times \vec{E}_{\lambda\perp}. \tag{A.20}$$

Since the fields are propagating in the z-direction with wavenumber  $k$ , we may assume an  $e^{\pm j k z}$  dependence for the fields where the top sign is for a forward-travelling wave and the bottom sign is for a backward-travelling wave. Substituting this condition into equations (A.19) and (A.20) we get

$$\mp j k \vec{E}_{\lambda\perp} + \vec{\nabla}_\perp E_{\lambda z} = k_\lambda \hat{z} \times \vec{H}_{\lambda\perp}, \tag{A.21a}$$

$$\mp j k \vec{H}_{\lambda\perp} + \vec{\nabla}_\perp H_{\lambda z} = k_\lambda \hat{z} \times \vec{E}_{\lambda\perp}. \tag{A.21b}$$

There are two sets of modes that can exist inside hollow waveguides and cavities. One set of modes is known as the *transverse electric mode* or *TE mode* in which the longitudinal electric field is zero everywhere in the cavity volume. The other set of modes is known as the *transverse magnetic mode* or *TM mode* in which the longitudinal magnetic field is zero everywhere in the cavity volume. We shall look at each mode set in more detail separately.

Figure A.2: Closed cavity of length  $d$  with arbitrary cross-section.**TE mode**

By substituting the condition  $E_{\lambda z} = 0$  into equations (A.21) we get

$$\vec{E}_{\lambda\perp} = \pm j \frac{k_\lambda}{k} \hat{z} \times \vec{H}_{\lambda\perp}, \quad (\text{A.22a})$$

$$\vec{H}_{\lambda\perp} = \pm j \frac{k}{\gamma_\lambda^2} \vec{\nabla}_\perp H_{\lambda z}, \quad (\text{A.22b})$$

$$\gamma_\lambda^2 = k_\lambda^2 - k^2. \quad (\text{A.22c})$$

Notice that once the longitudinal magnetic field is determined, the rest of the fields can be calculated from equations (A.22).

If we consider a cavity that has conducting walls normal to the  $z$ -direction at a distance  $d$  from each other (see Figure A.2), we expect to have a standing wave in that direction. The longitudinal magnetic field should vary as

$$H_{\lambda z} \sim A \sin(kz) + B \cos(kz). \quad (\text{A.23})$$

The normal component of the magnetic field must vanish on the surface (equation (A.7c)) so

$$H_{\lambda z}(z = 0) = B = 0, \quad (\text{A.24a})$$

$$H_{\lambda z}(z = d) = A \sin(kd) = 0, \quad (\text{A.24b})$$

$$k = \frac{p\pi}{d}, \quad (\text{A.24c})$$

where  $p$  is a positive integer not equal to zero.  $p = 0$  is not an interesting solution since it implies that the fields are zero everywhere in the cavity volume. Thus the longitudinal magnetic field has the form

$$H_{\lambda z} = \psi_{\lambda}(\vec{r}_{\perp}) \sin\left(\frac{p\pi z}{d}\right) \quad p = 1, 2, 3, \dots, \quad (\text{A.25})$$

where  $\psi_{\lambda}$  is a function of the perpendicular coordinates to be determined later. Substituting equation (A.25) into equations (A.22) and separating the forward and backward travelling waves we calculate the other fields as follows

$$\vec{H}_{\lambda\perp} = \frac{p\pi/d}{\gamma_{\lambda}^2} \cos\left(\frac{p\pi z}{d}\right) \vec{\nabla}_{\perp} \psi_{\lambda}(\vec{r}_{\perp}), \quad (\text{A.26a})$$

$$\vec{E}_{\lambda\perp} = -\frac{k_{\lambda}}{\gamma_{\lambda}^2} \sin\left(\frac{p\pi z}{d}\right) \hat{z} \times \vec{\nabla}_{\perp} \psi_{\lambda}(\vec{r}_{\perp}), \quad (\text{A.26b})$$

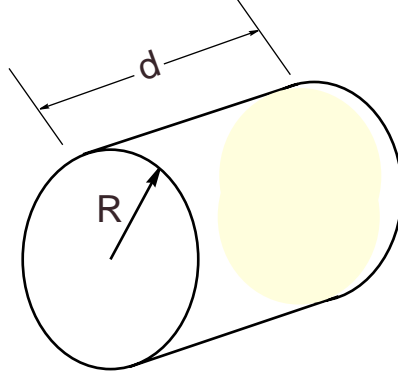
$$\gamma_{\lambda}^2 = k_{\lambda}^2 - \left(\frac{p\pi}{d}\right)^2. \quad (\text{A.26c})$$

$\psi_{\lambda}$  is determined by substituting equation (A.25) into equations (A.7)

$$[\nabla_{\perp}^2 + \gamma_{\lambda}^2] \psi_{\lambda}(\vec{r}_{\perp}) = 0. \quad (\text{A.27})$$

The above equation is true for any arbitrary cross-section of the cavity. The boundary condition for  $\psi_{\lambda}$  on the surface  $S$  of the cavity is found by taking the dot product of both sides of equation (A.21b) with  $\hat{n}$

$$\mp jk \left( \hat{n} \cdot \vec{H}_{\lambda\perp} \right) \Big|_S + \hat{n} \cdot \vec{\nabla}_{\perp} H_{\lambda z} \Big|_S = k_{\lambda} \hat{n} \cdot \hat{z} \times \vec{E}_{\lambda\perp} \Big|_S = -k_{\lambda} \hat{z} \cdot \left( \hat{n} \times \vec{E}_{\lambda\perp} \Big|_S \right). \quad (\text{A.28})$$

Figure A.3: Circularly cylindrical cavity of radius  $R$  and length  $d$ .

Since  $\hat{n} \cdot \vec{H}_{\lambda\perp} = 0$  and  $\hat{n} \times \vec{E}_{\lambda\perp} = 0$  on the cavity surface, we have

$$\hat{n} \cdot \vec{\nabla}_{\perp} H_{\lambda z} \Big|_S = \hat{n} \cdot \vec{\nabla}_{\perp} \psi_{\lambda}(\vec{r}_{\perp}) \Big|_S = 0. \quad (\text{A.29})$$

Since the experiment involves circularly cylindrical cavities, we will focus only on that geometry where  $\psi_{\lambda}(\vec{r}_{\perp}) = \psi_{\lambda}(r, \phi)$  (see Figure A.3). For a cavity with radius  $R$  we must solve the following equation

$$\frac{1}{r} \frac{\partial}{\partial r} \left( r \frac{\partial \psi_{\lambda}}{\partial r} \right) + \frac{1}{r^2} \frac{\partial^2 \psi_{\lambda}}{\partial \phi^2} + \gamma_{\lambda}^2 \psi_{\lambda} = 0, \quad (\text{A.30a})$$

$$\frac{\partial \psi_{\lambda}}{\partial r} \Big|_{r=R} = 0. \quad (\text{A.30b})$$

If we choose a reference such that  $H_{\lambda z} \sim \cos \phi$  then the general solution to equation (A.30a) is

$$\psi_{\lambda} = A_{TE} \cos(n\phi) J_n(\gamma_{\lambda} r), \quad (\text{A.31})$$

where we ignored  $Y_n(\gamma_{\lambda} r)$  since the fields must be finite at  $r = 0$ .  $A_{TE}$  is a normalization constant to be determined later. Applying the boundary condition (equation (A.30b))

$$\gamma_{\lambda} = \frac{x'_{nm}}{R} \quad \text{where} \quad J'_n(x'_{nm}) = 0, \quad (\text{A.32})$$

we get

$$\psi_\lambda = A_{TE} J_n \left( \frac{x'_{nm} r}{R} \right) \cos(n\phi). \quad (\text{A.33})$$

Substituting equation (A.33) into equations (A.25) and (A.26) we arrive at the fields for the TE modes of a circularly cylindrical cavity of radius  $R$  and length  $d$ :

$$H_{\lambda z} = A_{TE} \sin \left( \frac{p\pi z}{d} \right) J_n \left( \frac{x'_{nm} r}{R} \right) \cos(n\phi), \quad (\text{A.34a})$$

$$H_{\lambda r} = A_{TE} \frac{p\pi R}{dx'_{nm}} \cos \left( \frac{p\pi z}{d} \right) J'_n \left( \frac{x'_{nm} r}{R} \right) \cos(n\phi), \quad (\text{A.34b})$$

$$H_{\lambda\phi} = -A_{TE} \frac{np\pi R^2}{rd (x'_{nm})^2} \cos \left( \frac{p\pi z}{d} \right) J_n \left( \frac{x'_{nm} r}{R} \right) \sin(n\phi), \quad (\text{A.34c})$$

$$E_{\lambda z} = 0, \quad (\text{A.34d})$$

$$E_{\lambda r} = -A_{TE} \frac{n\omega_\lambda R^2}{cr (x'_{nm})^2} \sin \left( \frac{p\pi z}{d} \right) J_n \left( \frac{x'_{nm} r}{R} \right) \sin(n\phi), \quad (\text{A.34e})$$

$$E_{\lambda\phi} = -A_{TE} \frac{\omega_\lambda R}{cx'_{nm}} \sin \left( \frac{p\pi z}{d} \right) J'_n \left( \frac{x'_{nm} r}{R} \right) \cos(n\phi), \quad (\text{A.34f})$$

$$\omega_\lambda = c \left[ \left( \frac{x'_{nm}}{R} \right)^2 + \left( \frac{p\pi}{d} \right)^2 \right]^{1/2}, \quad (\text{A.34g})$$

where we have used  $k_\lambda = \omega_\lambda/c$ . We may now distinguish the modes by specifying the integers  $n$ ,  $m$ , and  $p$  and writing the modes as  $\text{TE}_{nmp}$ . The normalization constant  $A_{TE}$  is determined by substituting the fields into equation (A.12). Using the following integral [45, eqn. C.17]

$$\int_0^{x'_{nm}} \left[ J_n'^2(u) + \frac{n^2}{u^2} J_n^2(u) \right] u \, du = \frac{(x'_{nm})^2}{2} \left[ 1 - \frac{n^2}{(x'_{nm})^2} \right] J_n^2(x'_{nm}), \quad (\text{A.35})$$

we get

$$A_{TE} = \sqrt{\frac{2}{\pi d} \frac{c (x'_{nm})^2}{\omega_\lambda R^2 \sqrt{1 + \delta_{n0}}}} \left\{ \frac{(x'_{nm})^2}{2} \left[ 1 - \frac{n^2}{(x'_{nm})^2} \right] J_n^2(x'_{nm}) \right\}^{-1/2}. \quad (\text{A.36})$$

**TM mode**

The derivation of the fields for the TM modes is similar to that for the TE modes. Substituting the condition that  $H_{\lambda z} = 0$  into equations (A.21) and assuming an  $e^{\pm jkz}$  dependence as before we get

$$\vec{H}_{\lambda\perp} = \pm j \frac{k_\lambda}{k} \hat{z} \times \vec{E}_{\lambda\perp}, \quad (\text{A.37a})$$

$$\vec{E}_{\lambda\perp} = \pm \frac{k}{\gamma_\lambda^2} \vec{\nabla}_\perp E_{\lambda z}. \quad (\text{A.37b})$$

Because there is a standing-wave in the z-direction, the longitudinal electric field must also have the form

$$E_{\lambda z} \sim A \sin(kz) + B \cos(kz). \quad (\text{A.38})$$

Since the tangential electric field  $\vec{E}_{\lambda\perp}$  must vanish on the surface of the cavity we must have  $\vec{\nabla}_\perp \cdot \vec{E}_{\lambda\perp} = -\partial E_{\lambda z} / \partial z = 0$ . Therefore we have

$$\left. \frac{\partial E_{\lambda z}}{\partial z} \right|_{z=0} = Ak = 0, \quad (\text{A.39a})$$

$$\left. \frac{\partial E_{\lambda z}}{\partial z} \right|_{z=d} = -B \sin(kd) = 0, \quad (\text{A.39b})$$

$$k = \frac{p\pi}{d}, \quad (\text{A.39c})$$

where  $p$  is a non-negative integer. Thus the longitudinal electric field takes the form

$$E_{\lambda z} = \psi_\lambda(\vec{r}_\perp) \cos\left(\frac{p\pi z}{d}\right) \quad p = 0, 1, 2, \dots \quad (\text{A.40})$$

By separating the forward and backward travelling waves and substituting equation (A.40) into equations (A.37) we have

$$\vec{E}_{\lambda\perp} = -\frac{p\pi z/d}{\gamma_\lambda^2} \sin\left(\frac{p\pi z}{d}\right) \vec{\nabla}_\perp \psi_\lambda(\vec{r}_\perp), \quad (\text{A.41a})$$

$$\vec{H}_{\lambda\perp} = -\frac{k_\lambda}{\gamma_\lambda^2} \cos\left(\frac{p\pi z}{d}\right) \hat{z} \times \vec{\nabla}_\perp \psi_\lambda(\vec{r}_\perp), \quad (\text{A.41b})$$

$$\gamma_\lambda^2 = k_\lambda^2 - \left(\frac{p\pi}{d}\right)^2. \quad (\text{A.41c})$$

Substituting equation (A.40) into equations (A.7) we get the same governing equation as for the TE mode (equation (A.30a)) except with the boundary condition  $\psi_\lambda(r=R)=0$ . With this boundary condition we have

$$\gamma_\lambda = \frac{x_{nm}}{R} \quad \text{where} \quad J_n(x_{nm}) = 0. \quad (\text{A.42})$$

The general solution is then

$$\psi_\lambda = A_{TM} J_n\left(\frac{x_{nm}r}{R}\right) \cos(n\phi). \quad (\text{A.43})$$

The fields for the TM mode are given by (using equations (A.40) and (A.41))

$$E_{\lambda z} = A_{TM} \cos\left(\frac{p\pi z}{d}\right) J_n\left(\frac{x_{nm}r}{R}\right) \cos(n\phi), \quad (\text{A.44a})$$

$$E_{\lambda r} = -A_{TM} \frac{p\pi R}{dx_{nm}} \sin\left(\frac{p\pi z}{d}\right) J'_n\left(\frac{x_{nm}r}{R}\right) \cos(n\phi), \quad (\text{A.44b})$$

$$E_{\lambda\phi} = A_{TM} \frac{np\pi R^2}{rdx_{nm}^2} \sin\left(\frac{p\pi z}{d}\right) J_n\left(\frac{x_{nm}r}{R}\right) \sin(n\phi), \quad (\text{A.44c})$$

$$H_{\lambda z} = 0, \quad (\text{A.44d})$$

$$H_{\lambda r} = -A_{TM} \frac{n\omega_\lambda R^2}{rcx_{nm}^2} \cos\left(\frac{p\pi z}{d}\right) J_n\left(\frac{x_{nm}r}{R}\right) \sin(n\phi), \quad (\text{A.44e})$$

$$H_{\lambda\phi} = -A_{TM} \frac{\omega_\lambda R}{cx_{nm}} \cos\left(\frac{p\pi z}{d}\right) J'_n\left(\frac{x_{nm}r}{R}\right) \cos(n\phi), \quad (\text{A.44f})$$

$$\omega_\lambda = c \left[ \left(\frac{x_{nm}}{R}\right)^2 + \left(\frac{p\pi}{d}\right)^2 \right]^{1/2}, \quad (\text{A.44g})$$

where we have used  $k_\lambda = \omega_\lambda/c$ . We may now specify the TM modes with  $\text{TM}_{nmp}$ . The normalization constant  $A_{TM}$  is determined by substituting the fields into equation (A.14). Using the following integral [45, eqn. C.16]

$$\int_0^{x_{nm}} \left[ J_n'^2(u) + \frac{n^2}{u^2} J_n^2(u) \right] u \, du = \frac{x_{nm}^2}{2} J_n'^2(x_{nm}), \quad (\text{A.45})$$

we get

$$A_{TM} = \frac{2cx_{nm}}{\sqrt{\pi d} \omega_\lambda R^2 J_n'(x_{nm}) \sqrt{(1 + \delta_{n0})(1 + \delta_{p0})}}. \quad (\text{A.46})$$

### A.3 Time-domain

In the previous section we derived the basis functions for the expansion of electromagnetic fields in cavities. In this section we are interested in the behavior of the fields in the time-domain.

If we consider a closed-cavity with perfectly conducting walls, then we may simply substitute equations (A.9) into the Maxwell curl equations (equations (A.3a–A.3b)) to get

$$\eta \frac{dh_\lambda(t)}{dt} = -\omega_\lambda e_\lambda(t), \quad (\text{A.47a})$$

$$\frac{de_\lambda(t)}{dt} = \eta \omega_\lambda h_\lambda(t), \quad (\text{A.47b})$$

where  $\eta = \sqrt{\mu_0/\varepsilon_0}$  is the impedance of free space. Combining the above equations we get for the fields

$$\left[ \frac{d^2}{dt^2} + \omega_\lambda^2 \right] \begin{Bmatrix} e_\lambda(t) \\ h_\lambda(t) \end{Bmatrix} = 0, \quad (\text{A.48})$$

where  $\omega_\lambda$  is the angular resonant frequency of the cavity for mode  $\lambda$  as expected.

In reality, the conducting walls of a cavity are not lossless. These walls have a finite conductivity, and the electromagnetic fields will penetrate into the surface. Also, the cavity cannot be completely closed. There must be some openings in the device in order for the fields to be excited. Because of these two conditions, the basis functions derived in the last section are no longer exact. However, we will incorporate these

conditions as perturbations and use the previous basis functions as approximations to the mode fields in the cavity [57]. Thus we will still write the mode amplitudes as

$$e_\lambda(t) = \int dV \vec{E}(\vec{r}, t) \cdot \vec{E}_\lambda(\vec{r}), \quad (\text{A.49a})$$

$$h_\lambda(t) = \int dV \vec{H}(\vec{r}, t) \cdot \vec{H}_\lambda(\vec{r}), \quad (\text{A.49b})$$

where the integrals are over the unperturbed cavity volume. We will next obtain equations for the mode amplitudes for a weakly perturbed cavity.

If we take the dot product of equation (A.3a) with  $\vec{H}_\lambda(\vec{r})$  and integrate over the unperturbed cavity volume we get for the left-hand side

$$\begin{aligned} \int dV (\vec{\nabla} \times \vec{E}) \cdot \vec{H}_\lambda &= \int dV \vec{\nabla} \cdot (\vec{E} \times \vec{H}_\lambda) + \int dV (\vec{\nabla} \times \vec{H}_\lambda) \cdot \vec{E} \\ &= \int dS \hat{n} \cdot \vec{E} \times \vec{H}_\lambda + \int dV (k_\lambda \vec{E}_\lambda) \cdot \vec{E} \\ &= k_\lambda e_\lambda + \int dS \hat{n} \cdot \vec{E} \times \vec{H}_\lambda, \end{aligned} \quad (\text{A.50})$$

where we have used equation (A.49a) and the vector identity

$$\vec{\nabla} \cdot (\vec{f} \times \vec{g}) = (\vec{\nabla} \times \vec{f}) \cdot \vec{g} - (\vec{\nabla} \times \vec{g}) \cdot \vec{f}. \quad (\text{A.51})$$

$\hat{n}$  is the unit normal pointing out of the cavity (see Figure A.4) and the surface integral is over the unperturbed cavity boundary. The right-hand side of equation (A.3a) becomes

$$-\mu_0 \int dV \frac{\partial \vec{H}}{\partial t} \cdot \vec{H}_\lambda = -\mu_0 \sum_{\lambda'} \frac{dh_{\lambda'}}{dt} \int dV \vec{H}_{\lambda'} \cdot \vec{H}_\lambda = -\mu_0 \frac{dh_\lambda}{dt}, \quad (\text{A.52})$$

where we have used equation (A.49b). Putting these equations together we have for the mode amplitudes

$$-\mu_0 \frac{dh_\lambda(t)}{dt} = k_\lambda e_\lambda(t) + \int dS \hat{n} \cdot \vec{E}(\vec{r}, t) \times \vec{H}_\lambda(\vec{r}). \quad (\text{A.53})$$

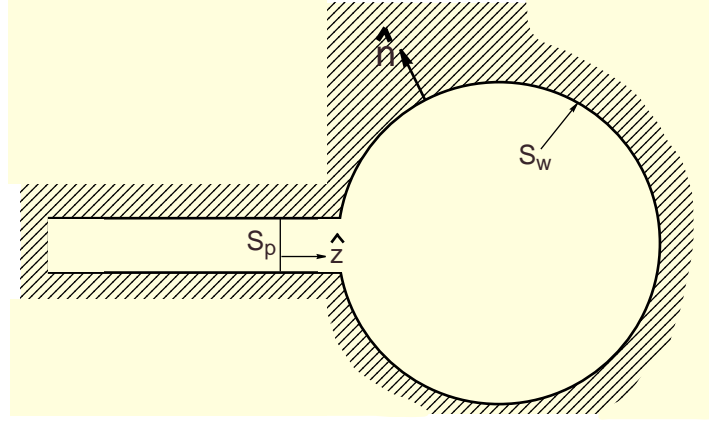


Figure A.4: Cavity with connecting waveguide.  $\hat{n}$  points out of the cavity and into the conductor.  $S_p$  is the reference plane for the waveguide and  $S_w$  is the cavity wall.

Similarly, by taking the dot product of equation (A.3b) with  $\vec{E}_\lambda(\vec{r})$  we have

$$\varepsilon_0 \frac{de_\lambda(t)}{dt} = k_\lambda h_\lambda(t) + \int dS \hat{n} \cdot \vec{H}(\vec{r}, t) \times \vec{E}_\lambda(\vec{r}). \quad (\text{A.54})$$

We are interested in a cavity in which power is coupled to it through an input waveguide. Since we are only working to first-order in the perturbations, we may consider each perturbation separately and add them together. Thus we may determine the mode amplitudes with

$$-\mu_0 \frac{dh_\lambda(t)}{dt} = k_\lambda e_\lambda(t) + \int_{S_w} dS \hat{n} \cdot \vec{E}(\vec{r}, t) \times \vec{H}_\lambda(\vec{r}) + \int_{S_p} dS \hat{n} \cdot \vec{E}(\vec{r}, t) \times \vec{H}_\lambda(\vec{r}), \quad (\text{A.55a})$$

$$\varepsilon_0 \frac{de_\lambda(t)}{dt} = k_\lambda h_\lambda(t) + \int_{S_w} dS \hat{n} \cdot \vec{H}(\vec{r}, t) \times \vec{E}_\lambda(\vec{r}) + \int_{S_p} dS \hat{n} \cdot \vec{H}(\vec{r}, t) \times \vec{E}_\lambda(\vec{r}), \quad (\text{A.55b})$$

where  $S_w$  is over the cavity surface and  $S_p$  is over the plane cross-section of the connecting waveguide (see Figure A.4).

To make the calculation of the perturbations more simple, we will assume the

fields to have an  $e^{-j\omega t}$  dependence

$$\vec{E}(\vec{r}, t) = \tilde{E}(\vec{r}, t)e^{-j\omega t}, \quad \vec{H}(\vec{r}, t) = \tilde{H}(\vec{r}, t)e^{-j\omega t}, \quad (\text{A.56})$$

$$\vec{e}_\lambda(t) = \tilde{e}_\lambda(t)e^{-j\omega t}, \quad \vec{h}_\lambda(t) = \tilde{h}_\lambda(t)e^{-j\omega t}, \quad (\text{A.57})$$

where  $\tilde{E}(\vec{r}, t)$ ,  $\tilde{H}(\vec{r}, t)$ ,  $\tilde{e}_\lambda(t)$  and  $\tilde{h}_\lambda(t)$  are complex slowly-varying functions of time. Substituting these relations into equations (A.55) we have for the mode amplitudes in the cavity

$$-\mu_0 \frac{d\tilde{h}_\lambda(t)}{dt} + j\mu_0\omega\tilde{h}_\lambda = k_\lambda \tilde{e}_\lambda(t) + \int_{S_w} dS \hat{n} \cdot \tilde{E}(\vec{r}, t) \times \vec{H}_\lambda(\vec{r}) + \int_{S_p} dS \hat{n} \cdot \tilde{E}(\vec{r}, t) \times \vec{H}_\lambda(\vec{r}), \quad (\text{A.58})$$

$$\varepsilon_0 \frac{d\tilde{e}_\lambda(t)}{dt} - j\varepsilon_0\omega\tilde{e}_\lambda = k_\lambda \tilde{h}_\lambda(t) + \int_{S_w} dS \hat{n} \cdot \tilde{H}(\vec{r}, t) \times \vec{E}_\lambda(\vec{r}) + \int_{S_p} dS \hat{n} \cdot \tilde{H}(\vec{r}, t) \times \vec{E}_\lambda(\vec{r}). \quad (\text{A.59})$$

We will look at each perturbation in more detail separately.

### A.3.1 Perturbation From Lossy Walls

When the finite conductivity of the cavity walls is included in the analysis, the fields no longer vanish inside the conductor. The fields will exponentially decay into the conductor. We will investigate the fields inside a conductor by starting with Ampere's law

$$\vec{\nabla} \times \vec{H}_c = \frac{\partial \vec{D}_c}{\partial t} + \vec{J}_c, \quad (\text{A.60})$$

where the current density  $\vec{J}_c$  inside a conductor is given by

$$\vec{J}_c = \sigma \vec{E}_c, \quad (\text{A.61})$$

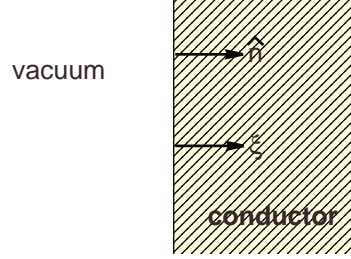


Figure A.5: Conductor with coordinate  $\xi$  normal to the surface and pointing into the conductor.

where  $\sigma$  is the electrical conductivity of the conductor. Inside the conductor we expect the displacement current to be small compared to the electrical current, so we may neglect it in Ampere's law. We also expect the spatial variation of the fields normal to the surface to be more rapid than the variation of the fields tangential to the surface. So we may ignore any derivatives with respect to the transverse coordinates and write  $\vec{\nabla} \approx \hat{n} \partial / \partial \xi$  where  $\hat{n}$  is the unit normal pointing into the conductor (see Figure A.5). Note that this is opposite of the convention adopted by [20]. The condition for the electric field in the conductor is then

$$\vec{E}_c = \frac{1}{\sigma} \vec{\nabla} \times \vec{H}_c = \frac{1}{\sigma} \hat{n} \times \frac{\partial \vec{H}_c}{\partial \xi}. \quad (\text{A.62})$$

If we use Faraday's law

$$\vec{\nabla} \times \vec{E}_c = -\mu_c \frac{\partial \vec{H}_c}{\partial t}, \quad (\text{A.63})$$

and take the curl of both sides of Ampere's law we get the following equation for the magnetic field inside the conductor

$$\nabla^2 \vec{H}_c - \mu_c \sigma \frac{\partial \vec{H}_c}{\partial t} = 0, \quad (\text{A.64})$$

where  $\mu_c$  is the magnetic permeability of the conductor. If we adopt the phasor

notation in equations (A.56) and keep to first-order by making the approximation

$$\left| \frac{\partial \tilde{H}_c}{\partial t} \right| \ll \omega \tilde{H}_c, \quad (\text{A.65})$$

then the magnetic field in the conductor is given by

$$\nabla^2 \tilde{H}_c + j \mu_c \sigma \omega \tilde{H}_c = 0, \quad (\text{A.66})$$

or, noting that only the tangential magnetic field will be significant, we can write

$$\frac{d^2}{d\xi^2} \tilde{H}_{\parallel} + j \frac{2}{\delta^2} \tilde{H}_{\parallel} = 0, \quad (\text{A.67})$$

where we have introduced the skin-depth

$$\delta = \sqrt{\frac{2}{\mu_c \sigma \omega}}. \quad (\text{A.68})$$

The solution for the magnetic field is

$$\tilde{H}_{\parallel}(\xi) = \tilde{H}_{\parallel}(\xi = 0) \exp \left[ -\frac{\xi}{\delta} (1 - j) \right]. \quad (\text{A.69})$$

The boundary condition for the tangential electric field at the cavity surface is then

$$\tilde{E} \Big|_{\text{surf}} = \frac{1}{\sigma} \hat{n} \times \frac{d\tilde{H}_{\parallel}}{d\xi} \Big|_{\text{surf}} = -\frac{1-j}{\sigma \delta} \hat{n} \times \tilde{H} \Big|_{\text{surf}} = -R_s (1-j) \hat{n} \times \tilde{H} \Big|_{\text{surf}}, \quad (\text{A.70})$$

where we have defined the surface resistance of the conductor as

$$R_s \equiv \frac{1}{\sigma \delta} = \sqrt{\frac{\mu_c \omega}{2\sigma}} = \sqrt{\frac{\mu_c \omega \rho_{res}}{2}}, \quad (\text{A.71})$$

where  $\rho_{res} = 1/\sigma$  is the electrical resistivity.

We now use this result to find the perturbation due to lossy walls. The surface

integral for the cavity wall in equation (A.58) is calculated as

$$\begin{aligned}
\int_{S_w} dS \hat{n} \cdot \tilde{\mathbf{E}} \times \vec{H}_\lambda &= - \int_{S_w} dS \hat{n} \cdot \left[ R_s(1-j)\hat{n} \times \tilde{\mathbf{H}} \right] \times \vec{H}_\lambda \\
&= \int_{S_w} dS R_s(1-j)\hat{n} \cdot \left[ \hat{n} \left( \vec{H}_\lambda \cdot \tilde{\mathbf{H}} \right) - \tilde{\mathbf{H}} \left( \hat{n} \cdot \vec{H}_\lambda \right) \right] \\
&= \int_{S_w} dS R_s(1-j)\tilde{\mathbf{H}} \cdot \vec{H}_\lambda,
\end{aligned} \tag{A.72}$$

where we have used the boundary condition that  $\hat{n} \cdot \vec{H}_\lambda = 0$  on the cavity surface. If we assume that only one mode in the cavity is excited then we may approximate the magnetic field as  $\tilde{\mathbf{H}} \approx \tilde{h}_\lambda \vec{H}_\lambda$ . If we also define the unloaded Q of the cavity for mode  $\lambda$  to be

$$\frac{1}{Q_{0\lambda}} \equiv \int_{S_w} dS \frac{\delta}{2} \left| \vec{H}_\lambda \right|^2 = \frac{1}{\sqrt{2\mu_c\omega}} \int_{S_w} dS \frac{1}{\sqrt{\sigma}} \left| \vec{H}_\lambda \right|^2, \tag{A.73}$$

then equation (A.72) is finally calculated as

$$\begin{aligned}
\int_{S_w} dS \hat{n} \cdot \tilde{\mathbf{E}} \times \vec{H}_\lambda &\approx \tilde{h}_\lambda \int_{S_w} dS R_s(1-j) \left| \vec{H}_\lambda \right|^2 \\
&= \tilde{h}_\lambda(1-j) \sqrt{\frac{\mu_c\omega}{2}} \int_{S_w} dS \frac{1}{\sqrt{\sigma}} \left| \vec{H}_\lambda \right|^2 \\
&= \frac{(1-j)\mu_c\omega}{Q_{0\lambda}} \tilde{h}_\lambda.
\end{aligned} \tag{A.74}$$

The surface integral for the cavity wall in equation (A.59) vanishes as shown below

$$\int_{S_w} dS \hat{n} \cdot \tilde{\mathbf{H}} \times \vec{E}_\lambda = - \int_{S_w} dS \tilde{\mathbf{H}} \cdot \hat{n} \times \vec{E}_\lambda = 0, \tag{A.75}$$

since  $\hat{n} \times \vec{E}_\lambda = 0$  on the surface of the cavity.

### A.3.2 Perturbation From Connecting Waveguide

The fields inside a cylindrical waveguide are completely defined if the fields parallel to the plane normal to the cylindrical axis are given [14, 45]. Similar to the cavity

fields, we may expand the perpendicular waveguide fields into modes  $a$  [57]

$$\vec{E}_\perp(\vec{r}_\perp, t) = \sum_a \vec{E}_{\perp a}(\vec{r}_\perp) V_a(t), \quad (\text{A.76a})$$

$$\vec{H}_\perp(\vec{r}_\perp, t) = \sum_a \vec{H}_{\perp a}(\vec{r}_\perp) Z_{ca} I_a(t), \quad (\text{A.76b})$$

where  $\vec{E}_{\perp a}$  and  $\vec{H}_{\perp a}$  are the basis functions for mode  $a$  and  $V_a$  and  $I_a$  are the expansion coefficients.  $Z_{ca}$  is the characteristic impedance for mode  $a$  and is given by

$$Z_{ca} = \eta \begin{cases} k_0/k_g & \text{for TE mode} \\ k_g/k_0 & \text{for TM mode,} \end{cases} \quad (\text{A.77})$$

where  $k_g^2 = k_0^2 - k_c^2$  and  $k_0 = \omega/c$ .  $k_c$  is the cutoff-wavenumber and for a rectangular waveguide operating in the dominant TE<sub>10</sub> mode with width  $w$ ,  $k_c = \pi/2w$ . The waveguide fields are also related by

$$Z_{ca} \vec{H}_{\perp a} = \hat{z} \times \vec{E}_{\perp a}, \quad (\text{A.78})$$

where the cylindrical axis of the waveguide is along  $\hat{z}$ . If we choose the plane  $S_p$  as the reference plane then we get the following orthogonality relations for the fields [57]

$$\int_{S_p} dS \vec{E}_{\perp a}(\vec{r}_\perp) \cdot \vec{E}_{\perp b}(\vec{r}_\perp) = \delta_{ab}, \quad (\text{A.79a})$$

$$\int_{S_p} dS \vec{H}_{\perp a}(\vec{r}_\perp) \cdot \vec{H}_{\perp b}(\vec{r}_\perp) = \frac{\delta_{ab}}{Z_{ca}^2}, \quad (\text{A.79b})$$

$$\int_{S_p} dS \hat{z} \cdot \vec{E}_{\perp a}(\vec{r}_\perp) \times \vec{H}_{\perp b}(\vec{r}_\perp) = \frac{\delta_{ab}}{Z_{ca}}. \quad (\text{A.79c})$$

We may also expand the cavity fields along the plane  $S_p$  by using the same waveguide basis functions but with different expansion coefficients

$$\vec{E}_{\perp\lambda}(\vec{r}_{\perp}) = \sum_a \vec{E}_{\perp a}(\vec{r}_{\perp}) V_{a\lambda}, \quad (\text{A.80a})$$

$$\vec{H}_{\perp\lambda}(\vec{r}_{\perp}) = \sum_a \vec{H}_{\perp a}(\vec{r}_{\perp}) Z_{ca} I_{a\lambda}, \quad (\text{A.80b})$$

where  $V_{a\lambda}$  and  $I_{a\lambda}$  are given by overlap integrals of the waveguide and cavity modes on plane  $S_p$

$$V_{a\lambda} = \int_{S_p} dS \vec{E}_{\lambda}(\vec{r}_{\perp}) \cdot \vec{E}_{\perp a}(\vec{r}_{\perp}), \quad (\text{A.81a})$$

$$I_{a\lambda} = Z_{ca} \int_{S_p} dS \vec{H}_{\lambda}(\vec{r}_{\perp}) \cdot \vec{H}_{\perp a}(\vec{r}_{\perp}). \quad (\text{A.81b})$$

As before with the cavity modes, we will adopt phasor notation for the waveguide expansion coefficients

$$V_a(t) = \tilde{V}_a(t) e^{-j\omega t}, \quad I_a(t) = \tilde{I}_a(t) e^{-j\omega t}, \quad (\text{A.82})$$

where we assume  $\tilde{V}_a$  and  $\tilde{I}_a$  are complex slowly-varying functions of time. Using the above relations we may now calculate the surface integral over the waveguide plane in equation (A.58) as

$$\begin{aligned} \int_{S_p} dS \hat{n} \cdot \tilde{\vec{E}} \times \vec{H}_{\lambda} &= \int_{S_p} dS \hat{n} \cdot \left[ \sum_a \vec{E}_{\perp a} \tilde{V}_a \right] \times \left[ \sum_b \vec{H}_{\perp b} Z_{cb} I_{b\lambda} \right] \\ &= - \sum_a \sum_b \tilde{V}_a Z_{cb} I_{b\lambda} \int_{S_p} dS \hat{z} \cdot \vec{E}_{\perp a} \times \vec{H}_{\perp b} \\ &= - \sum_a \sum_b \tilde{V}_a Z_{cb} I_{b\lambda} \frac{\delta_{ab}}{Z_{ca}} \\ &= - \sum_a \tilde{V}_a I_{a\lambda}, \end{aligned} \quad (\text{A.83})$$

where we have used equation (A.79c) and the fact that  $\hat{z}$  points in the opposite

direction of  $\hat{n}$  (see Figure A.4). The surface integral over the waveguide plane in equation (A.59) is calculated as

$$\begin{aligned}
\int_{S_p} dS \hat{n} \cdot \tilde{\mathbf{H}} \times \vec{\mathbf{E}}_\lambda &= \int_{S_p} dS \hat{n} \cdot \left[ \sum_a \vec{\mathbf{H}}_{\perp a} Z_{ca} \tilde{I}_a \right] \times \left[ \sum_b \vec{\mathbf{E}}_{\perp b} V_{b\lambda} \right] \\
&= - \sum_a \sum_b Z_{ca} \tilde{I}_a V_{b\lambda} \int_{S_p} dS \hat{z} \cdot \vec{\mathbf{H}}_{\perp a} \times \vec{\mathbf{E}}_{\perp b} \\
&= \sum_a \sum_b Z_{ca} \tilde{I}_a V_{b\lambda} \frac{\delta_{ab}}{Z_{ca}} \\
&= \sum_a \tilde{I}_a V_{a\lambda},
\end{aligned} \tag{A.84}$$

We are free to choose the location of  $S_p$  in the waveguide, so we will choose it such that  $I_{a\lambda} = 0$ . Thus

$$\int_{S_p} dS \hat{n} \cdot \tilde{\mathbf{E}} \times \vec{\mathbf{H}}_\lambda = 0. \tag{A.85}$$

### A.3.3 Mode Amplitudes

By substituting the perturbations found in equations (A.74), (A.75), (A.84) and (A.85) into equations (A.58) and (A.59) we get the following relations for the cavity mode amplitudes

$$-\mu_0 \frac{d\tilde{h}_\lambda(t)}{dt} + j\mu_0\omega\tilde{h}_\lambda(t) = k_\lambda\tilde{e}_\lambda(t) + \frac{\mu_c(1-j)\omega}{Q_{0\lambda}(t)}\tilde{h}_\lambda(t), \tag{A.86a}$$

$$\varepsilon_0 \frac{d\tilde{e}_\lambda(t)}{dt} - j\varepsilon_0\omega\tilde{e}_\lambda(t) = k_\lambda\tilde{h}_\lambda(t) + \sum_a \tilde{I}_a(t)V_{a\lambda}, \tag{A.86b}$$

where we have allowed  $Q_{0\lambda}$  and hence  $\sigma$  to be a function of time. We will also allow  $k_\lambda$  to be a function of time because the cavity volume may change during the heating. By solving equation (A.86a) for  $\tilde{e}_\lambda$  and substituting the result into equation (A.86b)

we get the following equation for the mode amplitude of the magnetic field

$$\begin{aligned} \frac{d^2 \tilde{h}_\lambda}{dt^2} + \frac{d\tilde{h}_\lambda}{dt} \left[ -\frac{1}{\omega_\lambda} \frac{d\omega_\lambda}{dt} - 2j\omega + \frac{(1-j)\mu_c\omega}{\mu_0 Q_{0\lambda}} \right] \\ + \tilde{h}_\lambda \left[ -\frac{(1-j)\mu_c\omega}{\mu_0 Q_{0\lambda}} \left( \frac{1}{Q_{0\lambda}} \frac{dQ_{0\lambda}}{dt} + \frac{1}{\omega_\lambda} \frac{d\omega_\lambda}{dt} + j\omega \right) + \frac{j\omega}{\omega_\lambda} \frac{d\omega_\lambda}{dt} - \omega^2 + \omega_\lambda^2 \right] \\ = -\omega_\lambda c \sum_a \tilde{I}_a V_{a\lambda}, \quad (\text{A.87}) \end{aligned}$$

where we have used  $k_\lambda = \omega_\lambda/c$ . Since we are considering copper we have  $\mu_c \approx \mu_0$ . Using this fact and grouping the real and imaginary terms, equation (A.87) becomes

$$\begin{aligned} \frac{d^2 \tilde{h}_\lambda}{dt^2} + \frac{d\tilde{h}_\lambda}{dt} \left[ \left( \frac{\omega}{Q_{0\lambda}} - \frac{1}{\omega_\lambda} \frac{d\omega_\lambda}{dt} \right) - j\omega \left( 2 + \frac{1}{Q_{0\lambda}} \right) \right] \\ + \tilde{h}_\lambda \left\{ -\frac{\omega}{Q_{0\lambda}} \left( \frac{1}{Q_{0\lambda}} \frac{dQ_{0\lambda}}{dt} + \frac{1}{\omega_\lambda} \frac{d\omega_\lambda}{dt} + \omega \right) - \omega^2 + \omega_\lambda^2 \right. \\ \left. + j\omega \left[ \frac{1}{\omega_\lambda} \frac{d\omega_\lambda}{dt} \left( 1 + \frac{1}{Q_{0\lambda}} \right) + \frac{1}{Q_{0\lambda}} \left( \frac{1}{Q_{0\lambda}} \frac{dQ_{0\lambda}}{dt} - \omega \right) \right] \right\} \\ = -\omega_\lambda c \sum_a \tilde{I}_a V_{a\lambda}, \quad (\text{A.88}) \end{aligned}$$

Since  $\tilde{h}_\lambda$  is a slowly-varying function of time we have the condition

$$\left| \frac{d^2 \tilde{h}_\lambda}{dt^2} \right| \ll \omega^2 \left| \tilde{h}_\lambda \right|. \quad (\text{A.89})$$

We also expect the unloaded Q of the cavity and the resonant frequency to change slowly compared to an RF period so we also have

$$\left| \frac{dQ_{0\lambda}}{dt} \right| \ll \omega Q_{0\lambda}, \quad \left| \frac{d\omega_\lambda}{dt} \right| \ll \omega \omega_\lambda. \quad (\text{A.90})$$

We do not expect the resonant frequency of the cavity to change more than one Q-bandwidth where  $\Delta\omega_\lambda = \omega_\lambda/Q_{0\lambda}$ . In our case,  $\omega \approx \omega_\lambda \sim 10^{10}$  and  $Q_{0\lambda} \sim 10^4$  with a pulse length on the order of 1  $\mu\text{s}$ . So,  $\Delta\omega_\lambda/\Delta t \sim 10^{12}$  and  $\omega\omega_\lambda/Q_{0\lambda} \sim 10^{16}$ . Therefore

we also have the condition

$$\left| \frac{d\omega_\lambda}{dt} \right| \ll \frac{\omega\omega_\lambda}{Q_{0\lambda}}. \quad (\text{A.91})$$

Using these approximations, the mode amplitude of the magnetic field is

$$\frac{d\tilde{h}_\lambda}{dt} \left[ \frac{\omega}{Q_{0\lambda}} - j\omega \frac{2 + \frac{1}{Q_{0\lambda}}}{1 + \frac{1}{Q_{0\lambda}}} \right] + \tilde{h}_\lambda \left[ \frac{\omega_\lambda^2}{1 + \frac{1}{Q_{0\lambda}}} - \omega^2 - \frac{j\omega^2}{Q_{0\lambda}} \right] = -\frac{\omega_\lambda c}{1 + \frac{1}{Q_{0\lambda}}} \sum_a \tilde{I}_a V_{a\lambda}, \quad (\text{A.92})$$

where we have divided equation (A.88) by the factor  $1 + 1/Q_{0\lambda}$  and used the approximation  $Q_{0\lambda} \gg 1$ .

Let us look more closely at the term on the right-hand side of equation (A.92). The transverse electric field at the waveguide port  $S_p$  must be continuous. If we consider only TE modes in the waveguide then we may expand the electric field in either basis

$$\tilde{\vec{E}}_\perp(\vec{r}_\perp, t) = \sum_a \vec{E}_{\perp a}(\vec{r}_\perp) \tilde{V}_a(t) = \sum_\lambda \vec{E}_\lambda(\vec{r}_\perp) \tilde{e}_\lambda(t). \quad (\text{A.93})$$

By taking the dot-product of both sides of equation (A.93) with a waveguide-mode,  $\vec{E}_{\perp a}$ , we get the condition

$$\tilde{V}_a(t) = \sum_\lambda V_{a\lambda} \tilde{e}_\lambda(t). \quad (\text{A.94})$$

We will simplify our problem by considering a waveguide operating in its first dominant mode ( $a = 1$ ) and driving only one cavity mode  $\lambda$  giving

$$\tilde{V}_1(t) = V_{1\lambda} \tilde{e}_\lambda(t). \quad (\text{A.95})$$

If we split the waveguide expansion coefficients into forward and backward-travelling waves

$$\tilde{V}_1 = \tilde{V}_1^+ + \tilde{V}_1^-, \quad \tilde{I}_1 = \tilde{I}_1^+ + \tilde{I}_1^-, \quad (\text{A.96})$$

and use the relation [57]

$$Z_{ca} \tilde{I}_a^\pm = \pm \tilde{V}_a^\pm, \quad (\text{A.97})$$

we get

$$\tilde{I}_1 = \frac{\tilde{V}_1^+ - \tilde{V}_1^-}{Z_{c1}} = \frac{2\tilde{V}_1^+ - V_{1\lambda} \tilde{e}_\lambda}{Z_{c1}}, \quad (\text{A.98})$$

where we have also used equation (A.95). We define the external Q for mode  $\lambda$  of the cavity as [57]

$$\frac{1}{Q_{e\lambda}} \equiv \frac{V_{1\lambda}^2}{\varepsilon_0 \omega_\lambda Z_{c1}}. \quad (\text{A.99})$$

If power  $P_{in}$  is flowing in the waveguide then [45, 57]

$$\tilde{V}_1^+ = \sqrt{2P_{in}Z_{c1}}. \quad (\text{A.100})$$

If we multiply both sides of equation (A.98) by  $V_{1\lambda}$ , substitute into it  $\tilde{e}_\lambda$  from equation (A.86a) and use equations (A.99) and (A.100) we get

$$V_{1\lambda}\tilde{I}_1 = \sqrt{\frac{8P_{in}\varepsilon_0\omega_\lambda}{Q_{e\lambda}}} + \frac{\mu_0\varepsilon_0\omega_\lambda}{Q_{e\lambda}k_\lambda} \frac{d\tilde{h}_\lambda}{dt} - \frac{j\mu_0\varepsilon_0\omega_\lambda}{Q_{e\lambda}k_\lambda} \tilde{h}_\lambda + \frac{\varepsilon_0\mu_0(1-j)\omega_\lambda}{k_\lambda Q_{0\lambda}Q_{e\lambda}} \tilde{h}_\lambda. \quad (\text{A.101})$$

Using equation (A.101) in equation (A.92) the mode amplitude for the magnetic field is finally written as

$$\begin{aligned} \frac{d\tilde{h}_\lambda}{dt} \left[ \left( \frac{\omega}{Q_{0\lambda}} + \frac{\omega_\lambda}{Q_{e\lambda} \left(1 + \frac{1}{Q_{0\lambda}}\right)} \right) - j\omega \frac{2 + \frac{1}{Q_{0\lambda}}}{1 + \frac{1}{Q_{0\lambda}}} \right] \\ + \tilde{h}_\lambda \left[ \left( \frac{\omega_\lambda^2}{1 + \frac{1}{Q_{0\lambda}}} - \omega^2 \right) - j\omega \left( \frac{\omega}{Q_{0\lambda}} + \frac{\omega_\lambda}{Q_{e\lambda}} \right) \right] = -\frac{1}{1 + \frac{1}{Q_{0\lambda}}} \sqrt{\frac{8P_{in}\omega_\lambda^3}{\mu_0 Q_{e\lambda}}}, \end{aligned} \quad (\text{A.102})$$

Note that by adopting the phasor notation in equations (A.82) we have assumed that the waveguide and cavity are driven at angular frequency  $\omega$ . Terms containing the factor  $1/Q_{0\lambda}$  are kept in equation (A.102) since  $Q_{0\lambda}$  is a function of time. However, if  $Q_{0\lambda}$  is constant and we drive the cavity at a frequency  $\omega = \omega_\lambda/\sqrt{1 + 1/Q_{0\lambda}}$  then equation (A.102) is further simplified as

$$\frac{d\tilde{h}_\lambda}{dt} \left[ \frac{1}{Q_{L\lambda}} - 2j \right] + \tilde{h}_\lambda \left[ -\frac{j\omega_\lambda}{Q_{L\lambda}} \right] = -\sqrt{\frac{8P_{in}\omega_\lambda}{\mu_0 Q_{e\lambda}}}, \quad (\text{A.103})$$

where we have divided by  $\omega_\lambda$  and used the definition of the loaded Q of a cavity

resonating in mode  $\lambda$

$$\frac{1}{Q_{L\lambda}} \equiv \frac{1}{Q_{0\lambda}} + \frac{1}{Q_{e\lambda}}. \quad (\text{A.104})$$

It is instructive to solve equation (A.103) for further insight into the behavior of the cavity. The solution for the mode amplitude of the magnetic field with the initial condition  $\tilde{h}_\lambda(t=0) = 0$  is

$$\begin{aligned} h_\lambda(t) &= \tilde{h}_\lambda(t)e^{-j\omega t} \\ &= -jQ_{L\lambda} \sqrt{\frac{8P_{in}}{\mu_0 Q_{e\lambda} \omega_\lambda}} \left[ 1 - \exp\left(-\frac{\omega_\lambda t}{2Q_{L\lambda}}\right) \exp\left(-\frac{j\omega_\lambda t}{4Q_{L\lambda}^2}\right) \right] \exp(-j\omega t), \end{aligned} \quad (\text{A.105})$$

where  $\omega = \omega_\lambda / \sqrt{1 + 1/Q_{0\lambda}^2}$ . Thus, the build-up of the magnetic field in the cavity is governed by the so-called fill-time

$$\tau \equiv \frac{2Q_{L\lambda}}{\omega_\lambda}. \quad (\text{A.106})$$

The oscillation term proportional to  $1/Q_{L\lambda}^2$  may be ignored, because it is negligible compared to the fill-time  $\tau$  when  $Q_{L\lambda} \gg 1$ . Hence, equation (A.105) may be more compactly written

$$h_\lambda(t) = -jQ_{L\lambda} \sqrt{\frac{8P_{in}}{\mu_0 Q_{e\lambda} \omega_\lambda}} [1 - e^{-t/\tau}] e^{-j\omega t}. \quad (\text{A.107})$$

Notice that the resonant frequency is no longer  $\omega_\lambda$ , but has been shifted slightly due to the lossy walls. This shift will be examined further in a later section.

Once the mode amplitude for the magnetic field is found, the mode amplitude for the electric field is found from equations (A.86a) and (A.57). The total fields in the cavity are finally calculated from

$$\vec{E}(\vec{r}, t) = \vec{E}_\lambda(\vec{r}) e_\lambda(t), \quad (\text{A.108a})$$

$$\vec{H}(\vec{r}, t) = \vec{H}_\lambda(\vec{r}) h_\lambda(t). \quad (\text{A.108b})$$

where we have already assumed that only one mode  $\lambda$  is excited in the cavity.

### A.3.4 Constant Cavity Parameters

In the previous section, the mode equations for the cavity fields were derived with the condition that  $Q_{0\lambda}$  and  $\omega_\lambda$  may be functions of time. Because of this possibility, it was necessary to adopt phasor notation (equations (A.57)) in order to make the problem tractable. If we now assume that  $Q_{0\lambda}$  and  $\omega_\lambda$  are constant, we may repeat the derivation of the mode equations to arrive at a simpler interpretation of the cavity response.

By taking the Fourier transform of the mode amplitudes in equations (A.55) and (A.76), we convert all quantities to the frequency domain. By following the same derivation with the condition that  $Q_{0\lambda}$  is constant and taking the inverse Fourier transform at the end [48, 57], the mode amplitude for the magnetic field is

$$\left[ \frac{d^2}{dt^2} + \frac{\omega_\lambda}{Q_{L\lambda}} \frac{d}{dt} + \frac{\omega_\lambda^2}{1 + \frac{1}{Q_{0\lambda}}} \right] h_\lambda(t) = -\frac{1}{1 + \frac{1}{Q_{0\lambda}}} \sqrt{\frac{8P_{in}\omega_\lambda^3}{\mu_0 Q_{e\lambda}}} e^{-j\omega_d t}, \quad (\text{A.109})$$

where  $\omega_d$  is the angular frequency at which the waveguide-cavity system is driven. Hence, the cavity is simply a damped, driven oscillator. If the cavity is initially empty of fields then the initial conditions are

$$h_\lambda(t=0) = 0, \quad \left. \frac{dh_\lambda}{dt} \right|_{t=0} = 0, \quad (\text{A.110})$$

Thus, the solution is simply

$$h_\lambda(t) = [C_1 e^{j\Omega t} + C_2 e^{-j\Omega t}] e^{-\omega_\lambda t/2Q_{L\lambda}} + K' e^{-j\omega_d t}, \quad (\text{A.111})$$

where

$$\Omega = \omega_\lambda \left[ \frac{1}{1 + \frac{1}{Q_{0\lambda}}} - \frac{1}{4Q_{L\lambda}^2} \right]^{1/2}, \quad (\text{A.112a})$$

$$K = -\frac{1}{1 + \frac{1}{Q_{0\lambda}}} \sqrt{\frac{8P_{in}\omega_\lambda^3}{\mu_0 Q_{e\lambda}}}, \quad (\text{A.112b})$$

$$K' = \frac{K}{\frac{\omega_\lambda^2}{1+1/Q_{0\lambda}} - \omega_d^2 - \frac{j\omega_d\omega_\lambda}{Q_{L\lambda}}}, \quad (\text{A.112c})$$

$$C_1 = K' \left[ \frac{j\omega_\lambda}{4Q_{L\lambda}\Omega} + \frac{\omega_d}{2\Omega} - \frac{1}{2} \right], \quad (\text{A.112d})$$

$$C_2 = K' \left[ -\frac{j\omega_\lambda}{4Q_{L\lambda}\Omega} - \frac{\omega_d}{2\Omega} - \frac{1}{2} \right]. \quad (\text{A.112e})$$

Notice that the natural resonant frequency of the system,  $\Omega$ , is shifted from the unperturbed resonant frequency  $\omega_\lambda$ . The perturbed resonant frequency is approximately written

$$\Omega \approx \omega_\lambda \left[ 1 - \frac{1}{2Q_{0\lambda}} - \frac{1}{8Q_{L\lambda}^2} \right]. \quad (\text{A.113})$$

The term proportional to  $1/Q_{L\lambda}^2$  in equation (A.113) represents the shift in frequency due to damping. The damping is caused by the loss of power to the cavity walls ( $Q_{0\lambda}$ ) and to leakage of power to the coupled waveguide ( $Q_{e\lambda}$ ). However, this frequency shift is negligible compared to the shift from the term proportional to  $1/Q_{0\lambda}$ .  $Q_{0\lambda}$  causes a shift in the resonant frequency of the cavity, because the fields are no longer zero in the conductor but penetrate to a distance characterized by the skin-depth  $\delta$  (see equation (A.68)). The effective volume of the cavity increases, which causes a decrease in the cavity's resonant frequency.

If we drive the cavity close to its perturbed resonant frequency,  $\omega_d \approx \Omega$ , and use the fact that  $Q_{0\lambda} \gg 1$  and  $Q_{L\lambda} \gg 1$  then

$$C_1 \approx 0, \quad C_2 \approx -K', \quad K' \approx -jQ_{L\lambda} \sqrt{\frac{8P_{in}}{\mu_0 Q_{e\lambda} \omega_\lambda}}, \quad (\text{A.114})$$

and the mode amplitude for the magnetic field is

$$h_\lambda(t) \approx -jQ_{L\lambda} \sqrt{\frac{8P_{in}}{\mu_0 Q_{e\lambda} \omega_\lambda}} \left[ 1 - \exp\left(-\frac{\omega_\lambda t}{2Q_{L\lambda}}\right) \right] e^{-j\omega_d t}. \quad (\text{A.115})$$

This solution is the same one found in the previous section, equation (A.107). This solution also demonstrates that if  $Q_{0\lambda} \gg 1$  and  $Q_{e\lambda} \gg 1$ , then the assumption that the cavity fields resonate at the drive frequency  $\omega_d$  is justified.

## A.4 Cavity Circuit Parameters

In sections A.2 and A.3, we derived equations for determining the electric and magnetic fields in a resonant cavity. These equations are useful for applications requiring the knowledge of the magnitude of the fields, such as calculations of pulsed heating. However, these equations are not very useful for determination of a cavity's properties through measurement. For this purpose, it would be useful to derive equations similar to equation (A.102) in terms of input and output power to the cavity, quantities which are easily measured with network analyzers or crystal detectors. Equivalently, we may think in terms of input and output voltages since power is proportional to the square of the voltage.

### A.4.1 Cavity Response

In microwave circuits, voltage is not unique since the RF wavelength is comparable with the size of the components [45]. However, we may choose a reference plane in which voltage may be defined. If we choose the reference plane  $S_p$  in the waveguide coupled to a cavity as in the previous sections, then this voltage becomes (see equation (A.96))

$$V_1(t) = V_1^+(t) + V_1^-(t), \quad (\text{A.116})$$

where  $V_1^+$  is the forward-travelling voltage wave in the waveguide and  $V_1^-$  is the backward-travelling wave. If we have another waveguide coupled to the cavity then we may also choose a reference plane in that waveguide and define a voltage on that

plane as

$$V_2(t) = V_2^+(t) + V_2^-(t). \quad (\text{A.117})$$

In general, we may have any number of waveguides or ports attached to the cavity. Since we are treating the perturbations of connecting waveguides to only first-order, we may easily incorporate additional ports by adding additional terms similar to  $\sum_a \tilde{I}_a V_{a\lambda}$  to equation (A.86b). For simplicity, we will subsume all of those terms under one summation and allow  $a$  to enumerate all modes in all waveguides.

Since equation (A.94) allows us to relate the fields in the cavity to waveguide voltage, we will solve for  $\tilde{e}_\lambda$  by eliminating  $\tilde{h}_\lambda$  from equations (A.86)

$$\begin{aligned} \frac{d^2 \tilde{e}_\lambda}{dt^2} + \frac{d\tilde{e}_\lambda}{dt} \left[ -\frac{1}{\omega_\lambda} \frac{d\omega_\lambda}{dt} - 2j\omega + \frac{(1-j)\mu_c\omega}{\mu_0 Q_{0\lambda}} \right] \\ + \tilde{e}_\lambda \left[ \frac{j\omega}{\omega_\lambda} \frac{d\omega_\lambda}{dt} - \omega^2 + \omega_\lambda^2 - \frac{j(1-j)\mu_c\omega^2}{\mu_0 Q_{0\lambda}} \right] \\ = \frac{1}{\varepsilon_0} \frac{d}{dt} \sum_a \tilde{I}_a V_{a\lambda} + \left[ \frac{(1-j)\mu_c\omega}{\varepsilon_0 \mu_0 Q_{0\lambda}} - \frac{1}{\varepsilon_0} \frac{1}{\omega_\lambda} \frac{d\omega_\lambda}{dt} - \frac{j\omega}{\varepsilon_0} \right] \sum_a \tilde{I}_a V_{a\lambda}, \end{aligned} \quad (\text{A.118})$$

where we have allowed  $\omega_\lambda$  and  $Q_{0\lambda}$  to be functions of time. Since we are considering copper, we have  $\mu_c \approx \mu_0$ . Using this approximation in equation (A.118) and grouping real and imaginary terms we have

$$\begin{aligned} \frac{d^2 \tilde{e}_\lambda}{dt^2} + \frac{d\tilde{e}_\lambda}{dt} \left[ \left( \frac{\omega}{Q_{0\lambda}} - \frac{1}{\omega_\lambda} \frac{d\omega_\lambda}{dt} \right) - j\omega \left( 2 + \frac{1}{Q_{0\lambda}} \right) \right] \\ + \tilde{e}_\lambda \left[ -\omega^2 \left( 1 + \frac{1}{Q_{0\lambda}} \right) + \omega_\lambda^2 + j\omega \left( \frac{1}{\omega_\lambda} \frac{d\omega_\lambda}{dt} - \frac{\omega}{Q_{0\lambda}} \right) \right] \\ = \frac{1}{\varepsilon_0} \frac{d}{dt} \sum_a \tilde{I}_a V_{a\lambda} - \frac{1}{\varepsilon_0} \left( \frac{1}{\omega_\lambda} \frac{d\omega_\lambda}{dt} - \frac{\omega}{Q_{0\lambda}} \right) \sum_a \tilde{I}_a V_{a\lambda} - \frac{j\omega}{\varepsilon_0} \left( 1 + \frac{1}{Q_{0\lambda}} \right) \sum_a \tilde{I}_a V_{a\lambda}. \end{aligned} \quad (\text{A.119})$$

Using the approximations in equations (A.89–A.91) and the approximation that

$Q_{0\lambda} \gg 1$ , the mode amplitude for the electric field is

$$\begin{aligned} \frac{d\tilde{e}_\lambda}{dt} \left[ \frac{\omega}{Q_{0\lambda}} - j\omega \frac{2 + \frac{1}{Q_{0\lambda}}}{1 + \frac{1}{Q_{0\lambda}}} \right] + \tilde{e}_\lambda \left[ \frac{\omega_\lambda^2}{1 + \frac{1}{Q_{0\lambda}}} - \omega^2 - \frac{j\omega^2}{Q_{0\lambda}} \right] \\ = \frac{1}{\varepsilon_0} \frac{1}{1 + \frac{1}{Q_{0\lambda}}} \frac{d}{dt} \sum_a \tilde{I}_a V_{a\lambda} + \frac{1}{\varepsilon_0} \frac{\omega}{Q_{0\lambda}} \sum_a \tilde{I}_a V_{a\lambda} - \frac{j\omega}{\varepsilon_0} \sum_a \tilde{I}_a V_{a\lambda}, \quad (\text{A.120}) \end{aligned}$$

where we have divided equation (A.119) by the factor  $1 + 1/Q_{0\lambda}$ .

Since the cavity described in Chapter 2 can be considered a two-port device for the diagnostic mode, we may use equation (A.120) to model its response to input signals. We will call  $a = 1$  the fundamental mode in port one and  $a = 2$  the fundamental mode in port two. Expanding equation (A.120) to  $a = 2$  and multiplying by  $V_{1\lambda}$  we get

$$\begin{aligned} \frac{d(V_{1\lambda}\tilde{e}_\lambda)}{dt} \left[ \frac{\omega}{Q_{0\lambda}} - j\omega \frac{2 + \frac{1}{Q_{0\lambda}}}{1 + \frac{1}{Q_{0\lambda}}} \right] + (V_{1\lambda}\tilde{e}_\lambda) \left[ \frac{\omega_\lambda^2}{1 + \frac{1}{Q_{0\lambda}}} - \omega^2 - \frac{j\omega^2}{Q_{0\lambda}} \right] \\ = \frac{1}{\varepsilon_0} \frac{1}{1 + \frac{1}{Q_{0\lambda}}} \frac{d}{dt} \left( V_{1\lambda}^2 \tilde{I}_1 + V_{1\lambda} V_{2\lambda} \tilde{I}_2 \right) + \frac{1}{\varepsilon_0} \frac{\omega}{Q_{0\lambda}} \left( V_{1\lambda}^2 \tilde{I}_1 + V_{1\lambda} V_{2\lambda} \tilde{I}_2 \right) \\ - \frac{j\omega}{\varepsilon_0} \left( V_{1\lambda}^2 \tilde{I}_1 + V_{1\lambda} V_{2\lambda} \tilde{I}_2 \right). \quad (\text{A.121}) \end{aligned}$$

Using the definition of external Q from equation (A.99) we have

$$V_{1\lambda} = \sqrt{\frac{\varepsilon_0 \omega_\lambda Z_{c1}}{Q_{e1\lambda}}}, \quad V_{2\lambda} = \sqrt{\frac{\varepsilon_0 \omega_\lambda Z_{c2}}{Q_{e2\lambda}}}, \quad (\text{A.122})$$

where  $Z_{c1}$  and  $Z_{c2}$  are the characteristic impedances of ports one and two and  $Q_{e1\lambda}$  and  $Q_{e2\lambda}$  are the external Q's for ports one and two respectively. Thus, using equation (A.97)

$$V_{1\lambda}^2 \tilde{I}_1 = \frac{\varepsilon_0 \omega_\lambda}{Q_{e1\lambda}} \left( \tilde{V}_1^+ - \tilde{V}_1^- \right), \quad (\text{A.123a})$$

$$V_{2\lambda} V_{1\lambda} \tilde{I}_2 = \frac{\varepsilon_0 \omega_\lambda}{\sqrt{Q_{e1\lambda} Q_{e2\lambda}}} \sqrt{\frac{Z_{c1}}{Z_{c2}}} \left( \tilde{V}_2^+ - \tilde{V}_2^- \right). \quad (\text{A.123b})$$

Using equations (A.94) and (A.96) we also have

$$\tilde{V}_1^+ - \tilde{V}_1^- = 2\tilde{V}_1^+ - V_{1\lambda}\tilde{e}_\lambda, \quad (\text{A.124a})$$

$$\tilde{V}_2^+ - \tilde{V}_2^- = 2\tilde{V}_2^+ - V_{2\lambda}\tilde{e}_\lambda = 2\tilde{V}_2^+ - \sqrt{\frac{Q_{e1\lambda}}{Q_{e2\lambda}}}\sqrt{\frac{Z_{c2}}{Z_{c1}}}V_{1\lambda}\tilde{e}_\lambda. \quad (\text{A.124b})$$

Using equations (A.123–A.124), the mode amplitude for the electric field is finally written as

$$\begin{aligned} \frac{d(V_{1\lambda}\tilde{e}_\lambda)}{dt} & \left[ \frac{\omega}{Q_{0\lambda}} + \frac{\omega_\lambda}{1 + \frac{1}{Q_{0\lambda}}} \left( \frac{1}{Q_{e1\lambda}} + \frac{1}{Q_{e2\lambda}} \right) - j\omega \frac{2 + \frac{1}{Q_{0\lambda}}}{1 + \frac{1}{Q_{0\lambda}}} \right] \\ & + (V_{1\lambda}\tilde{e}_\lambda) \left[ \frac{\omega_\lambda^2}{1 + \frac{1}{Q_{0\lambda}}} - \omega^2 - j\omega \left\{ \frac{\omega}{Q_{0\lambda}} + \omega_\lambda \left( \frac{1}{Q_{e1\lambda}} + \frac{1}{Q_{e2\lambda}} \right) \right\} \right] \\ & = \frac{2\omega_\lambda}{1 + \frac{1}{Q_{0\lambda}}} \left[ \frac{1}{Q_{e1\lambda}} \frac{d\tilde{V}_1^+}{dt} + \frac{1}{\sqrt{Q_{e1\lambda}Q_{e2\lambda}}}\sqrt{\frac{Z_{c1}}{Z_{c2}}}\frac{d\tilde{V}_2^+}{dt} \right] \\ & + 2\omega\omega_\lambda \left( \frac{1}{Q_{0\lambda}} - j \right) \left[ \frac{\tilde{V}_1^+}{Q_{e1\lambda}} + \frac{1}{\sqrt{Q_{e1\lambda}Q_{e2\lambda}}}\sqrt{\frac{Z_{c1}}{Z_{c2}}}\tilde{V}_2^+ \right], \quad (\text{A.125}) \end{aligned}$$

where we have used the approximations  $Q_{0\lambda} \gg 1$ ,  $Q_{e1\lambda} \gg 1$  and  $Q_{e2\lambda} \gg 1$ . Equation (A.125) allows us to find the mode amplitude of the electric field in the cavity knowing the input voltages  $\tilde{V}_1^+$  and  $\tilde{V}_2^+$ . The equation for a one-port cavity can be found by allowing  $Q_{e2\lambda} \rightarrow \infty$ .

What is usually measured in the lab are the reflected waveforms  $\tilde{V}_1^-$  and  $\tilde{V}_2^-$  with known inputs. We will show in the next sections that the measurement of the reflected waveforms may be used to determine  $\omega_\lambda$ ,  $Q_{0\lambda}$ ,  $Q_{e1\lambda}$  and  $Q_{e2\lambda}$ .

#### A.4.2 Reflection Coefficient For One-Port Cavity

In this section, we will consider a cavity with only one port. A two-port cavity is considered in section A.4.3.

If we let  $\omega_\lambda$  and  $Q_{0\lambda}$  remain constant, then we may repeat the analysis in the previous section with Fourier transforms instead of phasors as was done in section A.3.4.

Using the assumptions that  $Q_{0\lambda} \gg 1$  and  $Q_{e1\lambda} \gg 1$  and letting  $Q_{e2\lambda} \rightarrow \infty$  we have for the mode amplitude of the electric field [57]

$$\left[ \frac{d^2}{dt^2} + \frac{\omega_\lambda}{Q_{L\lambda}} \frac{d}{dt} + \omega_\lambda^2 \right] V_C(t) = \frac{2\omega_\lambda}{Q_{e\lambda}} \frac{dV_1^+(t)}{dt}, \quad (\text{A.126})$$

where we have rewritten  $Q_{e1\lambda}$  as  $Q_{e\lambda}$  and defined a *cavity voltage*

$$V_C = V_{1\lambda} e_\lambda, \quad (\text{A.127})$$

for simplicity. Equation (A.126) highlights the cavity as a damped-driven oscillator and is useful for most calculations of cavity response. This equation also shows that a cavity is understood if its resonant frequency,  $\omega_\lambda$ , as well as its unloaded and external Q's are known. These quantities can be determined by measuring the reflected waveform  $V_1^- = V_C - V_1^+$  in the time-domain or frequency-domain.

### Time-domain

As usual, we drive the cavity system at an angular frequency  $\omega$  and adopt the phasor notation in equations (A.57) and (A.82), except we will use an  $e^{j\omega t}$  dependence on time. The assumption of an  $e^{j\omega t}$  dependence for the cavity voltage is correct if  $Q_{0\lambda} \gg 1$  and  $Q_{e\lambda} \gg 1$ . If we use the approximation

$$\left| \frac{d^2 \tilde{V}_C}{dt^2} \right| \ll \omega^2 \left| \tilde{V}_C \right|, \quad (\text{A.128})$$

then equation (A.126) is reduced to

$$2j\omega \frac{d\tilde{V}_C}{dt} + \left( \frac{j\omega\omega_\lambda}{Q_{L\lambda}} + \omega_\lambda^2 - \omega^2 \right) \tilde{V}_C = \frac{2j\omega\omega_\lambda}{Q_{e\lambda}} \tilde{V}_1^+. \quad (\text{A.129})$$

Let us drive a cavity at its resonant frequency,  $\omega = \omega_\lambda$ , with a square input pulse of length  $T_p$ . The pulse length will be much longer than an RF period,  $2\pi/\omega$ , so we

may take  $\tilde{V}_1^+$  as a constant. Hence, equation (A.129) is reduced to

$$\frac{d}{dt} \left( \frac{\tilde{V}_C(t)}{\tilde{V}_1^+} \right) + \frac{\omega_\lambda}{2Q_{L\lambda}} \left( \frac{\tilde{V}_C(t)}{\tilde{V}_1^+} \right) = \frac{\omega_\lambda}{Q_{e\lambda}}. \quad (\text{A.130})$$

If the cavity is initially empty of fields then  $\tilde{V}_C(t=0) = 0$  so the solution for the cavity voltage is

$$\frac{\tilde{V}_C(t)}{\tilde{V}_1^+} = \frac{2Q_{L\lambda}}{Q_{e\lambda}} \left[ 1 - \exp \left( -\frac{\omega_\lambda t}{2Q_{L\lambda}} \right) \right]. \quad (\text{A.131})$$

We define the *coupling coefficient* as

$$\beta = \frac{Q_{0\lambda}}{Q_{e\lambda}}. \quad (\text{A.132})$$

If we remember that  $1/Q_{L\lambda} = 1/Q_{0\lambda} + 1/Q_{e\lambda}$  and use continuity  $\tilde{V}_1^- = \tilde{V}_C - \tilde{V}_1^+$  then the reflection coefficient is

$$\frac{\tilde{V}_1^-(t)}{\tilde{V}_1^+} = \frac{\beta - 1}{\beta + 1} - \frac{2\beta}{\beta + 1} e^{-t/\tau} \quad 0 \leq t \leq T_p, \quad (\text{A.133})$$

where  $\tau = 2Q_{L\lambda}/\omega_\lambda$  is known as the *fill-time*. Note that the loaded Q may also be written as

$$Q_{L\lambda} = \frac{Q_{0\lambda}}{1 + \beta}. \quad (\text{A.134})$$

For  $t > T_p$ , the RF drive is off and equation (A.129) is reduced to

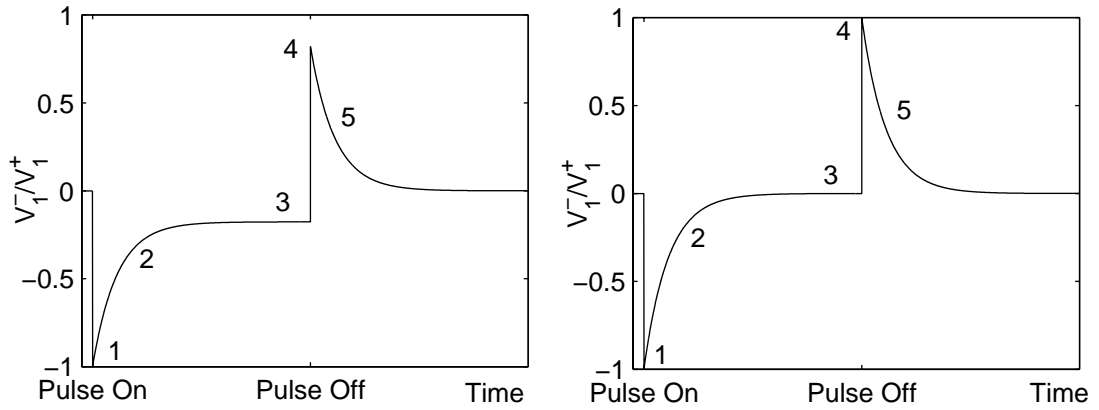
$$\frac{d\tilde{V}_C}{dt} + \frac{\omega_\lambda}{2Q_{L\lambda}} \tilde{V}_C = 0, \quad (\text{A.135})$$

where  $\tilde{V}_1^+ = 0$ . Using continuity at  $t = T_p$ , the reflection coefficient is

$$\frac{\tilde{V}_1^-(t)}{\tilde{V}_1^+} = \frac{2\beta}{1 + \beta} [e^{T_p/\tau} - 1] e^{-t/\tau} \quad t > T_p, \quad (\text{A.136})$$

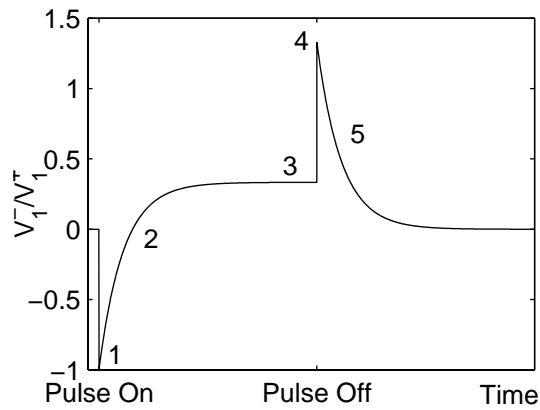
where  $\tilde{V}_C = \tilde{V}_1^- + \tilde{V}_1^+ = \tilde{V}_1^-$ .

Plots of  $V_1^-(t)/V_1^+$  are shown in Figure A.6 for three different values of  $\beta$ . For the



(a)  $\beta < 1$

(b)  $\beta = 1$



(c)  $\beta > 1$

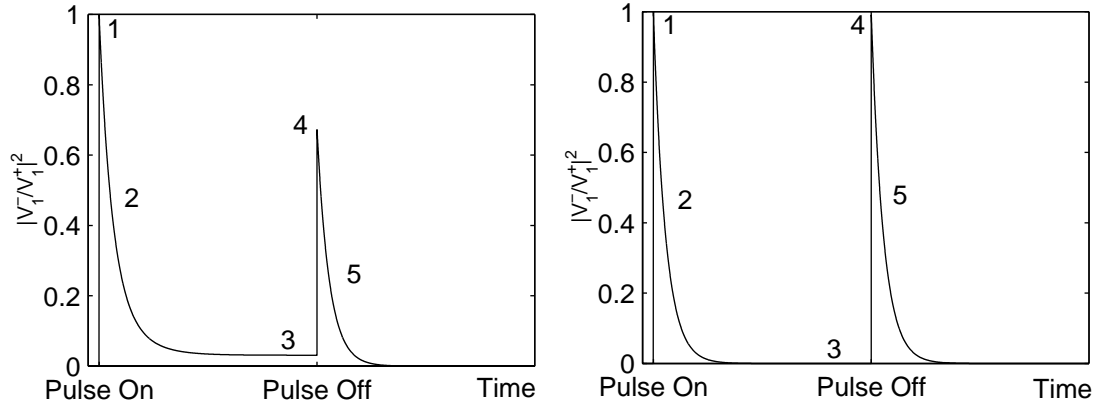
Figure A.6:  $V_1^-(t)/V_1^+$  for various  $\beta$ .

case where  $\beta = 1$ , the cavity is *critically-coupled*. In this case, the reflected waveform goes to zero as the cavity is filled with energy as shown in region 3 of Figure A.6. For  $\beta > 1$ , the cavity is *over-coupled* and the reflected waveform never reaches zero in region 3. For  $\beta < 1$ , the cavity is *under-coupled* and the reflected waveform crosses zero.

Initially at  $t = 0$ , the RF drive signal is fully-reflected and the cavity acts like an electric short as shown in region 1. In region 2, the cavity is filling with energy as characterized by the fill-time  $\tau$ , and the reflected waveform is decreasing. In region 3, the cavity reaches steady-state (if  $T_p \gtrsim 5\tau$ ) and the absolute value of the reflected waveform reaches a minimum. Another spike occurs in region 4 when the RF drive turns off. If  $\beta > 1$ , then the height of this spike is greater than the spike of region 1. If  $\beta < 1$ , the height of this spike is lower than that of region 1. Finally, in region 5, the reflected waveform decays with characteristic time  $\tau$  as energy leaks out of the cavity.

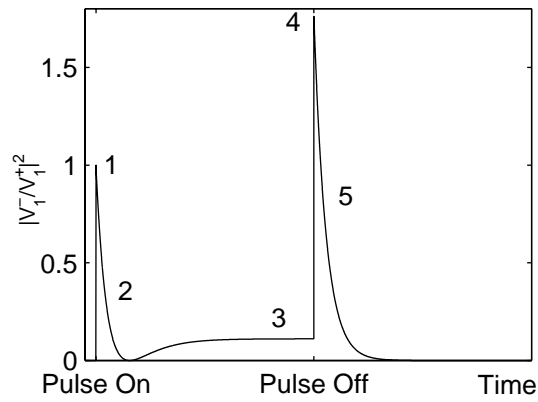
The coupling coefficient  $\beta$  is determined by measuring the signal in region 3.  $Q_{L\lambda}$  is found by measuring the fill-time,  $\tau$ , from either region 2 or region 5. From these two quantities,  $Q_{0\lambda}$  and  $Q_{e\lambda}$  are determined. The resonant frequency of the cavity is determined by sweeping the RF drive in frequency until the signal in region 3 reaches a minimum. The reflection from the cavity is always minimum at the resonant frequency.

In most cases, only the magnitude of the reflected waveform is measured. For example, if the waveform is measured with crystal detectors, then the voltage shown on an oscilloscope is proportional to the RF power. Hence the measurement is of  $|V_1^-(t)/V_1^+|^2$  as shown in Figure A.7. One qualitative difference is that the signal never crosses zero in the over-coupled case. The signal bounces from zero in region 3. We must also be careful when measuring  $Q_{L\lambda}$ . In region 2, the signal will decay with two different rates because we are measuring the square of  $V_1^-/V_1^+$ . Because of this fact, it is always best to measure the fill-time in region 5 as seen by squaring equation (A.136).



(a)  $\beta < 1$

(b)  $\beta = 1$



(c)  $\beta > 1$

Figure A.7:  $|V_1^-(t)/V_1^+|^2$  for various  $\beta$ .

### Frequency-domain

Another method to measure the circuit parameters of a cavity is by measuring its response in the frequency-domain. This type of measurement is most easily accomplished with a network analyzer. A network analyzer measures forward and reflected power from the cavity as a function of frequency and automatically displays the result as  $S_{11}(\omega)$ .  $S_{11}$  is the reflection coefficient,  $\tilde{V}_1^-(\omega)/\tilde{V}_1^+$ , in the frequency-domain and is part of a construct in microwave network theory known as S-parameters [37, 45].

In the frequency-domain, equation (A.126) becomes

$$\left(-\omega^2 + \frac{j\omega\omega_\lambda}{Q_{L\lambda}} + \omega_\lambda^2\right) \tilde{V}_C = \frac{2j\omega\omega_\lambda}{Q_{e\lambda}} \tilde{V}_1^+. \quad (\text{A.137})$$

If we define the *tuning angle*  $\psi$  as [57]

$$\tan \psi \equiv Q_{L\lambda} \left( \frac{\omega_\lambda}{\omega} - \frac{\omega}{\omega_\lambda} \right), \quad (\text{A.138})$$

then the cavity voltage can be written as

$$\tilde{V}_C = \frac{2\beta}{1+\beta} \cos \psi e^{j\psi} \tilde{V}_1^+. \quad (\text{A.139})$$

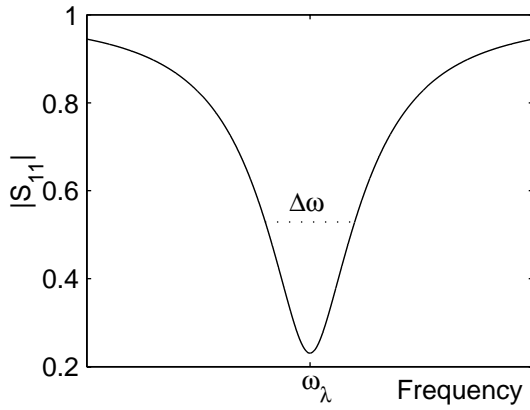
Since  $\tilde{V}_1^- = \tilde{V}_C - \tilde{V}_1^+$ , the reflection coefficient is

$$S_{11}(\omega) = \frac{\tilde{V}_1^-}{\tilde{V}_1^+} = \frac{2\beta}{1+\beta} \cos \psi e^{j\psi} - 1 \quad -\frac{\pi}{2} \leq \psi \leq \frac{\pi}{2}. \quad (\text{A.140})$$

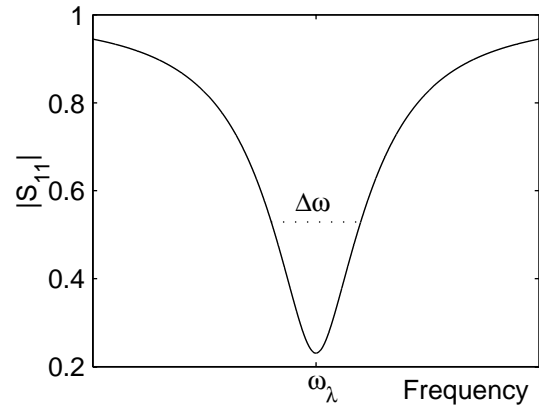
A vector network analyzer will measure and display the magnitude and phase of  $S_{11}(\omega)$ . The magnitude and phase of  $S_{11}$  is given below and plotted in Figure A.8 for over and under-coupled cases

$$|S_{11}| = \sqrt{1 - \frac{4\beta}{(1+\beta)^2} \cos^2 \psi}, \quad (\text{A.141a})$$

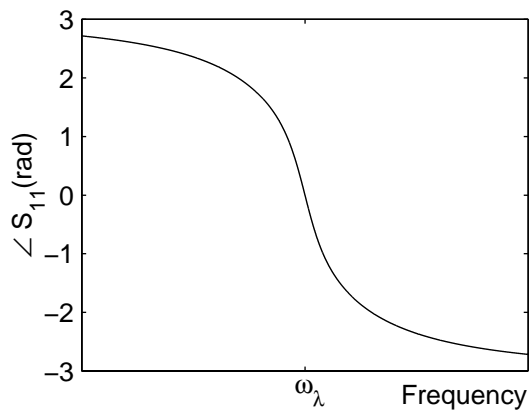
$$\angle S_{11} = \arctan \left( \frac{\sin 2\psi}{\cos 2\psi - \frac{1}{\beta}} \right). \quad (\text{A.141b})$$



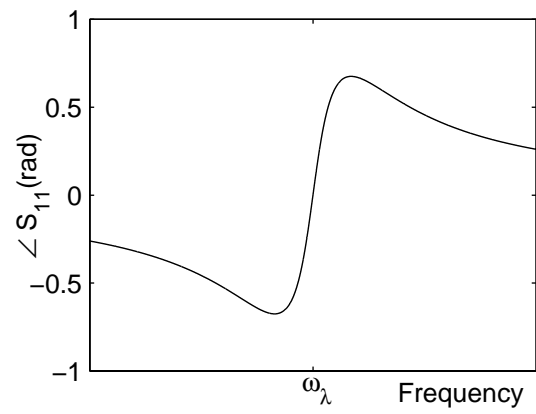
(a) Magnitude of  $S_{11}$  for  $\beta = 1.6$



(b) Magnitude of  $S_{11}$  for  $\beta = 1/1.6$



(c) Phase of  $S_{11}$  for  $\beta = 1.6$



(d) Phase of  $S_{11}$  for  $\beta = 1/1.6$

Figure A.8:  $S_{11}(\omega)$

The resonant frequency occurs where  $\psi = 0$  and  $|S_{11}|$  is a minimum.  $\beta$  is determined from the minimum of  $|S_{11}|$

$$\min |S_{11}| = \frac{|\beta - 1|}{\beta + 1}. \quad (\text{A.142})$$

However, we do not know from this measurement if  $\beta > 1$  or  $\beta < 1$ . This ambiguity can be determined by looking at the slope of the phase of  $S_{11}$  at  $\omega = \omega_\lambda$ . This slope is

$$\left. \frac{d\angle S_{11}}{d\omega} \right|_{\omega=\omega_\lambda} = \left. \frac{d\angle S_{11}}{d\psi} \right|_{\psi=0} \left. \frac{d\psi}{d\omega} \right|_{\omega=\omega_\lambda} = -\frac{4Q_{L\lambda}}{\omega_\lambda} \frac{1}{1 - \frac{1}{\beta}}. \quad (\text{A.143})$$

If  $\beta > 1$  then the slope is negative. If  $\beta < 1$  then the slope is positive.

The loaded Q is determined by measuring the frequency difference of a particular value of  $|S_{11}|$  about the resonant frequency  $\omega_\lambda$  (see Figure A.8). It is helpful to write the reflection coefficient as a function of this frequency difference,  $\Delta\omega$ ,

$$\omega = \omega_\lambda - \frac{1}{2}\Delta\omega \quad \text{where} \quad \Delta\omega \ll \omega_\lambda. \quad (\text{A.144})$$

The tuning angle becomes

$$\tan \psi = Q_{L\lambda} \left[ \frac{\omega_\lambda}{\omega} - \frac{\omega}{\omega_\lambda} \right] = Q_{L\lambda} \left[ \frac{(\omega_\lambda + \omega)(\omega_\lambda - \omega)}{\omega\omega_\lambda} \right] \approx Q_{L\lambda} \frac{\Delta\omega}{\omega_\lambda}. \quad (\text{A.145})$$

Hence the reflection coefficient becomes

$$|S_{11}(\Delta\omega)| = \sqrt{1 - \frac{4\beta}{(1 + \beta)^2} \frac{\omega_\lambda^2}{\omega_\lambda^2 + Q_{L\lambda}^2 \Delta\omega^2}}. \quad (\text{A.146})$$

Solving equation (A.146) for  $Q_{L\lambda}$  gives

$$Q_{L\lambda} = \frac{\omega_\lambda}{\Delta\omega} \sqrt{\frac{4\beta}{(1 + \beta)^2} \frac{1}{1 - |S_{11}(\Delta\omega)|^2} - 1}. \quad (\text{A.147})$$

After measuring  $\beta$  and  $Q_{L\lambda}$ ,  $Q_{o\lambda}$  and  $Q_{e\lambda}$  is determined from equations (A.132) and (A.134).

### A.4.3 S-parameters For Two-Port Cavity

In this section we will derive the S-parameters for a two-port cavity. S-parameters are only used in the frequency-domain, but we will keep this terminology for the time-domain for simplicity. If we repeat the analysis described in the last section with Fourier transforms, then the equation for the cavity voltage  $V_C = V_{1\lambda}e_\lambda$  is

$$\left[ \frac{d^2}{dt^2} + \frac{\omega_\lambda}{Q_{L\lambda}} + \omega_\lambda^2 \right] V_C(t) = \frac{2\omega_\lambda}{Q_{e1\lambda}} \frac{dV_1^+(t)}{dt} + \frac{2\omega_\lambda}{\sqrt{Q_{e1\lambda}Q_{e2\lambda}}} \sqrt{\frac{Z_{c1}}{Z_{c2}}} \frac{dV_2^+(t)}{dt}, \quad (\text{A.148})$$

where the loaded Q of the cavity is now defined as

$$\frac{1}{Q_{L\lambda}} = \frac{1}{Q_{0\lambda}} + \frac{1}{Q_{e1\lambda}} + \frac{1}{Q_{e2\lambda}}. \quad (\text{A.149})$$

The methods presented here will be used to characterize the diagnostic mode of the cavity described in Chapter 2.

#### Time-domain

As with the one-port case described in the previous section, we will drive the cavity system at an angular frequency  $\omega$  and adopt phasor notation with an  $e^{j\omega t}$  dependence on time. We will only drive port one,  $V_2^+ = 0$ . Using the approximation in equation (A.128), equation (A.148) is reduced to

$$2j\omega \frac{d\tilde{V}_C}{dt} + \left( \frac{j\omega\omega_\lambda}{Q_{L\lambda}} + \omega_\lambda^2 - \omega^2 \right) \tilde{V}_C = \frac{2j\omega\omega_\lambda}{Q_{e1\lambda}} \tilde{V}_1^+. \quad (\text{A.150})$$

Driving the cavity at its resonant frequency,  $\omega = \omega_\lambda$ , with a square input pulse of length  $T_p$  gives

$$\frac{d}{dt} \left( \frac{\tilde{V}_C(t)}{\tilde{V}_1^+} \right) + \frac{\omega_\lambda}{2Q_{L\lambda}} \left( \frac{\tilde{V}_C(t)}{\tilde{V}_1^+} \right) = \frac{\omega_\lambda}{Q_{e1\lambda}}, \quad (\text{A.151})$$

where  $\tilde{V}_1^+$  is constant. If the cavity is initially empty of fields then  $\tilde{V}_C(t=0) = 0$  so

the solution for the cavity voltage is

$$\frac{\tilde{V}_C(t)}{\tilde{V}_1^+} = \frac{2Q_{L\lambda}}{Q_{e1\lambda}} \left[ 1 - \exp\left(-\frac{\omega_\lambda t}{2Q_{L\lambda}}\right) \right]. \quad (\text{A.152})$$

If we define the coupling coefficients  $\beta_1$  and  $\beta_2$  for ports one and two respectively as

$$\beta_1 = \frac{Q_{0\lambda}}{Q_{e1\lambda}}, \quad \beta_2 = \frac{Q_{0\lambda}}{Q_{e2\lambda}}, \quad (\text{A.153})$$

and use continuity  $\tilde{V}_1^- = \tilde{V}_C - \tilde{V}_1^+$  then the reflection coefficient from port one (also known as  $S_{11}$ ) is

$$\frac{\tilde{V}_1^-(t)}{\tilde{V}_1^+} = \gamma - 1 - \gamma e^{-t/\tau} \quad 0 \leq t \leq T_p, \quad (\text{A.154})$$

where  $\tau = 2Q_{L\lambda}/\omega_\lambda$  and  $\gamma = 2\beta_1/(1 + \beta_1 + \beta_2)$ . Note that the loaded Q may also be written as

$$Q_{L\lambda} = \frac{Q_{0\lambda}}{1 + \beta_1 + \beta_2}. \quad (\text{A.155})$$

For  $t > T_p$ , the RF drive is off and equation (A.150) is reduced to

$$\frac{d\tilde{V}_C}{dt} + \frac{\omega_\lambda}{2Q_{L\lambda}} \tilde{V}_C = 0, \quad (\text{A.156})$$

where  $\tilde{V}_1^+ = 0$ . Using continuity at  $t = T_p$ , the reflection coefficient is

$$\frac{\tilde{V}_1^-(t)}{\tilde{V}_1^+} = \gamma [e^{T_p/\tau} - 1] e^{-t/\tau} \quad t > T_p, \quad (\text{A.157})$$

where  $\tilde{V}_C = \tilde{V}_1^- + \tilde{V}_1^+ = \tilde{V}_1^-$ .

Plots of  $V_1^-/V_1^+$  are similar to Figure A.6 except for the added complication of the second port. The determination of  $\beta_1$  by measuring the reflected power from port one depends on the value of  $\beta_2$  because of transmission out the second port.

### Frequency-domain

In the frequency-domain, equation (A.148) becomes

$$\left(-\omega^2 + \frac{j\omega\omega_\lambda}{Q_{L\lambda}} + \omega_\lambda^2\right) \tilde{V}_C = \frac{2j\omega\omega_\lambda}{Q_{e1\lambda}} \tilde{V}_1^+ + \frac{2j\omega\omega_\lambda}{\sqrt{Q_{e1\lambda}Q_{e2\lambda}}} \sqrt{\frac{Z_{c1}}{Z_{c2}}} \tilde{V}_2^+. \quad (\text{A.158})$$

Using the definition of the tuning angle from equation (A.138), the cavity voltage is rewritten as

$$\tilde{V}_C = 2Q_{L\lambda} \cos \psi e^{j\psi} \left( \frac{\tilde{V}_1^+}{Q_{e1\lambda}} + \sqrt{\frac{Z_{c1}}{Z_{c2}}} \frac{\tilde{V}_2^+}{\sqrt{Q_{e1\lambda}Q_{e2\lambda}}} \right). \quad (\text{A.159})$$

From [45, p. 230], the scattering parameters for a two-port network are

$$\begin{aligned} S_{11} &= \left. \frac{\tilde{V}_1^-}{\tilde{V}_1^+} \right|_{\tilde{v}_2^+=0}, & S_{21} &= \left. \frac{\tilde{V}_2^-}{\tilde{V}_1^+} \right|_{\tilde{v}_2^+=0} \sqrt{\frac{Z_{c1}}{Z_{c2}}}, \\ S_{12} &= \left. \frac{\tilde{V}_1^-}{\tilde{V}_2^+} \right|_{\tilde{v}_1^+=0} \sqrt{\frac{Z_{c2}}{Z_{c1}}}, & S_{22} &= \left. \frac{\tilde{V}_2^-}{\tilde{V}_2^+} \right|_{\tilde{v}_1^+=0}. \end{aligned} \quad (\text{A.160})$$

$S_{11}$  is the reflection coefficient from port one when port two is terminated in a matched load.  $S_{21}$  is the transmission coefficient from port one to port two. The same definitions apply to port two. For a reciprocal network like a two-port cavity,  $S_{21} = S_{12}$ .

Using the definition of the coupling coefficients from equation (A.153) with equations (A.124) the S-parameters for a two-port cavity are

$$S_{11} = \frac{2\beta_1}{1 + \beta_1 + \beta_2} \cos \psi e^{j\psi} - 1, \quad (\text{A.161a})$$

$$S_{21} = \frac{2\sqrt{\beta_1\beta_2}}{1 + \beta_1 + \beta_2} \cos \psi e^{j\psi}, \quad (\text{A.161b})$$

$$S_{22} = \frac{2\beta_2}{1 + \beta_1 + \beta_2} \cos \psi e^{j\psi} - 1. \quad (\text{A.161c})$$

Figure A.9 plots the magnitude and phase of  $S_{11}$ ,  $S_{22}$  and  $S_{21}$  for a particular choice of parameters. A vector network analyzer will measure and display the S-parameters of a two-port network. From these measurements, we can determine  $\omega_\lambda$ ,  $Q_{0\lambda}$ ,  $Q_{e1\lambda}$

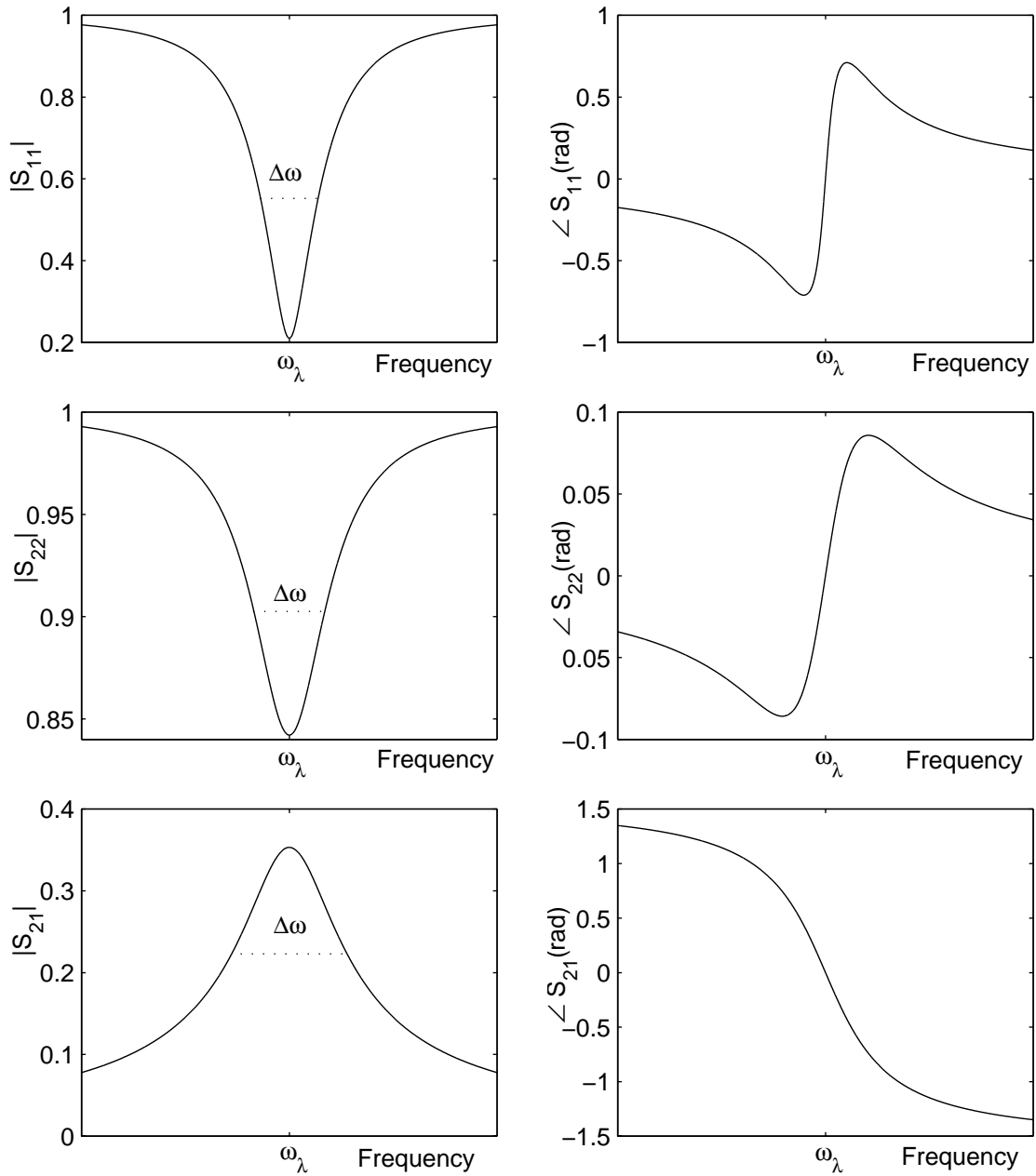


Figure A.9: S-parameters of two-port cavity for  $\beta_1 = 0.75$  and  $\beta_2 = 0.15$ . Notice that both port one and port two are under-coupled.

and  $Q_{e2\lambda}$ .

As in the case of a one-port cavity, the resonant frequency occurs at the minimum of  $|S_{11}|$ . The resonant frequency also occurs at the minimum of  $|S_{22}|$  and the maximum of  $|S_{21}|$ . There are two methods for determining the coupling coefficients. The first method requires the measurement of the minimums of  $|S_{11}|$  and  $|S_{22}|$  and the knowledge of the slope of their phases at the resonant frequency. The second method requires the minimums of  $|S_{11}|$  and  $|S_{22}|$  and the maximum of  $|S_{21}|$ .

The minimum of  $|S_{11}|$  is

$$S_{11m} \equiv \min |S_{11}| = \frac{|\beta_1 - (1 + \beta_2)|}{1 + \beta_1 + \beta_2}, \quad (\text{A.162})$$

and the minimum of  $|S_{22}|$  is

$$S_{22m} \equiv \min |S_{22}| = \frac{|\beta_2 - (1 + \beta_1)|}{1 + \beta_1 + \beta_2}. \quad (\text{A.163})$$

If  $\beta_1 > (1 + \beta_2)$ , then port one is said to be over-coupled. If  $\beta_1 < (1 + \beta_2)$ , then port one is said to be under-coupled. Similar definitions apply to port two. As with a one-port cavity, we need to know the slopes of the phases of  $S_{11}$  and  $S_{22}$  at the resonant frequency to determine if the ports are over or under-coupled. The slopes are

$$\left. \frac{d\angle S_{11}}{d\omega} \right|_{\omega=\omega_\lambda} = \left. \frac{d\angle S_{11}}{d\psi} \right|_{\psi=0} \left. \frac{d\psi}{d\omega} \right|_{\omega=\omega_\lambda} = -\frac{4Q_{L\lambda}}{\omega_\lambda} \frac{1}{1 - \frac{1+\beta_2}{\beta_1}}, \quad (\text{A.164a})$$

$$\left. \frac{d\angle S_{22}}{d\omega} \right|_{\omega=\omega_\lambda} = \left. \frac{d\angle S_{22}}{d\psi} \right|_{\psi=0} \left. \frac{d\psi}{d\omega} \right|_{\omega=\omega_\lambda} = -\frac{4Q_{L\lambda}}{\omega_\lambda} \frac{1}{1 - \frac{1+\beta_1}{\beta_2}}. \quad (\text{A.164b})$$

Therefore, if  $\beta_1 > (1 + \beta_2)$  then the slope of  $\angle S_{11}$  is negative and if  $\beta_1 < (1 + \beta_2)$  then the slope of  $\angle S_{11}$  is positive. A similar conclusion is made with  $\angle S_{22}$ . Note that it is possible for ports one and two to be both under-coupled but they cannot both be over-coupled.

Looking at equations (A.162–A.163) we may write

$$\beta_1 = A_1(1 + \beta_2), \quad \beta_2 = A_2(1 + \beta_1), \quad (\text{A.165})$$

where

$$A_1 = \begin{cases} \frac{1+S_{11m}}{1-S_{11m}} & \beta_1 > (1 + \beta_2) \\ \frac{1-S_{11m}}{1+S_{11m}} & \beta_1 < (1 + \beta_2), \end{cases} \quad (\text{A.166})$$

and

$$A_2 = \begin{cases} \frac{1+S_{22m}}{1-S_{22m}} & \beta_2 > (1 + \beta_1) \\ \frac{1-S_{22m}}{1+S_{22m}} & \beta_2 < (1 + \beta_1). \end{cases} \quad (\text{A.167})$$

From the knowledge of the maximum of  $|S_{21}|$

$$S_{21m} \equiv \max |S_{21}| = \frac{2\sqrt{\beta_1\beta_2}}{1 + \beta_1 + \beta_2}, \quad (\text{A.168})$$

with  $A_1$  and  $A_2$ , the coupling coefficients may also be determined from

$$\beta_1 = \frac{\left(\frac{S_{21m}}{2}\right)^2 (1 + A_2) \left(1 + \frac{1}{A_2}\right)}{1 - \left(\frac{S_{21m}}{2}\right)^2 (1 + A_2) \left(1 + \frac{1}{A_2}\right)}, \quad (\text{A.169a})$$

$$\beta_2 = \frac{\left(\frac{S_{21m}}{2}\right)^2 (1 + A_1) \left(1 + \frac{1}{A_1}\right)}{1 - \left(\frac{S_{21m}}{2}\right)^2 (1 + A_1) \left(1 + \frac{1}{A_1}\right)}. \quad (\text{A.169b})$$

Notice that the determination of the coupling coefficients from equations (A.169) is independent of whether ports one or two are under or over-coupled.

The loaded Q for the cavity may be found in a manner analogous to the method described in section A.4.2 using data from either  $|S_{11}|$ ,  $|S_{21}|$  or  $|S_{22}|$ . The formulas

are given below

$$Q_{L\lambda} = \frac{\omega_\lambda}{\Delta\omega} \sqrt{\frac{4\beta_1(1+\beta_2)}{(1+\beta_1+\beta_2)^2} \frac{1}{1-|S_{11}(\Delta\omega)|^2} - 1}, \quad (\text{A.170a})$$

$$Q_{L\lambda} = \frac{\omega_\lambda}{\Delta\omega} \sqrt{\frac{4\beta_1\beta_2}{(1+\beta_1+\beta_2)^2} \frac{1}{|S_{21}(\Delta\omega)|^2} - 1}, \quad (\text{A.170b})$$

$$Q_{L\lambda} = \frac{\omega_\lambda}{\Delta\omega} \sqrt{\frac{4\beta_2(1+\beta_1)}{(1+\beta_1+\beta_2)^2} \frac{1}{1-|S_{22}(\Delta\omega)|^2} - 1}. \quad (\text{A.170c})$$

$Q_{0\lambda}$ ,  $Q_{e1\lambda}$  and  $Q_{e2\lambda}$  are determined from equations (A.149) and (A.153).

#### A.4.4 Q Measurement With Lossy Coupling

Another method by which the coupling coefficients, loaded and unloaded Q of a one-port cavity may be determined is to examine the reflection circle on a Smith chart [45]. One such example is shown in Figure A.10 for an over-coupled cavity.

Some quick information may be gathered by inspection of the reflection coefficient plotted on the Smith chart. If the reflection circle encloses the center of the Smith chart, then the cavity is over-coupled ( $\beta > 1$ ). Likewise, if the reflection circle does not encompass the center of the Smith chart, then the cavity is under-coupled. If there is no loss in the coupling circuit, then the reflection circle will touch the circumference of the Smith chart. If loss does occur, then the reflection circle will be shifted away from the circumference of the Smith chart and the value of the overall coupling coefficient will also shift.

An equation may be developed for this circle using an equivalent circuit [21, p. 104]. The reflection coefficient is parameterized as [21, p. 112]

$$\Gamma(\delta) = \frac{a_1\delta + a_2}{a_3\delta + 1}, \quad (\text{A.171})$$

where  $\delta = 2(\omega - \omega_L)/\omega_L$  and  $a_1$ ,  $a_2$  and  $a_3$  are the coefficients to be fit.  $\omega_L$  is the loaded angular resonant frequency which is shifted slightly from the true resonant

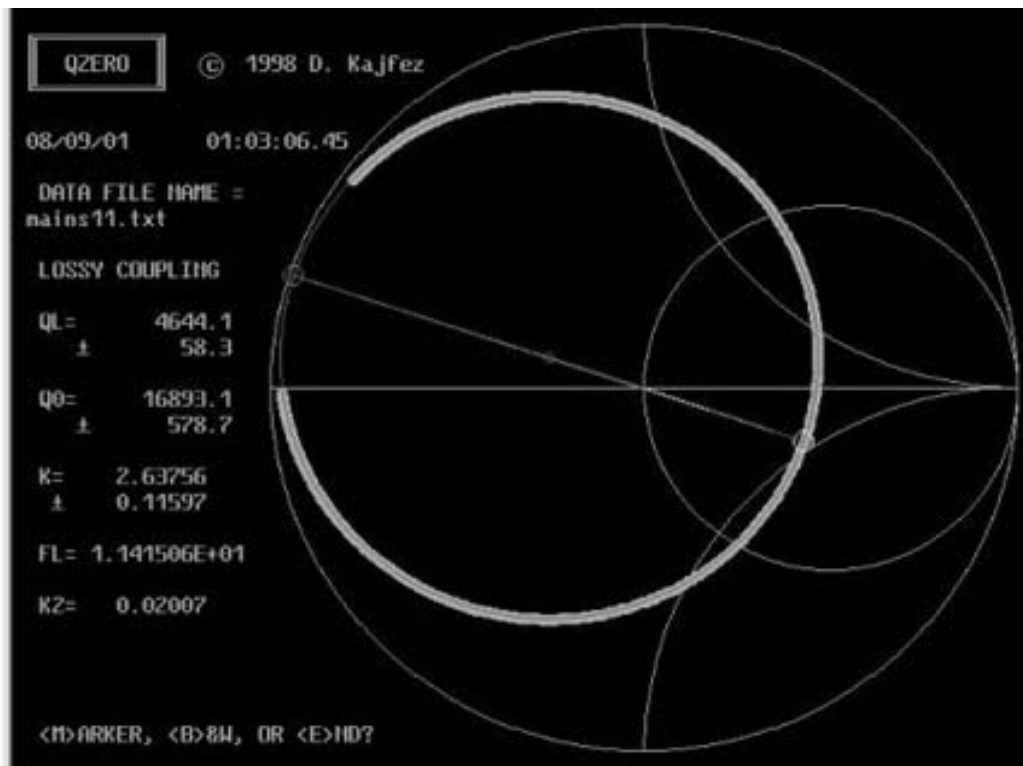


Figure A.10: Output from QZERO program from [21] in which the reflection circle from a cavity mode is fit to find  $Q_0$  and  $\beta$ .

frequency  $\omega_0$ . However, this shift is quite small and is not important in our analysis.

The overall coupling coefficient for a device with lossy coupling is split into two parts. One part describes the coupling to the actual cavity while the other part represents the loss due to the coupling mechanism. However, this parameterization assumes the loss occurs within an RF wavelength and may not be suitable for distributed loss due to long waveguides or scattering from other components. A consistency check can be performed by comparing the results to the equations given in Section A.4.2. The two coupling coefficients are

$$\kappa_{1i} = \frac{1}{2 \left( \frac{1}{d_{1i}} - \frac{1}{d_{1L}} \right)}, \quad (\text{A.172a})$$

$$\kappa_{1L} = \frac{\frac{2}{d_{1L}} - 1}{2 \left( \frac{1}{d_{1i}} - \frac{1}{d_{1L}} \right)}, \quad (\text{A.172b})$$

where  $d_{1i}$  is the diameter of the reflection circle given by

$$d_{1i} = 2 \frac{|a_2 a_3 - a_1|}{|a_3^* - a_3|}, \quad (\text{A.173})$$

and  $d_{1L}$  is a parameter representing the coupling loss and is given by

$$d_{1L} = \frac{1 - |\Gamma_d|^2}{1 - |\Gamma_d| \cos \phi}, \quad (\text{A.174})$$

where

$$\Gamma_d = \frac{a_1}{a_3}, \quad (\text{A.175a})$$

$$\Gamma_c = \frac{a_3^* a_2 - a_1}{a_3^* - a_3}, \quad (\text{A.175b})$$

$$\phi = \tan^{-1} \left[ \frac{\Im(\Gamma_d)}{\Re(\Gamma_d)} \right] + \tan^{-1} \left[ \frac{\Im(\Gamma_c - \Gamma_d)}{\Re(\Gamma_c - \Gamma_d)} \right]. \quad (\text{A.175c})$$

For lossless coupling,  $d_{1L} = 2$ .

The total coupling coefficient is now given by

$$\beta = \kappa_{1i} + \kappa_{1L}. \quad (\text{A.176})$$

The loaded Q of the cavity is given by

$$Q_L = \Im(a_3), \quad (\text{A.177})$$

and the unloaded Q is found from the usual formula

$$Q_0 = Q_L(1 + \beta). \quad (\text{A.178})$$

QZERO is a program presented in [21] that performs a fit to the data and outputs  $Q_L$ ,  $Q_0$  and  $\beta$ . An example of its output is given in Figure A.10.

For a two-port cavity, the techniques described above also apply since the S-parameters,  $S_{11}$ ,  $S_{21}$  and  $S_{22}$  are all of the same form as equation (A.171)[30]. Therefore the same fitting techniques described in [21] can be used to find the RF properties of a two-port cavity with lossy coupling.

The coupling coefficients are given by

$$\beta_1 = \kappa_{1i} + \kappa_{1L}, \quad (\text{A.179a})$$

$$\beta_2 = \kappa_{2i} + \kappa_{2L}, \quad (\text{A.179b})$$

with

$$\kappa_{1i} = \frac{d_{1i}}{2 \left[ 1 - \left( \frac{d_{1i}}{d_{1L}} + \frac{d_{2i}}{d_{2L}} \right) \right]}, \quad (\text{A.180a})$$

$$\kappa_{1L} = \kappa_{1i} \left( \frac{2}{d_{1L}} - 1 \right), \quad (\text{A.180b})$$

$$\kappa_{2i} = \frac{d_{2i}}{2 \left[ 1 - \left( \frac{d_{1i}}{d_{1L}} + \frac{d_{2i}}{d_{2L}} \right) \right]}, \quad (\text{A.180c})$$

$$\kappa_{2L} = \kappa_{2i} \left( \frac{2}{d_{2L}} - 1 \right), \quad (\text{A.180d})$$

where  $d_{1i}$  is the diameter of the reflection circle for  $S_{11}$ ,  $d_{1L}$  is the coupling loss parameter for  $S_{11}$ ,  $d_{2i}$  is the diameter of the reflection circle for  $S_{22}$  and  $d_{2L}$  is the coupling loss parameter for  $S_{22}$ . These parameters can be found from equations (A.173–A.174) with  $\Gamma_d$  replaced with  $S_{11}$  for  $d_{1i}$  and  $d_{1L}$  and likewise for  $S_{22}$ . The loaded  $Q$  is found from fitting the  $S_{21}$  circle on the Smith chart and using equation (A.177). The unloaded  $Q$  for the two-port cavity is finally given by

$$Q_0 = Q_L(1 + \beta_1 + \beta_2). \quad (\text{A.181})$$

This method for measuring the RF properties of a two-port cavity will be used in conjunction with the methods described in Section A.4.3 to check for consistency of the measurement results.

# Appendix B

## SEM Pictures of Endcaps

The following pages show additional pictures of damage to the copper endcaps presented in Chapter 4. These pictures are for documentation purposes and do not present any information additional to that which was already discussed in Chapter 4.

### B.1 Endcap 1L1

Figure B.1 shows pictures of damage to endcap 1L1 with a scale of 100  $\mu\text{m}$ . Figure B.2 shows various cracks on a smaller scale.

### B.2 Endcap 1R1

Figure B.3 shows pictures of damage to endcap 1R1 with a scale of 100  $\mu\text{m}$ . Figure B.4 shows various cracks on a smaller scale.

### B.3 Endcap 2L1

Figure B.5 shows pictures of damage to endcap 2L1 with a scale of 100  $\mu\text{m}$ . Figure B.6 shows various cracks on a smaller scale.

## **B.4 Endcap 2R1**

Figure B.7 shows pictures of damage to endcap 2R1 with a scale of 100  $\mu\text{m}$ . Figure B.8 shows various cracks on a smaller scale.

## **B.5 Endcap 1L2**

Figures B.9–B.10 shows pictures of damage to endcap 1L2 with a scale of 100  $\mu\text{m}$ . Figure B.11 shows various cracks and slip bands on a smaller scale.

## **B.6 Endcap 1R2**

Figures B.12–B.13 shows pictures of damage to endcap 1R2 with a scale of 100  $\mu\text{m}$ . Figure B.14 shows various cracks and slip bands on a smaller scale.

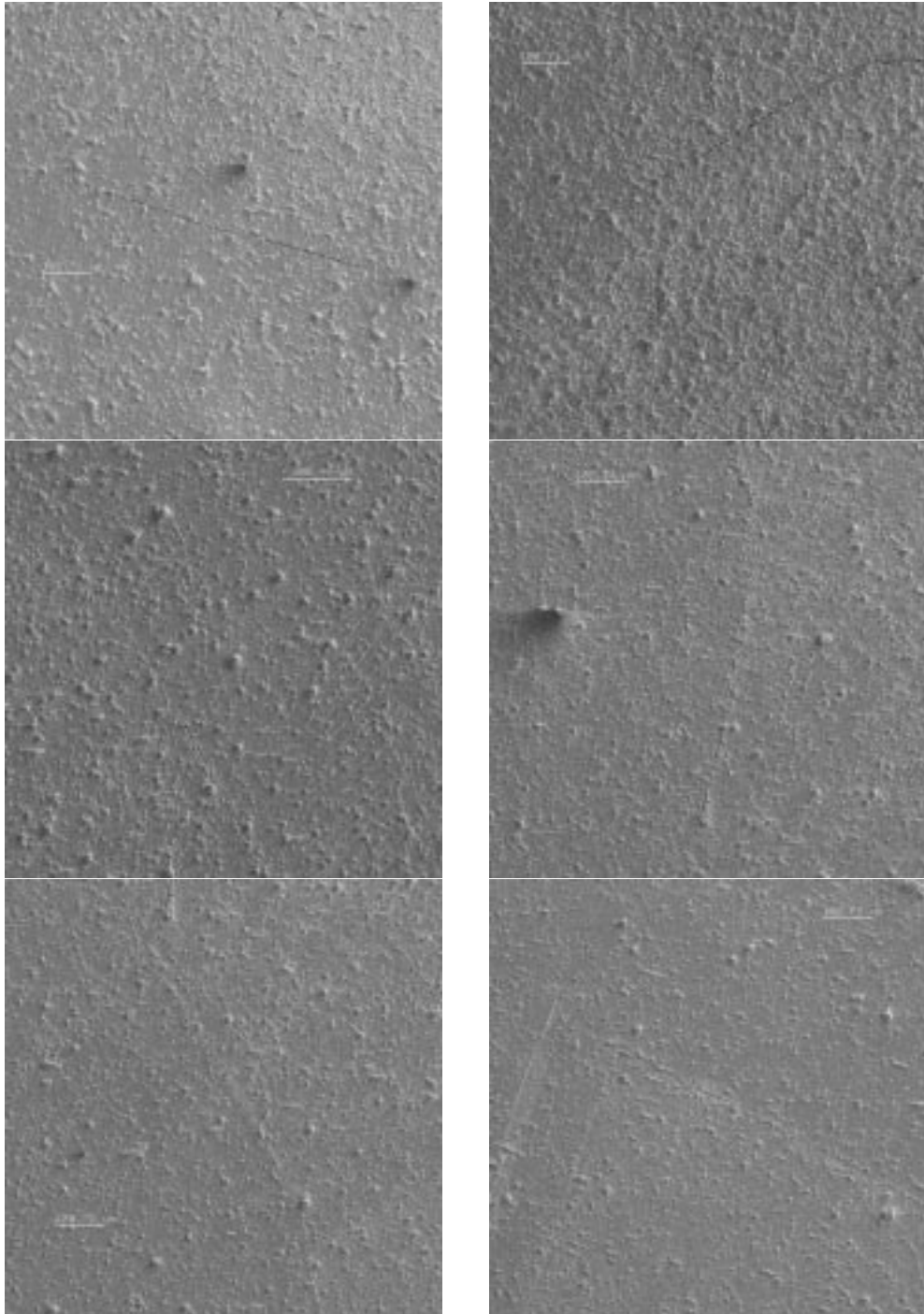


Figure B.1: Pictures of cracks on endcap 1L1 in the area of maximum temperature rise. The length scale in all pictures is 100  $\mu\text{m}$ .

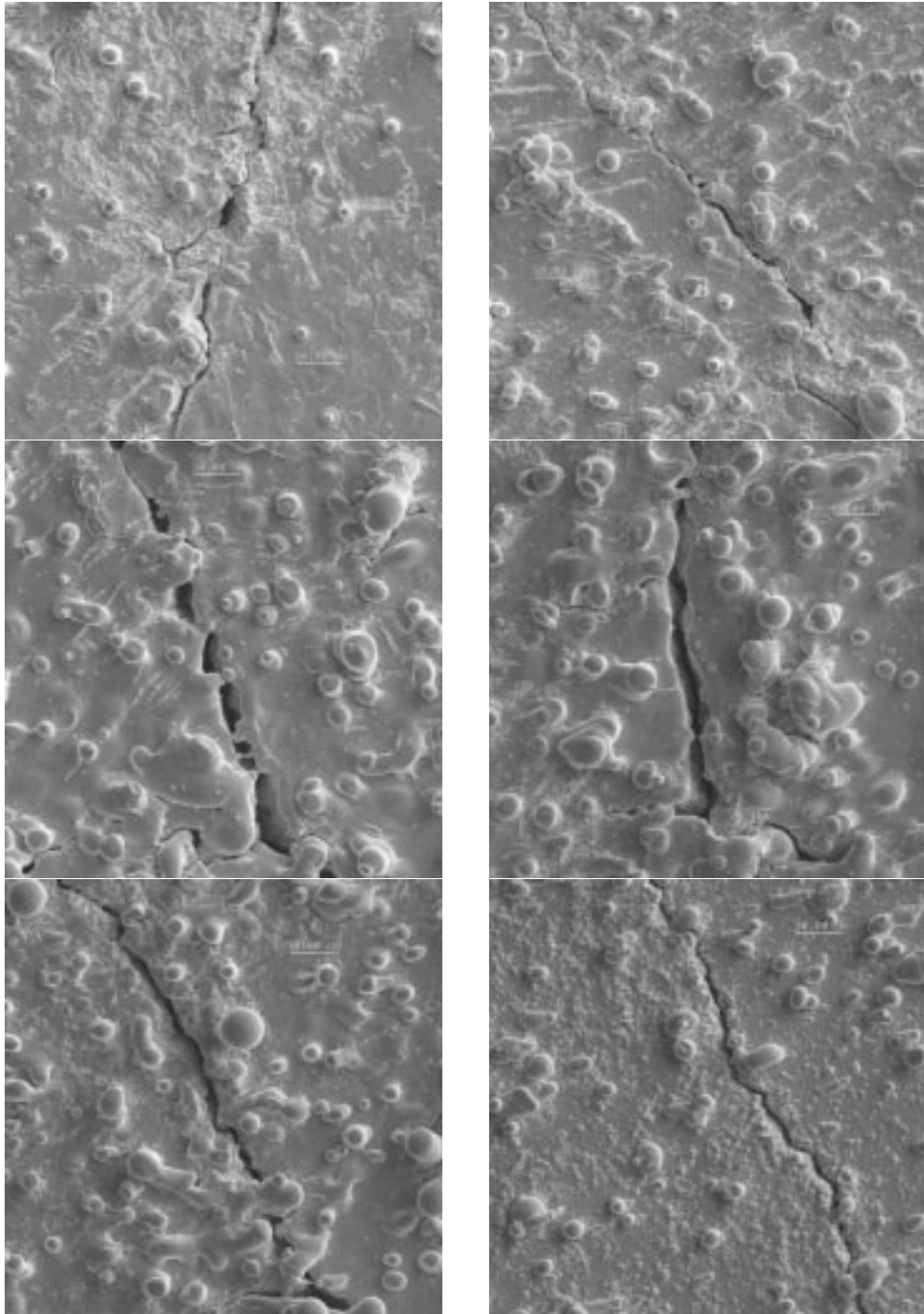


Figure B.2: Pictures of cracks on endcap 1L1 in the area of maximum temperature rise. The length scale in all pictures is 10  $\mu\text{m}$ .

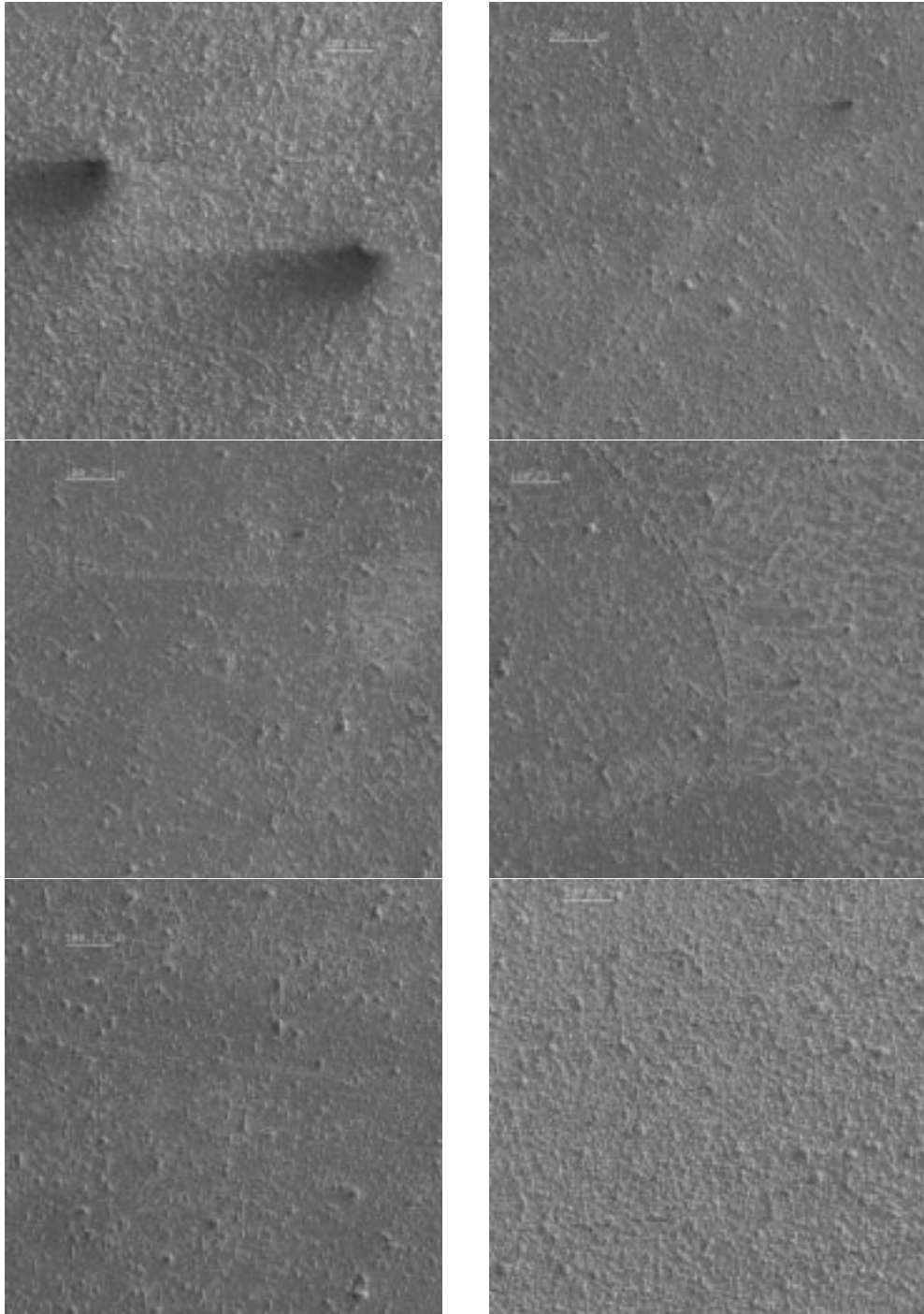


Figure B.3: Pictures of cracks on endcap 1R1 in the area of maximum temperature rise. The length scale in all pictures is 100  $\mu\text{m}$ .

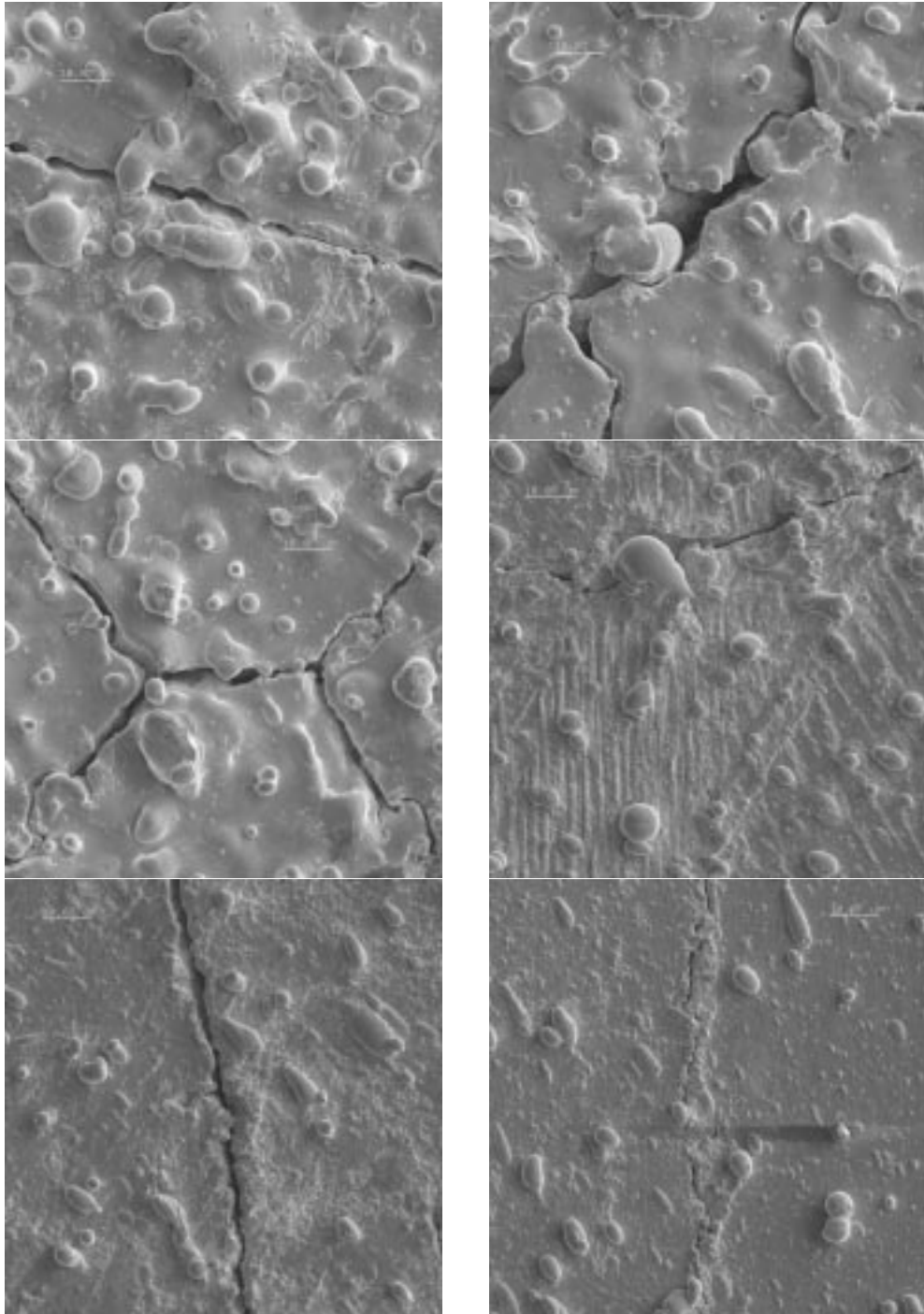


Figure B.4: Pictures of cracks on endcap 1R1 in the area of maximum temperature rise. The length scale in all pictures is 10  $\mu\text{m}$ .

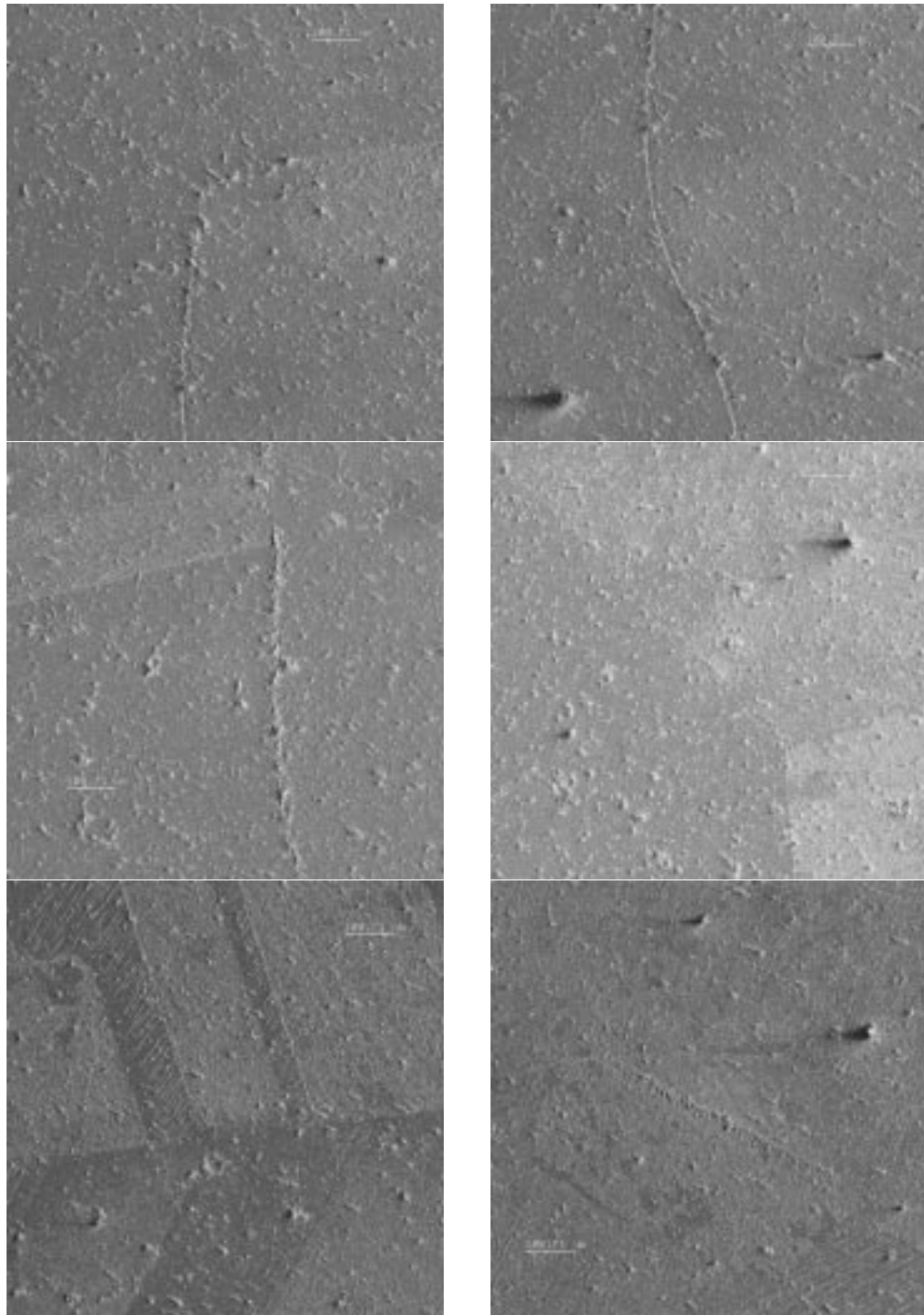


Figure B.5: Pictures of cracks on endcap 2L1 in the area of maximum temperature rise. The length scale in all pictures is 100  $\mu\text{m}$ .

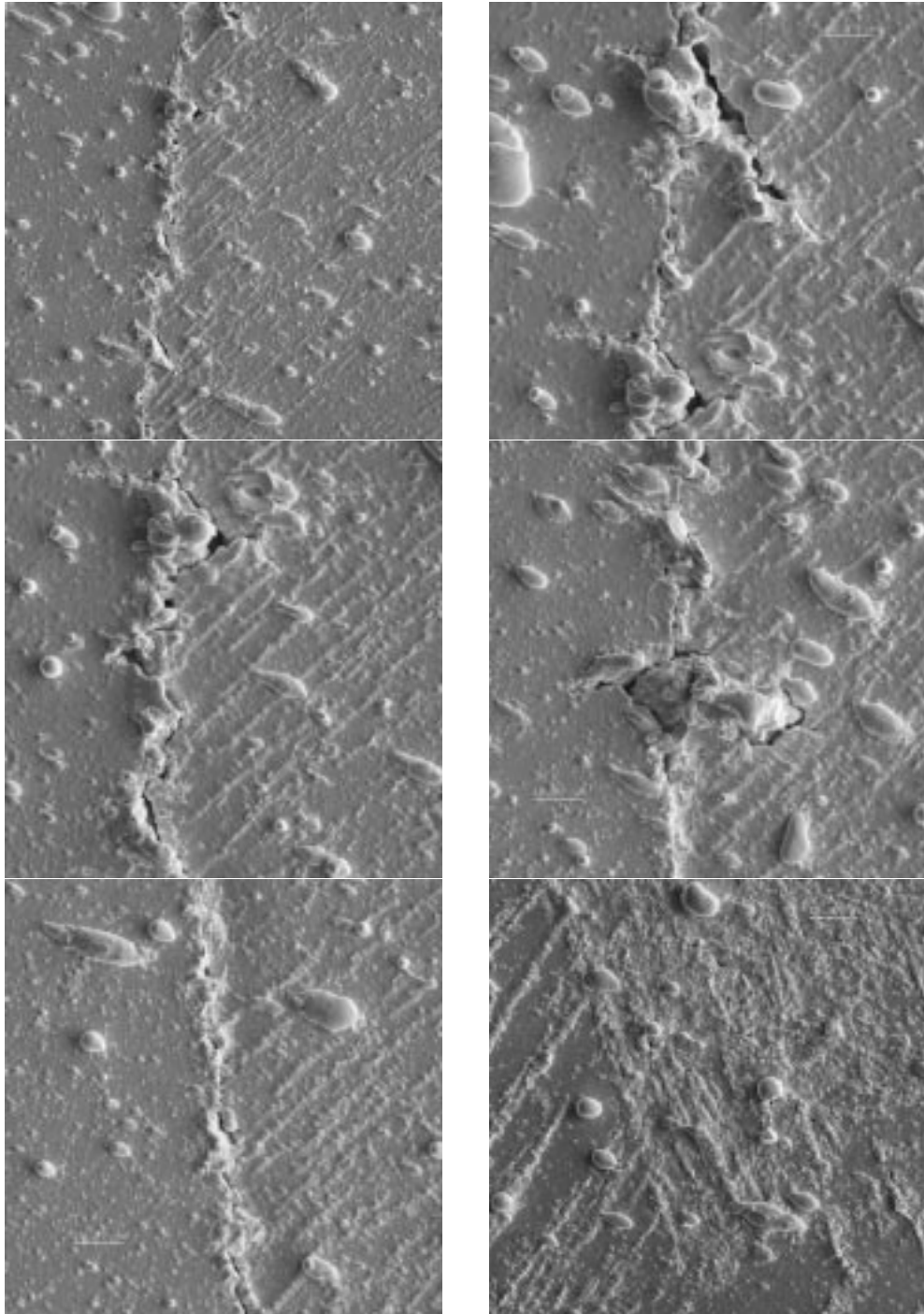


Figure B.6: Pictures of cracks on endcap 2L1 in the area of maximum temperature rise. The length scale in all pictures is 10  $\mu\text{m}$ .

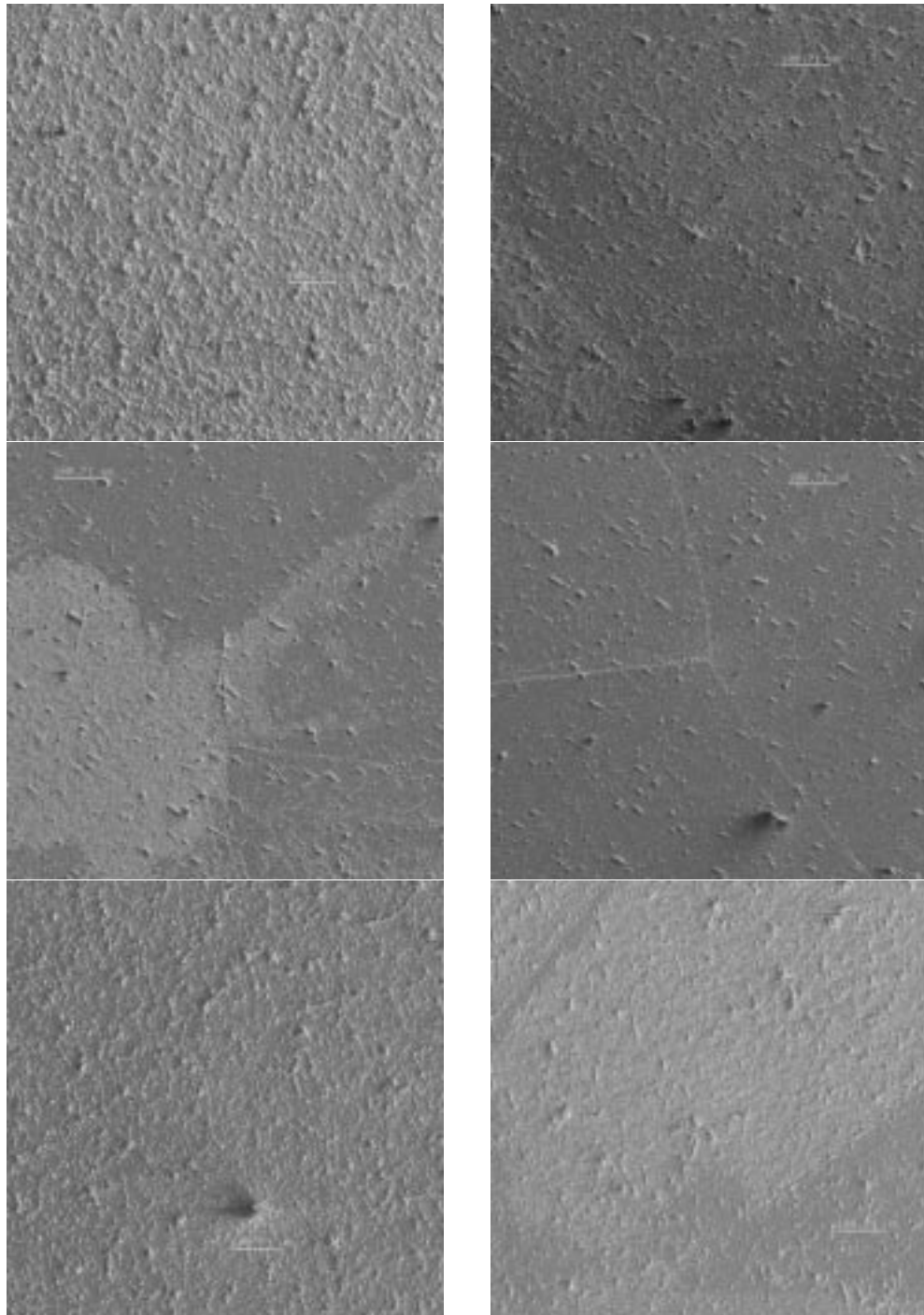


Figure B.7: Pictures of cracks on endcap 2R1 in the area of maximum temperature rise. The length scale in all pictures is 100  $\mu\text{m}$ .

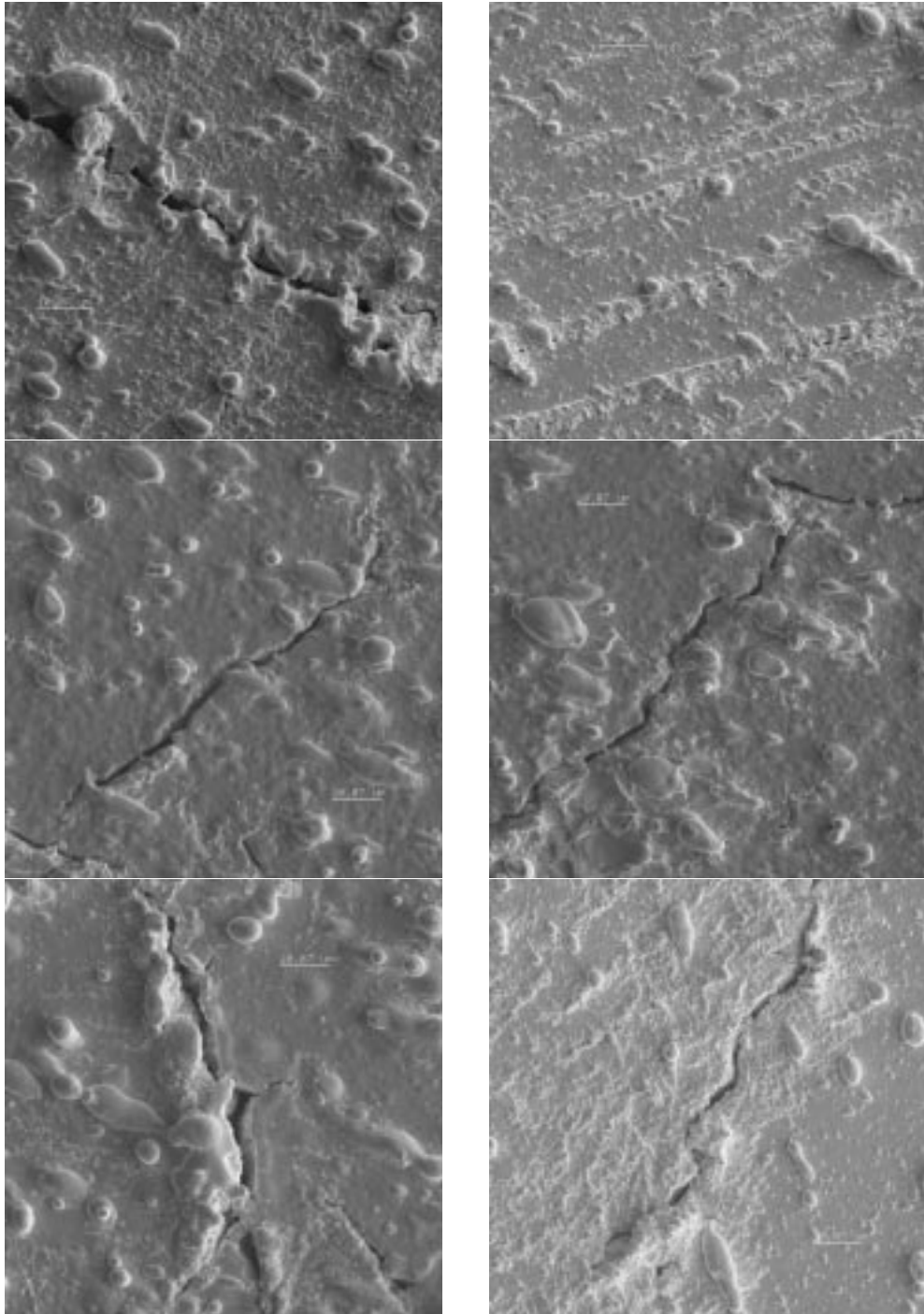


Figure B.8: Pictures of cracks on endcap 2R1 in the area of maximum temperature rise. The length scale in all pictures is 10  $\mu\text{m}$ .

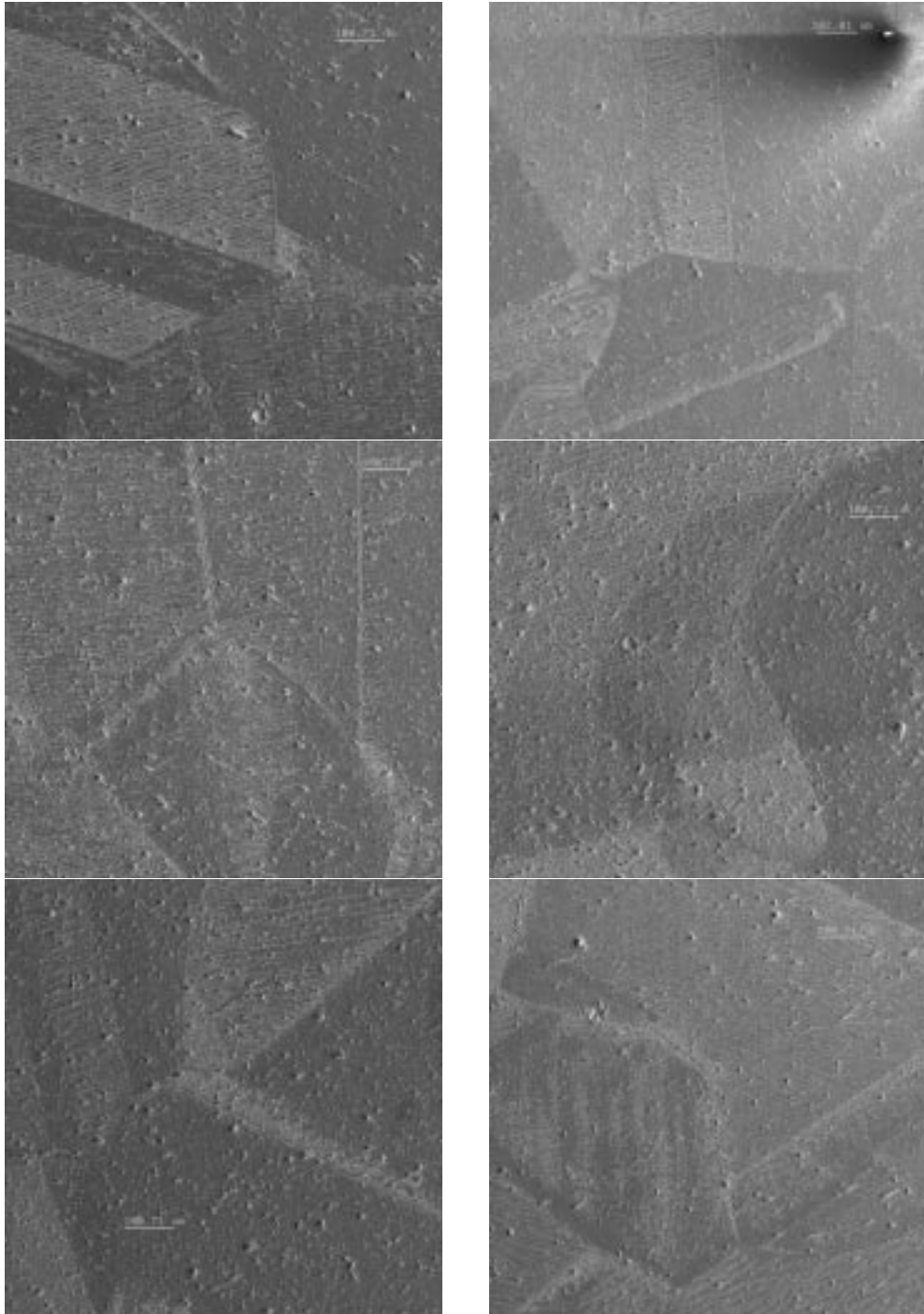


Figure B.9: Pictures of damage on endcap 1L2 in the area of maximum temperature rise. The length scale in all pictures is 100  $\mu\text{m}$ .

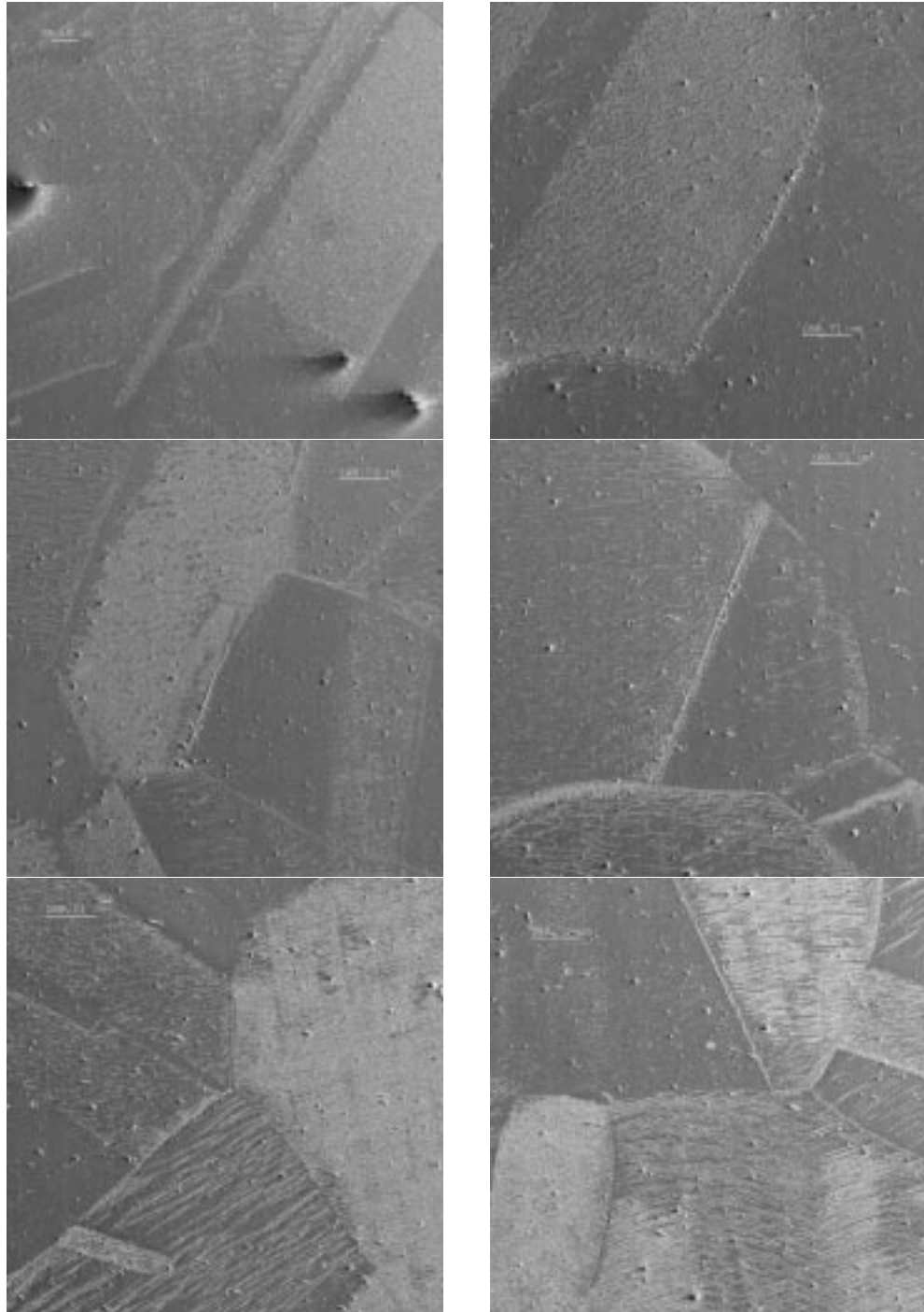


Figure B.10: Pictures of damage on endcap 1L2 in the area of maximum temperature rise. The length scale in all pictures is 100  $\mu\text{m}$ .

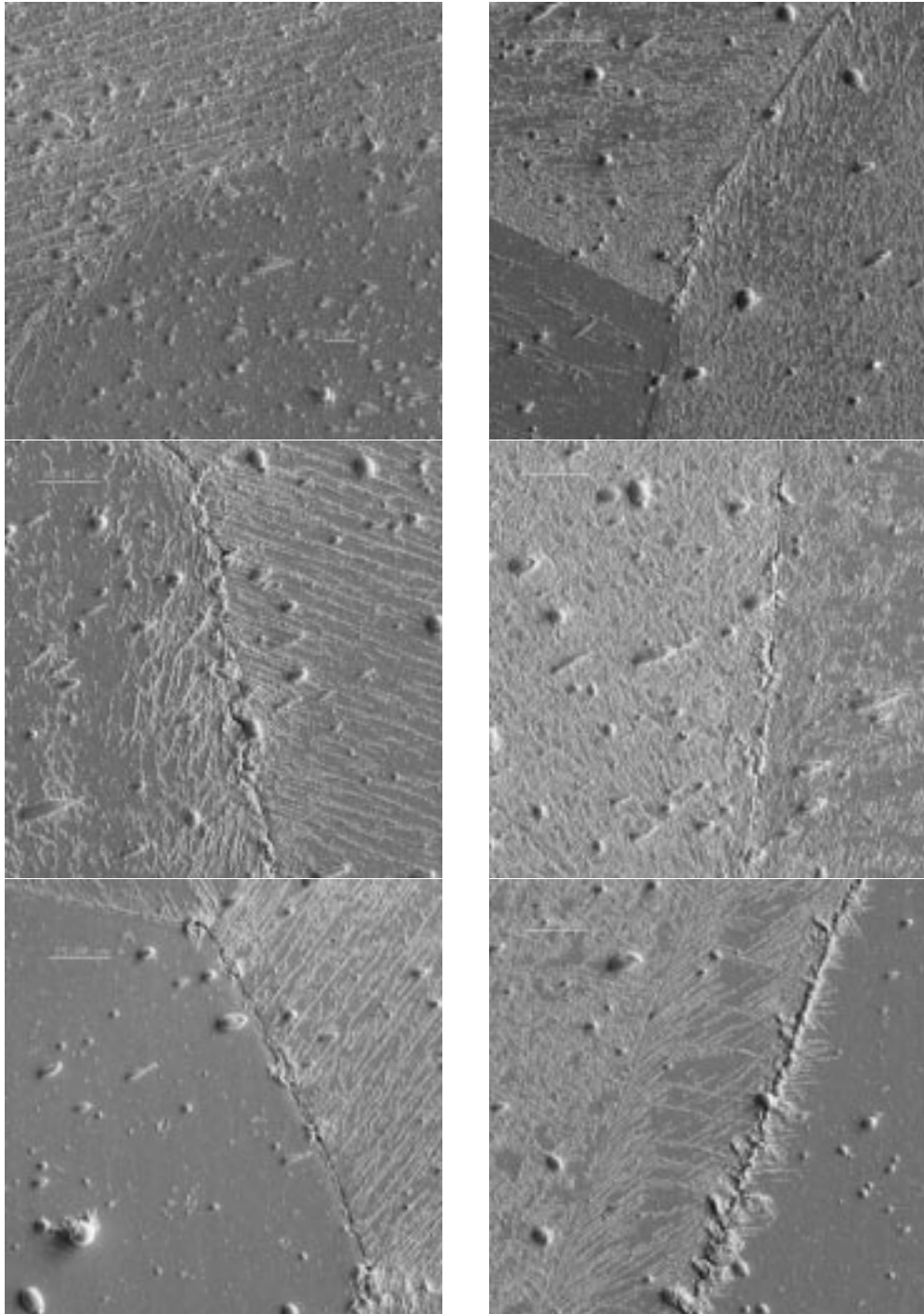


Figure B.11: Pictures of cracks on endcap 1L2 in the area of maximum temperature rise. The length scale in all pictures is 25  $\mu\text{m}$ .

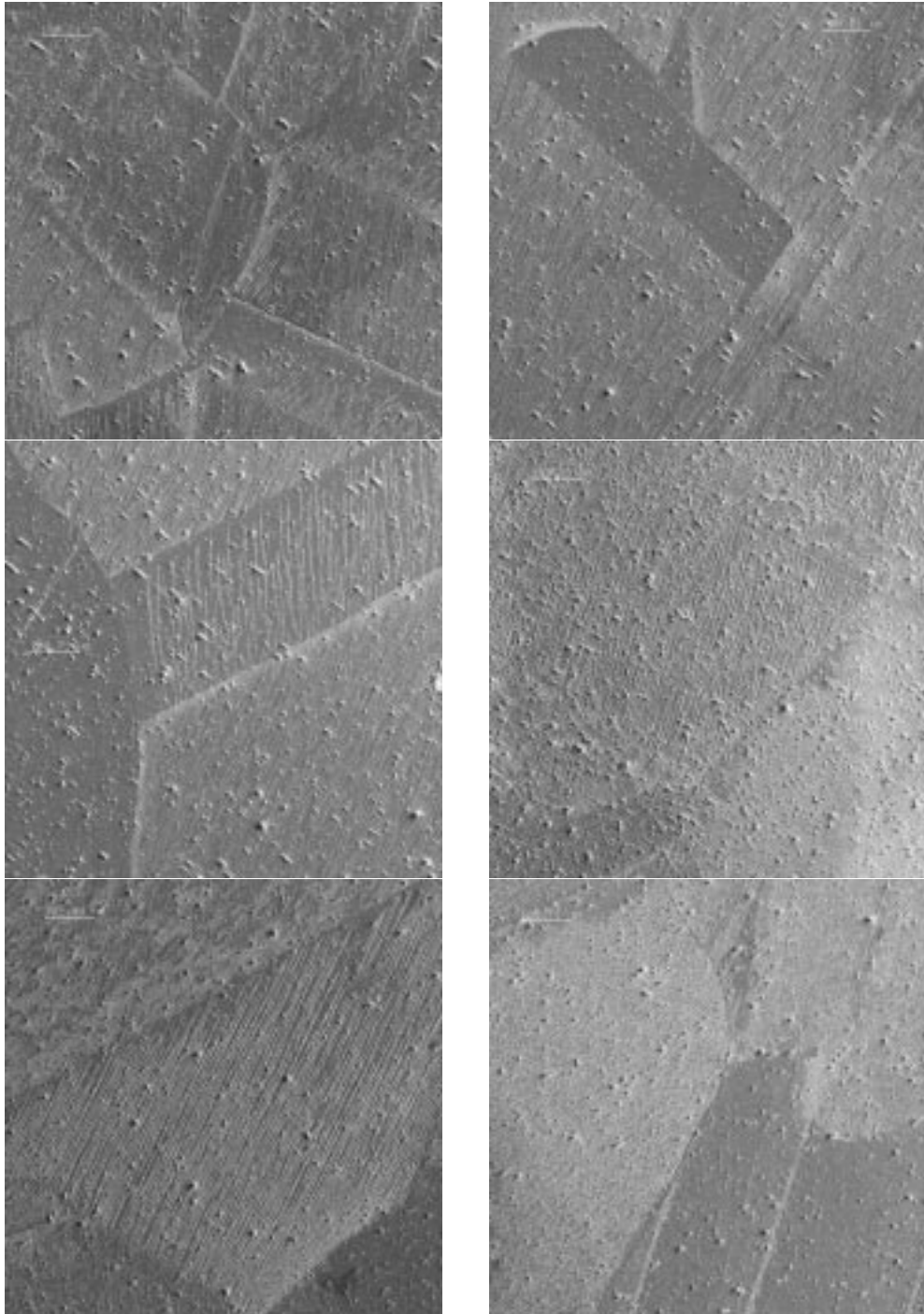


Figure B.12: Pictures of damage on endcap 1R2 in the area of maximum temperature rise. The length scale in all pictures is 100  $\mu\text{m}$ .

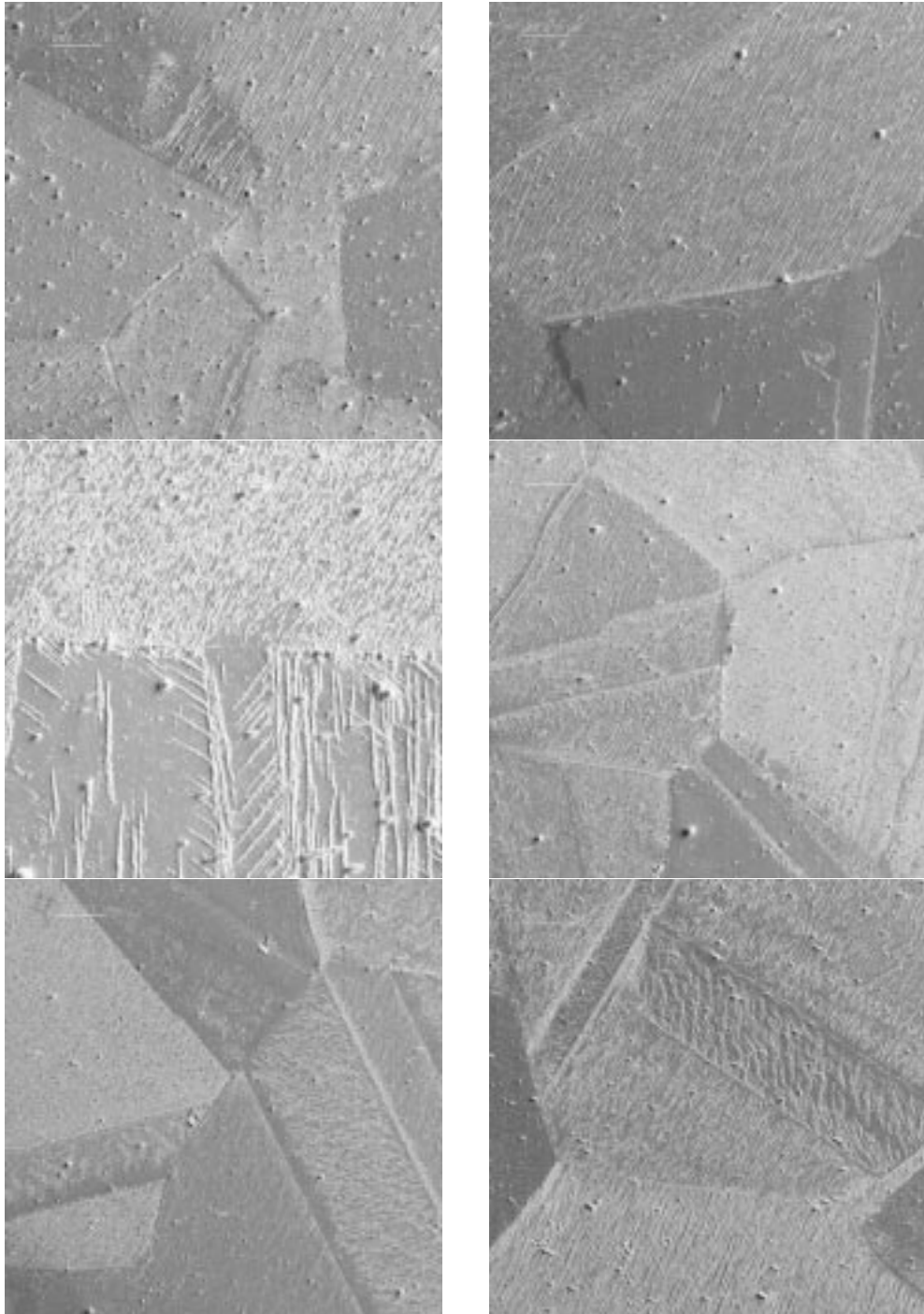


Figure B.13: Pictures of damage on endcap 1R2 in the area of maximum temperature rise. The length scale in all pictures is 100  $\mu\text{m}$ .

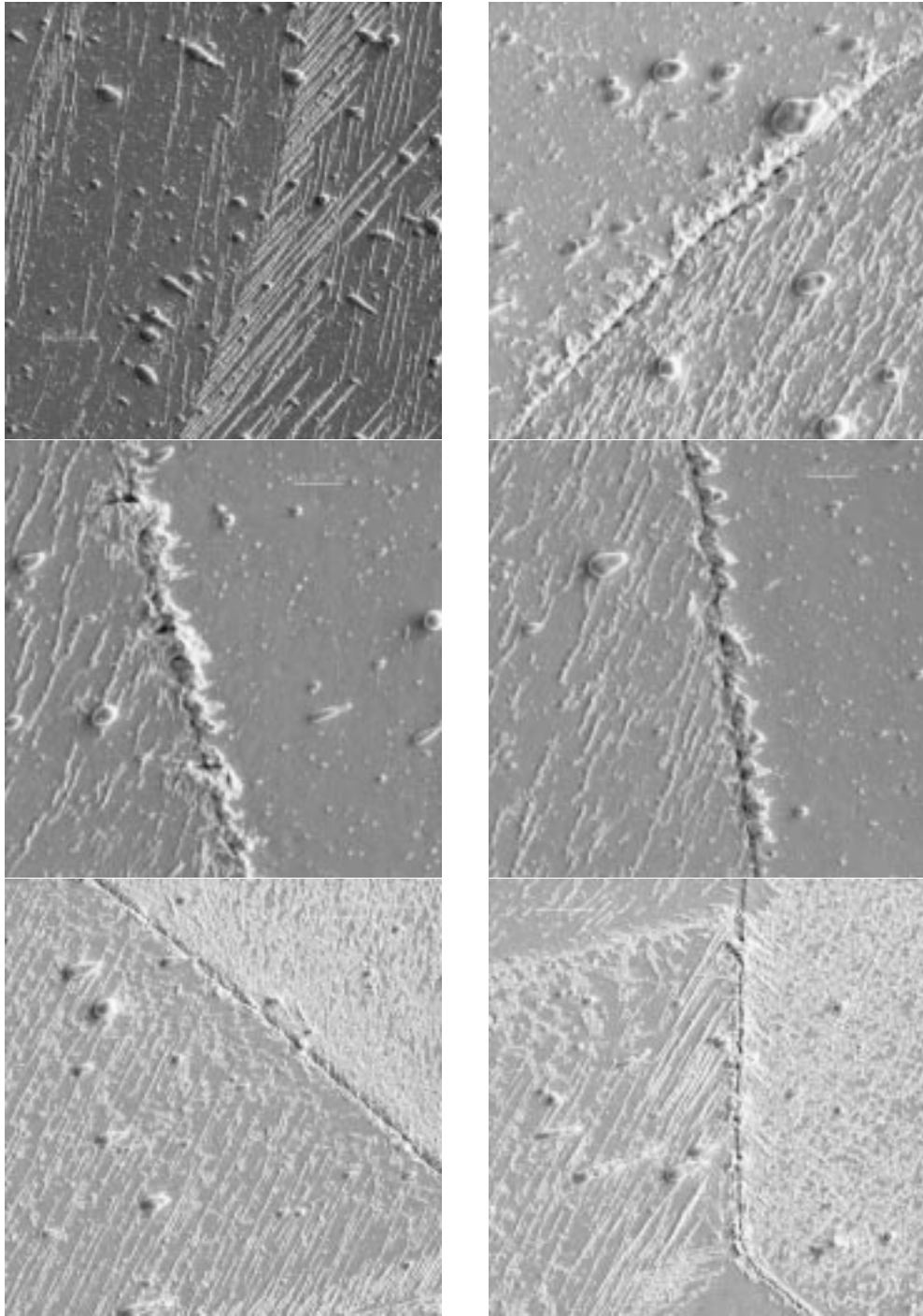


Figure B.14: Pictures of cracks on endcap 1R2 in the area of maximum temperature rise. The length scales in the pictures are 10  $\mu\text{m}$  and 25  $\mu\text{m}$ .

# Bibliography

- [1] Milton Abramowitz and Irene A. Stegun, editors. *Handbook of Mathematical Functions With Formulas, Graphs, and Mathematical Tables*. National Bureau of Standards, Washington, D.C., ninth edition, 1970.
- [2] Ansoft. *Ansoft HFSS Ver 5*. <http://www.ansoft.com>, Pennsylvania, 1998.
- [3] Julie A. Bannantine, Jess J. Comer, and James L. Handrock. *Fundamentals of Metal Fatigue Analysis*. Prentice Hall, New Jersey, 1990.
- [4] O. H. Basquin. The exponential law of endurance tests. *Am. Soc. Test. Mater. Proc.*, 10:625–630, 1910.
- [5] J. Bauschinger. *Mitt: Mech-Tech Lab.*, 13(1), 1886.
- [6] J. V. Beck, K. D. Cole, A. Haji-Sheikh, and B. Litkouhi. *Heat Conduction Using Green's Functions*. Hemisphere Publishing Corporation, London, 1992.
- [7] Matěj Bílý, editor. *Cyclic Deformation and Fatigue of Metals*. Number 78 in Materials Science Monographs. Elsevier, Amsterdam, 1993.
- [8] Bruno A. Boley and Jerome H. Weiner. *Theory of Thermal Stresses*. Dover Publications, Inc., New York, 1997.
- [9] Gordon B. Bowden. Rf surface heating stresses. Technical Report NLC ME NOTE 8-96, Stanford Linear Accelerator Center, August 1996.
- [10] W. Bruns. Improvements in gdfidl. In *Proceedings of the 1999 Particle Accelerator Conference*, pages 2767–2768. IEEE, 1999.

- [11] Richard L. Burden and J. Douglas Faires. *Numerical Analysis*. PWS Publishing Company, Boston, fifth edition, 1993.
- [12] Pei Chi Chou and Nicholas J. Pagano. *Elasticity: Tensor, Dyadic, and Engineering Approaches*. Dover Publications, Inc., New York, 1992.
- [13] L. F. Coffin, Jr. A study of the effects of cyclic thermal stresses on a ductile metal. *Trans. ASME*, 76:931–950, 1954.
- [14] Robert E. Collin. *Field Theory of Guided Waves*. IEEE Press, New York, second edition, 1991.
- [15] J. Gao. Analytical formula for the coupling coefficient  $\beta$  of a cavity-waveguide coupling system. *Nuclear Instruments and Methods in Physics Research A*, 309:5–10, 1991.
- [16] CST GmbH. *MAFIA User Guide 4.00*. <http://www.cst.de>, Darmstadt, Germany, 1998.
- [17] I. S. Gradshteyn and I. M. Ryzhik. *Table of Integrals, Series, and Products*. Academic Press, Inc., San Diego, California, fourth edition, 1980.
- [18] R. W. K. Honeycombe. *The Plastic Deformation of Metals*. Edward Arnold, London, 1984.
- [19] IEEE. *Proceedings of the 1997 Particle Accelerator Conference*, 1997.
- [20] John David Jackson. *Classical Electrodynamics*. John Wiley & Sons, New York, second edition, 1975.
- [21] Darko Kajfez. *Q Factor*. Vector Fields, Oxford, Mississippi, 1994.
- [22] Mirko Klesnil and Petr Lukáš. *Fatigue of Metallic Materials*. Number 71 in Materials Science Monographs. Elsevier, Amsterdam, 1992.
- [23] V. F. Kovalenko. *Physics of Heat Transfer and Electrovacuum Devices*. Sovetskoe Radio, Moscow, 1975.

- [24] Donald E. Kreinheder and Terrance D. Lingren. Improved selectivity in cylindrical  $te_{011}$  filters by  $te_{211}/te_{311}$  mode control. *IEEE Transactions on Microwave Theory and Techniques*, 30(9):1383–1387, 1982.
- [25] Norman M. Kroll and Xin-Tian Lin. Computer determinations of the properties of waveguide loaded cavities. In *Proceedings of the 1990 Linear Accelerator Conference*, 1990.
- [26] Norman M. Kroll and David U. L. Yu. Computer determination of the external  $q$  and resonant frequency of waveguide loaded cavities. *Partical Accelerators*, 34:231–250, 1990.
- [27] Kaneyuki Kurokawa. The expansions of electromagnetic fields in cavities. *IRE Transactions on Microwave Theory And Technology*, 6:178–187, 1958.
- [28] Kaneyuki Kurokawa. *An Introduction To The Theory Of Microwave Circuits*. Academic Press, New York, 1969.
- [29] L. D. Landau and E. M. Lifshitz. *Theory of Elasticity*. Number 7 in Course of Theoretical Physics. Pergamon Press, Oxford, second edition, 1970.
- [30] Kenneth Leong and Janina Mazierska. Accounting for lossy coupling in measurements of  $q$ -factors of transmission mode dielectric resonators. In *Proceedings of the Asia Pacific Microwave Conference*, pages 209–212, 1998.
- [31] David R. Lide, editor. *CRC Handbook of Chemistry and Physics*. CRC Press LLC, eightieth edition, 1999.
- [32] Xintian E. Lin. Diamond coating in accelerator structure. Technical Report ARDB-185, Accelerator Research Department B, Stanford Linear Accelerator Center, August 1998.
- [33] Peter Linz. *Analytical and Numerical Methods for Volterra Equations*. Society for Industrial and Applied Mathematics, Philadelphia, 1985.

- [34] Gregory A. Loew. Alternate approaches to future electron-positron linear colliders. In Siemann [51], pages 27–33.
- [35] Gregory A. Loew and J. W. Wang. Rf breakdown studies in room temperature electron linac structures. Technical Report SLAC-PUB-4647, Stanford Linear Accelerator Center, May 1988.
- [36] S. S. Manson. Behavior of materials under conditions of thermal stress. In *Heat Transfer Symposium*, pages 9–75. University of Michigan Engineering Research Institute, 1953.
- [37] R. Mavaddat. *Network Scattering Parameters*. Number 2 in Advanced Series in Circuits and Systems. World Scientific, Singapore, 1996.
- [38] William H. McAdams. *Heat Transmission*. McGraw-Hill Book Co., Inc., New York, third edition, 1954.
- [39] C. G. Montgomery, R. H. Dicke, and E. M. Purcell, editors. *Principles of Microwave Circuits*. Number 8 in Radiation Laboratory Series. McGraw-Hill Book Company, Inc., New York, 1948.
- [40] Philip M. Morse and Herman Feshbach. *Methods of Theoretical Physics, Part I*. McGraw-Hill, Inc., New York, 1953.
- [41] Henry M. Musal, Jr. Thermomechanical stress degradation of metal mirror surfaces under pulsed laser irradiation. In *Laser Induced Damage in Optical Materials 1979*, pages 159–173, 1980.
- [42] Oleg A. Nezhevenko. On the limitations of accelerating gradients in linear colliders due to the pulse heating. In *Proceedings of the 1997 Particle Accelerator Conference* [19], pages 3013–3014.
- [43] Hasan Padamsee, Jens Knobloch, and Tom Hays. *RF Superconductivity for Accelerators*. John Wiley & Sons, Inc., New York, 1998.

- [44] Jaroslav Polák. *Cyclic Plasticity and Low Cycle Fatigue Life of Metals*. Number 63 in Materials Science Monographs. Elsevier, Amsterdam, 1991.
- [45] David M. Pozar. *Microwave Engineering*. Addison-Wesley Publishing Company, Reading, Massachusetts, first edition, 1990.
- [46] William H. Press, Saul A. Teukolsky, William T. Vetterling, and Brian P. Flannery. *Numerical Recipes in C: The Art of Scientific Computing*. Cambridge University Press, New York, second edition, 1992.
- [47] D. P. Pritzkau et al. Experimental study of pulsed heating of electromagnetic cavities. In *Proceedings of the 1997 Particle Accelerator Conference* [19], pages 3036–3038.
- [48] David P. Pritzkau. Coupled cavity-waveguide calculations. Technical Report ARDB-43, Accelerator Research Department B, Stanford Linear Accelerator Center, April 1997.
- [49] David Roylance. *Mechanics of Materials*. John Wiley & Sons, Inc., New York, 1996.
- [50] Robert H. Siemann. Advanced electron linacs. In *Symposium on Electron Linear Accelerators: In Honor of Richard B. Neal's 80th Birthday* [51], pages 45–54.
- [51] Robert H. Siemann, editor. *Symposium on Electron Linear Accelerators: In Honor of Richard B. Neal's 80th Birthday*. Stanford Linear Accelerator Center, September 1997.
- [52] I. S. Sokolnikoff. *Mathematical Theory of Elasticity*. Robert E. Krieger Publishing Company, Malabar, Florida, second edition, 1956.
- [53] S. Suresh. *Fatigue of Materials*. Number 8 in Cambridge Solid State Science Series. Cambridge University Press, Great Britain, Cambridge, first edition, 1991.
- [54] Richard A. Swalin. *Thermodynamics of Solids*. John Wiley & Sons, Inc., New York, 1962.

- [55] S. P. Timoshenko and J. N. Goodier. *Theory of Elasticity*. McGraw-Hill Publishing Company, New York, third edition, 1970.
- [56] Arnold E. Vlieks et al. Breakdown phenomena in high power klystrons. Technical Report SLAC-PUB-4546, Stanford Linear Accelerator Center, March 1988.
- [57] David H. Whittum. Introduction to electrodynamics for microwave linear accelerators. Technical Report SLAC-PUB-7802, Stanford Linear Accelerator Center, April 1998.
- [58] Perry B. Wilson. Scaling linear colliders to 5 tev and above. In *ITP Conference on Future High Energy Colliders*. University of California, Santa Barbara, October 1996.